Isovalent and Aliovalent Doping Effects on the Structural and Magnetic Properties of A-Site Columnar-Ordered Quadruple Perovskites Synthesized under High Pressure

A Thesis

Submitted by

Xuan LIANG

In fulfillment for the award of the degree of

Doctor of Science

Graduate School of Chemical Sciences and Engineering,

Hokkaido University

2025

Abstract

Perovskite materials have been the focus of intensive research for decades due to their rich and diverse physical properties. They exhibit unique thermoelectric, electrochemical, catalytic, and magnetic behaviors, stemming from the complex interplay among spin, charge, and orbital degrees of freedom. The perovskite structure, typically represented by the general formula ABO_3, is one of the most adaptable structures in solid-state chemistry, giving rise to numerous structural variants. Among the various classes of perovskites, the A-site columnar ordered $A_2A'A''B_4O_{12}$ quadruple perovskite has garnered particular interest owing to its remarkable structural and magnetic characteristics. This thesis focuses on the design, synthesis, and investigation of new members of this family, employing rare-earth oxides and transition metals. The crystal structures and magnetic properties of the synthesized compounds are examined in detail.

Chapter 1 provides an overview of the fundamental background on perovskite materials, including their structural and magnetic properties, with particular emphasis on the characteristics of A-site columnar-ordered quadruple perovskites. This lays the foundation for the subsequent discussion.

Chapter 2 describes the experimental procedures employed in this study, including the synthesis methods and various characterization techniques, such as synchrotron X-ray powder diffraction and magnetic measurements. Chapters 3 to 5 present three distinct series of perovskites, highlighting the structure-property relationships within the $A_2A'A''B_4O_{12}$ family. Chapter 6 concludes the thesis by summarizing the key findings and proposing directions for future research.

Chapter 3 investigates the solid solution $Nd_2MnMn(Mn_{4-x}Sb_x)O_{12}$, which belongs to the A-site columnar ordered quadruple perovskite subfamily. These compounds were synthesized by adjusting the Sb^{5+} content ($0.2 \leq x \leq 2.0$) and characterized using synchrotron X-ray powder diffraction. Aliovalent Sb^{5+} substitution enabled a continuous modulation of the Mn oxidation states. The study identified two distinct cation-ordering regimes within the B-site sublattice: for $0.8 \leq x \leq 1.0$, the structure is B-site disordered with space group $P4_2/nmc$ (No. 137), whereas for $1.6 \leq x \leq 2.0$, a rock-salt-type B-site ordering appears with space group $P4_2/n$ (No. 86). Magnetic measurements revealed complex behavior featuring two ferromagnetic transitions. The transition temperature T_C

varies with *x*, reflecting the intricate correlation between cation ordering and magnetic properties.

Chapter 4 investigates the negative magnetization effect (NME) observed in the $Ce_2MnM(Mn_2Sb_2)O_{12}$ (M = Mn, Zn), A-site columnar-ordered quadruple perovskites derived from the previous series and incorporating the highest Sb content. These compounds exhibited pronounced NME under low-field field-cooled magnetic measurements. Their room-temperature crystal structures were examined using synchrotron X-ray powder diffraction. Both compounds crystallize in space group $P4_2/n$, featuring full rock-salt ordering of Mn and Sb at the B sites. Bond-valence sum analysis suggests that Ce is in the trivalent state. Magnetic measurements revealed a single magnetic transition in both compounds, with compensation points varying depending on the M-site ion. The robust, intrinsic NME is likely attributable to their ferrimagnetic structure.

Chapter 5 focuses on a new series of A-site columnar-ordered quadruple perovskites, $R_2MnZn(MnZnSb_2)O_{12}$ (R = La, Pr, Nd, and Sm), derived from the previous series, and investigates the effects of different rare-earth cations and non-magnetic Zn^{2+} doping on their structural and magnetic properties. The crystal structure of the R = Nd sample (space group $P4_2/n$) was analyzed using synchrotron X-ray powder diffraction data. Zn^{2+} cations were found to occupy both the octahedral B site (alongside Mn^{2+}) and the tetrahedral A″ site, although minor antisite disorder of Mn^{2+} and Zn^{2+} between the square-planar A′ site and the octahedral B site was also observed. The second B site is fully occupied by Sb^{5+}. Magnetic measurements revealed that rare-earth elements have a significant impact on the magnetic transitions. The presence of rare-earth cations enhanced the ferrimagnetic transition temperatures, indicating their role in strengthening exchange interactions among magnetic cations.

Chapter 6 summarizes the key findings of this study and outlines directions for future research. The results demonstrate that the structure and magnetic properties of $A_2A'A''B_4O_{12}$ quadruple perovskites can be finely tuned by manipulating cation distributions and introducing rare-earth elements. These insights open new avenues for exploring functional applications of these materials. Future studies can further synthesize more compounds and explore their potential in a variety of advanced materials applications.

Keywords: Quadruple perovskites, A-site columnar-ordered, High-pressure, Ferrimagnet, Crystal structures

List of Abbreviations

XRPD	X-ray powder diffraction
SXRPD	Synchrotron X-ray powder diffraction
RT	Room temperature
MPMS	Magnetic property measurement system
PPMS	Physical property measurement system
FCC	Field-cooled on cooling
ZFC	Zero-field-cooled
T_C	Curie temperature
T_N	Néel temperature
FM	Ferromagnetic
AFM	Antiferromagnetic
FIM	Ferrimagnetic
t	Tolerance factor
θ	Curie–Weiss temperature
C	Curie constant
μ_{eff}	Effective magnetic moment
μ_{calc}	Theoretical magnetic moment
χ	Magnetic susceptibility
H	Applied magnetic field
BVS	Bond-valance sum
C_p	Heat capacity
$C_{lattice}$	Lattice contribution
S_{mag}	Magnetic entropy
$-\Delta S_{mag}$	Magnetic entropy change
NIMS	National Institute for Materials Science

Isovalent and Aliovalent Doping Effects on the Structural and Magnetic Properties of A-Site Columnar-Ordered Quadruple Perovskites Synthesized under High Pressure

Contents

Chapter 1 Introduction

1.1 Perovskites

1.1.1 Conventional perovskites

The perovskite structure was initially discovered by German mineralogist Gustav Rose in 1839 for the $CaTiO_3$ mineral and named after Russian mineralogist Lev Perovski. The general chemical formula of perovskite-related compounds can be expressed as ABX_3, where A and B are cations and X is an anion, usually oxygen or halogen. Among ABX_3 compounds, the oxide perovskite with the chemical formula ABO_3 has been extensively investigated and is generally regarded as the conventional perovskite [1, 2].

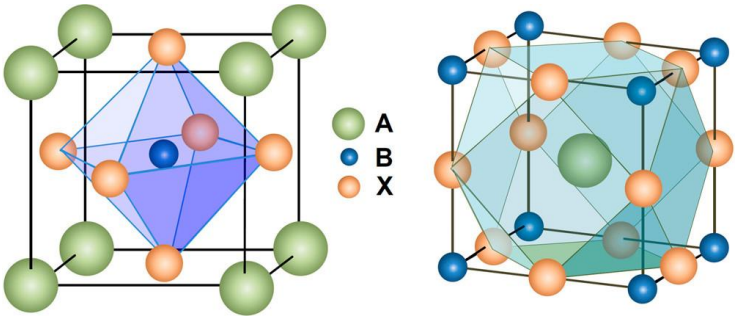

Figure 1.1 ABX_3 perovskite structure showing (left) BX_6 octahedral and (right) AX_{12} cuboctahedral geometry [3].

The ideal ABO_3 perovskite crystallizes in a cubic system with the *Pm*-3*m* space group. As shown in **Figure 1.1** [3], the A-site cation (commonly larger-radius alkali, alkaline-earth, or rare-earth elements) occupies the cube corner position (0, 0, 0) and coordinates with 12 nearest-neighbor oxygen ions to form an AO_{12} cuboctahedral polyhedron (when X = O). The B-site cation (typically smaller-radius 3*d*, 4*d*, or 5*d* transition metals) resides at the body-center position (0.5, 0.5, 0.5) and coordinates with 6 nearest-neighbor oxygen ions to form a BO_6 octahedron. Oxygen atoms are located at face-centered positions (0.5, 0.5, 0), (0.5, 0, 0.5), and (0, 0.5, 0.5), with each oxygen ion coordinated by two B-site cations and one A-site cation. Adjacent BO_6 octahedra are corner-shared and form cavities to accommodate the A-site cation. The structural stability of ABO_3 perovskites mainly depends on the relative sizes of effective ionic radii at the A

and B sites. To quantify this relationship, the Norwegian scientist Goldschmidt first defined the tolerance factor (t) [4]:

$$t = \frac{r\,(\mathrm{A}) + r\,(\mathrm{O})}{\sqrt{2}(r\,(\mathrm{B}) + r\,(\mathrm{O}))}$$

Where r (A) and r (B) represent the effective ionic radii of the A- and B-site cations, respectively, and r (O) is the radius of the oxygen ion. A tolerance factor close to unity ($t \approx 1$) typically indicates a stable cubic perovskite structure. For instance, in the case of $SrTiO_3$ with *Pm*-3*m* space group, the ionic radii r (Sr^{2+}) = 1.44 Å (in 12-fold coordination), r (Ti^{4+}) = 0.605 Å (in 6-fold coordination), r (O^{2-}) = 1.40 Å yield t =1.002 [5]. When t deviates slightly from 1, the BO_6 octahedral tends to tilt or distort to maintain structural stability. More significant deviations typically lead to structural distortion or the formation of alternative phases. If t is too high ($t > 1$), hexagonal or layered structures are often formed; if t is too low ($t < 0.71$), distorted low-symmetry structures such as trigonal, orthorhombic, tetragonal, or even amorphous phases are easily formed [6]. Notably, since t of most perovskites is not exactly equal to 1, the tilt and rotation of the BO_6 octahedra are widespread, particularly in double and quadruple perovskites. Consequently, the tolerance factor can be used as a predictive tool, which is essential for designing new perovskite materials with specific physical properties.

The physical properties of ABO_3 perovskites mainly depend on B-site cations. The tilt and distortion of BO_6 octahedra not only affect structural stability but also have a strong impact on the optical, electrical, and magnetic properties. As presented in **Figure 1.2**(a) [7], rotations of the octahedra can be decomposed about orthogonal axes that intersect at the transition metal center. In 1972, A. M. Glazer classified the tilt of the BO_6 octahedral based on crystallographic symmetry, employing a three-letter notation (x, x, x) (x = a, b, or c) with superscripts (+, −, 0) [8, 9]. The letters sequentially describe rotational tilts around the a, b, and c axes (or x, y, and z axes), where a/b/c denote distinct tilt magnitudes. A "+" superscript indicates in-phase tilting between consecutive octahedral layers perpendicular to the rotation axis, while "–" denotes out-of-phase tilting. The absence of tilting is marked by "0". **Figure 1.2**(b) illustrates several common types and demonstrates how the combination of tilt systems results in symmetry lowering of the cubic Bravais lattice. For instance, an ideal cubic ABO_3 perovskite (*Pm*-3*m* space group)

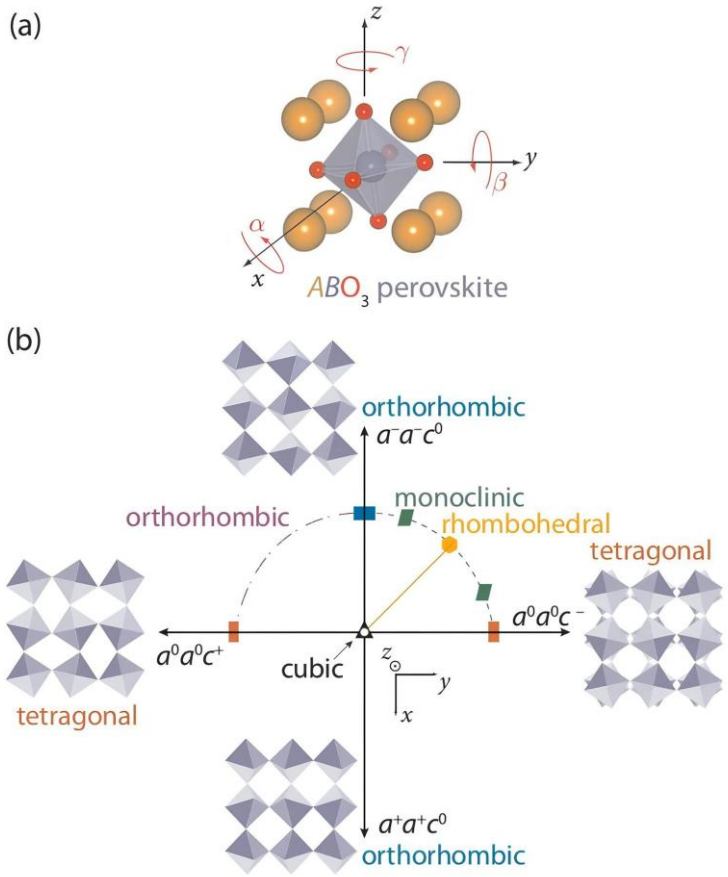

Figure 1.2 Octahedral rotation phase space in perovskite transition metal oxides. (a) Rotations of the octahedra can be decomposed about orthogonal axes that intersect at the transition metal center. (b) Several representative octahedral tilt patterns: $a^0a^0c^+$ and $a^0a^0c^-$ correspond to in-phase (c^+) and out-of-phase (c^-) rotations of the octahedra about the *z*-axis, respectively, while $a^+a^+c^0$ and $a^-a^-c^0$ produce similar rotations of the octahedra in the *xy*-plane. The relative rotation of adjacent octahedra from one layer to the next is clearly seen for the $a^0a^0c^-$ tilt pattern (far right) [7].

with no octahedral tilting will be classified as $a^0a^0a^0$. If the continuous layers of BO_6 octahedral tilting near *a* in the perovskite are tilted in phase, while the continuous layers of octahedral tilting near *b* and *c* are tilted out of phase and have the same tilt angle, then the system can be classified as $a^+b^-b^-$, corresponding to the orthorhombic space group *Pnma*. Glazer's classification encompasses 23 tilt patterns corresponding to 15 space groups. Subsequent work by C. J. Howard et al. further summarized the relationship among these space groups (**Figure 1.3**) [10]. The two space groups connected by the

dashed line will undergo a primary structural phase transition when they transition from one to another.

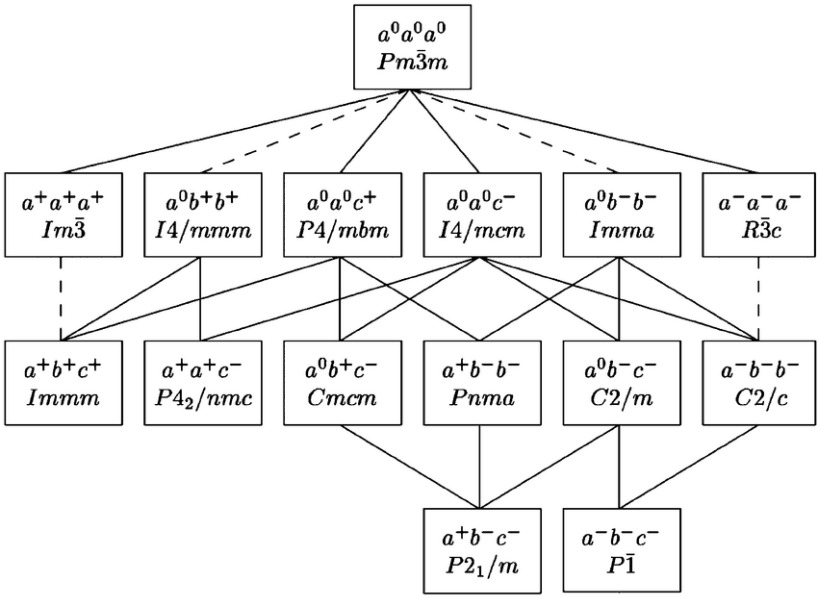

Figure 1.3 A schematic diagram indicating the group ± subgroup relationships among the 15 space groups. A dashed line joining a group with its subgroup indicates that the corresponding phase transition is required by Landau theory to be first order [10].

For many years, ABO_3 perovskites, characterized by their diverse elemental compositions and flexible crystal structures, have demonstrated a rich array of physical properties, including ferroelectricity [11], superconductivity [12], multiferroicity [13], giant magnetoresistance [14], and ionic conductivity [15]. These versatile properties have enabled perovskites to play a crucial role in various fields, including electronic devices, magnetic materials, energy storage and conversion, catalyst, and solid-state ionic applications [16-19].

1.1.2 Double perovskites

Double perovskites form a crystal structure with the chemical formula $A_2BB'O_6$ (**Figure 1.4**) by introducing two different B-site cations (B and B′) into the conventional ABO_3 structure [20]. The coordination numbers of A-site and B/B′-site cations remain the same as those in ABO_3 perovskites. The B/B′ sites are usually occupied by transition

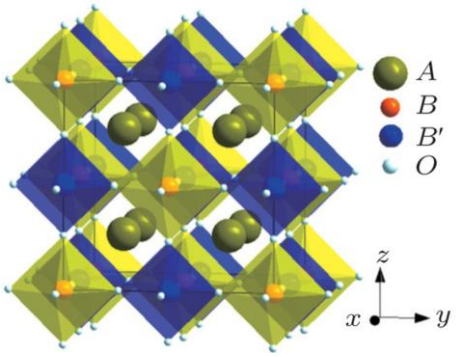

Figure 1.4 Crystal structure of B-site rock-salt ordered double perovskite $A_2BB'O_6$ with an *Fm*-3*m* space group. Atomic sites: A 8*c* (0.25, 0.25, 0.25), B 4*a* (0, 0, 0), B′ 4*b* (0.5, 0.5, 0.5), O 24*e* (*x*, 0, 0) [21].

metals of different oxidation state or size (e.g., Fe^{3+}/Mo^{5+}, Cu^{2+}/W^{6+}), forming an alternating BO_6 octahedral network. For example, in Sr_2CuWO_6 [22], CuO_6 and WO_6 octahedra are connected through shared vertices to form a three-dimensional framework. The size of the A-site cation (e.g., Sr^{2+}, Ba^{2+}, La^{2+}) should meet the modified tolerance factor condition:

$$t = \frac{r\,(\mathrm{A}) + r\,(\mathrm{O})}{\sqrt{2}(\frac{r\,(\mathrm{B}) + r\,(\mathrm{B}')}{2} + r\,(\mathrm{O}))}$$

It is well accepted that when the oxidation state difference (ΔZ) between B and B′ ions is less than 2, B-site disordered perovskite structures of $AB_{0.5}B'_{0.5}O_3$ form; ΔZ > 2 generally produce B-site ordered perovskite structures of $A_2BB'O_6$; ΔZ = 2 allows mixed ordering patterns (the B-site disordered, partially ordered, or completely ordered arrangement) according to the ionic radius difference and bonding preferences of B and B′ ions [20, 23, 24]. As shown in **Figure 1.5** [25], the B-site (A-site also) order includes three arrangements: rock-salt order features alternating B and B′ cations in three dimensions, resembling NaCl-type arrangements; layered order organizes B/B′ ions into alternating planar sheets; columnar order arranges B/B′ ions in parallel linear columns along specific crystallographic axes. These ordering patterns are directly influenced by the cooperative tilting of $B/B'O_6$ octahedra, which modifies the local coordination environment. Furthermore, A-site ordered double perovskite $AA'B_2O_6$ and A- and B-site multiply ordered double perovskite $AA'BB'O_6$ structures could also be formed [25].

Compared to conventional ABO_3 perovskites, double perovskites exhibit enhanced property control through two distinctive advantages: (1) expanded chemical flexibility via B/B′-site cationic combinations, and (2) enhanced magnetoelectric coupling arising from additional orbital interactions (such as B–B′). This structural versatility enables unique quantum phenomena, for example, Sr_2FeMoO_6 demonstrates semi-metallic behavior with spin-dependent conductivity (↑-channel conduction, ↓-channel insulation) [26]; Ca_2CuWO_6 manifests low-dimensional magnetism through its quasi-two-dimensional magnetic ordering [27]; and the hybrid multiferroic compound $(Ca_{0.5}Mn_{1.5})MnWO_6$ simultaneously combines ferroelectric and magnetic ordering through its complex cation arrangement [28].

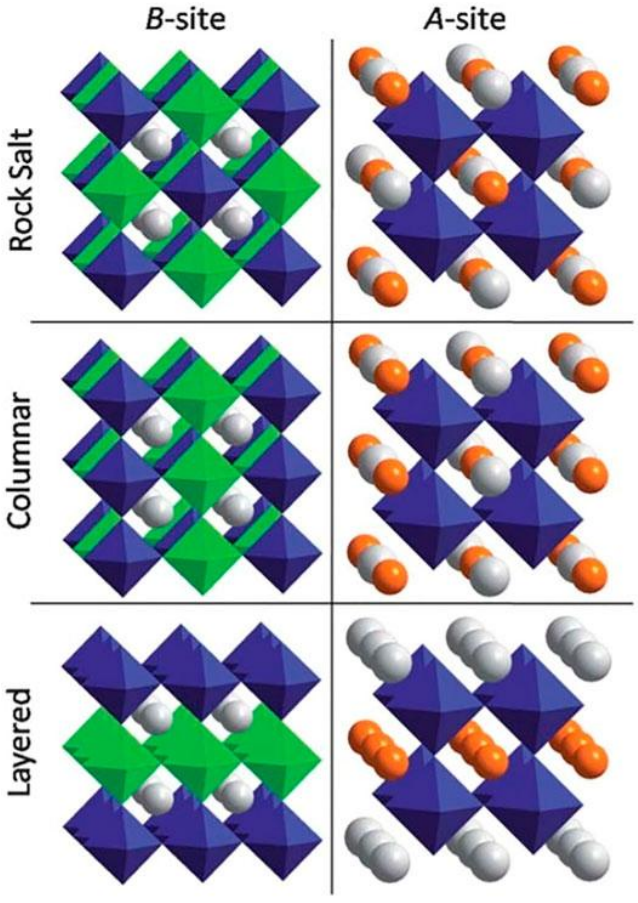

Figure 1.5 Cation ordering schemes in perovskites. From top to bottom, 0D (rock salt), 1D (columnar ordering), and 2D (layered ordering) are shown for B-site ordering in $A_2BB'X_6$ perovskites (left) and for A-site ordering in $AA'B_2X_6$ (right) perovskites [25].

1.1.3 Quadruple perovskites

In the perovskite-derived structure, transition metals can occupy the A site in addition to the B site. When 75% of the A-site cations in the conventional ABO_3 structure are replaced by transition metals, the quadruple perovskite $AA'_3B_4O_{12}$ ordered structure can form. In this structure, A and B correspond to the larger cations and smaller transition-metal ions, respectively, similar to the conventional perovskite ABO_3. Meanwhile, the A′ site is usually occupied by Jahn–Teller cations (e.g., Cu^{2+} and Mn^{3+}) or other cations that favor square-planar coordination, including Cu^{3+}, Fe^{2+}, Co^{2+}, Pd^{2+}, Pb^{4+}, and Mn^{2+} [29]. Most $AA'_3B_4O_{12}$ compounds require high pressure (HP) and high temperature (HT) for their synthesis. As presented in **Figure 1.6**, the significant size difference between the A′-site ion and the A-site ion causes sharp tilting of the BO_6 octahedra, reducing the B–O–B bond angle from the ideal value of 180° to about 140–145°. This distortion also alters the cation's coordination environment: the A site remains in a 12-fold coordinated AO_{12} polyhedron, while the A′ site forms a distinctive square-planar coordinated $A'O_4$, with adjacent $A'O_4$ planes arranged orthogonally [30].

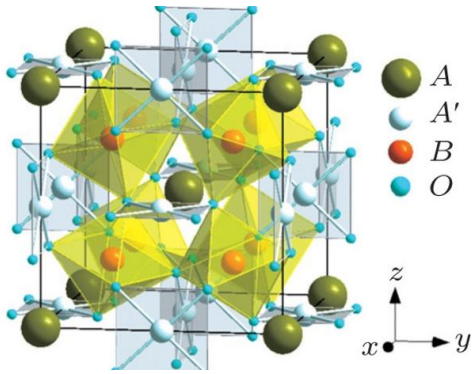

Figure 1.6 Crystal structure of A-site ordered quadruple perovskite $AA'_3B_4O_{12}$ with an *Im*-3 space group. Atomic sites: A 2*a* (0, 0, 0), A′ 6*b* (0, 0.5, 0.5), B 8*c* (0.25, 0.25, 0.25), O 24*g* (*x*, *y*, 0) [21].

The $AA'_3B_4O_{12}$ quadruple perovskites have a $2a_p \times 2a_p \times 2a_p$ cell (a_p represents the lattice constant of the cubic ABO_3 perovskite, which is approximately 3.8 Å) and adopt $a^+a^+a^+$ tile system, with the parent structure belonging to the *Im*-3 space group [30, 31]. This subfamily was first discovered in 1967 in $CaCu_3Ti_4O_{12}$ during Cu^{2+} doping of

$CaTiO_3$ [32]. Since then, extensive research has been conducted to synthesize and characterize new members of this quadruple perovskite family. These efforts have led to the discovery of numerous interesting physical and chemical properties, such as giant dielectric constant [30], inter-site charge transfer and disproportionation [31], multiferroic properties [33], reentrant structural transitions [34], and high catalytic activity [35]. Notably, both the A′ and B sites in the $AA'_3B_4O_{12}$ structure can accommodate transition metals, facilitating novel A′–A′ and A′–B interactions that further enhance the material's functional diversity [36].

By replacing 50% of the B-site transition metals in $AA'_3B_4O_{12}$ quadruple perovskite with B′-site ions, the A/B-site multiply ordered structure $AA'_3B_2B'_2O_{12}$ can be further formed [37, 38]. In this structure, A/A′ sites maintain an ordered arrangement of a 1:3 ratio and B/B′ sites form an ordered structure in a ratio of 1:1. As observed in B-site ordered double perovskites, the B/B′ site ordering degree is jointly governed by ionic radius mismatch and oxidation state difference. The introduction of new B′ position ions produces multiple exchange interactions (e.g., B–O–B′ superexchange, B′–A′–B indirect coupling), which may induce new physical properties [39, 40].

Another special type of quadruple perovskite, the A-site columnar-ordered $A_2A'A''B_4O_{12}$, will be discussed in **Section 1.5**.

1.2 Magnetism in perovskite systems

1.2.1 Origin of magnetism

Magnetism is a physical phenomenon that a material exhibits in an external magnetic field and arises primarily from the spin and orbital motion of unpaired electrons in solids. Many solid materials exhibit magnetism due to the presence of unpaired electrons in their valence electron shells [41, 42]. The spin and orbital angular momentum of unpaired electrons combine to determine magnetic properties of materials (**Figure 1.7**) [42, 43]. The relative contributions of these components can be quantitatively described by the magnetic moment formula, with the Bohr magneton (μ_B) serving as the standard unit for atomic or ionic magnetic moments [44].

Electron spin is a quantum property that describes the intrinsic angular momentum of electrons, which resembles a rotation around their axis, giving rise to the spin magnetic

moments. When orbital motions are neglected, the spin-derived magnetic moment is given by:

$$\mu_S = g\sqrt{S(S+1)}\mu_B$$

where S is the total spin angular momentum quantum number, and g is the Landé g-factor (g = 2.00023 for free electrons). Additionally, the orbital motion of electrons produces orbital magnetic moments. If both spin and orbital contributions are fully considered, the total magnetic moment becomes:

$$\mu_J = g\sqrt{J(J+1)}\mu_B$$

where $J = S + L$, J is the total angular momentum and L represents the total orbital angular momentum quantum number [41]. However, crystal field effects often partially suppress the orbital contributions in crystalline solids, especially in octahedral coordination environments (e.g., $L \approx 0$ for Fe^{3+}, Mn^{2+}, and Cr^{3+}). This suppression effect is less pronounced in heavy transition metals (e.g., the 4*d*/5*d* series), because the orbital–lattice interaction is enhanced by more substantial spin–orbit coupling [45].

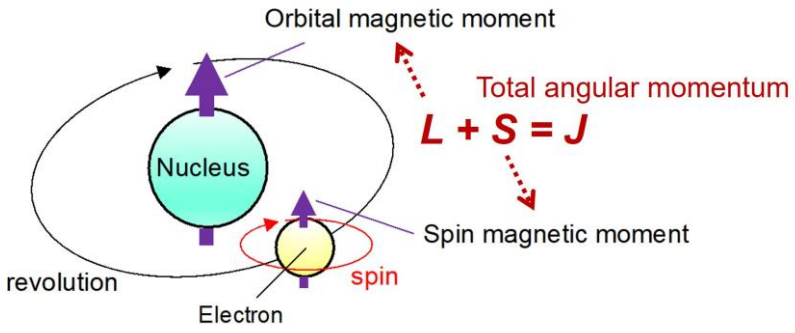

Figure 1.7 The magnetism of a single atom or ion is determined by the combined contributions of the spin magnetic moment and the orbital magnetic moment arising from electron motion around the nucleus [43].

In actual materials, the type of magnetic ions, the number of unpaired electrons, the local environment, and the interaction between electrons all affect the magnetic properties of a material [46]. These factors are particularly important in perovskite systems because the perovskite structure provides a variety of possible coordination environments and

exchange interaction pathways for magnetic ions, which determines their rich magnetic behavior.

1.2.2 Classification of magnetic behaviors

The spin orientation of unpaired electrons in atoms or ions and their interactions follow the principle of minimum energy, and this spin correlation behavior directly determines the macroscopic magnetic state of the material. As illustrated in **Figure 1.8** [47], there are 5 different types of common magnetic behaviors:

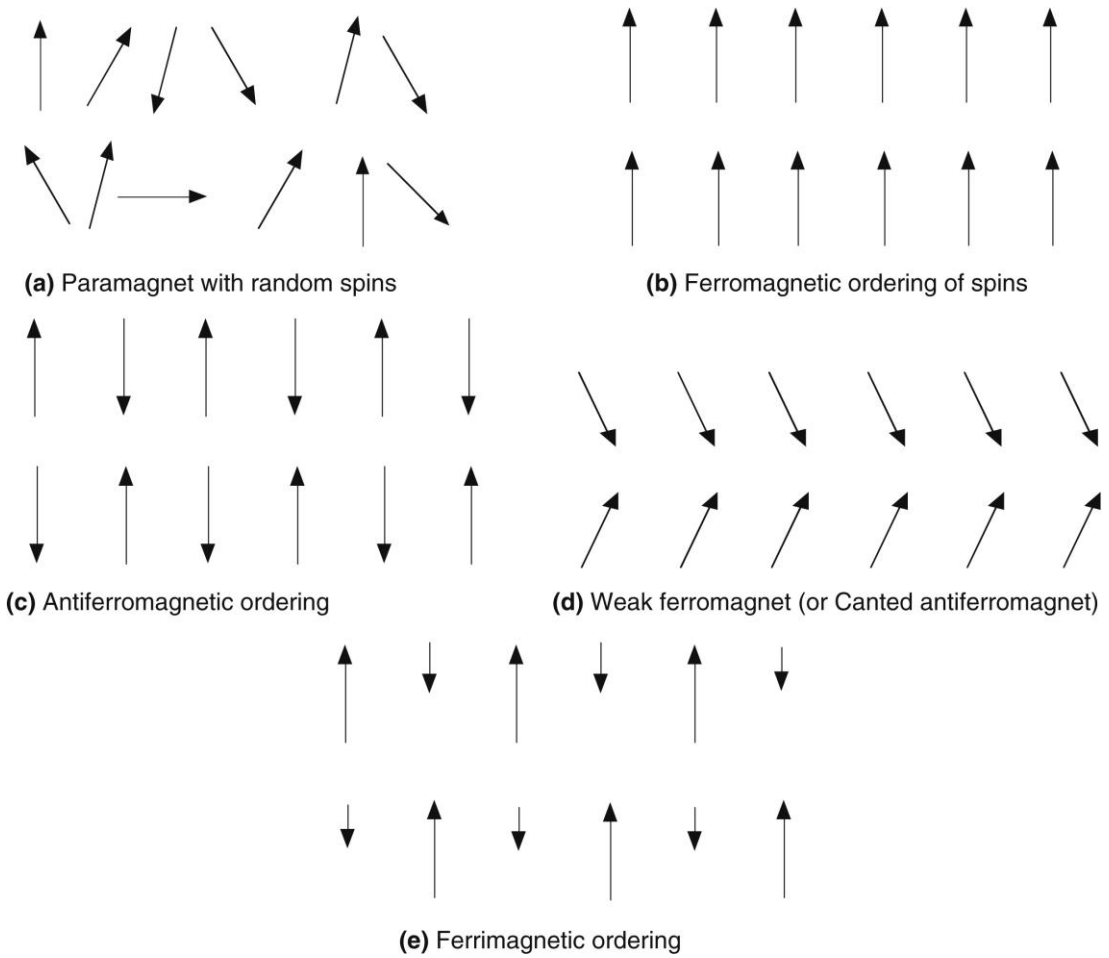

Figure 1.8 Schematic illustrations of spin interactions for several common magnetic behaviors: (a) paramagnet, (b) ferromagnetic ordering, (c) antiferromagnetic ordering, (d) weak ferromagnet or canted antiferromagnet, and (e) ferrimagnetic ordering. These schematic illustrations are 2D representations of 3D phenomena [47].

(a) Paramagnetism. In paramagnetic materials, the spins of unpaired electrons are randomly oriented without an external magnetic field, resulting in a net magnetic moment of zero (**Figure 1.8**(a)). With the introduction of the external magnetic field, these spins tend to align with the direction of the field, leading to a weak magnetization. However, due to the presence of thermal agitation, this magnetization is usually very small and disappears once the magnetic field is removed.

(b) Ferromagnetism. Ferromagnetic materials have spontaneous magnetization, the spins of unpaired electrons are parallel oriented even in the absence of an external magnetic field, resulting in a large net magnetic moment (**Figure 1.8**(b)). This phenomenon originates from the strong exchange interaction between magnetic ions.

(c) Antiferromagnetism. For antiferromagnetic materials, the spins of unpaired electrons of adjacent magnetic ions are antiparallelly arranged (**Figure 1.8**(c)), and the magnetic moments are completely offset, so the material does not show a net magnetization effect on a macroscopic scale.

(d) Weak ferromagnetism or canted antiferromagnetism. In some materials, the spin orientations are usually arranged in reverse, but there are small tilted or asymmetric exchange interactions that cannot completely offset the magnetic moments, resulting in a weak net magnetic moment on a macroscopic scale (**Figure 1.8**(d)). This behavior is called weak ferromagnetism or canted antiferromagnetism.

(e) Ferrimagnetism. The spin orientations of ferromagnetic materials are similar to those of antiferromagnetic materials, but the magnetic moments on different sublattices are not completely equal, resulting in a constant net magnetization of the material (**Figure 1.8**(e)).

In addition to the above common magnetic ordered states, two special magnetic behaviors need attention: diamagnetism and the spin glass state. In diamagnetic materials, all electrons are arranged in pairs, and there is no net magnetic moment. When an external magnetic field is applied, a weak magnetic moment opposite to the direction of the external magnetic field is induced inside the material. This phenomenon originates from the change in the orbital motion of the electrons [48]. The spin glass state is a special disordered magnetic state in which unpaired electron spins are frozen in a randomly oriented state below the freezing temperature [49].

1.2.3 Magnetic transitions

In the discussion of magnetic classifications, a magnetic transition is a critical phenomenon that cannot be ignored. With the changes in temperature or external magnetic field, the arrangement of electron spins in the material may be reorganized, leading to phase transitions between different magnetic states. Common magnetic transitions include the following:

(a) Curie transition. For ferromagnetic materials, when the temperature exceeds a certain critical temperature (Curie temperature, T_C), thermal agitation will destroy the ordering arrangement of spins, and the materials will transit from a ferromagnetic state to a paramagnetic state. This type of magnetic phase transition is a typical second-order phase transition.

(b) Néel transition. Similar to ferromagnetic materials, when the temperature exceeds a certain critical temperature (Néel temperature, T_N), the spin order in antiferromagnetic materials will be destroyed and the materials will become paramagnetic.

(c) Ferrimagnetic-paramagnetic transition. Ferrimagnets also have a Curie temperature (T_C), but due to the asymmetry of the sublattice magnetic moments, the magnetization of the materials and the thermodynamic behavior after the magnetic transition are significantly different from ferromagnetism.

(d) Spin glass transition. Above the freezing temperature, the spin glass system exhibits paramagnetic properties; when the temperature drops below freezing temperature, the magnetic moment enters a metastable frozen state due to frustration interaction, forming a spatially disordered but temporally “frozen” magnetic moment configuration. The spin glass transition is usually accompanied by complex physical phenomena, such as hysteresis, memory effect, and aging behavior [49-51].

1.2.4 Magnetic susceptibility and Curie–Weiss law

The total magnetic moment of a magnetic material is the vector sum of individual ionic magnetic moments and the magnetization (M) represents the total magnetic moment per unit volume. The unit of magnetization is generally emu/cm^3 or emu/mol. In this thesis, emu/mol will be used primarily because it focuses more on the microscopic

magnetic behavior within per chemical unit or ion. Magnetic susceptibility (χ) refers to the magnitude of the magnetization under an applied magnetic field (H), defined as:

$$\chi = \frac{M}{H}$$

The parameter is crucial to understanding various magnetic states and related magnetic transitions. **Figure 1.9** [52] illustrates the relationship between χ and temperature for different magnetic states. The relative value of χ is consistent with the relative magnitude of net magnetic moment discussed in **section 1.2.2**: paramagnetic and antiferromagnetic materials usually exhibit low χ while ferromagnetic materials show high χ due to spontaneous magnetization. When the temperature is higher than the magnetic transition temperature (T_C or T_N), all materials show a paramagnetic-like behavior where χ is inversely proportional to the temperature. At low temperatures, the magnetic moment of paramagnetic material tends to align along the direction of the field. As the temperature increases, the thermal disturbance increases and the alignment of the magnetic moment becomes more difficult, leading to the decrease of χ. Ferromagnetic materials show high χ at low temperatures because of the existence of spontaneous magnetization. The temperature-dependent χ curve of ferrimagnetic materials shows similar performance to that of ferromagnetic materials, and the χ at low temperatures is generally higher than that of antiferromagnetic materials.

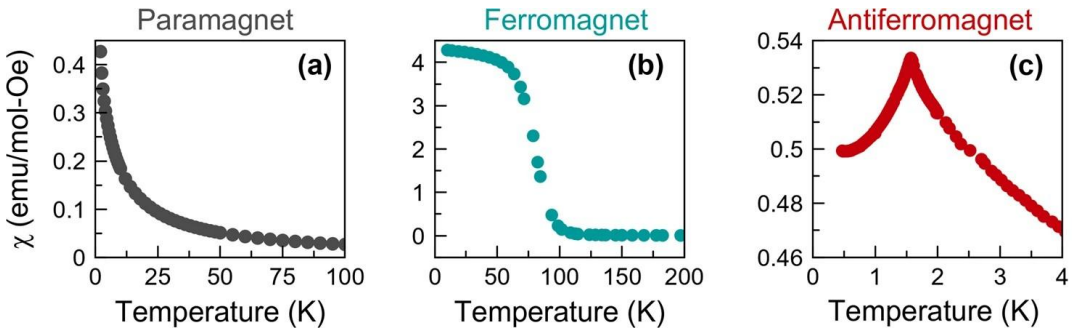

Figure 1.9 The temperature dependence of the magnetic susceptibility (χ) of (a) paramagnet, (b) ferromagnet, and (c) antiferromagnet [52].

For paramagnetic, ferromagnetic, ferrimagnetic, and antiferromagnetic materials, χ usually follows the Curie–Weiss law at elevated temperatures:

$$\chi = \frac{C}{T - \theta}$$

where C is the Curie constant, which is related to the effective magnetic moment (μ_{eff}) and ion concentration of the material; θ is the Curie–Weiss temperature, indicating the exchange interaction types between spins. As shown in **Figure 1.10**(a) [52], Curie–Weiss susceptibility due to paramagnetic local moments goes as $1/T$ and is typically at least an order of magnitude larger than other temperature independent contributions to susceptibility, such as paramagnetism or diamagnetism. The inverse susceptibility of a material that follows the Curie–Weiss law will be linear in temperature and the x−intercept gives the θ value. Specifically, $\theta > 0$ indicates dominant ferromagnetic interactions, $\theta < 0$ indicates predominant antiferromagnetic interactions, and $\theta = 0$ indicates an ideal paramagnetic without interaction (**Figure 1.10**(b)) [52]; T is the absolute temperature. Furthermore, the Curie–Weiss law can be rewritten as the following equation:

$$\chi(T) = \mu_{\text{eff}}^2 N(3k_B(T - \theta))^{-1}$$

where N is Avogadro's number and k_B is Boltzmann's constant. Through magnetic susceptibility measurement and fitting, we can deeply study the magnetic transition behavior of materials and their intrinsic electronic structure characteristics.

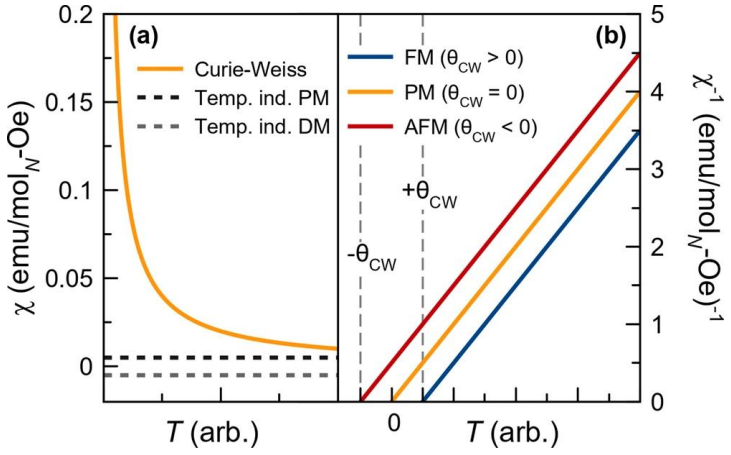

Figure 1.10 (a) Curie–Weiss susceptibility compared with that of temperature-independent paramagnetism (PM) and diamagnetism (DM). (b) The inverse susceptibility of materials that follows the Curie–Weiss law [52].

1.3. Electronic and magnetic interactions

1.3.1 Crystal field theory

Crystal field theory is mainly used to describe the effect of coordination environments (such as oxygen octahedral, tetrahedral, square-planar, etc.) on the energy levels of *d* orbitals in transition metal ions. When transition metal ions are surrounded by anions or ligands, the negative charge fields of these ligands interact with the *d* electrons of the metal ions, resulting in the splitting of the originally degenerate *d* orbital energy levels [53]. In a typical octahedral coordination, the five *d* orbitals split into two groups, whose energies depend on their directions, including the e_g orbitals with higher energy and the t_{2g} orbitals with lower energy (**Figure 1.11**(a)) [54]. The energy difference between these two groups is called the crystal field splitting energy (Δ_O). As shown in **Figure 1.11**(b), the e_g orbitals point directly toward the negative charges of the ligands. This increases the electrostatic repulsion, making their energy higher than in a spherical charge distribution. In contrast, the t_{2g} orbitals are all oriented at 45° to the axis. This alignment places them between the ligands, reducing electrostatic repulsion and lowering their energy. It should be noted that the splitting of the *d* orbitals in the crystal field does not change the total energy of the five *d* orbitals. In addition, the interaction between the positively charged metal ions and the ligands leads to an overall stabilization of the system, thereby reducing the energy of all five *d* orbitals without affecting their splitting (as shown at the far right in **Figure 1.11**(a)**)**. In perovskite structures, transition metal ions are located at the center of the BO_6 octahedral. Crystal field theory can explain the *d* orbital splitting of these metal ions, which in turn affects the electron distribution and magnetic properties. Depending on the crystal field splitting energy and the spin pairing energy of the electrons, electrons either fill the low energy level (low-spin state) or maximize unpaired electrons (high-spin state), which directly affects the magnetic behavior of the perovskite. For example, in $LaCoO_3$ [55-57], Co^{3+} (d^6) ions adopt a low-spin state at low temperatures due to the strong crystal field, resulting in diamagnetism. Upon heating, the crystal field splitting energy decreases, and thermal excitations promote a gradual spin-state transition. This transition may involve an intermediate-spin state before reaching the high-spin state, accompanied by a progressive increase in unpaired electrons (from 0 to 4), thereby enhancing paramagnetic susceptibility.

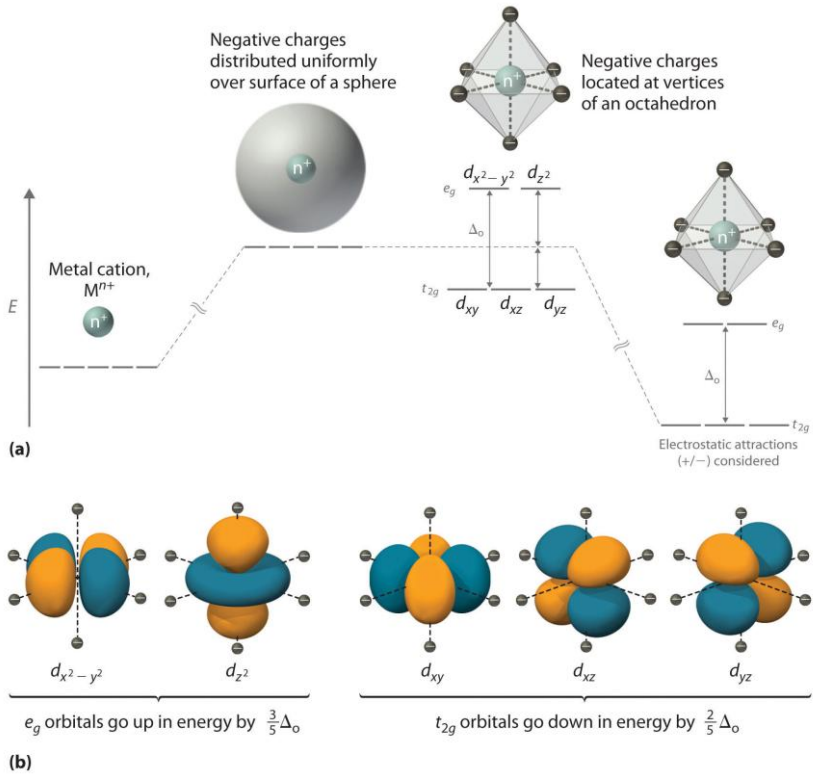

Figure 1.11 (a) Crystal field splitting in octahedral. (b) Energy differences (Δ_O) between e_g and t_{2g} orbitals in an octahedral crystal field [54].

1.3.2 Jahn–Teller effect

The Jahn–Teller (JT) effect describes how certain electronic orbitals in coordination complexes become unstable and lead to geometric distortions when the symmetry is broken [58]. When transition metal ions are in a symmetrical coordination environment (such as octahedral or tetrahedral coordination), the degenerate state of the orbits may be unstable due to the interaction of ligands. According to the JT effect, if the filling of an orbit makes the system energetically unstable, the system will reduce the energy by distorting the symmetry, thus forming a distorted geometric structure. For example, in octahedral coordination, when a *d* orbital is partially filled (such as in the case of d^4, d^7, or d^9 configurations, **Figure 1.12**(a) [59]), due to the antisymmetric interaction of these electrons, the system will deform in shape to reduce the energy instability caused by electron occupation. The common manifestation of the JT effect is the distortion of the oxygen octahedral structure, which is usually manifested as the

stretching or compression of the octahedra in a certain direction, resulting in the JT distortion of the coordination geometry (**Figure 1.12**(b)).

In perovskite materials, the JT effect of transition metal ions often occurs in the case of incompletely filled *d* orbitals, especially in Mn^{3+} and Cu^{2+}. Since the electronic configuration of these metal ions is not completely symmetrical, the JT effect not only affects their geometric structure but also further affects their electronic state distribution and magnetism. For example, in the perovskite structured $LaMnO_3$ (**Figure 1.12**(c)), the d^4 configuration of Mn^{3+} leads to a strong JT effect, accompanied by the distortion of the oxygen octahedral, which makes the material exhibit unique magnetic and electrical properties [59]. The JT effect may also lead to ferromagnetic or antiferromagnetic behavior of materials at low temperatures [60, 61], as well as changes in the interaction between magnetism and electrical properties. This effect is especially important under high-pressure conditions because compression enhances the interaction between orbitals, which in turn affects the electronic configuration of metal ions and the overall performance of the crystal [62, 63].

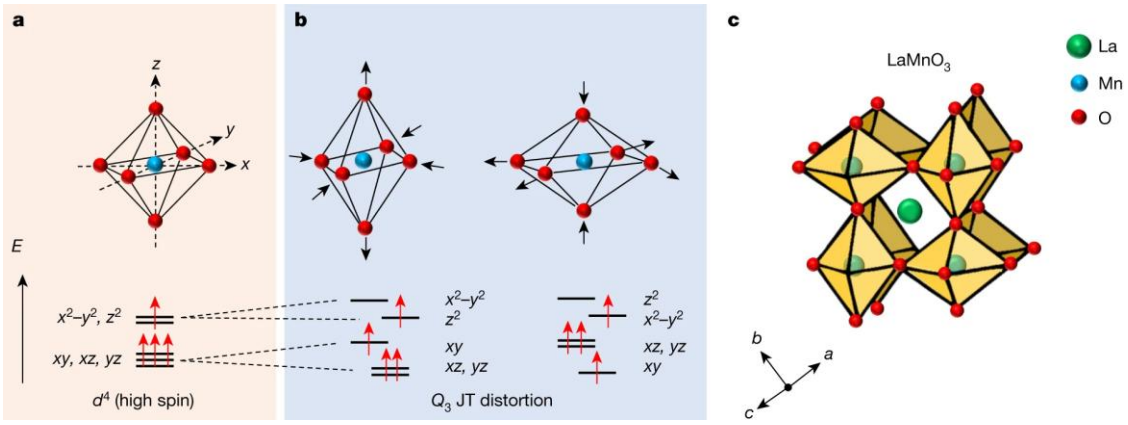

Figure 1.12 (a) Schematic MO_6 (where M is a transition metal) octahedron and crystal field structure for a high-spin d^4 electron configuration. (b) Octahedral distortions and associated orbital levels for a Jahn–Teller (JT) distortion. (c) Strong JT-distorted $LaMnO_3$ crystal structure with high-spin d^4 Mn^{3+} as an example of a cooperative JT distortion [59].

1.3.3 Exchange interactions

To better understand the origin and transition mechanism of different magnetic states, exchange interactions (including direct exchange, superexchange, and double exchange) form the key theoretical basis. Exchange interaction refers to the interaction between spins caused by the overlap or indirect coupling of electron wavefunctions, which in turn determines the stability and evolution of electron spin arrangement in the material. Direct exchange describes the local interaction between magnetic ions due to the overlap of electron wavefunctions, superexchange mediates the indirect coupling between magnetic ions through non-magnetic ligands, and double exchange mainly occurs in mixed-valence systems, promoting ferromagnetic coupling through electron hopping. The three exchange mechanisms create an important framework for understanding the magnetic behavior transitions in materials, especially in perovskite oxides.

1.3.3.1 Direct exchange

In 1928, Werner Heisenberg proposed a quantum model to describe the exchange interaction of magnetic materials and used spin operators to describe the interaction between neighboring atoms [64]. By considering the symmetry of electron spins and the overlap of wavefunctions, he explained the origin of spontaneous magnetization in ferromagnetic materials. Direct exchange interaction occurs between neighboring magnetic ions when their electron clouds overlap. This creates exchange energy and depends on the symmetry of their spin wavefunctions. This effect usually requires short distances between magnetic ions, leading to significant orbit overlap, which directly affects the spin arrangement. For example, in metals like iron, two neighboring iron atoms will be coupled to each other through direct exchange due to the partial overlap of their *d* orbitals [65]. If the overlap of the wavefunction lowers the parallel spin alignment energy, the material will exhibit ferromagnetism; conversely, if the antiparallel alignment energy is more stable, antiferromagnetism will be formed.

1.3.3.2 Superexchange

For certain electrons like 3*d* or 4*f* electrons, due to the spatial localization of their wavefunctions, the exchange of electrons between different ions cannot occur directly but

requires a certain medium. In 1950, P. W. Anderson pointed out that even in the absence of direct overlap, the interaction between magnetic ions could occur through the mediation of non-magnetic ligands. He discussed antiferromagnetism and proposed the Anderson superexchange model [66]. Subsequently, Goodenough (1955) [67] and Kanamori (1959) [68] expanded the theory and developed the famous Goodenough-Kanamori rules to qualitatively determine the coupling (ferromagnetism or antiferromagnetism) between magnetic ion–ligand–magnetic ion under different geometric configurations. These rules emphasize the key role of factors such as bond angle, orbital orientation, and ligand energy level in the superexchange process.

Superexchange is an indirect exchange mechanism that occurs between two magnetic ions without direct wavefunction overlap but is coupled through the mediation of one or more non-magnetic ions (usually oxygen, fluorine, etc.). In a magnetic ion–ligand–magnetic ion pathway, electrons may undergo virtual hopping through the ligand orbits, thereby establishing effective magnetic coupling. Depending on the coupling between nearest-neighbor (NN) cations, superexchange results in either ferromagnetic or antiferromagnetic ordering. As seen in **Figure 1.13** [6], antiferromagnetic ordering results from the superexchange contact between the NN cations with antiparallel spins, and ferromagnetic ordering results from the opposite. Through a 180° B–O–B bond, superexchange is evident between two singly occupied metal orbitals, and electrons alternate between occupied and unoccupied states.

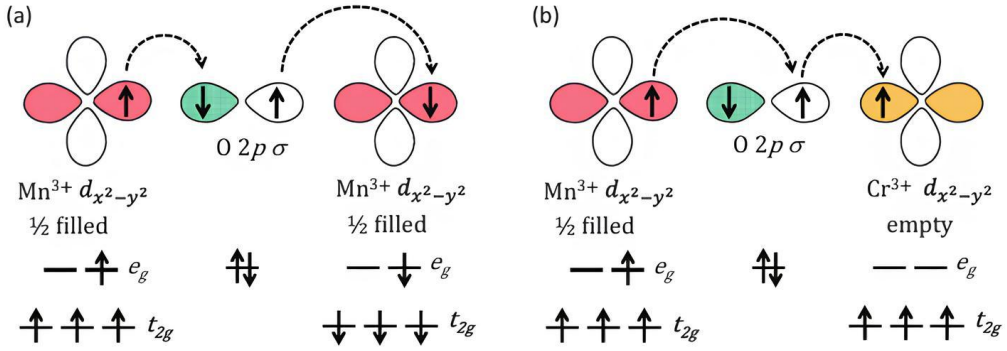

Figure 1.13 Superexchange interactions: (a) the covalent interaction through the O 2*p* orbital leading to antiferromagnetic coupling and (b) Mn^{3+}–O–Cr^{3+} interaction leading to ferromagnetic coupling [6].

1.3.3.3 Double exchange

The double exchange theory was first proposed by Clarence Zener in 1951 [69, 70]. He studied manganese-based compounds and found that electron hopping was linked to parallel spin alignment, and thus proposed the double exchange model. Subsequent research expanded the theory based on the Zener model by considering factors like electron-phonon coupling, localization effects, and the influence of impurities [71-73]. The double exchange typically occurs in mixed-valence perovskite systems, such as the same magnetic ions with different valences. The key idea is that an electron can "hop" between two magnetic ions with different valence states (like Mn^{3+} and Mn^{4+}). This hopping not only helps the conduction of electrons but also promotes the parallel alignment of spins to reduce energy during the process. **Figure 1.14** [6] illustrates the schematic double-exchange interaction in $La_{1-x}A_xMnO_3$ (A = Ca or Sr). In $LaMnO_3$, the B-site Mn^{3+} is in a high valence state, also a Jahn–Teller distorted ion. The divalent substitution of La^{3+} with Ca^{2+} or Sr^{2+} results in the formation of Mn^{4+} ions to neutralize the subsequent charge imbalance. Because the *p*-orbitals are fully occupied, one Mn^{3+} ion donates an electron to the nearby O^{2-} ion in this instance, while the O^{2-} ion transmits it to the nearby Mn^{4+} ion at the same time. The spin-up electron from Mn^{3+} pushes a spin-up electron from the O^{2-} ion onto the Mn^{4+} ion during the charge transfer process. Only two cations with parallel spins can undergo the double exchange, which eventually results in ferromagnetic alignment and metallic behavior.

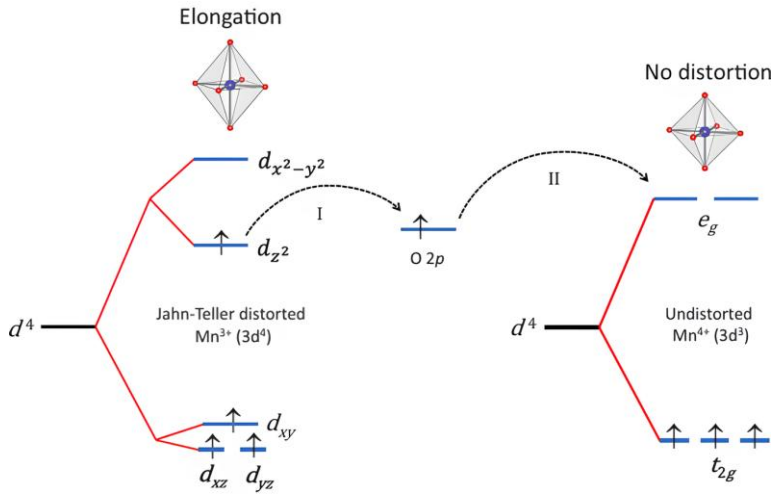

Figure 1.14 Schematic representation of the double-exchange mechanism [6].

1.4 High-pressure science and techniques

High-pressure science that studies the changes in the structure, electronic state, and magnetism of matter under extreme pressure is an important field of materials science, physics, and geology. Since the American physicist Percy Williams Bridgman pioneered high-pressure research in the early 20th century, high-pressure technology has developed a lot, from the early piston-cylinder device to the modern diamond anvil cell (DAC) and belt-type high-pressure apparatus. These systems can now generate pressure of hundreds of gigapascals (GPa) [74]. High-pressure science is of great significance in discovering new phases, revealing new properties, synthesizing new materials, and studying the deep earth environment [74, 75].

There are several types of high-pressure devices. The modern diamond anvil cell can generate hundreds of GPa pressure, which is suitable for in-situ spectroscopy and diffraction research; belt-type high-pressure apparatuses are flexible and used to synthesize materials under high-pressure and high-temperature (HPHT) conditions; multi-anvil devices apply uniform pressure and are used for research on minerals and other high-density materials. These devices have their unique advantages in function, application scenarios, and pressure range, which promote the research of materials science under extreme conditions [76].

Compared with normal pressure synthesis technology, high-pressure synthesis offers special advantages. It can stabilize metastable structures that are difficult to exist under normal conditions, and induce profound changes in the structure, electronic state, and magnetism of materials [74]. For perovskite materials, high pressure can compress the lattice, change the coordination environment of transition metal ions, and distort the oxygen octahedral framework. These changes can modify the electronic band structure, affecting the conductivity, magnetism, and ferroelectricity of materials. For example, in perovskite manganites [77, 78], high pressure changes the oxidation state and electronic configuration of Mn ions (such as Mn^{3+} and Mn^{4+}). This affects magnetic exchange interactions, such as superexchange or double exchange, which control the material's spin and orbital ordering.

In addition, high pressure can effectively reduce lattice defects, adjust oxygen content, and stabilize mixed-valence states. In perovskite manganites like $La_{1-x}Ca_xMnO_3$

[79, 80], under high-pressure conditions, the bending and bond length changes of oxygen octahedrons will directly affect the Mn–O–Mn superexchange path, thereby changing the magnetic order state of the material. In some cases, high pressure can even stabilize high-temperature superconductors [81] or enhance properties like giant magnetoresistance (CMR) [82], which has potential in applications such as spin electronics and catalysis. High-pressure synthesis also opens new possibilities for exploring new functional materials [83], such as multiferroic materials and strongly correlated electronic system materials [84]. Since high-pressure devices (such as belt-type high-pressure apparatus and multi-anvil devices) can provide high-temperature conditions, it is possible to synthesize complex multicomponent perovskite oxides in situ, thereby improving the uniformity and stability of the material [85].

1.5 Research progress on A-site columnar-ordered quadruple perovskites

In perovskite structures, the different numbers of the in-phase BO_6 tilts create different numbers and types of cavities for A cations. When the ratio of A-site cations with significantly different sizes is 1:1, a special tilt system can form under the right conditions. This system has a $2a_p \times 2a_p \times 2a_p$ cell and the $a^+a^+c^-$ tilt system, which means that BO_6 octahedra are rotated in one direction along the *a* and *b* axes and in opposite directions along the *c* axis. As shown in **Figure 1.15**(a), the A-site cations are distributed in three different coordination environments: 10-fold-coordinated (A), square-planar-coordinated (A′), and tetrahedrally coordinated (A″). Among them, the A′–O and A″–O bond lengths are similar (1.9–2.1 Å), but the coordination environments are very different, so they can be occupied by different cations (**Figure 1.15**(b)), making the chemical formula of this perovskite more suitable to be written as $A_2A'A''B_4O_{12}$, showing a unique triple A-site ordering [86]. The AO_{10} polyhedra are connected through edges and form $–AO_{10}–AO_{10}–$ columns along the *c* axis (**Figure 1.15**(a)). The $A'O_4$ square units and $A''O_4$ tetrahedra are separated from each other, but they are connected through edges if four longer A′–O bonds are considered, and the $–A'O_4–A''O_4–$ columns also run along the *c* axis. Considering these structural features and generic chemical formula $A_2A'A''B_4O_{12}$, such perovskites are called A-site columnar-ordered quadruple perovskites [86].

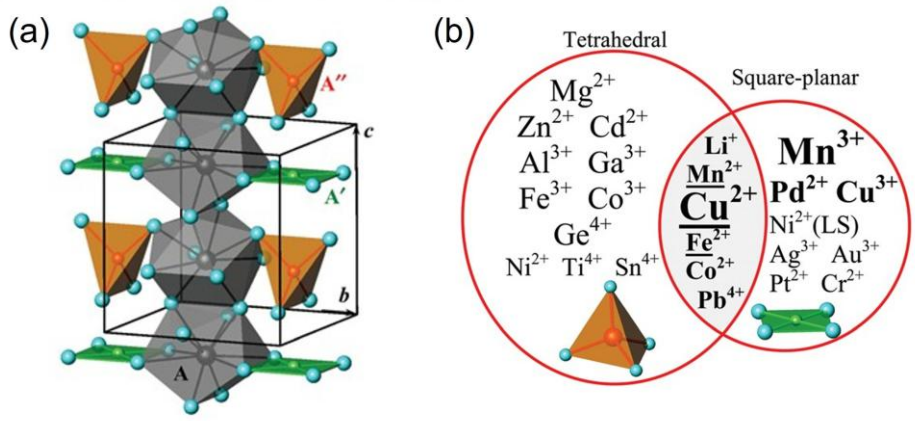

Figure 1.15 (a) Fragments of structures with polyhedra for the A, A′, and A″ sites in $A_2A'A''B_4O_{12}$ quadruple perovskites. B atoms are omitted for clarity. (b) A schematic figure with some cations that can have a tetrahedral coordination and a square-planar coordination in oxides and their overlap [87]. Bold letters show cations found at the A′ site of $AA'_3B_4O_{12}$. Cu^{2+}, Fe^{2+}, and Mn^{2+} (underlined) were found so far in the A″ site of $A_2A'A''B_4O_{12}$ quadruple perovskites [86].

The $A_2A'A''B_4O_{12}$ compounds of this structure are greatly restricted in actual synthesis. To form A′ and A″ sites, the BO_6 octahedra need to be tilted significantly, so that the B–O–B angle reaches 130–150° [88]. The A–O bond lengths in the structure are strictly limited (2.3–2.4 Å, 2.4–2.5 Å, and 2.7–2.9 Å), which further limits the types of available A-site elements. So far, only Ca^{2+}, Na^{+}, Y^{3+}, and all rare earth elements (except Ce and Pm) cations have been reported at the A site. However, this thesis presents the first report of Ce in this position. Their synthesis requires HPHT conditions (except $Ca_{2-x}Mn_xTi_2O_6$, $0.3 \leq x \leq 0.6$ [89]). In addition, due to the spatial distribution of A′ and A″ sites, anti-site disorder may occur in some compounds and even lead to the shift of the overall composition, making the actual stoichiometric ratio of some compounds different from the ideal chemical formula.

The parent structure of $A_2A'A''B_4O_{12}$ has the $P4_2/nmc$ (no. 137) space group. As presented in **Figure 1.16** [86], several structural distortions from the direct group–subgroup relations are possible, and three have been experimentally confirmed. Rock-salt ($P4_2/n$ space group) and layered ($Pmmn$ space group) B-site orders have already been realized in $A_2A'A''B_4O_{12}$. The $P4_2/n$ distortion is primarily driven by the composition,

while the *Pmmn* distortion seen in $RMnMn_2O_6$ can be driven by temperature. However, no structural transitions to the parent structure were observed so far in $RMnMn_2O_6$, so the *Pmmn* distortion is considered to be composition-driven. Additional A-site ordering may occur in some cases. In the *Pmmn* structure, there may be a 1:1 rock-salt A-site order, implying two independent A-sites (A1 and A2). Nevertheless, such ordering has not yet been experimentally confirmed. A similar effect may also exist in the $P4_2mc$ structure, resulting in a 1:1 columnar A-site order. Such an order was experimentally observed in $NaYMn_2Ti_4O_{12}$ [90]. Additional ordering may be influenced by the different oxidation states and sizes of the cations.

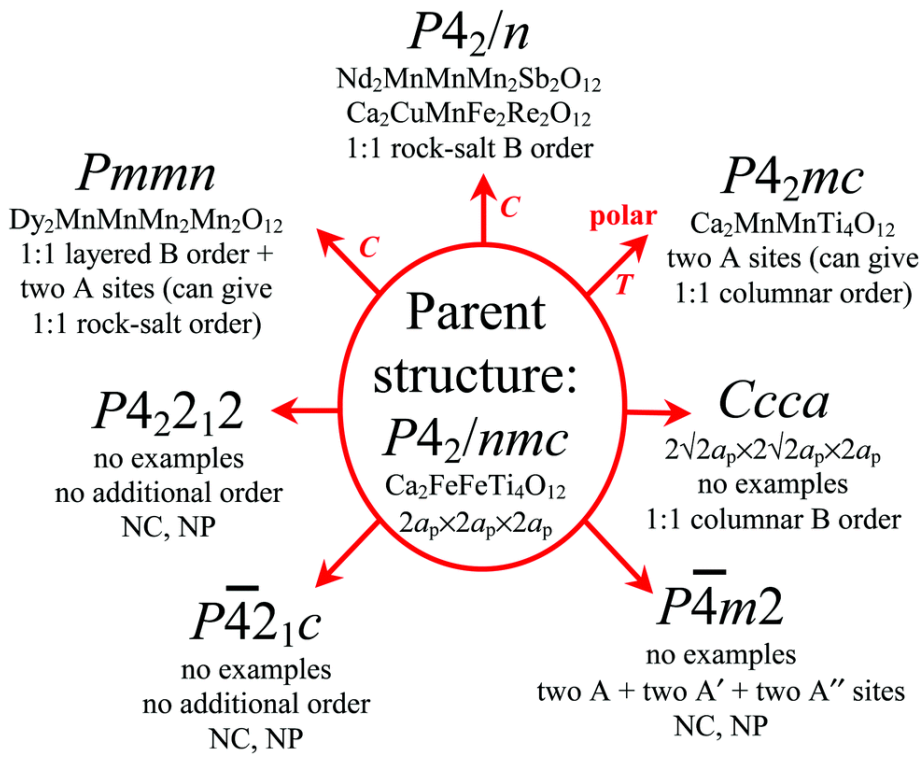

Figure 1.16 A schematic diagram of all direct group–subgroup distortions of the parent structure of $A_2A'A''B_4O_{12}$ quadruple perovskites (space group $P4_2/nmc$). Examples of known distortions are given. Types of A- and B-site orders or number of distinct sites are highlighted. All distortions keep the $2a_p \times 2a_p \times 2a_p$ cell except *Ccca*. *T*: a temperature-driven distortion, *C*: a composition-driven distortion, NC: non-centrosymmetric, NP: non-polar [86].

In terms of magnetism, due to the large tilts of BO_6, the magnetic exchange interaction between the transition metals at the B site is weakened, and the magnetic interaction between the A, A′, A″ sites, and the B site becomes dominant. Therefore, the magnetic ordering of the system can be selectively controlled by regulating the cations at the A, A′, A″, and B sites. In the reported systems, the vast majority of $A_2A'A''B_4O_{12}$ have ferromagnetic or ferrimagnetic order, and the magnetic ions at the A′ and A″ sites usually interact with the B-site ions. For example, some compounds exhibit multiple magnetic transitions involving different magnetic order establishment processes at the B site and the A′/A″ sites [91-93]. In addition, the *f-d* exchange interaction of rare earth ions at the A site may induce spin reorientation [94, 95] or lead to instability of the magnetic ground state, such as the antiferromagnetic spin canting [96, 97].

Besides magnetism, some $A_2A'A''B_4O_{12}$ also have ferroelectricity [90, 98]. For instance, in the $CaMnTi_2O_6$ system, due to the cooperative shifts of the A′ site Mn^{2+} ions along the *c*-axis and the off-center displacements of the Ti^{4+} ions in the TiO_6 octahedra, the material exhibits switchable ferroelectric polarization and a high ferroelectricity Curie temperature of 630 K [98]. In addition, some systems may exhibit different symmetries under specific pressure and temperature conditions. For example, $NaRMn_2Ti_4O_{12}$ forms a $P4_2/nmc$ structure at 6 GPa, 1750 K, while it may form a $P4_2mc$ polar structure at 6 GPa, 1550 K [90, 99].

1.6 Aims and objectives of this thesis

This thesis aims to expand the family of A-site columnar ordered quadruple perovskites using high-pressure and high-temperature synthesis techniques. The precise synthesis of this unique type of perovskite under extreme conditions can stabilize new structural variants that are difficult to obtain or cannot exist at normal pressure. The core goal is to explore the crystal structure and magnetic properties of synthetic perovskites and to understand the complex relationship between structural features such as columnar cation ordering, oxygen octahedral distortion, and cation valence and their impact on magnetic behavior. By systematically adjusting the composition of A-site cations and their columnar arrangement, this thesis will summarize the regulation of the structure and physical properties of quadruple perovskite materials by different components, providing guidance for material design.

In this work, we focused on Mn-based A-site columnar ordered quadruple perovskites synthesized under high-pressure and high-temperature conditions using rare-earth oxides, MnO_x, Sb_2O_3, and ZnO. Due to the flexible oxidation states and structural adaptability of Mn, this thesis will present the following three types of materials:

(i) $Nd_2MnMn(Mn_{4-x}Sb_x)O_{12}$ – Exploring the effects of aliovalent doping of Sb^{5+} on the structure and magnetic properties

Solid solutions $Nd_2MnMn(Mn_{4-x}Sb_x)O_{12}$, belonging to the A-site columnar-ordered quadruple perovskite subfamily $A_2A'A''B_4O_{12}$, were investigated in a compositional range of $0.2 \leq x \leq 2.0$. Crystal structures were studied using synchrotron X-ray powder diffraction. Two regions with different cation orders in the B sublattice were found: a narrow region of $0.8 \leq x \leq 1.0$ had a B-site disordered structure with space group $P4_2/nmc$ (No. 137), and a wider region of $1.6 \leq x \leq 2.0$ had a B-site rock-salt-ordered structure with space group $P4_2/n$ (No. 86). The samples showed complex magnetic behavior with two ferrimagnetic transitions. T_{C1} monotonically increased (from 66 K to 75 K) and T_{C2} was almost constant (about 6–7 K) for $0.8 \leq x \leq 1.0$. T_{C1} monotonically decreased (from 77 K to 63 K) and T_{C2} monotonically increased (from 19 K to 39 K) for $1.6 \leq x \leq 2.0$. There was evidence for the third magnetic transition in the $1.7 \leq x \leq 2.0$ samples, and T_{C3} increased from 13 K to 20 K with increasing x.

(ii) $Ce_2MnM(Mn_2Sb_2)O_{12}$ (M = Mn, Zn) – Observation of the negative magnetization effect in $A_2A'A''B_4O_{12}$ quadruple perovskite

A phenomenon of magnetization reversal in response to an applied magnetic field is very common and forms the basis of magnetic memories. In contrast, a phenomenon of magnetization reversal in response to a temperature change is rarer. We demonstrated a pronounced negative magnetization effect (NME) during field-cooled measurements in small magnetic fields in members of the A-site columnar-ordered quadruple perovskites, $Ce_2MnM(Mn_2Sb_2)O_{12}$ with M = Mn and Zn. Their crystal structures at room temperature were investigated with synchrotron X-ray powder diffraction data. Both compounds crystallize in space group $P4_2/n$ with full rock-salt ordering of Mn and Sb at the B sites. The bond-valence sum analysis and the charge balance suggest that cerium is present in the oxidation state of +3. They show one magnetic transition at T_C = 52 K with the compensation point near 20 K for M = Mn, and at T_C = 34 K with the compensation point

near 29 K for M = Zn. A robust, intrinsic NME was also observed on zero-field-cooled curves when measured in small magnetic fields. The NME could originate from their ferrimagnetic structures.

(iii) $R_2MnZn(MnZnSb_2)O_{12}$ (R = La, Pr, Nd, and Sm) – Examining the impact of rare-earth elements on structural stability and magnetic properties

New members of the A-site columnar-ordered quadruple perovskites, $R_2MnZn(MnZnSb_2)O_{12}$ (R = La, Pr, Nd, and Sm), with additional rock-salt B-site ordering were prepared. The crystal structure of the R = Nd sample (space group $P4_2/n$) was investigated with synchrotron X-ray powder diffraction data at room temperature. It was found that Zn^{2+} cations are located in one octahedral B site (together with Mn^{2+}) and in the tetrahedral A″ site even though small antisite disorder of Mn^{2+} and Zn^{2+} cations between the square-planar A′ site and octahedral B site exists. The second B site is solely occupied by Sb^{5+}. The R = La sample showed a long-range ferrimagnetic transition below T_C = 11 K despite the presence of antisite disorder and low concentration of magnetic Mn^{2+} cations. Other samples demonstrated enhanced ferrimagnetic transition temperatures of 21 K (R = Pr), 18 K (R = Nd), and 23 K (R = Sm). Therefore, we suggested that magnetic rare-earth cations promote exchange interactions between all magnetic cations and are involved in long-range ordering together with Mn^{2+} just below T_C.

References in chapter 1

[1] Peña, M. A.; Fierro, J. L. G. Chemical structures and performance of perovskite oxides. *Chem. Rev.* **2001**, *101*, 1981–2018.

[2] Mitchell, R. H. *Perovskites: modern and ancient*; Almaz Press, 2002.

[3] Kim, H.-S.; Im, S. H.; Park, N.-G. Organolead halide perovskite: new horizons in solar cell research. *J. Phys. Chem. C.* **2014**, *118*, 5615–5625.

[4] Goldschmidt, V. M. Die Gesetze der Krystallochemie. *Naturwissenschaften* **1926**, *14*, 477–485.

[5] Shannon, R. Revised effective ionic radii and systematic studies of interatomic distances in halides and chalcogenides. *Acta Crystallogr. Sect. A* **1976**, *32*, 751–767.

[6] George, G.; Ede, S. R.; Luo, Z. *Fundamentals of perovskite oxides: synthesis, structure, properties and applications*; CRC Press, 2020.

[7] Rondinelli, J. M.; Spaldin, N. A. Structure and properties of functional oxide thin films: insights from electronic-structure calculations. *Adv. Mater.* **2011**, *23*, 3363–3381.

[8] Glazer, A. M. The classification of tilted octahedra in perovskites. *Acta Crystallogr. Sect. B* **1972**, *28*, 3384−3392.

[9] Glazer, A. Simple ways of determining perovskite structures. *Acta Crystallogr. Sect. A* **1975**, *31*, 756–762.

[10] Howard, C. J.; Stokes, H. T. Group-theoretical analysis of octahedral tilting in perovskites. *Acta Crystallogr. Sect. B* **1998**, *54*, 782–789.

[11] Cohen, R. E. Origin of ferroelectricity in perovskite oxides. *Nature* **1992**, *358*, 136–138.

[12] Bednorz, J. G.; Müller, K. A. Perovskite-type oxides-The new approach to high-T_C superconductivity. *Rev. Mod. Phys.* **1988**, *60*, 585–600.

[13] Liou, Y.-D.; Chiu, Y.-Y.; Hart, R. T.; Kuo, C.-Y.; Huang, Y.-L.; Wu, Y.-C.; Chopdekar, R. V.; Liu, H.-J.; Tanaka, A.; Chen, C.-T. Deterministic optical control of room temperature multiferroicity in $BiFeO_3$ thin films. *Nat. Mater.* **2019**, *18*, 580–587.

[14] Moritomo, Y.; Asamitsu, A.; Kuwahara, H.; Tokura, Y. Giant magnetoresistance of manganese oxides with a layered perovskite structure. *Nature* **1996**, *380*, 141–144.

[15] Hayashi, H.; Inaba, H.; Matsuyama, M.; Lan, N.; Dokiya, M.; Tagawa, H. Structural consideration on the ionic conductivity of perovskite-type oxides. *Solid State Ionics* **1999**, *122*, 1–15.

[16] Bhalla, A. S.; Guo, R.; Roy, R. The perovskite structure—a review of its role in ceramic science and technology. *Mater. Res. Innov.* **2000**, *4*, 3–26.

[17] Green, M. A.; Ho-Baillie, A.; Snaith, H. J. The emergence of perovskite solar cells. *Nat. Photonics* **2014**, *8*, 506–514.

[18] Snaith, H. J. Present status and future prospects of perovskite photovoltaics. *Nat. Mater.* **2018**, *17*, 372–376.

[19] Zhang, L.; Mei, L.; Wang, K.; Lv, Y.; Zhang, S.; Lian, Y.; Liu, X.; Ma, Z.; Xiao, G.; Liu, Q.; Zhai, S.; Zhang, S.; Liu, G.; Yuan, L.; Guo, B.; Chen, Z.; Wei, K.; Liu, A.; Yue, S.; Niu, G.; Pan, X.; Sun, J.; Hua, Y.; Wu, W. Q.; Di, D.; Zhao, B.; Tian, J.; Wang, Z.; Yang, Y.; Chu, L.; Yuan, M.; Zeng, H.; Yip, H. L.; Yan, K.; Xu, W.; Zhu, L.; Zhang, W.; Xing, G.; Gao, F.; Ding, L. Advances in the application of perovskite materials. *Nano-Micro Lett.* **2023**, *15*, 177.

[20] Vasala, S.; Karppinen, M. $A_2B'B''O_6$ perovskites: A review. *Prog. Solid State Chem.* **2015**, *43*, 1–36.

[21] Long, Y. A-site ordered quadruple perovskite oxides $AA'_3B_4O_{12}$. *Chin. Phys. B* **2016**, *25*, 078108.

[22] Vasala, S.; Cheng, J. G.; Yamauchi, H.; Goodenough, J. B.; Karppinen, M. Synthesis and characterization of $Sr_2Cu(W_{1-x}Mo_x)O_6$: A quasi-two-dimensional magnetic system. *Chem. Mater.* **2012**, *24*, 2764–2774.

[23] Alam, M.; Chatterjee, S. B-site order/disorder in $A_2BB'O_6$ and its correlation with their magnetic property. *J. Phys.: Condens. Matter* **2023**, *35*, 223001.

[24] Hossain, A.; Bandyopadhyay, P.; Roy, S. An overview of double perovskites $A_2B'B''O_6$ with small ions at A site: Synthesis, structure and magnetic properties. *J. Alloy. Compd.* **2018**, *740*, 414–427.

[25] King, G.; Woodward, P. M. Cation ordering in perovskites. *J. Mater. Chem.* **2010**, *20*, 5785–5796.

[26] Kobayashi, K. I.; Kimura, T.; Sawada, H.; Terakura, K.; Tokura, Y. Room-temperature magnetoresistance in an oxide material with an ordered double-perovskite structure. *Nature* **1998**, *395*, 677–680.

[27] Liang, X.; Yamaura, K.; Tsirlin, A. A.; Belik, A. A. Ca_2CuWO_6: A triclinically distorted double perovskite with low-dimensional magnetic behavior. *Phys. Rev. B* **2025**, *111*, 094432.

[28] Belik, A. A. Hybrid multiferroic behavior in the double perovskite $(Ca_{0.5}Mn_{1.5})Mn$-WO_6. *Chem. Mater.* **2024**, *36*, 7604–7609.

[29] Ding, J.; Zhu, X. Research progress on quadruple perovskite oxides. *J. Mater. Chem. C* **2024**, *12*, 9510–9561.

[30] Vasil'ev, A. N.; Volkova, O. S. New functional materials $AC_3B_4O_{12}$ (Review). *Low Temp. Phys.* **2007**, *33*, 895–914.

[31] Yamada, I. High-pressure synthesis, electronic states, and structure–property relationships of perovskite oxides, $ACu_3Fe_4O_{12}$ (A: divalent alkaline earth or trivalent rare-earth ion). *J. Ceram. Soc. Jpn.* **2014**, *122*, 846–851.

[32] Deschanvres, A.; Raveau, B.; Tollemer, F. Substitution of copper for a divalent metal in perovskite-type titanates. *Bull. Soc. Chim. Fr.* **1967**, *11*, 4077–4078.

[33] Zhao, J.; Gao, J.; Li, W.; Qian, Y.; Shen, X.; Wang, X.; Shen, X.; Hu, Z.; Dong, C.; Huang, Q.; Cao, L.; Li, Z.; Zhang, J.; Ren, C.; Duan, L.; Liu, Q.; Yu, R.; Ren, Y.; Weng, S.-C.; Lin, H.-J.; Chen, C.-T.; Tjeng, L.-H.; Long, Y.; Deng, Z.; Zhu, J.; Wang, X.; Weng, H.; Yu, R.; Greenblatt, M.; Jin, C. A combinatory ferroelectric compound bridging simple ABO_3 and A-site-ordered quadruple perovskite. *Nat. Commun.* **2021**, *12*, 747.

[34] Belik, A. A.; Matsushita, Y.; Khalyavin, D. D. Reentrant structural transitions and collapse of charge and orbital orders in quadruple perovskites. *Angew. Chem. Int. Ed.* **2017**, *56*, 10423–10427.

[35] Yamada, I. Novel catalytic properties of quadruple perovskites. *Sci. Technol. Adv. Mater.* **2017**, *18*, 541–548.

[36] Shimakawa, Y.; Mizumaki, M. Multiple magnetic interactions in A-site-ordered perovskite-structure oxides. *J. Phys.: Condens. Matter* **2014**, *26*, 473203.

[37] Chen, W.-t.; Mizumaki, M.; Saito, T.; Shimakawa, Y. Frustration relieved ferrimagnetism in novel A- and B-site-ordered quadruple perovskite. *Dalton Trans.* **2013**, *42*, 10116–10120.

[38] Yin, Y.-Y.; Liu, M.; Dai, J.-H.; Wang, X.; Zhou, L.; Cao, H.; dela Cruz, C.; Chen, C.-T.; Xu, Y.; Shen, X. $LaMn_3Ni_2Mn_2O_{12}$: An A- and B-site ordered quadruple

perovskite with A-site tuning orthogonal spin ordering. *Chem. Mater.* **2016**, *28*, 8988–8996.

[39] Chen, W.-t.; Mizumaki, M.; Seki, H.; Senn, M. S.; Saito, T.; Kan, D.; Attfield, J. P.; Shimakawa, Y. A half-metallic A- and B-site-ordered quadruple perovskite oxide $CaCu_3Fe_2Re_2O_{12}$ with large magnetization and a high transition temperature. *Nat. Commun.* **2014**, *5*, 3909.

[40] Liu, Z.; Wang, X.; Ye, X.; Shen, X.; Bian, Y.; Ding, W.; Agrestini, S.; Liao, S.-C.; Lin, H.-J.; Chen, C.-T. Observation of A-site antiferromagnetic and B-site ferrimagnetic orderings in the quadruple perovskite oxide $CaCu_3Co_2Re_2O_{12}$. *Phys. Rev. B* **2021**, *103*, 014414.

[41] Cotton, F. A.; Wilkinson, G.; Murillo, C. A.; Bochmann, M. *Advanced inorganic chemistry*; John Wiley & Sons, 1999.

[42] Singh, M. K.; Kumar, S.; Sahu, R. K. *Origin of Magnetism, Synthesis, Characterization and Perspective Application of Magnetic Graphene*; Springer Nature Singapore, 2024.

[43] Yuki, K. W.; Yoshiharu, K.; Yoshitaka, T.; Hideki, Y. Creation of novel material Sr_3OsO_6 with the highest ferromagnetic transition temperature among insulators. *NTT Tech. Rev.* **2019**, *17*, 7–11.

[44] O'Handley, R. C. *Modern Magnetic Materials: Principles and Applications*; Wiley: New York, 1999.

[45] Khomskii, D. I.; Streltsov, S. V. Orbital Effects in Solids: Basics, recent progress, and opportunities. *Chem. Rev.* **2021**, *121*, 2992–3030.

[46] Landrum, G. A.; Dronskowski, R. The orbital origins of magnetism: from atoms to molecules to ferromagnetic Alloys. *Angew. Chem. Int. Ed.* **2000**, *39*, 1560–1585.

[47] Miller, J. S. Organic- and molecule-based magnets. *Materials Today* **2014**, *17*, 224–235.

[48] Pople, J. Molecular-orbital theory of diamagnetism. I. an approximate LCAO scheme. *J. Chem. Phys.* **1962**, *37*, 53–59.

[49] Souletie, J. Hysteresis and after-effects in massive substances. From spin-glasses to the sand hill. *J. Phys.* **1983**, *44*, 1095–1116.

[50] Bag, P.; Baral, P.; Nath, R. Cluster spin-glass behavior and memory effect in $Cr_{0.5}Fe_{0.5}Ga$. *Phys. Rev. B* **2018**, *98*, 144436.

[51] Wills, A. S.; Dupuis, V.; Vincent, E.; Hammann, J.; Calemczuk, R. Aging in a topological spin glass. *Phys. Rev. B* **2000**, *62*, R9264–R9267.

[52] Mugiraneza, S.; Hallas, A. M. Tutorial: a beginner's guide to interpreting magnetic susceptibility data with the Curie-Weiss law. *Commun. Phys.* **2022**, *5*, 95.

[53] Tokura, Y.; Nagaosa, N. Orbital physics in transition-metal oxides. *Science* **2000**, *288*, 462–468.

[54] Averill, B. A.; Eldredge, P. *Principles of General Chemistry*; 2012.

[55] Korotin, M. A.; Ezhov, S. Y.; Solovyev, I. V.; Anisimov, V. I.; Khomskii, D. I.; Sawatzky, G. A. Intermediate-spin state and properties of $LaCoO_3$. *Phys. Rev. B* **1996**, *54*, 5309–5316.

[56] Rao, C. N. R.; Seikh, M. M.; Narayana, C. Spin-State Transition in $LaCoO_3$ and Related Materials. In *Spin Crossover in Transition Metal Compounds II*, Gütlich, P., Goodwin, H. A. Eds.; Springer Berlin Heidelberg, 2004; pp 1–21.

[57] Hoch, M. J. R.; Nellutla, S.; van Tol, J.; Choi, E. S.; Lu, J.; Zheng, H.; Mitchell, J. F. Diamagnetic to paramagnetic transition in $LaCoO_3$. *Phys. Rev. B* **2009**, *79*, 214421.

[58] O'Brien, M. C.; Chancey, C. The Jahn–Teller effect: An introduction and current review. *Am. J. Phys.* **1993**, *61*, 688–697.

[59] Kim, W. J.; Smeaton, M. A.; Jia, C.; Goodge, B. H.; Cho, B. G.; Lee, K.; Osada, M.; Jost, D.; Ievlev, A. V.; Moritz, B.; Kourkoutis, L. F.; Devereaux, T. P.; Hwang, H. Y. Geometric frustration of Jahn–Teller order in the infinite-layer lattice. *Nature* **2023**, *615*, 237–243.

[60] Kugel, K. I.; Khomskiĭ, D. The Jahn-Teller effect and magnetism: transition metalcompounds. *Phys. Usp.* **1982**, *25*, 231.

[61] Bersuker, I. B. Modern aspects of the Jahn−Teller effect theory and applications to molecular problems. *Chem. Rev.* **2001**, *101*, 1067–1114.

[62] Congeduti, A.; Postorino, P.; Caramagno, E.; Nardone, M.; Kumar, A.; Sarma, D. Anomalous high pressure dependence of the Jahn-Teller phonon in $La_{0.75}Ca_{0.25}MnO_3$. *Phys. Rev. Lett.* **2001**, *86*, 1251.

[63] Waskowska, A.; Gerward, L.; Olsen, J. S.; Steenstrup, S.; Talik, E. $CuMn_2O_4$: properties and the high-pressure induced Jahn-Teller phase transition. *J. Phys.: Condens. Matter* **2001**, *13*, 2549.

[64] Heisenberg, W. Mehrkörperproblem und Resonanz in der Quantenmechanik. *Z.*

Physik **1926**, *38*, 411–426.

[65] Freeman, A. J.; Watson, R. E. Theory of direct exchange in ferromagnetism. *Phys. Rev.* **1961**, *124*, 1439–1454.

[66] Anderson, P. W. Antiferromagnetism. Theory of superexchange interaction. *Phys. Rev.* **1950**, *79*, 350.

[67] Goodenough, J. B. Theory of the role of covalence in the perovskite-type manganites [La, *M*(II)]MnO_3. *Phys. Rev.* **1955**, *100*, 564.

[68] Kanamori, J. Superexchange interaction and symmetry properties of electron orbitals. *J. Phys. Chem. Solids* **1959**, *10*, 87–98.

[69] Zener, C. Interaction between the *d* shells in the transition metals. *Phys. Rev.* **1951**, *81*, 440.

[70] Zener, C. Interaction between the *d*-shells in the transition metals. II. Ferromagnetic compounds of manganese with perovskite structure. *Phys. Rev.* **1951**, *82*, 403.

[71] Anderson, P. W.; Hasegawa, H. Considerations on double exchange. *Phys. Rev.* **1955**, *100*, 675.

[72] De Gennes, P.-G. Effects of double exchange in magnetic crystals. *Phys. Rev.* **1960**, *118*, 141.

[73] Kubo, K.; Ohata, N. A quantum theory of double exchange. I. *J. Phys. Soc. Jpn.* **1972**, *33*, 21-32.

[74] Lin, K.; Li, Q.; Yu, R.; Chen, J.; Attfield, J. P.; Xing, X. Chemical pressure in functional materials. *Chem. Soc. Rev.* **2022**, *51*, 5351–5364.

[75] Hirose, K.; Sinmyo, R.; Hernlund, J. Perovskite in Earth's deep interior. *Science* **2017**, *358*, 734-738.

[76] Loveday, J. *High-pressure physics*; CRC Press, 2012.

[77] Pinsard-Gaudart, L.; Rodríguez-Carvajal, J.; Daoud-Aladine, A.; Goncharenko, I.; Medarde, M.; Smith, R. I.; Revcolevschi, A. Stability of the Jahn-Teller effect and magnetic study of $LaMnO_3$ under pressure. *Phys. Rev. B* **2001**, *64*, 064426.

[78] Belik, A. A.; Johnson, R. D.; Khalyavin, D. D. The rich physics of A-site-ordered quadruple perovskite manganites AMn_7O_{12}. *Dalton Trans.* **2021**, *50*, 15458–15472.

[79] Markovich, V.; Fita, I.; Puzniak, R.; Rozenberg, E.; Martin, C.; Wisniewski, A.; Yuzhelevski, Y.; Gorodetsky, G. Pressure effects on magnetic and transport properties of electron-doped $La_{1-x}Ca_xMnO_3$ (x= 0.8, 0.9). *Phys. Rev. B* **2005**, *71*,

134427.

[80] Kozlenko, D.; Dubrovinsky, L.; Goncharenko, I.; Savenko, B.; Voronin, V.; Kiselev, E.; Proskurnina, N. Pressure-induced monoclinic distortion and charge and orbital ordering in $La_{0.5}Ca_{0.5}MnO_3$. *Phys. Rev. B* **2007**, *75*, 104408.

[81] Gor'kov, L. P.; Kresin, V. Z. Colloquium: high pressure and road to room temperature superconductivity. *Rev. Mod. Phys.* **2018**, *90*, 011001.

[82] Pena, V.; Sefrioui, Z.; Arias, D.; Leon, C.; Santamaria, J.; Martinez, J.; te Velthuis, S. G.; Hoffmann, A. Giant magnetoresistance in ferromagnet/superconductor superlattices. *Phys. Rev. Lett.* **2005**, *94*, 057002.

[83] Wang, X.; Liu, X. High pressure: a feasible tool for the synthesis of unprecedented inorganic compounds. *Inorg. Chem. Front.* **2020**, *7*, 2890-2908.

[84] Zhou, L.; Wang, X.; Zhang, H.-M.; Shen, X.-D.; Dong, S.; Long, Y.-W. High pressure synthesis and physical properties of multiferroic materials with multiply-ordered perovskite structure. *Acta Phys. Sin.* **2018**, *67*.

[85] Mao, H.-K.; Chen, B.; Chen, J.; Li, K.; Lin, J.-F.; Yang, W.; Zheng, H. Recent advances in high-pressure science and technology. *Matter Radiat. Extremes* **2016**, *1*, 59–75.

[86] Belik, A. A. Rise of A-site columnar-ordered $A_2A'A''B_4O_{12}$ quadruple perovskites with intrinsic triple order. *Dalton Trans.* **2018**, *47*, 3209–3217.

[87] Waroquiers, D.; Gonze, X.; Rignanese, G.-M.; Welker-Nieuwoudt, C.; Rosowski, F.; Gobel, M.; Schenk, S.; Degelmann, P.; André, R.; Glaum, R. Statistical analysis of coordination environments in oxides. *Chem. Mater.* **2017**, *29*, 8346–8360.

[88] Azuma, M.; Yamada, I.; Yamaura, K.; Belik, A. A.; Yamamoto, T.; Fukuda, M. High pressure studies of transition metal oxides. In *Comprehensive Inorganic Chemistry III*, Reedijk, J., Poeppelmeier, K. R. Eds.; Vol. 4; Elsevier, 2023; pp 681–718.

[89] Li, Z.; Cho, Y.; Li, X.; Li, X.; Aimi, A.; Inaguma, Y.; Alonso, J. A.; Fernandez-Diaz, M. T.; Yan, J.; Downer, M. C.; Henkelman, G.; Goodenough, J. B.; Zhou, J. New mechanism for ferroelectricity in the perovskite $Ca_{2-x}Mn_xTi_2O_6$ synthesized by spark plasma sintering. *J. Am. Chem. Soc.* **2018**, *140*, 2214–2220.

[90] Scatena, R.; Liu, R.; Shvartsman, V. V.; Khalyavin, D. D.; Inaguma, Y.; Yamaura, K.; Belik, A. A.; Johnson, R. D. Hybrid improper ferroelectricity in columnar $(NaY)MnMnTi_4O_{12}$. *Angew. Chem. Int. Ed.* **2023**, *62*, e202305994.

[91] Solana-Madruga, E.; Arevalo-Lopez, A. M.; Dos Santos-Garcia, A. J.; Urones-Garrote, E.; Avila-Brande, D.; Saez-Puche, R.; Attfield, J. P. Double double cation order in the high-pressure perovskites $MnRMnSbO_6$. *Angew. Chem. Int. Ed.* **2016**, *55*, 9340–9344.

[92] Belik, A. A.; Zhang, L.; Liu, R.; Khalyavin, D. D.; Katsuya, Y.; Tanaka, M.; Yamaura, K. Valence variations by B-site doping in A-site columnar-ordered quadruple perovskites $Sm_2MnMn(Mn_{4-x}Ti_x)O_{12}$ with $1 \leq x \leq 3$. *Inorg. Chem.* **2019**, *58*, 3492–3501.

[93] Vibhakar, A. M.; Khalyavin, D. D.; Manuel, P.; Liu, R.; Yamaura, K.; Belik, A. A.; Johnson, R. D. Effects of magnetic dilution in the ferrimagnetic columnar ordered $Sm_2MnMnMn_{4-x}Ti_xO_{12}$ perovskites. *Phys. Rev. B* **2020**, *102*, 214428.

[94] Solana-Madruga, E.; Arévalo-López, Á. M.; Dos Santos-García, A. J.; Ritter, C.; Cascales, C.; Sáez-Puche, R.; Attfield, J. P. Anisotropic magnetic structures of the $Mn*R*MnSbO_6$ high-pressure doubly ordered perovskites (*R* = La, Pr, and Nd). *Phys. Rev. B* **2018**, *97*, 134408.

[95] Vibhakar, A. M.; Khalyavin, D. D.; Manuel, P.; Zhang, L.; Yamaura, K.; Radaelli, P. G.; Belik, A. A.; Johnson, R. D. Magnetic structure and spin-flop transition in the A-site columnar-ordered quadruple perovskite $TmMn_3O_6$. *Phys. Rev. B* **2019**, *99*, 104424.

[96] Belik, A. A.; Khalyavin, D. D.; Zhang, L.; Matsushita, Y.; Katsuya, Y.; Tanaka, M.; Johnson, R. D.; Yamaura, K. Intrinsic Triple order in A-site columnar-ordered quadruple perovskites: Proof of concept. *ChemPhysChem* **2018**, *19*, 2449–2452.

[97] Vibhakar, A. M.; Khalyavin, D. D.; Manuel, P.; Liu, J.; Belik, A. A.; Johnson, R. D. Spontaneous rotation of ferrimagnetism driven by antiferromagnetic spin canting. *Phys. Rev. Lett.* **2020**, *124*, 127201.

[98] Aimi, A.; Mori, D.; Hiraki, K.-I.; Takahashi, T.; Shan, Y. J.; Shirako, Y.; Zhou, J.; Inaguma, Y. High-pressure pynthesis of *A*-site ordered double perovskite $CaMnTi_2O_6$ and ferroelectricity driven by coupling of *A*-site ordering and the second-order Jahn–Teller effect. *Chem. Mater.* **2014**, *26*, 2601–2608.

[99] Liu, R.; Scatena, R.; Khalyavin, D. D.; Johnson, R. D.; Inaguma, Y.; Tanaka, M.; Matsushita, Y.; Yamaura, K.; Belik, A. A. High-pressure synthesis, crystal structures, and properties of A-site columnar-ordered quadruple perovskites $NaRMn_2Ti_4O_{12}$

with R = Sm, Eu, Gd, Dy, Ho, Y. *Inorg. Chem.* **2020**, *59*, 9065–9076.

Chapter 2 Experimental techniques

All the samples discussed in this thesis were synthesized under high-pressure and high-temperature conditions. Their crystal structure and magnetic properties were investigated by a variety of characterization techniques. X-ray powder diffraction (XRPD) was used to determine the crystal structure and phase purity. Both laboratory based XRPD and synchrotron XRPD were utilized to achieve high-quality structural analysis. The magnetic properties of the materials were studied using a magnetic property measurement system (MPMS), while the thermal properties of the materials were analyzed using a physical property measurement system (PPMS). These techniques provided comprehensive insights into the structural and functional properties of the A-site columnar-ordered quadruple perovskites discussed in this thesis.

2.1 High-pressure synthesis

In this thesis, all samples were prepared using the belt-type high-pressure apparatus (Kobe Steel, Ltd.) which can reach pressures up to 8 GPa and temperatures up to 2000 °C. As shown in **Figure 2.1**(a), its main body consists of two conical anvils and a steel binding ring. It also includes a pressure control system, a temperature control system, and a data recording system. The pressure and temperature of the system should be calibrated to ensure good control of the experimental conditions. Before high-pressure and high-temperature synthesis, the starting materials powders should be mixed well and then sealed in gold (Au) capsule or platinum (Pt) capsule. The capsule is placed inside a high-pressure cell (HP cell, see **Figure 2.1**(c) [1]) which contains pyrophyllite, graphite heaters, and NaCl (with ZrO_2) sleeve and cylindrical pieces. During synthesis, the HP cell is placed at the central area of the steel binding ring, positioned by the core anvil in the horizontal direction and opposite to the conical anvil in the vertical direction (**Figure 2.1**(b)). The upper conical anvil is fixed and the bottom conical anvil moves up when hydraulic oil pushes it. When the pressure slowly increases to a certain level and stabilizes, the heating process begins. The target temperature is maintained for several hours. The pressure release must also be done slowly.

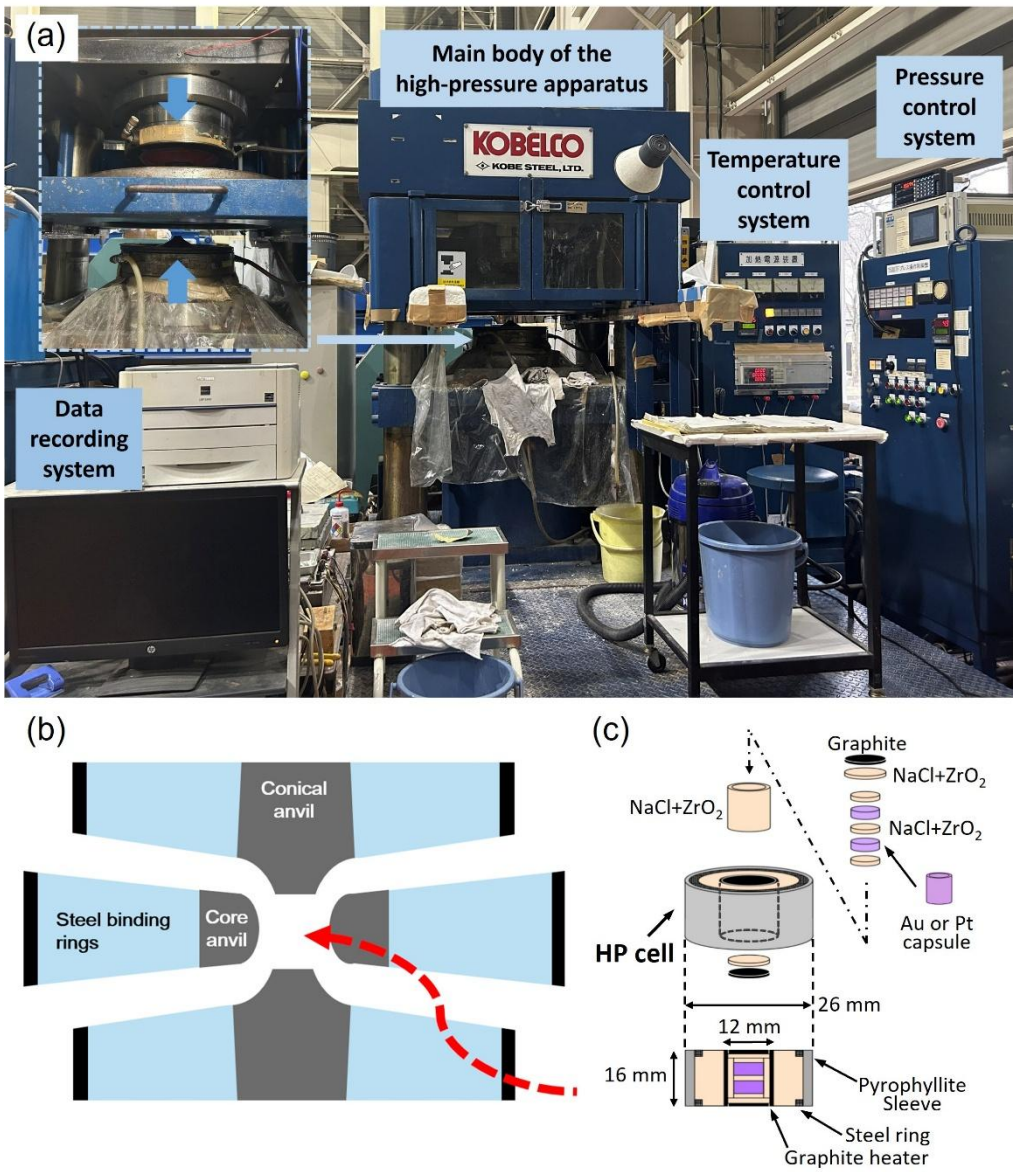

Figure 2.1 (a) The photograph of the belt-type high-pressure apparatus set in National Institute for Materials Science (NIMS). (b) Assembled views of the anvils. (c) Schematic diagram of a typical high-pressure cell (HP cell). The view does not correctly represent relative sizes and shapes of the apparatus (anvils are somewhat exaggerated) [1].

2.2 X-ray powder diffraction

2.2.1 Laboratory X-ray sources

The X-ray powder diffraction (XRPD) is a commonly used characterization

technique for analyzing sample's compositions and atomic structures of materials. As illustrated in **Figure 2.2**(a), a crystal consists of regularly arranged atoms. When X-rays with a certain wavelength are directed at the crystal, the atoms act as scattering centers. The scattering of each atom interferes with each other and produce strong diffraction signals at certain angles. This phenomenon is described by the Bragg equation:

$$2d\sin\theta = n\lambda$$

where d is the interplanar spacing, θ is the diffraction angle, defined as the angle between the incident X-ray beam and the crystal plane; n is the diffraction order, and in most cases, it is set to n = 1; λ is the wavelength of the X-ray.

In this thesis, room temperature (RT) XRPD data were collected using a MiniFlex Benchtop X-ray Powder Diffraction instrument (Rigaku) (**Figure 2.2**(b)), which was equipped with a graphite monochromator and Cu Kα radiation (λ = 1.54059Å). Data were recorded over the 2θ range of 5 to 100° (or 20 to 70°), with a step of 0.02° and a scanning rate of 3°/min.

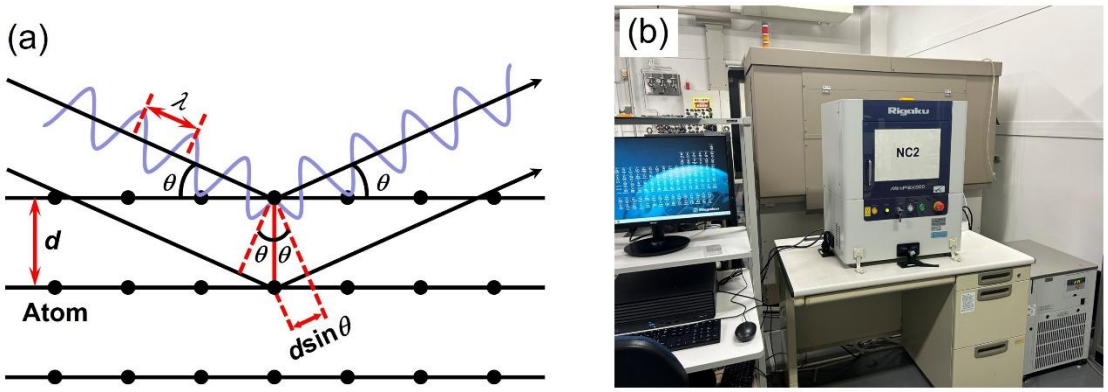

Figure 2.2 (a) Schematic diagram of X-ray powder diffraction (XRPD). (b) The photograph of MiniFlex Benchtop X-ray Powder Diffraction instrument (Rigaku).

2.2.2 Synchrotron X-ray sources

When charged particles (such as electrons) moving at relativistic speeds pass through a magnetic field and are forced to change direction, they radiate an electromagnetic radiation called synchrotron radiation. To generate this radiation,

electrons or positrons are first accelerated to near the speed of light in an accelerator and then introduced into a storage ring equipped with bending magnets and other magnetic structures for cyclic motion. A simplified sketch of a typical storage ring is shown in **Figure 2.3**(a) [2]. It usually has a diameter of several hundred meters and consists of straight and curved sections. When electrons pass through the bending magnets in the curved sections, the radiation is emitted along the tangent direction of the orbit, thus forming a beamline. Compared with laboratory X-ray sources, synchrotron X-rays have significant advantages such as high intensity, excellent collimation, and a continuously tunable wavelength, so they can provide high-quality data in XRPD.

In this thesis, all synchrotron XRPD data were collected at the BL02B2 beamline of the SPring-8 (**Figure 2.3**(b)). The beamline has an angle range (2θ coverage) of 1–75° and can be measured over a wide temperature range (30–1100 K). During measurements, the samples were sealed into Lindemann glass capillaries (inner diameter: 0.2 mm) and rotated during the test to improve the orientation averaging and data quality.

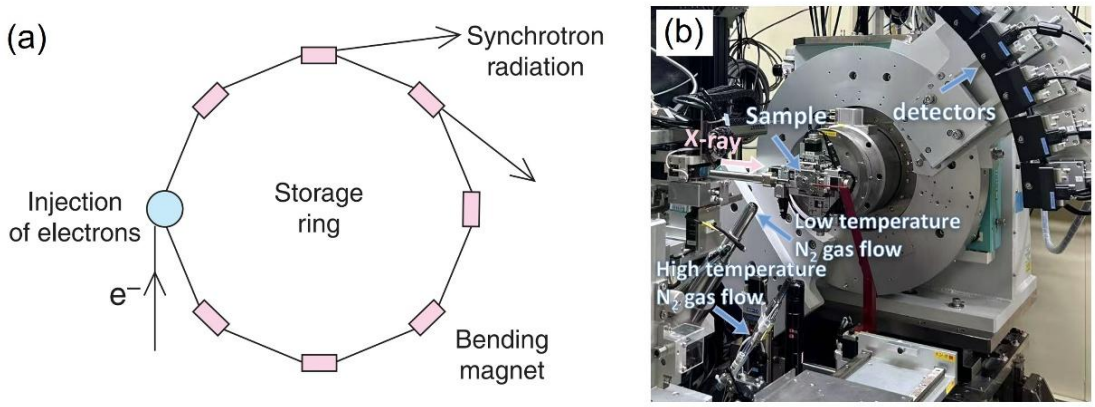

Figure 2.3 (a) Schematic diagram of a synchrotron storage ring [2]. (b) The photograph of the BL02B2 beamline in SPring-8.

2.3 Rietveld refinement

In the structure analysis of materials, it is often difficult to obtain single crystals of sufficient size, so polycrystalline materials are more commonly used. However, due to the randomness of grain orientation and the overlap between diffraction peaks,

conventional powder diffraction data may lose structural information. To solve this problem, Dutch scientist Hugo M. Rietveld first proposed a method of refining the crystal structure by fitting the full neutron powder diffraction pattern in 1967, which was later called the Rietveld refinement [3]. In 1977, Malmros and Thomas first extended this method to the structural refinement of XRPD data [4].

The core idea of the Rietveld refinement method is to calculate the theoretical powder diffraction pattern based on the initial structural model, and compare it with the measured pattern point by point through a computer program, and then optimize the structural model by least-squares fitting. Adjustable parameters include: (1) crystal structure parameters: unit cell parameters, fractional coordinates of atoms, atom occupation factors, atomic displacement parameters, etc.; (2) peak shape parameters: full width at half maximum (FWHM) (U, V, W factors), peak shape asymmetry, etc.; (3) instrumental factors: X-ray wavelength, zero-point shift, background, etc.; (4) other factors: particle size, preferred orientation, microstrain, etc. The general refinement procedure includes: first, adjusting zero-point and background; refining the unit cell parameters and the scale factor; followed by optimization of the peak profile function, typically Gaussian-based; and finally, modify atomic positions, occupancies, and thermal factors.

The structural refinements in this thesis were performed using the RIETAN program [5]. Compared with the traditional Rietveld method, RIETAN adopts the Maximum Entropy Method (MEM)-based Pattern Fitting approach (MPF). By alternately performing Rietveld fitting and maximum entropy analysis (REMEDY cycles), the degree of deviation of the structural model from the final electron/nuclear density is minimized in each iteration, thereby significantly improving the reliability of the refinement results. RIETAN defines four reliability factors to evaluate the quality of fitting, namely: R_p (profile R factor)**,** R_{wp} (weighted profile R factor)**,** R_B (Bragg R factor)**,** and χ^2 (goodness-of-fit). In general, R_p and R_{wp} values below 10%, indicate a reliable structural model. Originally, χ^2 values below 2 were considered as good refinement results. However, with high-quality synchrotron XRPD, which gives very high intensities and very low background, χ^2 values can become quite large because of very small R_{exp} values.

2.4 Magnetic properties measurement system

The magnetic measurements in this thesis were completed using the Magnetic Property Measurement System (MPMS3, Quantum Design, USA, **Figure 2.4**). This system is based on superconducting quantum interference device (SQUID) technology and has extremely high magnetic susceptibility sensitivity, which is suitable for studying weak magnetic systems. The MPMS system can achieve controllable changes in the temperature range of 1.8–400 K and the magnetic field range of –7 T to +7 T, and can accurately measure the magnetic parameters such as DC magnetization and magnetic hysteresis loops of the sample under different temperature and magnetic field conditions. In this study, the MPMS system was used to characterize the paramagnetic-ferrimagnetic transition behavior and low-temperature magnetic order characteristics of the material, providing important experimental basis for revealing its magnetic origin and evolution mechanism.

Figure 2.4 The photograph of Magnetic Property Measurement System (MPMS3) in NIMS.

2.5 Physical properties measurement system

The specific heat capacity measurements in this thesis were carried out using the Physical Property Measurement System (PPMS-9T, Quantum Design, USA, **Figure 2.5**). The system is equipped with a high-precision specific heat module (Heat Capacity Option) and uses the relaxation method to collect data. It can achieve quasi-adiabatic measurement of samples under controlled temperature conditions from 1.8 K to 400 K and magnetic fields up to ±9 T. During the measurement, the sample is fixed on the heat capacity platform. The system applies a small heat pulse while monitoring the resulting temperature response over time to determine the specific heat at constant pressure (C_p) as a function of temperature.

In this study, the specific heat capacity test is mainly used to reveal the magnetic heat capacity anomaly of the material in the low temperature region, and extract the magnetic heat part by fitting the background (such as lattice heat capacity), and further estimate the key parameters such as magnetic entropy change (S_{mag}) and magnetic phase transition temperature (T_C), revealing the magnetic evolution process of the material from a thermodynamic perspective.

Figure 2.5 The photograph of Physical Property Measurement System (PPMS-9T) in NIMS.

References in chapter 2

[1] K. Yamaura. Short review of high-pressure crystal growth and magnetic and electrical properties of solid-state osmium oxides. *J. Solid State Chem.* **2016**, *236*, 45–54.

[2] A. R. West. *Solid State Chemistry and Its Applications*; John Wiley & Sons, Ltd, 2014.

[3] H. Rietveld. A profile refinement method for nuclear and magnetic structures. *J. Appl. Crystallogr.* **1969**, *2*, 65–71.

[4] G. Malmros; J. Thomas. Least-squares structure refinement based on profile analysis of powder film intensity data measured on an automatic microdensitometer. *Applied Crystallography* **1977**, *10*, 7–11.

[5] F. Izumi; T. Ikeda. A Rietveld-analysis programm RIETAN-98 and its applications to zeolites. *Mater. Sci. Forum* **2000**, *321–324*, 198–205.

Chapter 3 B-site ordered and disordered phases in A-site columnar-ordered quadruple perovskites $Nd_2MnMn(Mn_{4-x}Sb_x)O_{12}$

3.1 Introduction

Perovskite-structure compounds have been identified as one of the most promising materials owing to their rich physical properties. They already have a wide range of applications, for example, in photovoltaics, catalysis, and other various devices [1-4]. The perovskite ABO_3 structure is built from a framework of corner-shared BO_6 octahedra that form cavities, which are filled with A cations. Depending on the size mismatch of A, B, and O, the BO_6 octahedral framework requires different distortions to stabilize the structure. One of such distortions is rigid BO_6 octahedral tilts, which can be described by the Glazer tilt system and B–O–B bond angles [5]. Different tilts give rise to diverse and distinct numbers and types of cavities for A cations. In the case of the most commonly observed tilt system of $a^-b^+a^-$ (written in the Glazer notation [5]), only one type of an A-site cavity is created; but the coordination number of A cations in ABO_3 perovskites can be reduced from 12 (for small tilts) to 8 (for large tilts). The $a^+a^+a^+$ tilt produces two types of cavities in the case of $AA'_3B_4O_{12}$ quadruple perovskites. The A site has a 12-fold coordination similar to the coordination number in the ideal undistorted ABO_3 structure, while the A′ site has a square-planar coordination [6, 7]. Another special class of the perovskite family with the $a^+a^+c^-$ tilt system, $A_2A'A''B_4O_{12}$, has original columnar-type arrangements of three types of cavities: 10-coordinated A, 4-coordinated square-planar A′, and 4-coordinated tetrahedral A″ sites [8]. In $AA'_3B_4O_{12}$ and $A_2A'A''B_4O_{12}$ quadruple perovskites, the square-planar A′ site is usually occupied by Jahn–Teller cations (such as Cu^{2+} and Mn^{3+}). However, other cations (such as Mn^{2+}, Co^{2+}, and Fe^{2+}) can also be incorporated using a high-pressure high-temperature preparation method [8].

To enhance and customize properties of perovskite-type materials, various combinations of A and B cations are frequently incorporated. The distribution of these cations within the A- and B- sites can either be random or result in ordered structures depending on characteristics of A and B cations, including their ionic radii, oxidation

states, and electronic configurations. Since the coordination environment of the B cations in perovskites is fixed to octahedral, oxidation state differences are the main factor influencing the ordering of B-site cations. The large difference in the oxidation state of B and B′ cations favors ordered distributions; B and B′ cations are usually ordered when the charge difference is larger than 2 [9]. A lot of B-site-ordered $A_2BB'O_6$ double perovskites have been reported to date [10]. However, A-site-ordered $AA'B_2O_6$ double perovskites are significantly less common and are often achieved together with simultaneous 1:1 cation orders at both A- and B-sites, which are known as doubly ordered (or double double [11]) perovskites, $AA'BB'O_6$ [12, 13]. A-site-ordered structures can also be stabilized by octahedral tilts combined with large differences in size and electronic properties of A cations as in $AA'_3B_4O_{12}$ quadruple perovskites with 1:3 double A-site ordering and $A_2A'A''B_4O_{12}$ quadruple perovskites with 2:1:1 triple A-site ordering [8, 14]. Triple A-site ordering by different cations was found, for example, in $Ho_2MnGa(Mn_{4-x}Ga_x)O_{12}$ [14], $Y_2MnGa(Mn_{4-x}Ga_x)O_{12}$ [15], $Y_2CuGaMn_4O_{12}$ [16], and $Dy_2CuZnMn_4O_{12}$ [17]. However, in many cases, triple ordering in such perovskites is hidden because A′ = A″.

Some perovskite materials can be synthesized in both cation-ordered structures and disordered structures resulting in significant alterations in their properties. For example, the ferromagnetic Curie temperature increased from 270 K in the disordered $LaBaMn_2O_6$ with colossal magnetoresistance to 335 K for the cation-ordered phase [18]. The gradual introduction of B-site disorder progressively overwhelmed the long-range ferrimagnetic ordering in Y_2CoIrO_6 sample with B-site ordering [19]. Noticeable changes of magnetic properties have also been reported in A-site-ordered and A-site-disordered modifications of the $CaMnMnWO_6$ perovskite [11]. Some $A_2A'A''B_4O_{12}$ quadruple perovskites can also be prepared in different modifications depending on synthesis conditions, for example, polar and non-polar phases of $NaYMn_2Ti_4O_{12}$ were reported [20].

In this work, $Nd_2MnMn(Mn_{4-x}Sb_x)O_{12}$ solid solutions were prepared at 6 GPa. They belong to the A-site columnar-ordered quadruple perovskite subfamily. Two regions with different cation orders in the B sublattice were found: the $0.8 \le x \le 1.0$ compositions had a B-site disordered structure while the $1.6 \le x \le 2.0$ compositions had a B-site rock-salt-ordered structure. Other compositions were multi-phase mixtures. Two

magnetic transitions were found with systematic changes of phase transition temperatures as a function of the composition. There was evidence for the third magnetic transition in the $1.7 \leq x \leq 2.0$ compositional range. The $x = 2.0$ sample was prepared before at 10 GPa and investigated using neutron diffraction and magnetic measurements [21].

3.2 Experimental details

$Nd_2MnMn(Mn_{4-x}Sb_x)O_{12}$ samples were prepared from stoichiometric mixtures of Nd_2O_3 (99.9%), Sb_2O_3 (99.9%), and Mn_2O_3. Mn_2O_3 was prepared from commercial MnO_2 (99.99%) by heating in air at 920 K for 24 h. Nd_2O_3 was dried in air at 1270 K for 1 h and the other two oxides were dried in air at 390 K for 4 h before use. All $Nd_2MnMn(Mn_{4-x}Sb_x)O_{12}$ samples were synthesized at about 6 GPa and about 1700 K for 2 h in Pt capsules using a belt-type high-pressure machine. After annealing, the samples were cooled down to room temperature (RT) by turning off the heating current, and the pressure was slowly released.

X-ray powder diffraction (XRPD) data at RT were collected on a RIGAKU MiniFlex600 diffractometer using CuKα radiation at RT (in a 2θ range of 5–100° with a step of 0.02°, and a scan speed of 3°/min). Synchrotron XRPD data were collected at RT on the BL02B2 beamline of SPring-8 at RT between 1.95° and 78.09° at a 0.006° interval in 2θ with the wavelength of $\lambda = 0.42019$ Å [22]. The data up to 70° were used in the refinements as no experimental reflections were observed above 70°. The samples were placed into Lindemann glass capillary tubes (inner diameter: 0.2 mm), which were rotated during measurements. The Rietveld analysis of all XRPD data was performed using the *RIETAN-2000* program [23].

Magnetic measurements were performed on a SQUID magnetometer (Quantum Design, MPMS3) between 2 K and 150 K (or 300 K) in an applied magnetic field of 100 Oe and between 2 K and 400 K in an applied field of 10 kOe under both zero-field-cooled (ZFC) and field-cooled on cooling (FCC) conditions. Isothermal magnetization measurements were performed between −70 and 70 kOe at 5 K, 25 K, 60 K, and 100 K. Specific heat was measured on a Quantum Design PPMS-9T instrument on cooling (and on heating in some cases) at magnetic fields of 0 Oe and 90 kOe.

3.3 Results and discussion

3.3.1 Phase compositions and crystal structure refinements

XRPD patterns of all members of the $Nd_2MnMn(Mn_{4-x}Sb_x)O_{12}$ solid solutions under CuKα radiation are shown in **Figure 3.1**. Our phase analysis showed that the x = 0.2 sample contained about 46.6 wt. % of a $P4_2/nmc$ phase, about 44.0 wt. % of a $NdMn_7O_{12}$ ($AA'_3B_4O_{12}$-type perovskite) phase, and about 9.4 wt. % of a $NdMnO_3$-related (ABO_3-type perovskite) phase. The $NdMnO_3$-related phase disappeared in the x = 0.4 sample, and the amount of the $NdMn_7O_{12}$ phase also decreased with increasing the x value. The x = 0.6 sample contained 10.1 wt. % of the $NdMn_7O_{12}$ impurity, while the x = 0.8 sample contained traces of the $NdMn_7O_{12}$ impurity (2.3 wt. %) indicating that the $Nd_2MnMn(Mn_{4-x}Sb_x)O_{12}$ solid solutions form from about x = 0.8. Samples with x = 0.8, 0.9, and 1.0 adopted the parent structure of the A-site columnar-ordered quadruple perovskite family with space group $P4_2/nmc$ which can be represented by $SmMnGaTiO_6$, $GdMnGaTiO_6$ [24], and $CaFeTi_2O_6$ [25]. A characteristic reflection of the $P4_2/nmc$ structure near 33.2° (for CuKα radiation) was still observed in samples up to x = 1.5 (**Figure 3.1**(c)). At the same time, a characteristic reflection of the $P4_2/n$ structure [due to B-site ordering, with the Miller index of (111)] near 19.8° (for CuKα radiation) appeared in samples from x = 1.2 (**Figure 3.1**(b)). These observations suggested that a two-phase region realized for the $1.2 \le x \le 1.5$ compositions. The x = 1.2 sample contained 42.8 wt. % of $P4_2/n$ phase, the x = 1.4 sample – 71.2 wt. %, and the x = 1.5 sample – 88.9 wt. %. The $1.6 \le x \le 2.0$ compositions contained only the $P4_2/n$ phase. Note that we also observed traces of a pyrochlore-type phase in majority of samples, (**Figures 3.2–3.3**), but since it is not a perovskite-type phase, it is not discussed further; the $1.6 \le x \le 2.0$ samples also contained a small amount (about 1-2 wt. %, except x = 1.7 with about 3.6 wt. %) of a $GdFeO_3$-type *Pnma* impurity. The x = 1.9 and 2.0 samples additionally contained small amounts of an unknown impurity; all impurity peaks could be indexed in space group $R\bar{3}$ with a = 7.4552 Å and c = 8.8154 Å (for x = 1.9) and with a = 7.4667 Å and c = 8.8133 Å (for x = 2.0). We also note that the x = 1 (and x = 1.2) sample showed a very weak (111) reflection, which is forbidden in the $P4_2/nmc$ structure; the appearance of this reflection could originate from short-range order of Mn and Sb at the B sites.

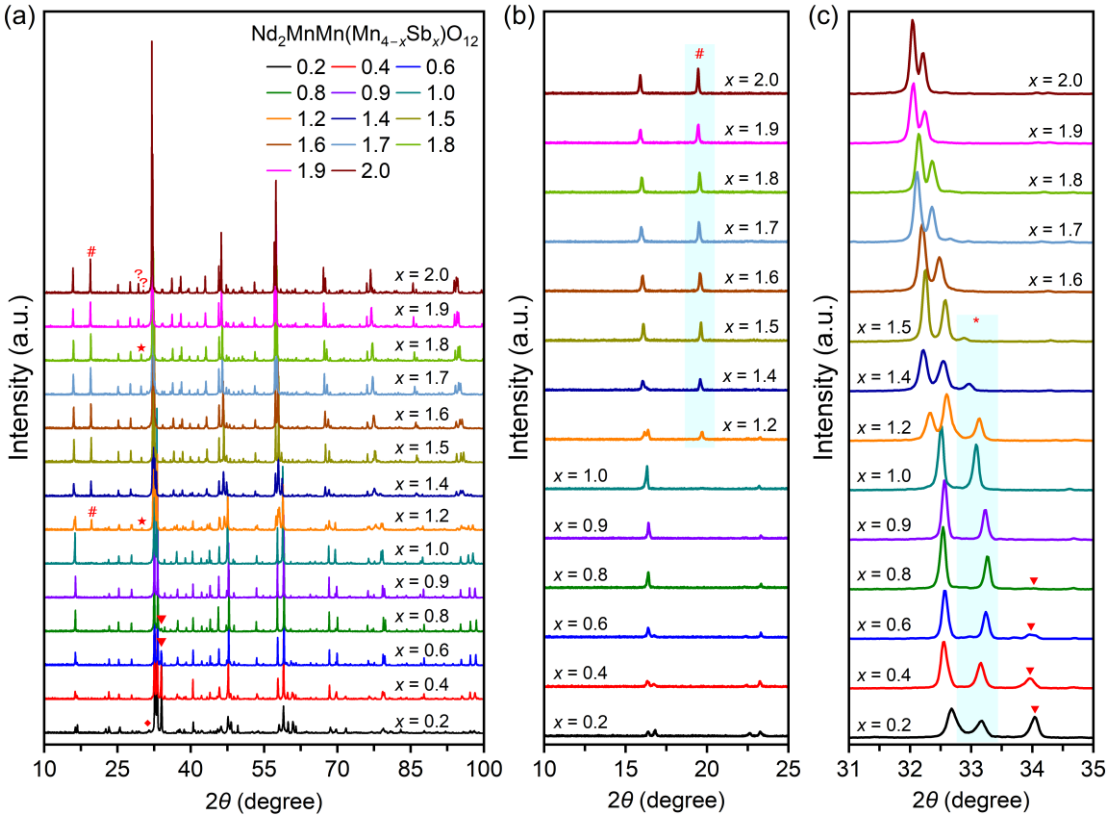

Figure 3.1 (a) X-ray powder diffraction patterns of $Nd_2MnMn(Mn_{4-x}Sb_x)O_{12}$ with x = 0.2, 0.4, 0.6, 0.8, 0.9, 1.0, 1.2, 1.4, 1.5, 1.6, 1.7, 1.8, 1.9, and 2.0 at T = 295 K (CuKα radiation). (b-c) Fragments of (a). The red octothorpes show the characteristic peak of the $P4_2/n$ phase (with the Miller index of (111)). The red stars show the 100% peak of a pyrochlore-type phase. The red triangles show a characteristic peak of $NdMn_7O_{12}$. The red square shows a characteristic peak of $NdMnO_3$. The red question marks show unknown impurity.

Experimental, calculated, and difference synchrotron XRPD patterns are shown in **Figures 3.2–3.3**. Structure parameters of $Nd_2MnMn(MnTi_3)O_{12}$ with space group $P4_2/nmc$ and $Nd_2MnMn(Mn_2Sb_2)O_{12}$ with space group $P4_2/n$ were used as the initial models in the Rietveld analysis of $Nd_2MnMn(Mn_{4-x}Sb_x)O_{12}$ with $0.8 \le x \le 1.0$ and $1.5 \le x \le 2.0$, respectively [21, 26]. In the final structural models, the Sb content was fixed according to the target compositions because the refined occupation factors were very close to the expected ones (**Tables A.1–A.3** in Appendix A). The square-planar Mn1 site

was split from ideal (fully occupied) sites to half-occupied sites as such models noticeably reduced an atomic displacement parameter of the Mn1 site.

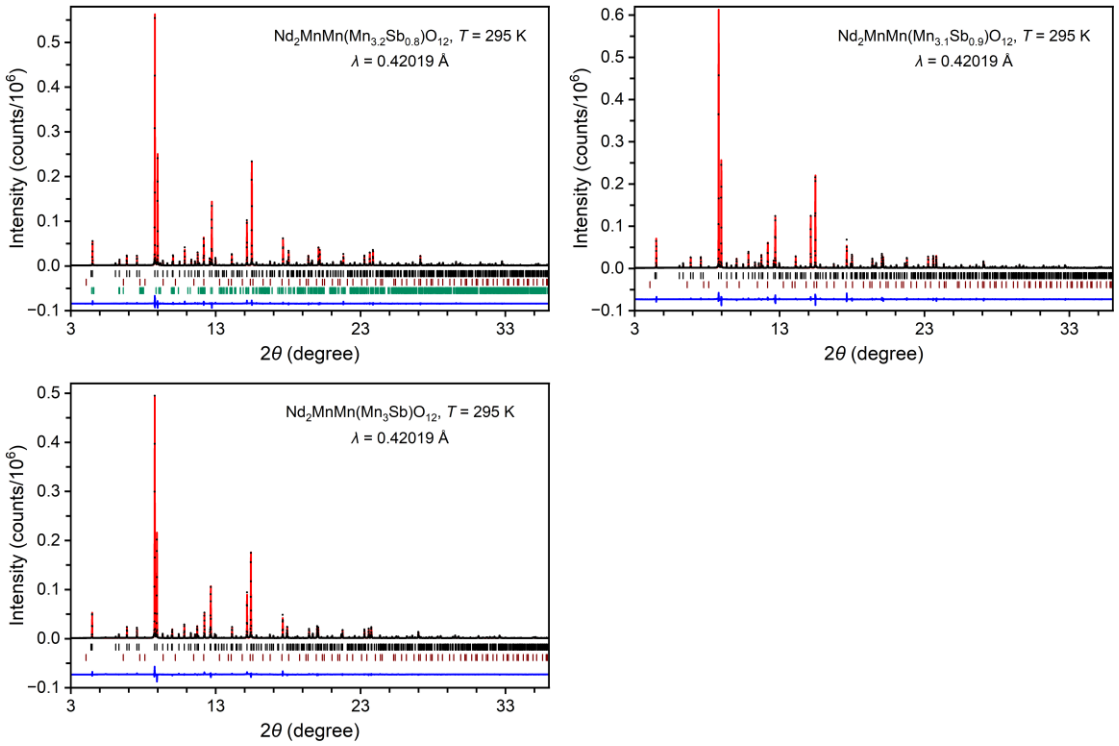

Figure 3.2 Fragments of experimental (black circles), calculated (red line), and difference (blue line) synchrotron XRPD patterns of $Nd_2MnMn(Mn_{4-x}Sb_x)O_{12}$ with x = 0.8, 0.9, and 1.0 at T = 295 K. The tick marks show possible Bragg reflection positions of the main perovskite phase ($P4_2/nmc$ phase, the first black row), pyrochlore impurity (the second claret row), and $NdMn_7O_{12}$ impurity (the third green row, only appears in x = 0.8 sample).

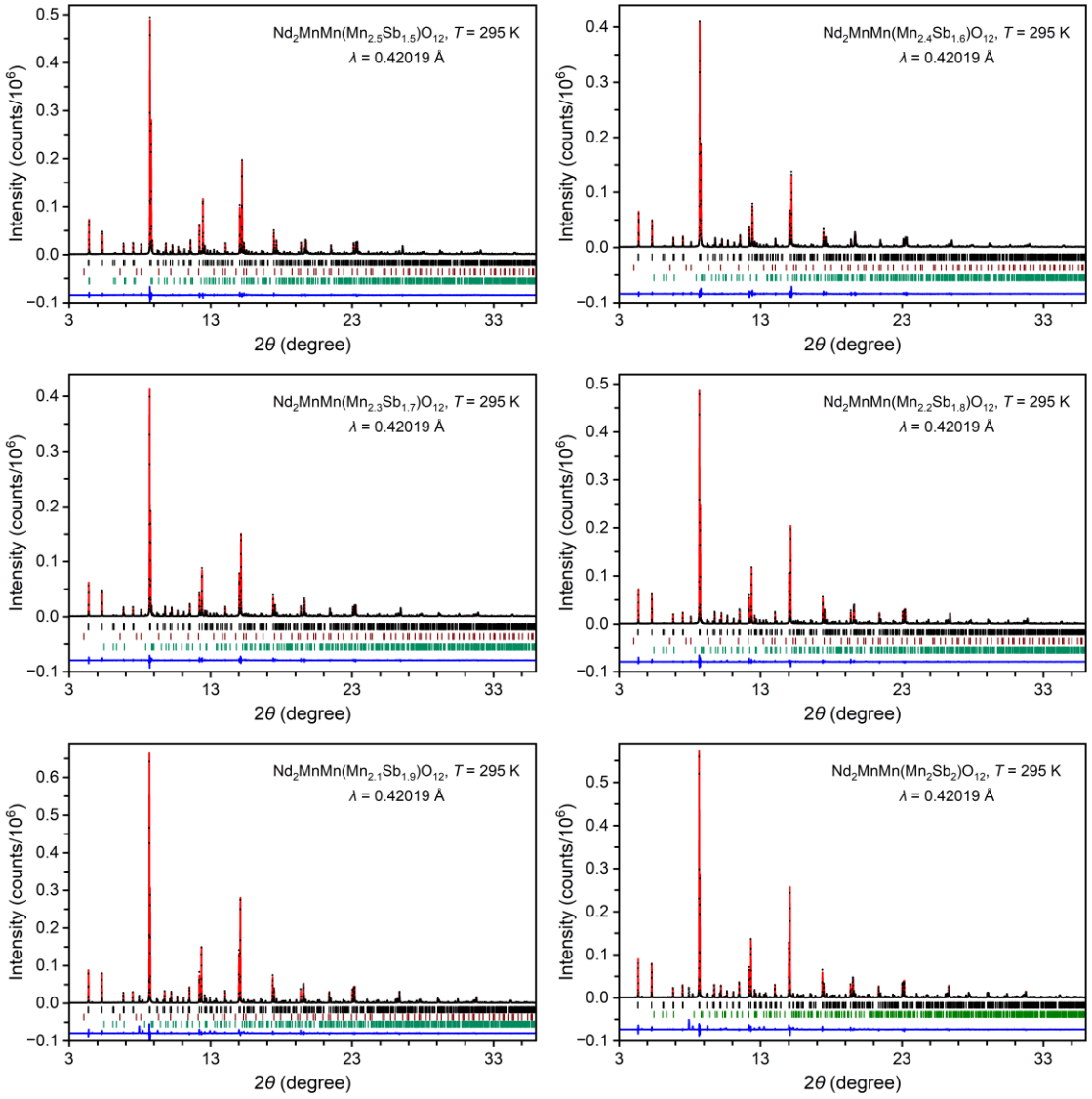

Figure 3.3 Fragments of experimental (black circles), calculated (red line), and difference (blue line) synchrotron XRPD patterns of $Nd_2MnMn(Mn_{4-x}Sb_x)O_{12}$ with x = 1.5, 1.6, 1.7, 1.8, 1.9, and 2.0 at T = 295 K. For x = 1.5 sample, the tick marks show possible Bragg reflection positions of the main perovskite phase ($P4_2/n$ phase, the first row), pyrochlore impurity (the second row), and $P4_2/nmc$ phase (the third row). For other samples, the tick marks show possible Bragg reflection positions of the main perovskite phase ($P4_2/n$ phase, the first black row), pyrochlore impurity (the second claret row, which does not appear in x = 2.0 sample), and impurity with *Pnma* symmetry (the third green row).

To check possible anti-site disorder, only Nd was assumed at the Nd site, and only Mn was assumed at Mn1 and Mn2 sites in intermediate structural models. Refined occupations factors, *g*, of such models are summarized on **Figure 3.4**(c), *g*(Nd) values were slightly smaller than 1. On the other hand, 2**g*(Mn1) and *g*(Mn2) values were higher than 1. All these facts suggested the presence of anti-site disorder. Anti-site disorder monotonically decreased with increasing the *x* value and almost vanished in the *x* = 2.0 sample. In the final structural models, the occupations factors of the Nd, Mn1, and Mn2 sites were refined with the following constraints: *g*(Nd) + *g*(Mn) = 1 for the Nd and Mn2 sites and *g*(Nd) + *g*(Mn) = 0.5 for the split Mn1 site. The Nd content, refined in such a way, agreed quite well with the target compositions in many cases. Therefore, the total Nd content was not fixed and was refined freely.

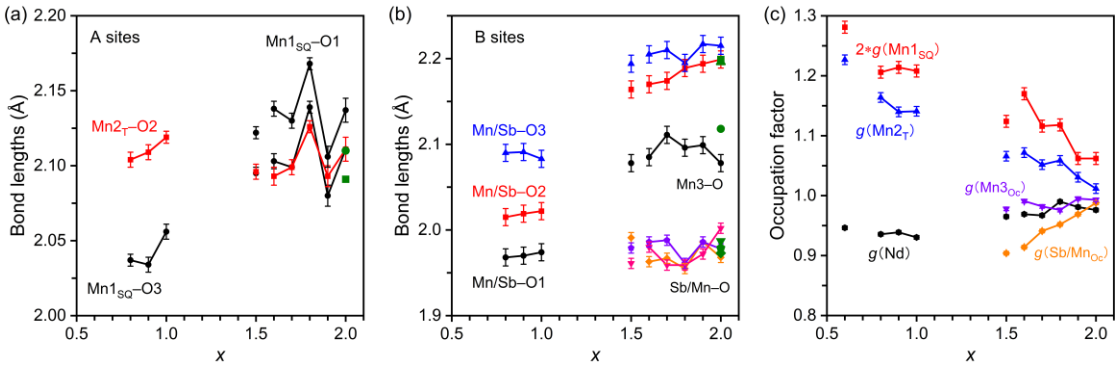

Figure 3.4 Compositional dependence of (a) Mn1–O (square-planar, SQ) and Mn2–O (tetrahedral, T) bond lengths, (b) Mn/Sb–O, Mn3–O, and Sb/Mn–O (octahedral, Oc) bond lengths, and (c) cation occupation factors in $Nd_2MnMn(Mn_{4-x}Sb_x)O_{12}$ solid solutions for $x = 0.6$, $0.8 \leq x \leq 1.0$, and $1.5 \leq x \leq 2.0$ from synchrotron XRPD data at $T = 295$ K. Only Mn was assumed at the Mn1, Mn2, and Mn3 sites, only Nd was assumed at the Nd site, and only Sb was assumed at the Sb/Mn site. The data presented in green symbols on panels (a) and (b) are sourced from the literature (the single-crystal data at $T = 120$ K) [21].

Table 3.1 Structure parameters of $Nd_2MnMn(Mn_{4-x}Sb_x)O_{12}$ (x = 0.8, 0.9, and 1.0) at T = 295 K from synchrotron X–ray powder diffraction data.

x	0.8	0.9	1
a (Å)	7.58349(2)	7.59899(2)	7.62652(2)
c (Å)	7.92523(2)	7.91997(3)	7.89916(3)
V (Å^3)	455.775(2)	457.336(2)	459.445(3)
g(Nd)	0.890(3)Nd+0.110Mn	0.892(4)Nd+0.108Mn	0.880(3)Nd+0.120Mn
z(Nd)	0.22303(7)	0.22296(8)	0.22309(7)
B(Nd) (Å^2)	1.291(11)	1.233(13)	1.241(12)
g(Mn1-SQ)	0.424(3)Mn+0.076Nd	0.447(2)Mn+0.053Nd	0.423(3)Mn+0.077Nd
z(Mn1)	0.7867(4)	0.7854(4)	0.7871(4)
B(Mn1) (Å^2)	1.65(8)	1.00	2.05(10)
g(Mn2-T)	0.884(5)Mn+0.116Nd	0.888(4)Mn+0.112Nd	0.900(5)Mn+0.100Nd
B(Mn2) (Å^2)	1.00(6)	1.00	0.93(6)
g(Mn/Sb-Oc)	0.8Mn+0.2Sb	0.775Mn+0.225Sb	0.75Mn+0.25Sb
B(Mn/Sb) (Å^2)	0.932(15)	0.969(16)	0.939(16)
y(O1)	0.0572(5)	0.0565(6)	0.0561(5)
z(O1)	–0.0380(6)	–0.0374(6)	–0.0356(6)
B(O1) (Å^2)	1.25(9)	1.06(10)	1.27(9)
y(O2)	0.5388(6)	0.5377(6)	0.5374(6)
z(O2)	0.5777(5)	0.5785(6)	0.5773(5)
B(O2) (Å^2)	1.50(10)	1.49(12)	1.18(10)
x(O3)	0.4380(4)	0.4375(5)	0.4387(4)
B(O3) (Å^2)	2.24(11)	2.55(14)	2.74(12)
R_{wp} (%)	7.64	8.74	7.59
R_p (%)	5.46	6.22	5.46
R_I (%)	6.12	5.68	5.54
R_F (%)	8.13	7.39	7.41
Impurities	pyrochlore: 0.1% $NdMn_7O_{12}$: 2.3%	pyrochlore: 0.4% –	pyrochlore: 0.2% –

Crystal data: space group $P4_2/nmc$ (No. 137, cell choice 2), Z = 2.

Nd – 4*d* site (0.25, 0.25, *z*); Mn1-SQ – 4*c* site (0.75, 0.25, *z*) near 2*a* site (0.75, 0.25, 0.75); Mn2-T – 2*b* site (0.75, 0.25, 0.25); Mn/Sb-Oc – 8*e* site (0, 0, 0); O1 and O2 – 8*g* site (0.25, *y*, *z*), and O3 – 8*f* site (*x*, –*x*, 0.25). *g*(O1) = *g*(O2) = *g*(O3) = 1, *g* is the occupation factor.

SQ: square-planar (site), T: tetrahedral (site), Oc: octahedral (site).

Table 3.2 Structure parameters of $Nd_2MnMn(Mn_{4-x}Sb_x)O_{12}$ (x = 1.5, 1.6, and 1.7) at T = 295 K from synchrotron X–ray powder diffraction data.

x	1.5	1.6	1.7
a (Å)	7.74834(2)	7.76781(4)	7.78827(2)
c (Å)	7.90920(2)	7.90366(4)	7.90647(3)
V (Å^3)	474.843(2)	476.898(4)	479.584(3)
g(Nd)	0.902(3)Nd+0.098Mn	0.930(4)Nd+0.070Mn	0.920(4)Nd+0.080Mn
z(Nd)	0.77703(6)	0.77703(7)	0.77691(7)
B(Nd) (Å^2)	0.993(11)	0.908(15)	0.825(12)
g(Mn1-SQ)	0.463(3)Mn+0.037Nd	0.443(4)Mn+0.057Nd	0.464(3)Mn+0.036Nd
z(Mn1)	0.7833(5)	0.7870(5)	0.7824(5)
B(Mn1) (Å^2)	1.70(10)	1.62(11)	1.34(10)
g(Mn2-T)	0.970(5)Mn+0.030Nd	0.955(6)Mn+0.045Nd	0.973(5)Mn+0.027Nd
B(Mn2) (Å^2)	0.57(6)	0.42(7)	0.44(6)
g(Mn3-Oc)	1Mn	1Mn	1Mn
B(Mn3) (Å^2)	0.86(3)	0.81(3)	0.78(3)
g(Sb/Mn-Oc)	0.75Sb+0.25Mn	0.8Sb+0.2Mn	0.85Sb+0.15Mn
B(Sb/Mn) (Å^2)	0.579(13)	0.436(16)	0.408(12)
x(O1)	–0.0433(8)	–0.0494(14)	–0.0491(11)
y(O1)	0.5769(8)	0.5695(13)	0.5711(10)
z(O1)	0.2365(6)	0.2339(8)	0.2338(7)
B(O1) (Å^2)	1.17(12)	1.51(15)	1.07(12)
x(O2)	–0.2373(13)	–0.2373(16)	–0.2373(13)
y(O2)	–0.0391(6)	–0.0396(7)	–0.0402(6)
z(O2)	0.5846(5)	0.5851(7)	0.5839(6)
B(O2) (Å^2)	1.27(11)	1.40(14)	1.25(12)
x(O3)	–0.2579(12)	–0.2571(15)	–0.2602(12)
y(O3)	0.0642(5)	0.0682(6)	0.0674(6)
z(O3)	–0.0352(5)	–0.0358(6)	–0.0343(6)
B(O3) (Å^2)	1.24(9)	1.06(11)	0.87(10)
R_{wp} (%)	6.44	7.70	6.96
R_p (%)	4.68	5.51	5.09
R_I (%)	3.77	2.96	2.91
R_F (%)	3.90	2.07	2.46
Impurities	pyrochlore: 2.0% $P4_2/nmc$-per.: 9.1%	pyrochlore: 1.1% *Pnma*-per.: 1.5%	pyrochlore: 1.9% *Pnma*-per.: 3.6%

Crystal data: space group $P4_2/n$ (No. 86, cell choice 2), Z = 2. Nd – 4*e* site (0.25, 0.75, *z*); Mn1-SQ – 4*f* site (0.25, 0.25, *z*); Mn2-T – 2*a* site (0.75, 0.75, 0.75); Mn3-Oc – 4*c* site (0, 0.5, 0.5); Sb/Mn-Oc – 4*d* site (0, 0, 0.5); O1, O2 and O3 – 8*g* site (*x*, *y*, *z*).

g(O1) = g(O2) = g(O3) = 1, g is the occupation factor.
SQ: square-planar (site), T: tetrahedral (site), Oc: octahedral (site).
$P4_2/nmc$-per.: a $Nd_2MnMn(Mn_3Sb)O_{12}$-type perovskite phase with $P4_2/nmc$ symmetry.
Pnma-per.: a $GdFeO_3$-type perovskite phase with *Pnma* symmetry.

The structural analysis of the samples with the B-site-ordered structure (space group $P4_2/n$) showed that one B site (called Mn3) was always occupied by Mn, while the second B″ site (called Sb/Mn) had a mixture of Sb and Mn (**Figure 3.4**(c)). Refined structural parameters and bond lengths are summarized in **Figures 3.4**(a–b), **Tables 3.1**–**3.2**, and **Tables A.4**–**A.7** in Appendix A.

The compositional dependence of lattice parameters obtained from synchrotron XRPD data is illustrated in **Figure 3.5** (values are given in **Table A.8** in Appendix A), where weight fractions are also given for samples containing several perovskite-type phases. Data obtained from XRPD under CuKα radiation for sample $0.2 \le x \le 1.4$ are also shown. In the samples containing (almost) the $P4_2/nmc$ phase ($0.8 \le x \le 1.0$), the *a* parameter increased monotonically, and the *c* parameter decreased monotonically with increasing *x*. On the other hand, in the samples containing (almost) the $P4_2/n$ phase ($1.6 \le x \le 2.0$), the *a* parameter increased monotonically with increasing *x*, and the *c* parameter was almost constant.

The lattice parameters of the samples with $0.2 \le x \le 0.6$ continued to change monotonically and did not match with the $Nd_2MnMn(Mn_{3.2}Sb_{0.8})O_{12}$ sample ($x = 0.8$) as would be expected for $Nd_2MnMn(Mn_{4-x}Sb_x)O_{12}$ solid solutions with the solubility limit near $x = 0.8$. These features could be explained by an additional composition variation. The $Nd_2MnMn(Mn_{4-x}Sb_x)O_{12}$ samples with $0.2 \le x \le 0.6$ had a $NdMn_7O_{12}$ impurity, which is Nd-poor in comparison with the target $Nd_2MnMn(Mn_{4-x}Sb_x)O_{12}$ compositions. Therefore, the main phase should be Nd-rich: $Nd_{2+y}Mn_{2-y}(Mn_{4-x}Sb_x)O_{12}$. Indeed, the refinement of the crystal structure of the $x = 0.6$ sample (from synchrotron XRPD data at RT; results are not shown) gave the following Nd-rich composition: $Nd_{2.18}Mn_{1.82}(Mn_{3.4}Sb_{0.6})O_{12}$. The $x = 0.6$ sample also showed the largest deviations of the 2**g*(Mn1) and *g*(Mn2) occupation factors from 1 (**Figure 3.4**(c)). Rare-earth-rich chemical compositions were observed before in such $A_2A'A''B_4O_{12}$-type perovskites, for

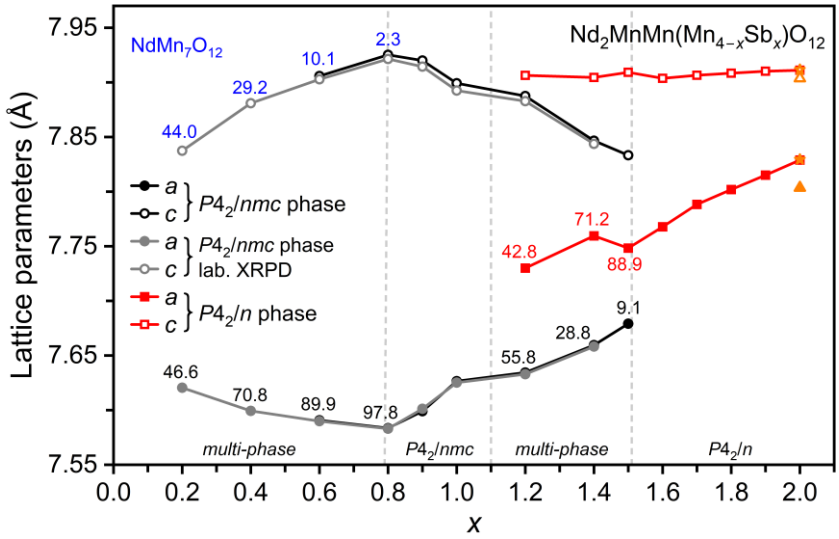

Figure 3.5 Compositional dependence of lattice parameters in $Nd_2MnMn(Mn_{4-x}Sb_x)O_{12}$ solid solutions for $0.2 \leq x \leq 2.0$ from laboratory and synchrotron XRPD data at T = 295 K. Numbers show weight fractions (in %) of corresponding phases for multi-phased samples; see the text and Tables 3.1–3.2 and A1–A8 for details. The data presented in orange symbols are sourced from the literature (the lattice parameters a (filled triangle) and c (empty triangle) from synchrotron XRPD data at T = 295 K, the lattice parameters a (filled star) and c (empty star) from neutron data at T = 200 K the single-crystal data at T = 120 K) [21].

example, in $Gd_{2.13}Mn_{5.87}O_{12}$ [27]. The formation of rare-earth-rich compositions can be explained as follows. $A_2A'A''B_4O_{12}$ quadruple perovskites with the distinct A, A′, and A″ sites are formed through the $a^+a^+c^-$ tilts with large tilt angles (large deviations of the B–O–B angles from 180°). However, the difference between the A, A′, and A″ sites will be reduced when the tilt angles are reduced. Therefore, the A′ and A″ sites can accommodate large Nd^{3+} cations through the local reduction in structural distortions, and such areas can be considered as tilt defects in the structure, for example, by analogy with stacking fault defects in layered materials.

We also note that the use of smaller rare-earth cations, such as Sm^{3+} [28], can significantly expand the stability range of the $P4_2/nmc$ B-site-disordered structure as $Sm_2MnMn(Mn_{4-x}Sb_x)O_{12}$ solid solutions with such a structure were formed for $0.5 \leq x \leq 1.0$.

3.3.2 Crystal structure descriptions

The bond-valence-sum (BVS) [29] values for the Nd site (+2.84 to +3.04) were close to the excepted value of +3. The BVS values for the Mn1 and Mn2 sites were close to the excepted value of +2 even through small fractions of Mn^{3+} cations should present at the Mn1 site in the x = 0.8 and 0.9 samples. The Mn–O bond lengths for the square-planar Mn1 sites and tetrahedral Mn2 sites were nearly the same for the samples with the B-site-ordered structure with space group $P4_2/n$ and with $1.5 \leq x \leq 2.0$ (**Figure 3.4**(a)). In addition, they were also close to the Mn–O bond lengths reported in the literature for the x =2 sample and obtained using single-crystal data [21]. The Mn3–O and Sb/Mn–O bond lengths in the $1.5 \leq x \leq 2.0$ samples were also close to those bond lengths reported in the literature for the x = 2 sample (**Figure 3.4**(b)) [21]. Therefore, our structural results from synchrotron X-ray powder diffraction data are consistent with the results from single-crystal X-ray data.

The two crystal structures are shown in **Figure 3.6**. Both two structures have two in-phase and one out-of-phase tilts of the BO_6 (or $B/B'O_6$) octahedra (the tilt system of $a^+b^+c^-$) and three types of A cations: 10-coordinated Nd (A), 4-coordinated square-planar Mn1 (A′), and 4-coordinated tetrahedral Mn2 (A″). The original columnar-type arrangements of A cations were observed in all samples while the occupation of the B-site was disordered (a mixture of Mn and Sb) in the x = 0.8–1.0 samples, and B cations were ordered in the rock-salt-type manner in the x = 1.6–2.0 samples in such a way that one B site (Mn3) is always occupied by Mn, while the second B′ site (Sb/Mn) has a mixture of Sb and Mn.

The B-site-ordered structure is formed for compositions with $x > 1.5$ (for x = 1.5, an ideal charge distribution is $Nd_2Mn^{2+}Mn^{2+}(Mn^{2+}Mn^{3+})_B(Mn^{3+}_{0.5}Sb^{5+}_{1.5})_{B'}O_{12}$). In other words, B-site ordering happens from the composition, where the charge difference between average oxidation states of cations at the B and B′ sites exceeds 2. This is consistent with the general tendency emphasized in the literature [9].

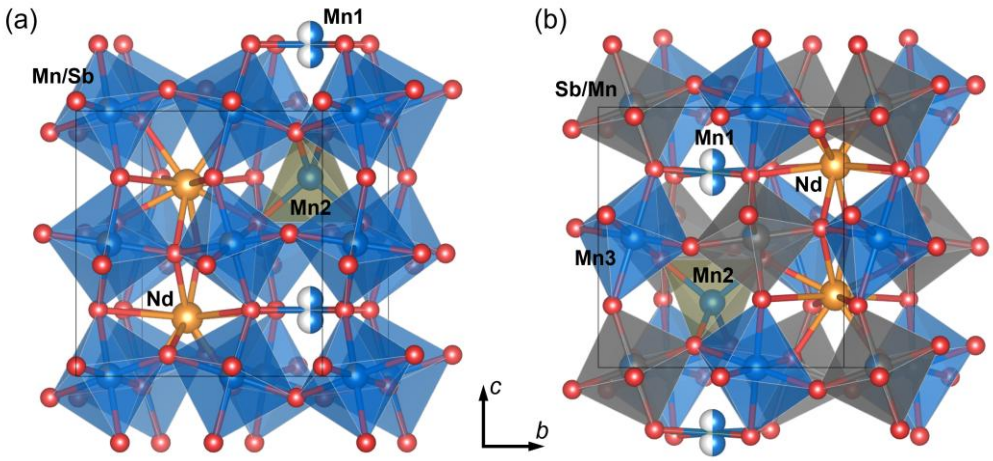

Figure 3.6 Fragments of crystal structures of $Nd_2MnMn(Mn_{4-x}Sb_x)O_{12}$ with different space groups in a polyhedral presentation. (a) $P4_2/nmc$ and (b) $P4_2/n$. $Mn1O_4$ square-planar units, $Mn2O_4$ tetrahedra, $(Mn/Sb)O_6$ or $(Sb/Mn)O_6$ octahedra, and $Mn3O_6$ octahedra are shown. Nd atoms are presented by large orange spheres.

3.3.3 Magnetic properties

The samples with x = 1.0 and 1.6 were taken as representatives in each structural region and the ZFC and FCC magnetic susceptibility curves (χ versus T) measured at H = 100 Oe and 10 kOe are presented in **Figure 3.7**, while detailed magnetic properties of other samples are given in **Figures 3.8**–**3.9**. All samples demonstrated two obvious transitions on the ZFC and FCC χ versus T curves below T_{C1} and T_{C2}, where T_C is a ferrimagnetic Curie temperature. T_C was determined from sharp peaks on the 100 Oe FCC $d\chi/dT$ versus T curves. As shown in **Figures 3.7**–**3.9**, there were clear divergences between the 100 Oe ZFC and FCC curves just below T_{C1}, while the 10 kOe ZFC and FCC curves almost coincided with each other in the whole temperature range.

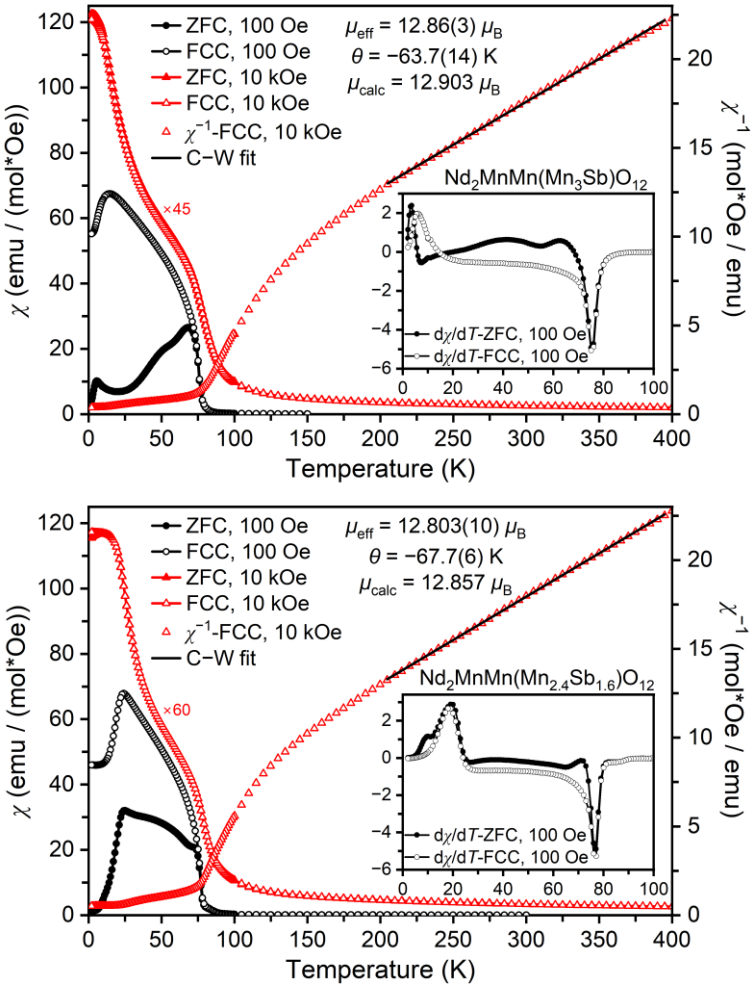

Figure 3.7 ZFC (filled symbols) and FCC (empty symbols) dc magnetic susceptibility ($\chi = M/H$) curves of $Nd_2MnMn(Mn_{4-x}Sb_x)O_{12}$ with x = 1.0 and 1.6 measured at 100 Oe (black, circles) and 10 kOe (red, triangles). The black line gives the Curie–Weiss fit (C–W fit) based on the FCC χ^{-1} versus T curve at 10 kOe. Each inset shows 100 Oe ZFC and FCC $d\chi/dT$ versus T curves in each panel.

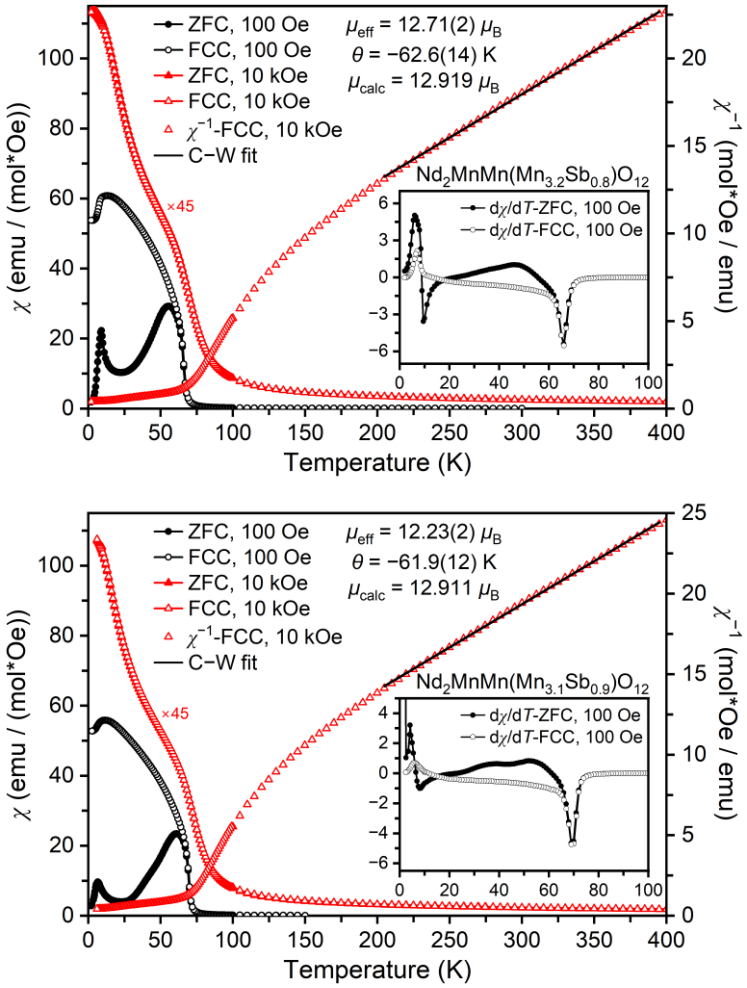

Figure 3.8 ZFC (filled symbols) and FCC (empty symbols) dc magnetic susceptibility ($\chi = M/H$) curves of $Nd_2MnMn(Mn_{4-x}Sb_x)O_{12}$ with x = 0.8 and 0.9 measured at 100 Oe (black, circles) and 10 kOe (red, triangles). The black line gives the Curie–Weiss fit (C–W fit) based on the FCC χ^{-1} versus T curve at 10 kOe. Each inset shows 100 Oe ZFC and FCC $d\chi/dT$ versus T curves in each panel.

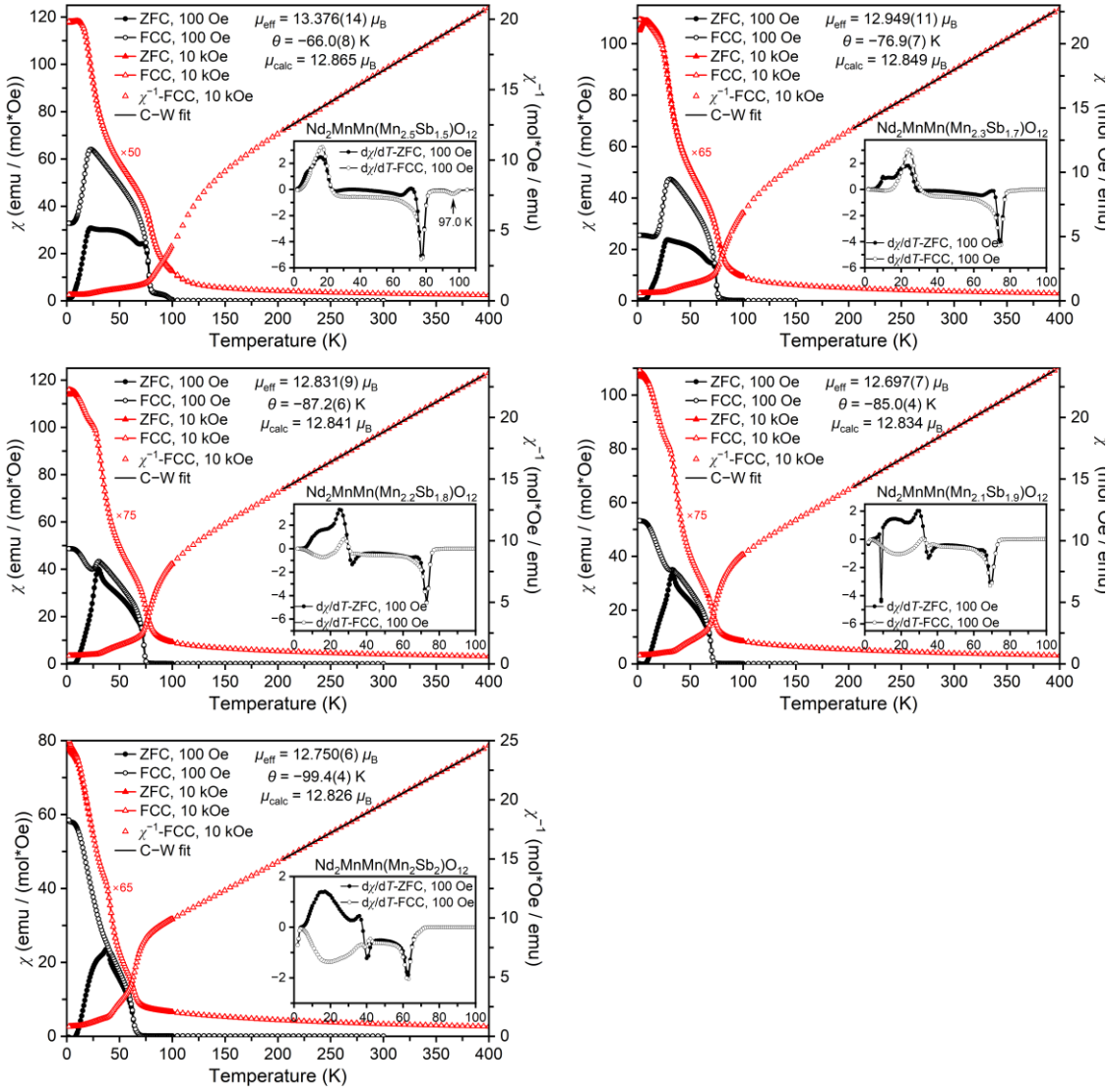

Figure 3.9 ZFC (filled symbols) and FCC (empty symbols) dc magnetic susceptibility ($\chi = M/H$) curves of $Nd_2MnMn(Mn_{4-x}Sb_x)O_{12}$ with x = 1.5, 1.7, 1.8, 1.9, and 2.0 measured at 100 Oe (black, circles) and 10 kOe (red, triangles). The black line gives the Curie–Weiss fit (C–W fit) based on the FCC χ^{-1} versus T curve at 10 kOe. Each inset shows 100 Oe ZFC and FCC dχ/dT versus T curves in each panel.

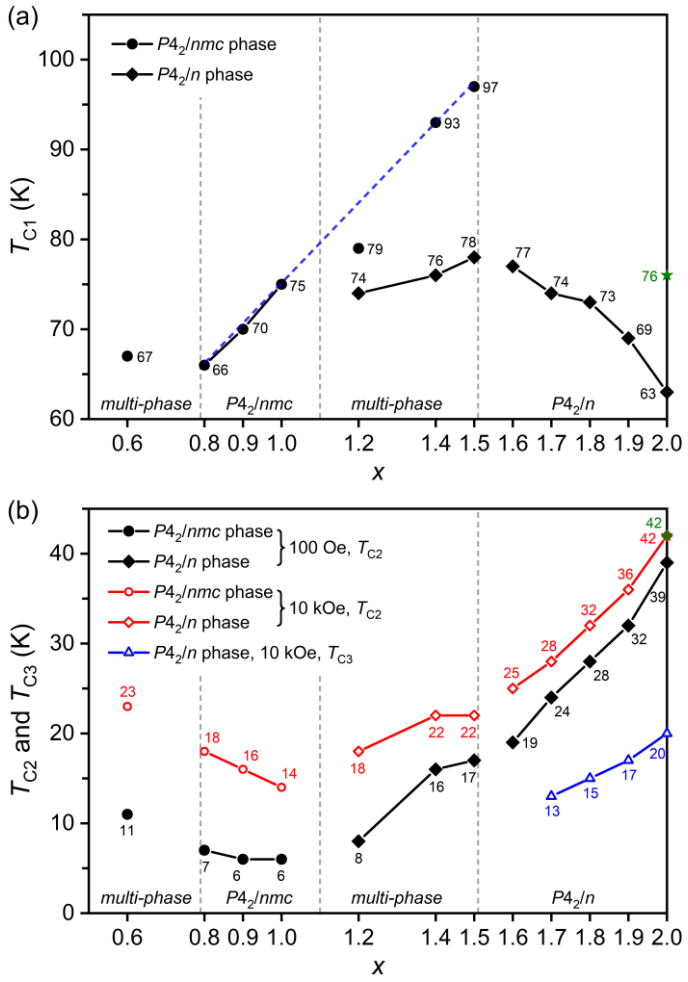

Figure 3.10 The ferrimagnetic Curie temperature (T_C) of $Nd_2MnMn(Mn_{4-x}Sb_x)O_{12}$ with $0.4 \leq x \leq 2.0$. (a) T_{C1} and (b) T_{C2} and T_{C3}. On panel (b): the black, filled circles show T_{C2} related to $P4_2/nmc$ phase at 100 Oe, the black, filled diamonds show T_{C2} related to $P4_2/n$ phase at 100 Oe. The red, empty circles show T_{C2} related to $P4_2/nmc$ phase at 10 kOe, the red, empty diamonds show T_C related to $P4_2/n$ phase at 10 kOe. The blue, empty triangles show T_{C3}. Numbers show the T_C values in K. The data presented in green stars are sourced from the literature [21].

The T_C values of all the samples are shown in **Figure 3.10** and summarized in **Table 3.3**. Below T_{C1}, magnetic susceptibilities increased sharply indicating the appearance of a noticeable ferromagnetic component. Below T_{C2}, magnetic susceptibilities dropped at H = 100 Oe apparently looking as an antiferromagnetic (AFM) transition, but they showed an additional increase at H = 10 kOe. Magnetic structures

were determined from neutron powder diffraction for the $x = 2.0$ sample [21]. It was found that a spin reorientation transition takes place and the Nd sublattice starts to order below T_{C2}. Therefore, the drop of magnetic susceptibilities below T_{C2} at $H = 100$ Oe can be explained by a spin reorientation transition, where spins are aligned perpendicular to their initial direction and to the direction of a magnetic field resulting in an apparent decrease of ordered magnetic moments along the direction of a magnetic field. However, a measurement magnetic field of $H = 10$ kOe, which is above the coercive fields (see below), can aligned spins along the direction of a magnetic field resulting in a continuous increase of magnetic susceptibilities below T_{C2} as total ordered moments continue to increase [21].

Table 3.3 Temperatures of magnetic anomalies (T_{C1} and T_{C2}), parameters of Curie–Weiss fits, and parameters of M versus H curves at $T = 5$ K for $Nd_2MnMn(Mn_{4-x}Sb_x)O_{12}$ with $0.8 \leq x \leq 1.0$ and $1.5 \leq x \leq 2.0$.

x	T_{C1} (K)	T_{C2} (K)	μ_{eff} (μ_B/f.u.)	μ_{calc} (μ_B/f.u.)	θ (K)	M_S (μ_B/f.u.)	M_R (μ_B/f.u.)	M_R(extr.) (μ_B/f.u.)	H_C (kOe)
0.8	66	7	12.71(2)	12.919	–62.6(14)	5.929	3.060	4.666	0.80
0.9	70	6	12.23(2)	12.911	–61.9(12)	6.329	2.466	5.229	0.39
1.0	75	6	12.86(3)	12.903	–63.7(14)	5.921	1.574	4.996	0.36
1.5	78	17	13.376(14)	12.865	–66.0(8)	5.212	2.279	4.375	0.62
1.6	77	19	12.803(10)	12.857	–67.7(6)	4.543	2.506	3.693	0.89
1.7	74	24	12.949(11)	12.849	–76.9(7)	4.195	2.371	3.169	1.49
1.8	73	28	12.831(9)	12.841	–87.2(6)	3.655	2.315	2.913	1.95
1.9	69	32	12.697(7)	12.834	–85.0(4)	3.553	2.263	2.642	4.02
2.0	63	39	12.750(6)	12.826	–99.4(4)	3.194	1.757	2.118	1.90

Curie–Weiss fits were performed between 200 and 395 K using the FCC χ^{-1} versus T data at 10 kOe. M_S is the magnetization value at $T = 5$ K and $H = 70$ kOe. M_R is the remnant magnetization at $T = 5$ K. M_R(extr.) at $T = 5$ K is obtained by the extrapolation between 40 kOe and 70 kOe to zero field. H_C is the coercive field at $T = 5$ K. T_C is determined from sharp peaks on the 100 Oe FCC $d\chi/dT$ versus T curves.

The positions of peaks on the FCC dχ/dT versus T curves near T_{C1} were almost independent of a magnetic field. On the other hand, the peak positions near T_{C2} noticeably depended on the measured magnetic field (100 Oe or 10 kOe, see **Figures A.1–A.2** in Appendix A). Therefore, **Figure 3.10**(b) also shows the T_{C2} values at different magnetic fields. In the B-site-ordered $P4_2/n$ phases, T_{C1} monotonically decreased (from 77 K to 63 K) and T_{C2} monotonically increased (from 19 K to 39 K) for $1.6 \leq x \leq 2.0$.

The samples with x = 1.2, 1.4, and 1.5, which contained both $P4_2/nmc$ and $P4_2/n$ phases, clearly showed two magnetic anomalies at higher temperatures in the region of T_{C1} (clearly seen on the 100 Oe FCC dχ/dT versus T curves (the insets in **Figure 3.9** and **Figure A.3** in Appendix A). The T_{C1} values associated with the $P4_2/nmc$ phase increased almost linearly from 66 K in the x = 0.8 sample to 97 K in the x = 1.5 sample. We note that the observed magnetic anomalies cannot be caused by the presence of small amounts of a pyrochlore-type impurity. Moreover, the x = 1.4 sample did not contain any detectable impurities (even on high quality synchrotron XRPD data). Therefore, the observed magnetic anomalies should originate from the $P4_2/nmc$ and $P4_2/n$ phases. The observed behaviour of the $Nd_2MnMn(Mn_{4-x}Sb_x)O_{12}$ solid solutions at $1.2 \leq x \leq 1.5$ does not correspond to a classical solid solution at an equilibrium state, where properties of each phase inside a two-phase region should match with properties of phases at the solid solution boundaries. The lattice parameters of the $Nd_2MnMn(Mn_{4-x}Sb_x)O_{12}$ solid solutions at $1.2 \leq x \leq 1.5$ continue to change with the composition especially for the $P4_2/nmc$ phase (**Figure 3.5**). All these facts suggest a non-equilibrium state, where chemical compositions of each phase at $1.2 \leq x \leq 1.5$ continue to vary with x.

We note that there is evidence for the third magnetic transition in the $1.7 \leq x \leq 2.0$ samples with T_{C3} = 13 K (x = 1.7) and T_{C3} = 20 K (x = 2.0). It can be clearly seen from the appearance of the third additional peak on the 10 kOe differential dχ/dT versus T curves (**Figure A.2** in Appendix A). The third transition was also observed in Ref. 21 in the x = 2.0 sample (Figure S6(c) in Ref. 21); however, this transition was not noticed and discussed. No clear specific heat anomalies were detected near T_{C3} (**Figure 3.15**). From the reported magnetic structure for the x = 2.0 sample [21], we can suggest that the third transition (or an additional rise of magnetic susceptibilities) could be associated with the rise of the ordered moment on the Nd sublattice. The third transition could not be caused

by an unknown impurity in the x = 1.9 and 2.0 samples as the x = 1.7 and 1.8 samples did not contain this impurity.

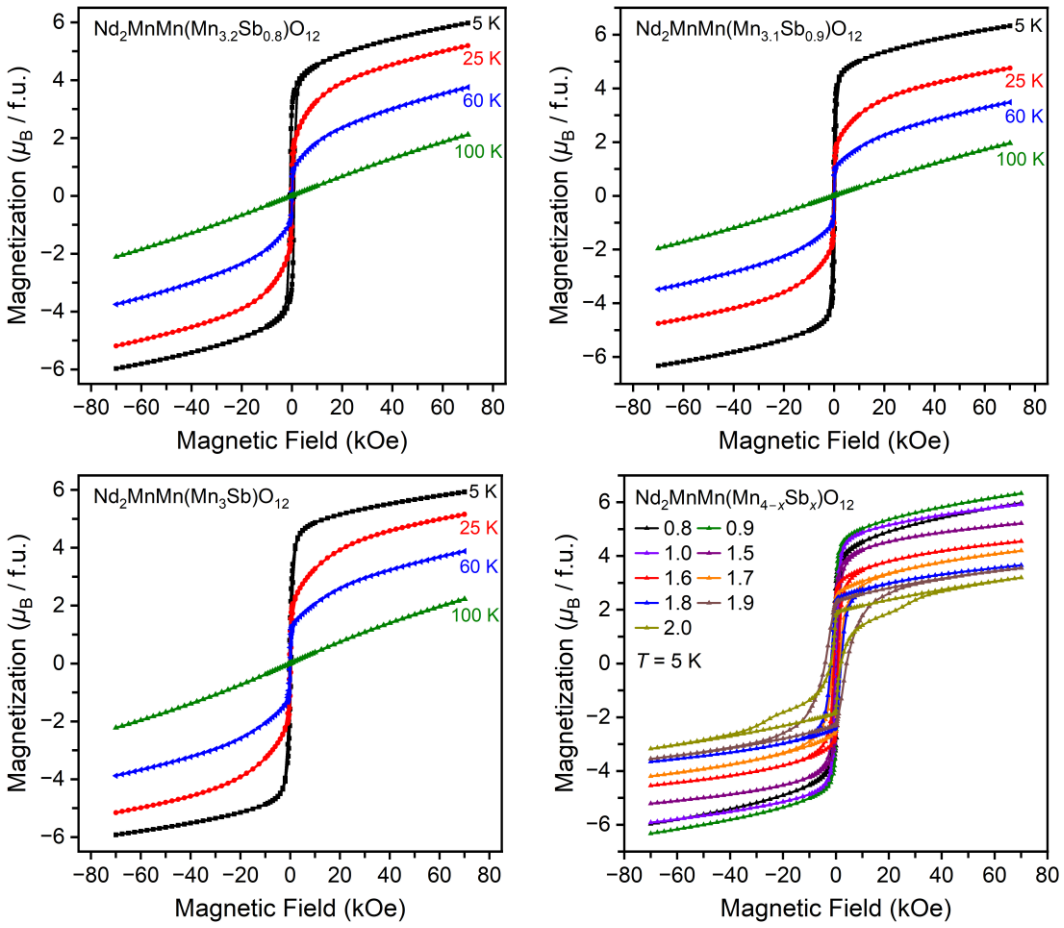

Figure 3.11 M versus H curves of $Nd_2MnMn(Mn_{4-x}Sb_x)O_{12}$ with x = 0.8, 0.9, 1.0 at different temperatures and with $0.8 \leq x \leq 1.0$ and $1.5 \leq x \leq 2.0$ at T = 5 K.

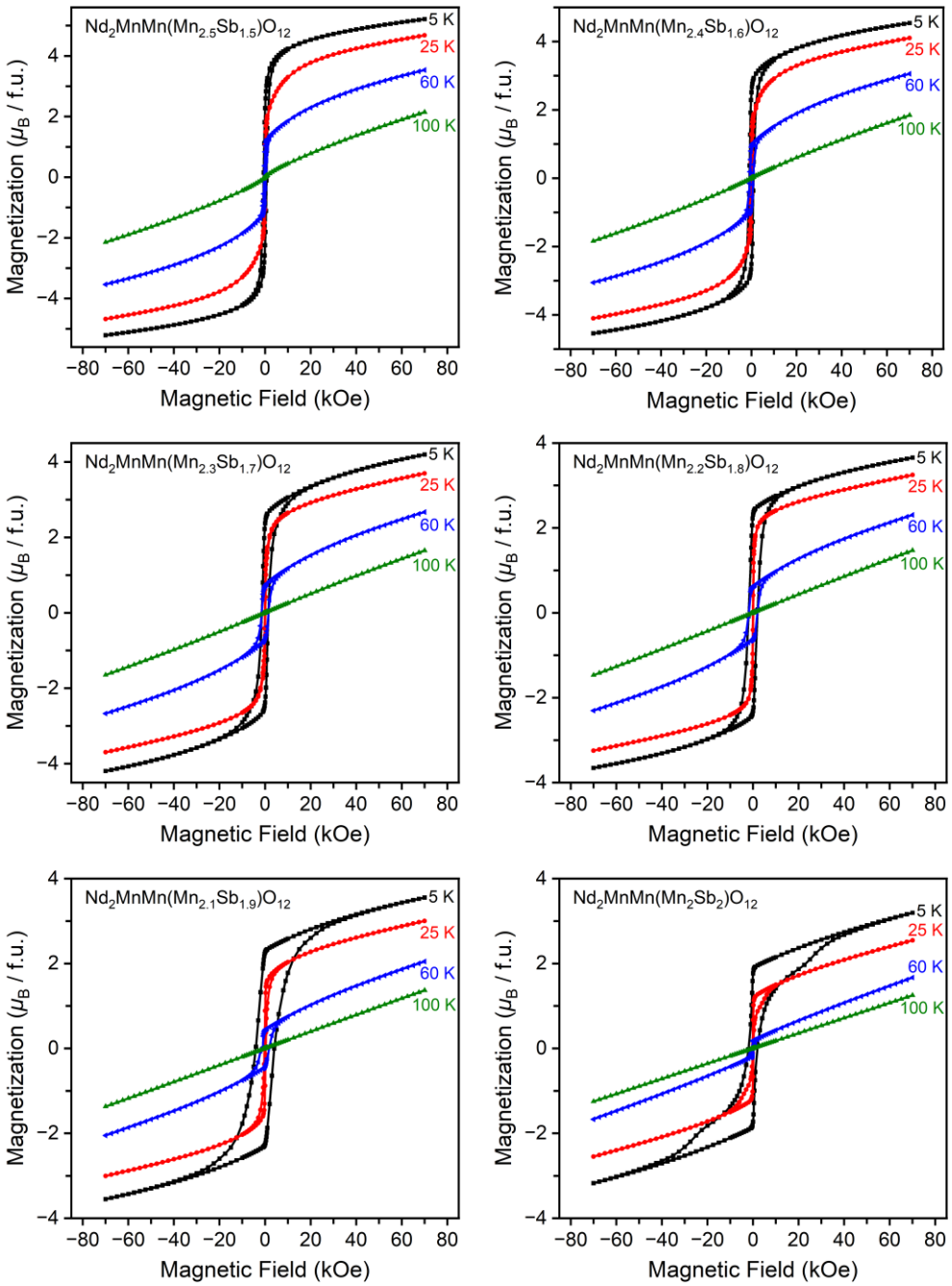

Figure 3.12 *M* versus *H* curves of $Nd_2MnMn(Mn_{4-x}Sb_x)O_{12}$ with x = 1.5, 1.6, 1.7, 1.8, 1.9, and 2.0 at different temperatures.

The inverse magnetic susceptibilities followed the Curie–Weiss law at high temperatures above about 200 K, and the FCC data at H = 10 kOe were fit by the Curie–Weiss equation (see **section 1.2.4**) between 200 K and 395 K. The obtained values are

summarized in **Table 3**, where μ_{cal} was calculated using 3.5 μ_B for Nd^{3+} [30]. The observed magnetic moments (μ_{eff}) agree with the theoretically predicted spin-only moments (μ_{calc}).

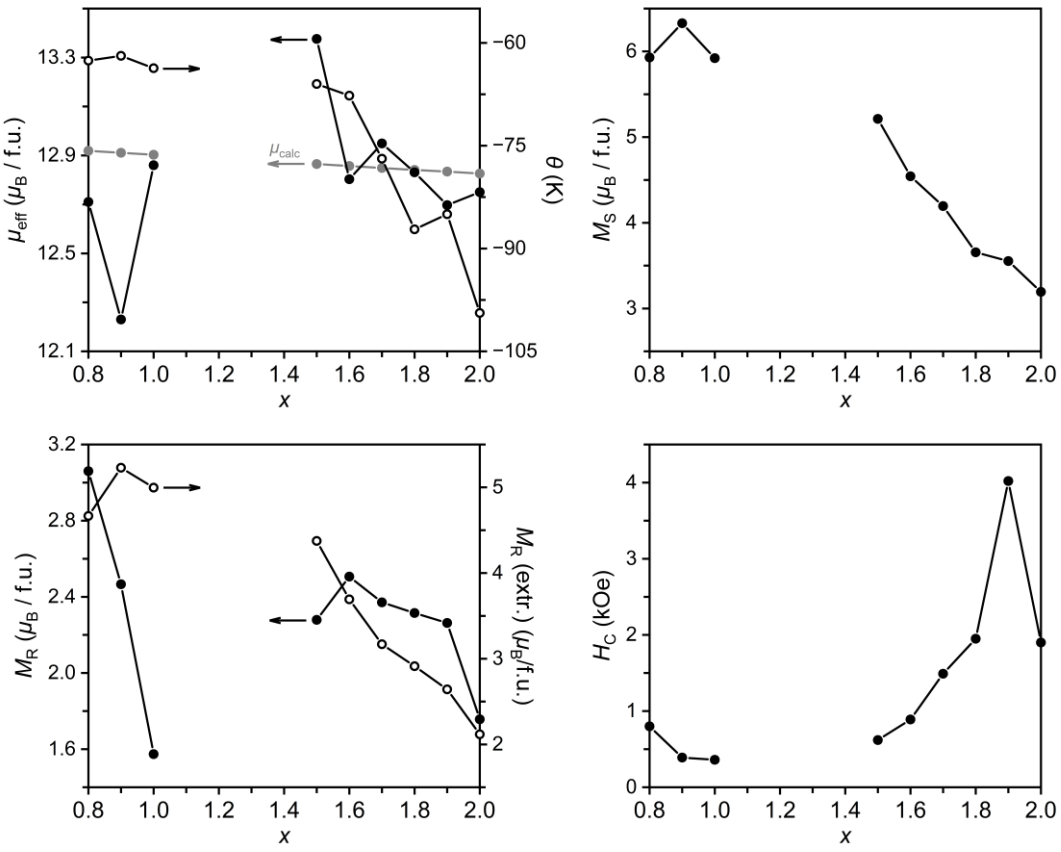

Figure 3.13 Compositional dependence of the effective paramagnetic moment μ_{eff}, calculate paramagnetic moment μ_{calc}, weiss constant θ, magnetization value M_S, remnant magnetization M_R, extrapolation of remnant magnetization M_R(extr.), coercive field H_C in $Nd_2MnMn(Mn_{4-x}Sb_x)O_{12}$ solid solutions for $0.8 \leq x \leq 1.0$ and $1.5 \leq x \leq 2.0$.

Figures 3.11–**3.12** illustrates the isothermal magnetization curves (M versus H) for the samples with $0.8 \leq x \leq 1.0$ and $1.5 \leq x \leq 2.0$, measured at various temperatures including a comparison at $T = 5$ K. Parameters of the M versus H curves are summarized in **Table 3.3** and **Figure 3.13**. All samples demonstrated step-like hysteresis at $T = 5$ K with small coercive fields H_C (0.36 kOe to 4.02 kOe) which is typical for ferrimagnetic materials. The extrapolated remnant magnetization (M_R(extr.)) at $T = 5$ K was obtained by the extrapolation between 40 kOe and 70 kOe to zero field. The investigation of the

magnetic structure of the x = 2.0 sample found that the Mn^{2+} sublattices cancel each other leaving only the Nd^{3+} uncompensated moment, and the refined ordered moment was 1.1 μ_B per Nd [21]. This value is in very good agreement with the M_R(extr.) value (= 2.1 μ_B) observed for the x = 2.0 sample. The M_R(extr.) values rapidly increased with decreasing x and reached about 5μ_B for the x = 1.0 sample; this is what is expected in this sample with an ideal charge distribution of $Nd_2Mn^{2+}Mn^{2+}(Mn^{3+}{}_3Sb^{5+})O_{12}$, where two Nd^{3+} and approximately one Mn^{3+} (approximately, because ordered moments for Mn^{2+} and Mn^{3+} are different) could now be uncompensated.

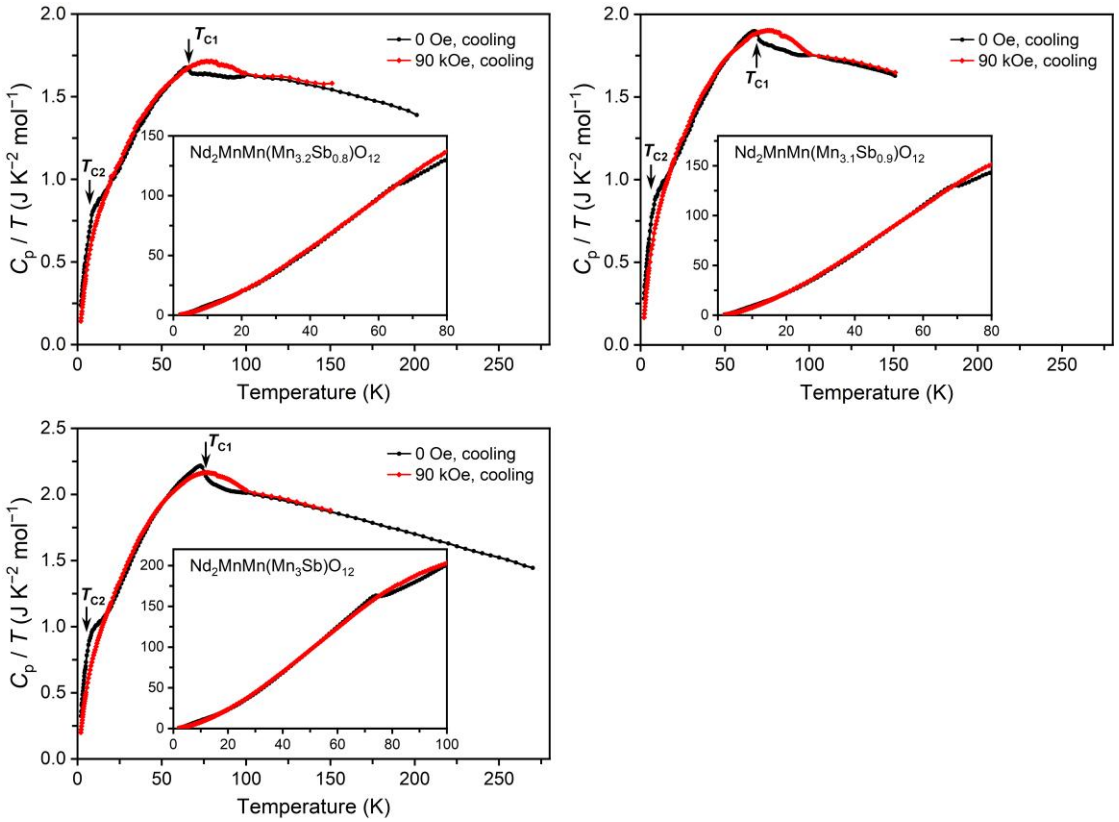

Figure 3.14 Specific heat data of $Nd_2MnMn(Mn_{4-x}Sb_x)O_{12}$ with x = 0.8, 0.9, and 1.0, plotted as C_p/T versus T. Measurements were performed on cooling at H = 0 Oe and 90 kOe. Insets present the C_p (in J K^{-1} mol^{-1}) versus T curves.

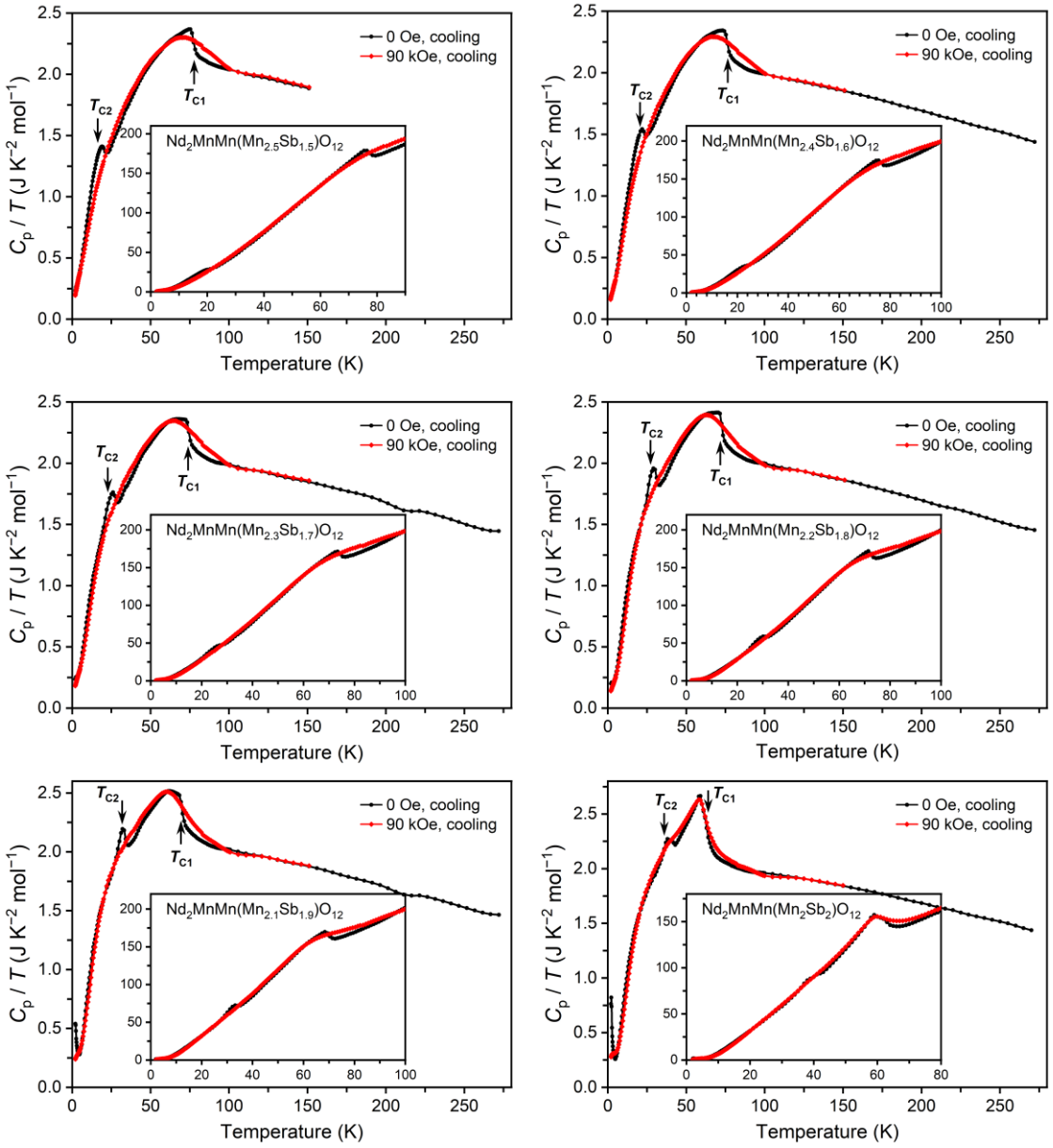

Figure 3.15 Specific heat data of $Nd_2MnMn(Mn_{4-x}Sb_x)O_{12}$ with x = 1.5, 1.6, 1.7, 1.8, 1.9, and 2.0, plotted as C_p/T versus T. Measurements were performed on cooling at H = 0 Oe and 90 kOe. Insets present the C_p (in J K^{-1} mol^{-1}) versus T curves. The rise of the C_p/T values at low temperatures in the x = 1.9 and 2.0 samples could be caused by the presence of an unknown impurity.

Figures 3.14–3.15 gives the results of specific heat measurements of all samples at H = 0 and 90 kOe. The large anomalies were observed at T_{C1} and weaker anomalies were observed at T_{C2} for all samples confirming long-range ordering. Specific heat was measured on cooling and heating for the x = 1.6 and 2.0 samples, but no hysteresis was detected suggesting magnetic phase transitions of the second order (**Figure 3.16**).

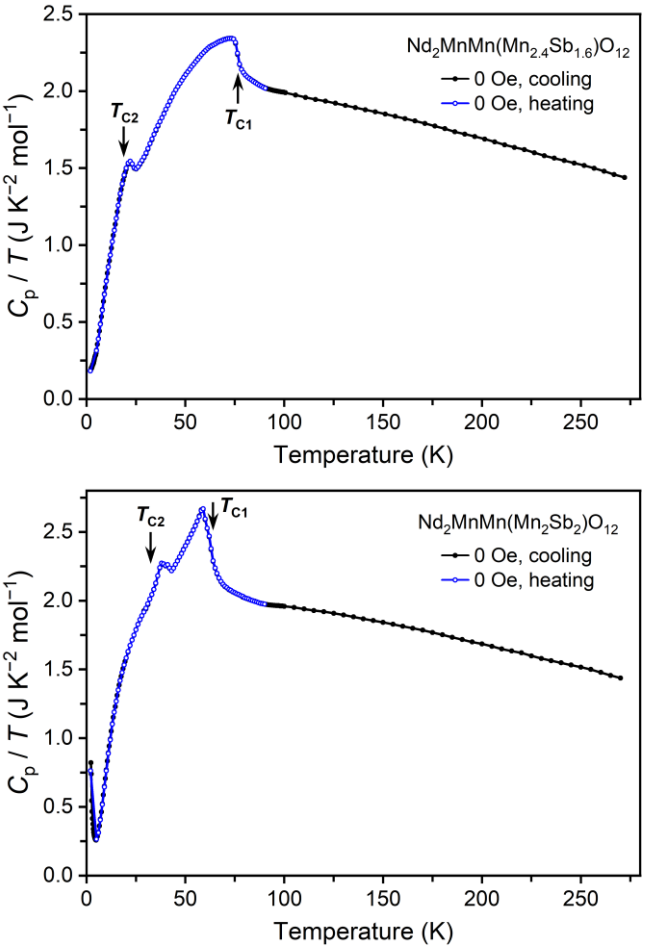

Figure 3.16 Specific heat data of $Nd_2MnMn(Mn_{4-x}Sb_x)O_{12}$ with x = 1.6 and 2.0, plotted as C_p/T versus T. Measurements were performed on cooling and heating at H = 0 Oe.

3.4 Summary of chapter 3

In summary, we prepared $Nd_2MnMn(Mn_{4-x}Sb_x)O_{12}$ with $0.2 \leq x \leq 2.0$ which belong to the A-site columnar-ordered quadruple perovskite subfamily. Their crystal structures were studied by synchrotron X-ray powder diffraction at room temperature, and cation

distributions were determined. Small degrees of anti-site disorder between the Nd and Mn sites were found. We found a transformation from the A-site columnar-ordered and B-site disordered structure to the A-site columnar-ordered and B-site rock-salt ordered structure. In the B-site rock-salt ordered structures, one B site was solely occupied by Mn, the second B site had a mixture of Sb and Mn. Two ferrimagnetic transitions were found with evidence for the third transition in the $1.7 \leq x \leq 2.0$ compositional range.

References in chapter 3

[1] J. G. Bednorz; K. A. Müller. Perovskite-type oxides—The new approach to high-T_C superconductivity. *Rev. Mod. Phys.* **1988**, *60*, 585–600.

[2] K. Hirose; R. Sinmyo; J. Hernlund. Perovskite in Earth's deep interior. *Science* **2017**, *358*, 734–738.

[3] W.-J. Yin; B. Weng; J. Ge; Q. Sun; Z. Li; Y. Yan. Oxide perovskites, double perovskites and derivatives for electrocatalysis, photocatalysis, and photovoltaics. *Energ. Environ. Sci.* **2019**, *12*, 442–462.

[4] Y. Zhang; X. Feng; Z. Zheng; Z. Zhang; K. Lin; X. Sun; G. Wang; J. Wang; J. Wei; P. Vallobra; Y. He; Z. Wang; L. Chen; K. Zhang; Y. Xu; W. Zhao. Ferrimagnets for spintronic devices: From materials to applications. *Appl. Phys. Rev.* **2023**, *10*, 011301.

[5] A. M. Glazer. The classification of tilted octahedra in perovskites. *Acta Crystallogr. Sect. B* **1972**, *28*, 3384−3392.

[6] A. A. Belik; R. D. Johnson; D. D. Khalyavin. The rich physics of A-site-ordered quadruple perovskite manganites AMn_7O_{12}. *Dalton Trans.* **2021**, *50*, 15458–15472.

[7] Y. Long. A-site ordered quadruple perovskite oxides $AA'_3B_4O_{12}$. *Chin. Phys. B* **2016**, *25*, 078108.

[8] A. A. Belik. Rise of A-site columnar-ordered $A_2A'A''B_4O_{12}$ quadruple perovskites with intrinsic triple order. *Dalton Trans.* **2018**, *47*, 3209–3217.

[9] A. M. Abakumov; A. A. Tsirlin; E. V. Antipov. Transition-Metal Perovskites. In *Comprehensive Inorganic Chemistry II: From Elements to Applications 2nd*, Reedijk, J., Poeppelmeier, K. Eds.; Vol. 2; Elsevier, 2013; pp 1–40.

[10] S. Vasala; M. Karppinen. $A_2B'B''O_6$ perovskites: A review. *Prog. Solid State Chem.* **2015**, *43*, 1–36.

[11] K. Ji; K. N. Alharbi; E. Solana-Madruga; G. T. Moyo; C. Ritter; J. P. Attfield. Double double to double perovskite transformations in quaternary manganese oxides. *Angew. Chem. Int. Ed.* **2021**, *60*, 22248–22252.

[12] G. King; P. M. Woodward. Cation ordering in perovskites. *J. Mater. Chem.* **2010**, *20*, 5785–5796.

[13] M. C. Knapp; P. M. Woodward. A-site cation ordering in $AA'BB'O_6$ perovskites. *J.*

Solid State Chem. **2006**, *179*, 1076–1085.

[14] A. A. Belik; D. D. Khalyavin; L. Zhang; Y. Matsushita; Y. Katsuya; M. Tanaka; R. D. Johnson; K. Yamaura. Intrinsic triple order in A-site columnar-ordered quadruple perovskites: Proof of concept. *ChemPhysChem* **2018**, *19*, 2449–2452.

[15] R. Liu; D. D. Khalyavin; N. Tsunoda; Y. Kumagai; F. Oba; Y. Katsuya; M. Tanaka; K. Yamaura; A. A. Belik. Spin-glass magnetic properties of A-site columnar-ordered quadruple perovskites $Y_2MnGa(Mn_{4-x}Ga_x)O_{12}$ with $0 \leq x \leq 3$. *Inorg. Chem.* **2019**, *58*, 14830–14841.

[16] A. A. Belik; D. D. Khalyavin; Y. Matsushita; K. Yamaura. Triple A-site cation ordering in the ferrimagnetic $Y_2CuGaMn_4O_{12}$ perovskite. *Inorg. Chem.* **2022**, *61*, 14428–14435.

[17] A. A. Belik. Anisotropic thermal expansion and a second-order charge order transition in the ferrimagnetic $Dy_2CuZnMn_4O_{12}$ perovskite with triple A-site cation ordering. *Inorg. Chem.* **2023**, *62*, 20042–20049.

[18] F. Millange; V. Caignaert; B. Domengès; B. Raveau; E. Suard. Order−Disorder phenomena in new $LaBaMn_2O_{6-x}$ CMR perovskites. Crystal and magnetic structure. *Chem. Mater.* **1998**, *10*, 1974–1983.

[19] Z. Deng; C. J. Kang; M. Croft; W. Li; X. Shen; J. Zhao; R. Yu; C. Jin; G. Kotliar; S. Liu; T. A. Tyson; R. Tappero; M. Greenblatt. A pressure-induced inverse order-disorder transition in double perovskites. *Angew. Chem. Int. Ed.* **2020**, *59*, 8240–8246.

[20] R. Scatena; R. Liu; V. V. Shvartsman; D. D. Khalyavin; Y. Inaguma; K. Yamaura; A. A. Belik; R. D. Johnson. Hybrid improper ferroelectricity in columnar $(NaY)MnMnTi_4O_{12}$. *Angew. Chem. Int. Ed.* **2023**, *62*, e202305994.

[21] E. Solana-Madruga; A. M. Arevalo-Lopez; A. J. Dos Santos-Garcia; E. Urones-Garrote; D. Avila-Brande; R. Saez-Puche; J. P. Attfield. Double double cation order in the high-pressure perovskites $MnRMnSbO_6$. *Angew. Chem. Int. Ed.* **2016**, *55*, 9340–9344.

[22] S. Kawaguchi; M. Takemoto; K. Osaka; E. Nishibori; C. Moriyoshi; Y. Kubota; Y. Kuroiwa; K. Sugimoto. High-throughput powder diffraction measurement system consisting of multiple MYTHEN detectors at beamline BL02B2 of SPring-8. *Rev. Sci. Instrum.* **2017**, *88*, 085111.

[23] F. Izumi; T. Ikeda. A Rietveld-analysis programm RIETAN-98 and its applications to zeolites. *Mater. Sci. Forum* **2000**, *321–324*, 198–205.

[24] G. Shimura; K. Niwa; Y. Shirako; M. Hasegawa. High-pressure synthesis and magnetic behavior of A-site columnar-ordered double perovskites, $LnMn(Ga_{0.5}Ti_{0.5})_2O_6$ (Ln = Sm, Gd). *Eur. J. Inorg. Chem.* **2017**, *2017*, 835–839.

[25] K. Leinenweber; J. Parise. High-pressure synthesis and crystal structure of $CaFeTi_2O_6$, a new perovskite structure type. *J. Solid State Chem.* **1995**, *114*, 277–281.

[26] R. Liu; M. Tanaka; H. Mori; Y. Inaguma; K. Yamaura; A. A. Belik. Ferrimagnetic and relaxor ferroelectric properties of $R_2MnMn(MnTi_3)O_{12}$ perovskites with R = Nd, Eu, and Gd. *J. Mater. Chem. C* **2021**, *9*, 947–956.

[27] A. A. Belik; L. Zhang; Y. Matsushita; Y. Katsuya; M. Tanaka; K. Yamaura. Crystal structures of cation non-stoichiometric RMn_3O_6 (R = Gd, Er, and Tm) manganites belonging to A-site columnar-ordered quadruple perovskite family. *J. Solid State Chem.* **2019**, *275*, 43–48.

[28] X. Liang; K. Yamaura; A. Belik. Three perovskite phases with different cation orders in $Sm_2MnMn(Mn_{4-x}Sb_x)O_{12}$. *Chem. - Eur. J.* **2024**, *30*, e202401960.

[29] N. E. Brese; M. O'Keeffe. Bond-valence parameters for solids. *Acta Crystallogr. Sect. B* **1991**, *47*, 192–197.

[30] C. Kittel. *Introduction to Solid State Physics*; John Wiley & Sons, 2005.

Chapter 4 Negative magnetization phenomena in A-site columnar-ordered quadruple perovskites $Ce_2MnM(Mn_2Sb_2)O_{12}$ with M = Mn and Zn

4.1 Introduction

The negative magnetization effect (NME) or phenomenon, also known as magnetization reversal, refers to an uncommon magnetic behavior in which the magnetization of a material aligns antiparallel to an applied magnetic field. Specifically, NME describes the crossover of direct-current magnetization from positive to negative under a positive magnetic field as temperature decreases [1-3]. This effect deviates from conventional magnetism, where magnetization typically aligns with the applied field, and arises due to competing magnetic interactions that disrupt conventional ordering. The origins of this behavior are linked to complex interplays between spin dynamics, magnetic anisotropy, crystal symmetry, and the interactions among magnetic ions [4-8].

Research into NME has garnered considerable interest due to its potential to reveal new magnetic states and provide deeper insights into the fundamental physics governing magnetic materials [1-3]. Moreover, the dual tunability of magnetization by both magnetic fields and temperature offers promising avenues for future applications in advanced magnetic storage technologies, spintronic devices, and other areas where precise control of magnetic states is critical [3, 9-11].

This phenomenon has been observed and studied in various perovskite materials. In ABO_3 perovskites, magnetic interactions are primarily dictated by the arrangement of magnetic ions at the A and B sites, where competition between different exchange pathways can lead to magnetization reversal [12]. For instance, in $(Tm_{1-x}Mn_x)MnO_3$ solid solutions, the ordered Tm^{3+} moments significantly increase at low temperatures, overpowering the saturated magnetic Mn moments at the B site. This results in magnetization reversal, with a compensation temperature (T_{comp}) of around 15 K in the x = 0.2 and 0.3 samples under small magnetic fields [13]. Similarly, in rare-earth-based manganite materials such as $NdMnO_3$ and $Gd_{0.5}Sr_{0.5}MnO_3$, negative magnetization arises from the negative exchange interaction between the rare-earth ions and Mn sublattices

[14, 15].

In double perovskites ($A_2BB'O_6$), the coexistence of two distinct magnetic ions at the B and B′ sites introduces additional complexity to the magnetic interactions [16]. For example, in A_2CoMnO_6 double perovskites, where A is a rare-earth element, the competition between ferromagnetic (FM) superexchange interaction of Jahn–Teller (JT)-active Co^{2+} and JT-inactive Mn^{4+} and supplementary antiferromagnetic (AFM) interactions arising from the antisite disorder caused by the interchange of crystallographic positions between Co and Mn, can result in spin frustration and the emergence of NME [17, 18].

Quadruple perovskites also present promising candidates for NME due to the inclusion of additional magnetic sites, which enhances inter-sublattice interactions. Quadruple perovskites with the general composition $AA'_3B_4O_{12}$ feature a 12-fold coordinated A site and a square-planar coordinated A′ site, where A′ site is usually occupied by Cu^{2+}, Fe^{2+}, Mn^{2+}, or Mn^{3+} [19-23]. Strong interactions between the 3d transition metals at the A′ and B sites can lead to simultaneous magnetic ordering across these cations [19, 20]. However, to the best of our knowledge, NME was not observed in $AA'_3B_4O_{12}$ perovskites. Quadruple perovskites $A_2A'A''B_4O_{12}$ have original columnar-type arrangements of A cations with one column containing A positions and another column containing alternating A′ and A″ positions (so-called A-site columnar-ordered quadruple perovskite). The presence of magnetic cations in new arrangements and unusual coordination environments could lead to complex interactions among magnetic cations located in the A′, A″, and B sites resulting in different magnetic ground states and spin-reorientation transitions [21, 22].

It was recently found that the majority of $A_2A'A''B_4O_{12}$ perovskites have ferrimagnetic (FIM) structures; however, no significant NME was observed [21, 23]. This outcome was unexpected as FIM systems are especially prone to exhibiting NME [3]. In FIM systems, magnetic moments of different ions are aligned in opposite directions, similar to AFM systems, but with unequal magnitudes [24, 25]. This imbalance results in a net magnetization. Under certain conditions, such as low temperatures or specific external magnetic fields, the antiparallel moments in FIM materials can become dominant, leading to a reversal of the overall magnetization. This makes FIM materials highly susceptible to magnetization reversal, as the delicate competition between sublattice

magnetizations can easily shift, resulting in a crossover from positive to negative magnetization [26-28]. For example, neutron diffraction measurements reveal that the origin of negative magnetization in $(Tm_{0.7}Mn_{0.3})MnO_3$ lies in its FIM structure and the differing temperature dependencies of the sublattice magnetizations [13].

In this work, we report the observation of negative magnetization effect (NME) in A-site columnar-ordered quadruple perovskites, $Ce_2MnM(Mn_2Sb_2)O_{12}$ (M = Mn, Zn). These compounds crystallize in the $P4_2/n$ (No. 86) with full Mn and Sb rock-salt ordering at the B sites. They undergo one magnetic transition near T_C = 52 K for M = Mn and T_C = 34 K for M = Zn. During field-cooled measurements in small magnetic fields, both materials display pronounced NME, which is also evident in zero-field-cooled curves under similar conditions. The observed NME is likely attributable to their FIM structures, highlighting the influence of complex magnetic interactions in these materials and the critical role of multi-moment vector arrangements and anisotropy coupling.

4.2 Experimental details

$Ce_2MnM(Mn_2Sb_2)O_{12}$ samples with M = Mn and Zn were prepared from stoichiometric mixtures of CeO_2 (99.9%), MnO or ZnO, Mn_3O_4, and Sb_2O_3 (99.9%) at about 6 GPa and about 1600 K for 2 h in Au capsules by a high-pressure, high-temperature method. After being annealed at 1600 K, the samples were cooled down to room temperature (RT) by turning off the heating current, and the pressure was slowly released. Before use, CeO_2 was dried in air at 1270 K for 1 h and the other oxides were dried in air at 390 K for 4 h.

X-ray powder diffraction (XRPD) data were collected on a RIGAKU MiniFlex600 diffractometer using CuKα radiation at RT (2θ range of 5–100° with a step of 0.02°, and a scan speed of 3°/min). Synchrotron XRPD data were collected on the BL02B2 beamline of SPring-8 at RT between 1.95° and 71.25° at a 0.006° interval in 2θ with the wavelength of λ = 0.61974 Å.[29] The data from 5° (for M = Mn) and 4° (for M = Zn) were used in the refinements as no experimental reflections were observed below these values. The samples were placed into Lindemann glass capillary tubes (inner diameter: 0.2 mm), which were rotated during measurements. The Rietveld analysis of all XRPD data was performed using the *RIETAN-2000* program.[30]

Magnetic measurements were performed on a SQUID magnetometer (Quantum Design, MPMS3) between 2 K and 300 K in an applied magnetic field of 100 Oe and 10 kOe under both zero-field-cooled (ZFC) and field-cooled on cooling (FCC) conditions. Additional magnetic measurements were also performed between 2 K and 70 K in different applied fields under ZFC and FCC conditions. The inverse magnetic susceptibilities (χ^{-1}) were fit by the Curie−Weiss equation (see **section 1.2.4**). For fitting, we used the FCC data at H = 10 kOe between 200 K and 295 K. Isothermal magnetization measurements were performed between −70 and 70 kOe at different temperatures (5, 10, 20, 30, 40, 50, and 60 K). Specific heat was measured on a Quantum Design PPMS-9T instrument on cooling at magnetic fields of 0 Oe and 90 kOe.

4.3 Results and discussion

4.3.1 Crystal structure determination and description

The synchrotron XRPD patterns of $Ce_2MnM(Mn_2Sb_2)O_{12}$ samples with M = Mn and Zn are shown in **Figures 4.1** and **4.2**. Both samples crystallize in a tetragonal system with space group $P4_2/n$. The M = Mn sample contained 3.6 wt% CeO_2, 0.2 wt% cubic-pyrochlore (space group Fd-3m, a = 10.2633 Å, which could be Sb_2O_{4+x}), and 2.9 wt% $La_3Mn_2Sb_3O_{14}$-type pyrochlore [31] (space group R-3m, a = 7.4262 Å and c = 17.6394 Å) impurities while the M = Zn sample contained 4.2 wt% CeO_2, 7.9 wt% $La_3Mn_2Sb_3O_{14}$-type pyrochlore [31] (space group R-3m, a = 7.4428 Å and c = 17.6257 Å), and 3.7 wt% $Na_5Co_{15.5}Te_6O_{36}$-type [32] (space group $P6_3/m$, a = 9.6229 Å and c = 9.3509 Å) impurities. The lattice parameters of $Ce_2MnMn(Mn_2Sb_2)O_{12}$ were a = 7.84545(1) Å and c = 7.95529(2) Å, and those of $Ce_2MnZn(Mn_2Sb_2)O_{12}$ were a = 7.81270(1) Å and c = 7.94100(1) Å. The rare-earth stability range (at certain synthesis conditions) of A-site columnar ordered quadruple perovskites usually strongly depends on the occupation of the A′, A″, and B sites and is a subject to considerable restrictions [21, 23], for example, $R_2MnMnMn_4O_{12}$ is stable for R = Gd–Er, Y [33], $R_2MnMn(MnTi_3)O_{12}$ is stable for R = Nd–Gd [34], and $NaRMn_2Ti_4O_{12}$ is stable for Sm, Eu, Gd, Dy, Ho, and Y [35], It was found that $R_2MnMn(Mn_2Sb_2)O_{12}$ is stable for R = La, Pr, Nd, and Sm [36-38]; however, R = Ce was omitted from the investigation in Ref. 36. As $R_2MnZn(Mn_2Sb_2)O_{12}$ has a different combination of A′, A″, and B cations, we preliminary investigated the rare-earth

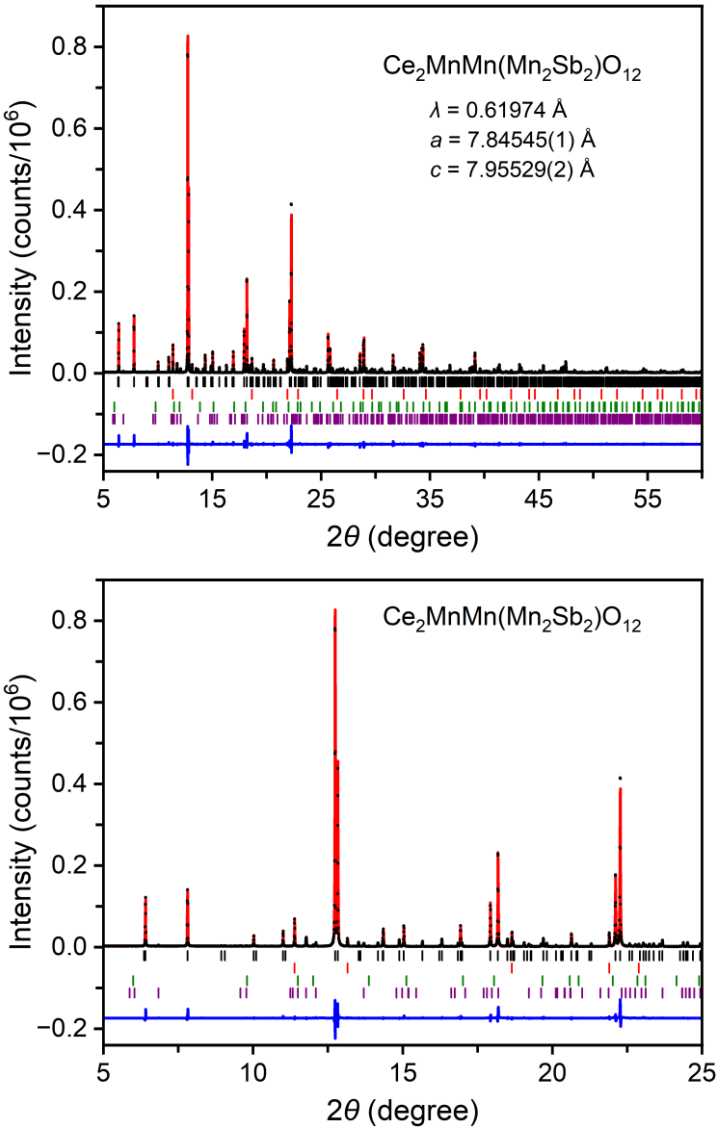

Figure 4.1 Fragments of experimental (black circles), calculated (red line), and difference (blue line) synchrotron X-ray powder diffraction patterns of $Ce_2MnMn(Mn_2Sb_2)O_{12}$ at T = 295 K and a zoomed-in view in the 5–25° 2θ range. The tick marks show possible Bragg reflection positions of the main perovskite phase (the first black row), CeO_2 impurity (the second red row), cubic pyrochlore impurity (the third green row), and $La_3Mn_2Sb_3O_{14}$-related pyrochlore impurity (the fourth purple row).

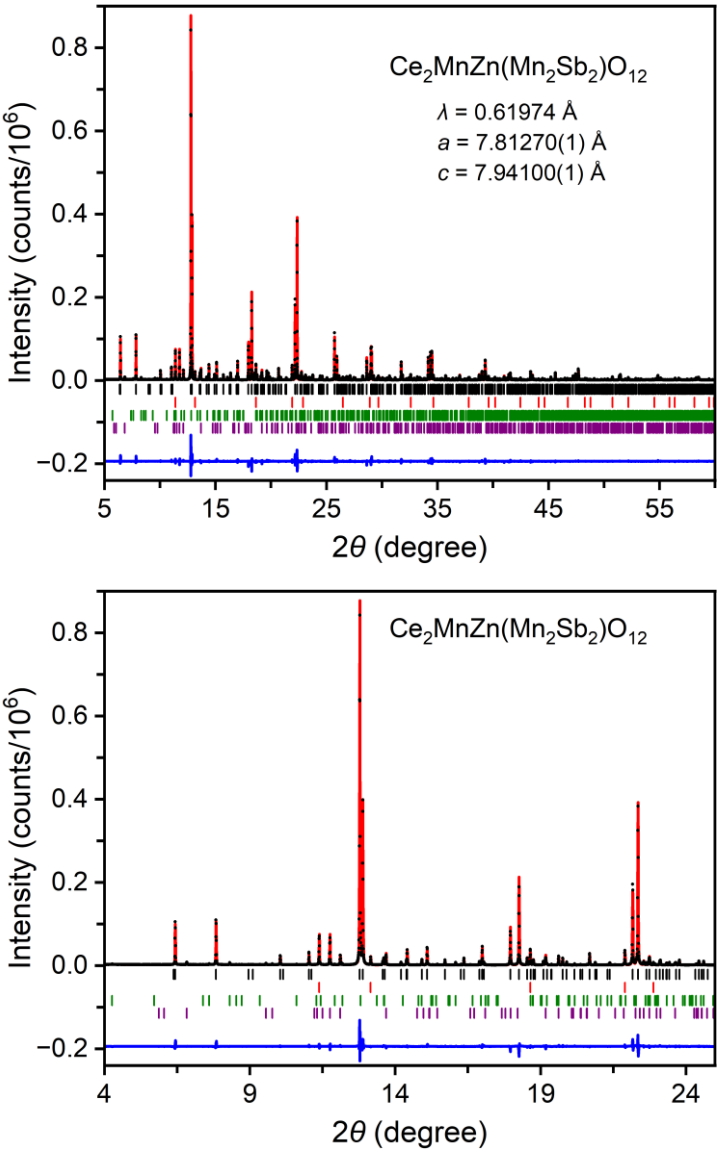

Figure 4.2 Fragments of experimental (black circles), calculated (red line), and difference (blue line) synchrotron X-ray powder diffraction patterns of $Ce_2MnZn(Mn_2Sb_2)O_{12}$ at T = 295 K and a zoomed-in view in the 4–25° 2θ range. The tick marks show possible Bragg reflection positions of the main perovskite phase (the first black row), CeO_2 impurity (the second red row), cubic pyrochlore impurity (the third green row), and $La_3Mn_2Sb_3O_{14}$-related pyrochlore impurity (the fourth purple row).

stability range of $R_2MnZn(Mn_2Sb_2)O_{12}$ and prepared such compounds with R = Nd, Eu, Dy, and Yb. It was found that $R_2MnZn(Mn_2Sb_2)O_{12}$ can be stabilized for R = Nd and Eu (unpublished data) in the A-site columnar-ordered perovskite structure. On the other

hand, samples with R = Dy and Yb crystallized in a double-perovskite structure (space group $P2_1/n$) with statistical distribution of R^{3+}, Mn^{2+}, and Zn^{2+} cations at one A site. Stabilization of Ce^{3+} (see below for confirmation) in the A site of quadruple perovskites is uncommon [39] because the Ce^{4+} oxidation state in the most stable form in comparison with R_2O_3 (R = La, Nd, Sm, Eu, Gd, Dy–Lu, and Y) with the R^{3+} oxidation state, and Ce_2O_3 is easily oxidized [40]. We also tried to synthesize $Ce_2MnMn(Mn_2Sb_2)O_{12}$ and $Ce_2MnZn(Mn_2Sb_2)O_{12}$ at a higher temperature of 1800 K (at 6 GPa in Pt capsules for 2 h), however, the samples contained CeO_2 and Sb_2O_{4+x} (a pyrochlore-type structure) as main phases suggesting that the samples decomposed (**Figures 4.3–4.4**).

Structure parameters of $Nd_2MnMn(Mn_{4-x}Sb_x)O_{12}$ [36, 38] were used as the initial model for the crystal structure refinements of $Ce_2MnM(Mn_2Sb_2)O_{12}$ with M = Mn and Zn. We initially assume all cations were distributed in ideal sites: Ce^{3+} at the 10-fold-coordinated A site, Mn^{2+} at the square-planar A′ site (Mn1), and Mn^{2+}/Zn^{2+} at the tetrahedral A″ site (M2). For the sample $Ce_2MnZn(Mn_2Sb_2)O_{12}$, Mn^{2+} cations (23 electrons) and Zn^{2+} cations (28 electrons) differ by 5 electrons. This difference is enough to identify them with high quality synchrotron X-ray powder diffraction.

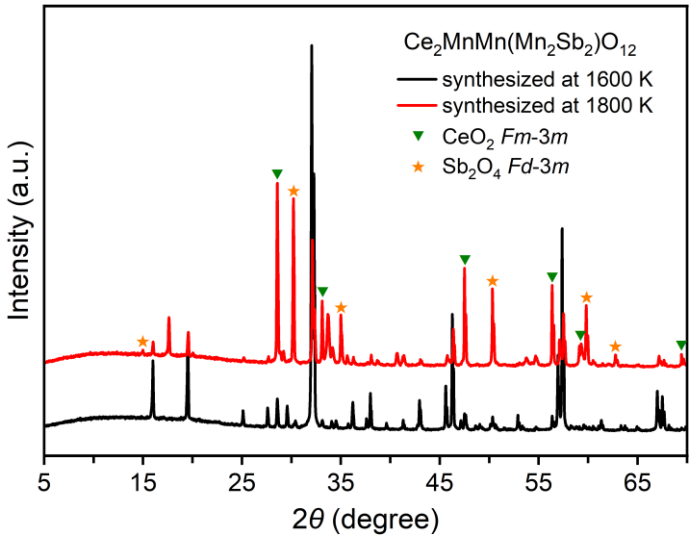

Figure 4.3 Comparison of laboratory X-ray powder diffraction (XRPD) patterns of $Ce_2MnMn(Mn_2Sb_2)O_{12}$ prepared under 1600 K and 1800 K (at 6 GPa for 2 h). The green triangles show characteristic peaks of CeO_2 (space group *Fm*-3*m*) and the orange stars show characteristic peaks of Sb_2O_4 (space group *Fd*-3*m*).

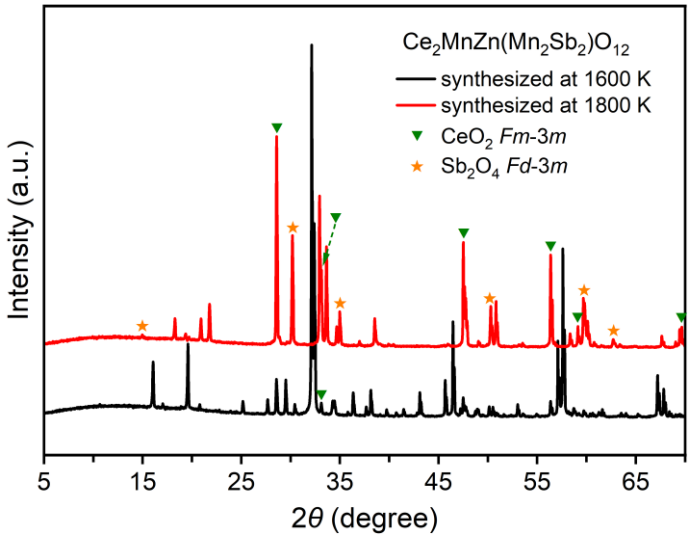

Figure 4.4 Comparison of laboratory X-ray powder diffraction (XRPD) patterns of $Ce_2MnZn(Mn_2Sb_2)O_{12}$ prepared under 1600 K and 1800 K (at 6 GPa for 2 h). The green triangles show characteristic peaks of CeO_2 (space group *Fm*-3*m*) and the orange stars show characteristic peaks of Sb_2O_4 (space group *Fd*-3*m*).

Refinements of the occupation factors (*g*) of the Ce site (simultaneously with all atomic displacement parameters (and other parameters), but with fixed *g* parameters for other sites) gave the following values: *g*(Ce) = 0.960(2) for M = Mn and *g*(Ce) = 0.991(2) for M = Zn. Such deviations can be absorbed by reasonable atomic displacement parameters (for example, *B*(Ce) = 0.693(10) $Å^2$ with *g*(Ce) = 1 for M = Mn). Nevertheless, we assumed the presence of an antisite disorder when *g* values deviated from 1 for more than 3 %. Therefore, the presence of Mn at the Ce site for M = Mn was assumed in the final model, and we refined the cation distribution with a constraint on the full site occupation, e.g., *g*(Ce) + *g*(Mn) =1. The occupation factor of the Ce site was fixed at 1 for M = Zn in the final model. Refined *g* parameters (simultaneously) for the Sb and Mn3 sites (under the same conditions as above) were *g*(Sb) = 1.001(3) and *g*(Mn3) = 0.979(4) for M = Mn and *g*(Sb) = 1.022(3) and *g*(Mn3) = 1.050(5) for M = Zn. Therefore, the *g*(Sb) values were fixed at 1 in the final models. Refined *g* parameters for the Mn1 site (under the same conditions as above) were *g*(Mn1) = 0.972(3) for M = Mn and *g*(Mn1) = 1.018(7) for M = Zn. Therefore, the *g*(Mn1) values were fixed at 1 in the final models. Refined *g* parameters for the M2 site (under the same conditions as above) were *g*(Mn2) = 0.974(6) for M = Mn and *g*(Zn2) = 0.922(6) for M = Zn. Based on these values, *g*(Mn2)

was fixed at 1 for M = Mn. On the other hand, *g*(Zn2) and *g*(Mn3) values for M = Zn could suggest some antisite disorder of Zn^{2+} and Mn^{2+} between the M2 and Mn3 sites. Therefore, we refined the cation distribution between these two sites with the constraints on the full site occupation and the total chemical composition. The final crystallographic and structure parameters are presented in **Tables 4.1** and **4.2**.

Table 4.1 Crystallographic parameters and structure refinement details of $Ce_2MnM(Mn_2Sb_2)O_{12}$ with M = Mn and Zn.

M	Mn	Zn
a (Å)	7.84545(1)	7.81270(1)
c (Å)	7.95529(2)	7.94100(1)
V (Å^3)	489.657(1)	484.705(1)
molecular weight (g/mol)	935.5048	945.9468
R_{wp} (%)	8.49	9.08
R_p (%)	6.42	6.88
R_I (%)	3.21	3.50
R_F (%)	1.92	2.23

Synchrotron X-ray powder diffraction (λ = 0.61974 Å). T = 295 K. 2θ range used in the refinement: 5°–71.25° for M = Mn sample, 4°–71.25° for M = Zn sample. Crystal system: tetragonal. Space group: $P4_2/n$ (No. 86, cell choice 2), Z = 2.

Table 4.2 Structure parameters of $Ce_2MnM(Mn_2Sb_2)O_{12}$ with M = Mn and Zn at 295 K from synchrotron X-ray powder diffraction data.

M	Site	WP	*x*	*y*	*z*	B_{iso} (Å^2)
Mn	Ce	4*e*	0.25	0.75	0.7761(1)	0.580(11)
	Mn1-SQ	2*b*	0.25	0.25	0.75	1.17(9)
	Mn2-T	2a	0.75	0.75	0.75	0.61(8)
	Mn3-Oc	4*c*	0	0.5	0.5	0.65(2)
	Sb-Oc	4*d*	0	0	0.5	0.375(9)
	O1	8*g*	–0.0461(9)	0.5739(9)	0.2345(7)	0.52(11)
	O2	8*g*	–0.2348(12)	–0.0430(7)	0.5831(6)	0.90(12)
	O3	8*g*	–0.2587(10)	0.0671(6)	–0.0319(6)	0.51(9)
Zn	Ce	4*e*	0.25	0.75	0.7750(1)	0.647(10)
	Mn1-SQ	2*b*	0.25	0.25	0.75	0.63(10)
	M2-T	2a	0.75	0.75	0.75	1.00(11)
	M3-Oc	4*c*	0	0.5	0.5	0.69(3)
	Sb-Oc	4*d*	0	0	0.5	0.364(11)
	O1	8*g*	–0.0532(15)	0.5700(15)	0.2327(9)	1.10(15)
	O2	8*g*	–0.2291(13)	–0.0480(8)	0.5889(8)	0.85(14)
	O3	8*g*	–0.2591(13)	0.0701(8)	–0.0365(8)	1.28(14)

WP is Wyckoff position. For M = Mn sample, *g*(Ce) = 0.928(4)Ce + 0.072Mn and *g*(Mn1-SQ) = *g*(Mn2-T) = *g*(Mn3-Oc) = *g*(Sb-Oc) = *g*(O1) = *g*(O2) = *g*(O3) = 1, where *g* is the occupation factor. For M = Zn sample, *g*(Ce) = *g*(Mn1-SQ) = *g*(Sb-Oc) = *g*(O1) = *g*(O2) = *g*(O3) = 1, *g*(M2-T) = 0.65(2)Zn + 0.35Mn, and *g*(M3-Oc) = 0.823Mn + 0.177Zn. Abbreviations: SQ: square-planar (site), T: tetrahedral (site), Oc: octahedral (site).

The crystal structure of $Ce_2MnM(Mn_2Sb_2)O_{12}$ samples with M = Mn and Zn is illustrated in **Figure 4.5**. In this A-site columnar-ordered quadruple perovskite structure with the $P4_2/n$ space group (No. 86), the Mn (Mn3) and Sb atoms each are located at an octahedral center, and the $Mn3/SbO_6$ octahedra are alternately corner-connected in a rock-salt arrangement [41]. It has two in-phase and one out-of-phase tilts of the $Mn3/SbO_6$ octahedra (written $a^+a^+c^-$ in the Glazer notation [42]) which creates 10 and 4 coordination numbers around the three A sites [21]. As shown on the right of **Figure 4.5**, the 10-coordinated A-site CeO_{10} polyhedra are connected through edges and form

columns along *c* axis. The 4-coordinated A′-site $Mn1O_4$ squares and 4-coordinated A″-site $M2O_4$ tetrahedra (M2 = Mn/Zn) are separated from each other but connected with A-site CeO_{10} polyhedra through edges and corners, respectively.

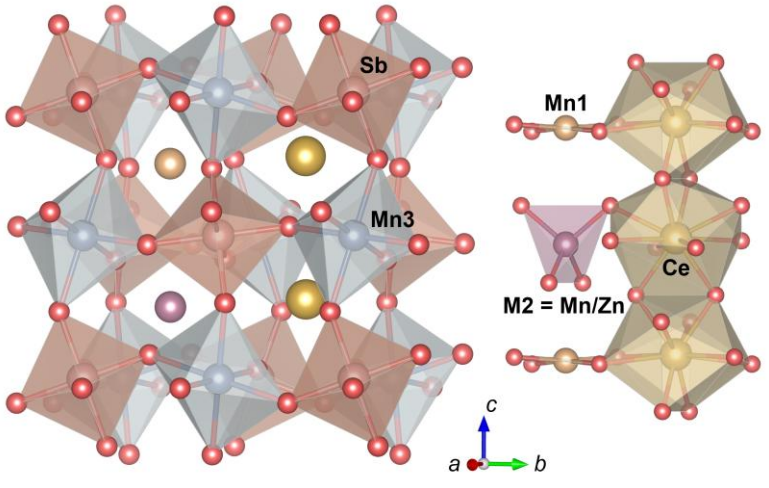

Figure 4.5 Crystal structure of $Ce_2MnM(Mn_2Sb_2)O_{12}$ with M = Mn and Zn in a polyhedral presentation. The rock-salt-type arrangement of $Mn3O_6$ and SbO_6 octahedra is shown on the left. The columnar-type arrangement of CeO_{10} polyhedra, $Mn1O_4$ square planar units, and $(Mn/Zn)O_4 = M2O_4$ tetrahedra is shown on the right.

Table 4.3 shows the bond lengths, bond angles, bond-valence sum (BVS) [43, 44], and distortion parameters. The BVS values for the Ce site (+2.82 and +2.91) [44] confirm the +3 oxidation state. There are two quite long Ce–O1 bond lengths (3.004(9) and 2.936(15)) in the $P4_2/n$ structure of $Ce_2MnM(Mn_2Sb_2)O_{12}$ samples in agreement with other $R_2MnMn(Mn_2Sb_2)O_{12}$ samples [36-38], but in contrast with the $P4_2/nmc$ structure of other related compounds without B-site double ordering [37, 38]. The BVS value of +1.77 for the Mn1 site in the M = Mn sample significantly deviated from the expected value of +2, which is consistent with the slightly elongated bond length of Mn1–O1 at 2.117(5) Å (compared with the M = Zn sample, BVS = +1.90, *l*(Mn1–O1) = 2.088(6)). For the M2 and M3 sites, the BVS values (+1.86 and +2.11 for the M = Mn sample; +1.74 and +1.99 for the M = Zn sample) are closer to the ideal +2 value. The M2–O2 bond lengths differ noticeably for M = Mn (2.101(5) Å) and M = Zn (2.038(6) Å) reflecting different ionic radii of Mn^{2+} (r_{IV} = 0.66 Å) and Zn^{2+} (r_{IV} = 0.60 Å) [45]. The Zn–O bond

Table 4.3 Bond lengths (in Å), bond angles (in deg), bond-valence sum (BVS), and distortion parameters of MnO_6 and SbO_6 (Δ) in $Ce_2MnM(Mn_2Sb_2)O_{12}$ with M = Mn and Zn at T = 295 K from synchrotron X-ray powder diffraction data.

M	Mn	Zn
Ce–O1 × 2	2.723(9)	2.775(15)
Ce–O1 × 2	3.004(9)	2.936(15)
Ce–O2 × 2	2.560(5)	2.572(6)
Ce–O3 × 2	2.417(5)	2.359(6)
Ce–O3 × 2	2.491(5)	2.508(6)
BVS(Ce^{3+})	+2.82	+2.91
Mn1–O1 × 4	2.117(5)	2.088(6)
Mn1–O2 × 4	3.110(5)	3.124(6)
BVS($Mn1^{2+}$)	+1.77	+1.90
M2–O2 × 4	2.101(5)	2.038(6)
M2–O3 × 4	3.034(5)	3.022(6)
BVS($M2^{2+}$)	+1.86	+1.74
M3–O1 × 2	2.220(5)	2.232(7)
M3–O2 × 2	2.210(9)	2.263(10)
M3–O3 × 2	2.112(8)	2.117(11)
$\Delta(M3O_6)$	5.0×10^{-4}	8.1×10^{-4}
BVS($M3^{2+}$)	+2.11	+1.99
Sb–O1 × 2	1.987(5)	1.971(7)
Sb–O2 × 2	1.986(9)	1.960(10)
Sb–O3 × 2	1.981(8)	1.982(10)
$\Delta(SbO_6)$	1.7×10^{-6}	2.1×10^{-5}
BVS(Sb^{5+})	+5.35	+5.55
Mn3–O1–Sb × 2	142.0(4)	141.6(6)
Mn3–O2–Sb × 2	138.4(3)	135.2(4)
Mn3–O3–Sb × 2	146.8(3)	144.7(4)

BVS = $\sum_{i=1}^{N} v_i$, $v_i = \exp[(R_0 - l_i)/B]$, N is the coordination number, B = 0.37, $R_0(Ce^{3+})$ = 2.121, $R_0(Mn^{2+})$ = 1.79, $R_0(Zn^{2+})$ = 1.704, $R_0(Sb^{5+})$ = 1.942.

lengths in $Ce_2MnZn(Mn_2Sb_2)O_{12}$ were close, for example, to those of $Dy_2MnZn(Mn_3Ti)O_{12}$ and $Dy_2MnZn(Mn_2Ti_2)O_{12}$ [46]. The BVS values at the Sb site (+5.35 and +5.55) were slightly higher than anticipated, implying that Sb^{5+} cations tend to be overbonded. This conclusion is further supported by the relatively short Sb–O bond lengths (1.981(8) Å to 1.987(5) Å for the M = Mn sample and 1.960(10) Å to 1.982(10) Å for the M = Zn sample). Interestingly, similar trends in the BVS values of Sb^{5+} and bond lengths have been observed in other A-site columnar-ordered quadruple perovskites where Sb occupies the B-site [36-38]. The charge distribution of $Ce^{3+}{}_2Mn^{2+}M^{2+}(Mn^{2+}{}_2Sb^{5+}{}_2)O_{12}$ is quite unique since Ce usually takes the +4 oxidation state in other A-site-ordered quadruple perovskites, such as $CeCu_3Fe_4O_{12}$ [47], $CeCu_3Mn_4O_{12}$ [48], and $CeCu_3Cr_4O_{12}$ [49].

4.3.2 Magnetic Properties

Figure 4.6 presents the magnetic susceptibility of $Ce_2MnM(Mn_2Sb_2)O_{12}$ samples with M = Mn and Zn as a function of temperature at H = 100 Oe and 10 kOe under ZFC and FCC conditions. In the 100 Oe ZFC and FCC measurements, both samples display sharp susceptibility increases below T_C = 52 K (M = Mn) and T_C = 34 K (M = Zn), suggesting a rapid arrangement of FM-like domains along the direction of the field, where the T_C values (ferrimagnetic Curie temperatures) were determined from sharp peaks on the ZFC and FCC dχT/dT versus T curves at H = 100 Oe and 10 kOe (**Figure 4.7**). Both 100 Oe ZFC and FCC curves of $Ce_2MnMn(Mn_2Sb_2)O_{12}$ show a maximum χ value at 47 K ($T\chi_{max}$), decrease and then go through a zero point of magnetic susceptibility (χ = 0) at T_{comp}. Below T_{comp}, the magnetizations (judge from the magnetic susceptibilities) remain negative down to the lowest temperature of ~2 K, showing the NME or magnetization reversal. The 100 Oe ZFC and FCC curves of $Ce_2MnZn(Mn_2Sb_2)O_{12}$ below $T\chi_{max}$ (~20 K, determined from 100 Oe ZFC curve) follow totally different paths. The ZFC curve shows a maximum at $T\chi_{max}$, then decrease and remain negative below ~13.6 K. On the other hand, the FCC curve increases steadily as the temperature is decreased and eventually approaches a saturation value at ~5 K. Notably, no divergence is observed in both samples between the ZFC and FCC curves at 100 Oe down to $T\chi_{max}$, while the ZFC and FCC curves nearly overlap under the 10 kOe field. We note that CeO_2 and Sb_2O_{4+x} impurities are non-magnetic, and $La_3Mn_2Sb_3O_{14}$-type impurity may be paramagnetic or

weakly magnetic. No magnetic transitions were found in $La_3Mn_2Sb_3O_{14}$, and $Nd_3Mn_2Sb_3O_{14}$ showed a magnetic transition near 2 K [50]. Thus, specific heat anomalies in our samples near 2 K (see below) could originate from $La_3Mn_2Sb_3O_{14}$-type impurity (namely, from a phase with a composition close to $Ce_3Mn_2Sb_3O_{14}$), and similar specific heat anomalies were observed in $Nd_2MnMn(Mn_{4-x}Sb_x)O_{12}$ samples (with x = 1.9 and 2), which also had a similar impurity [38]. Therefore, impurities should have small effects on the observed magnetic properties.

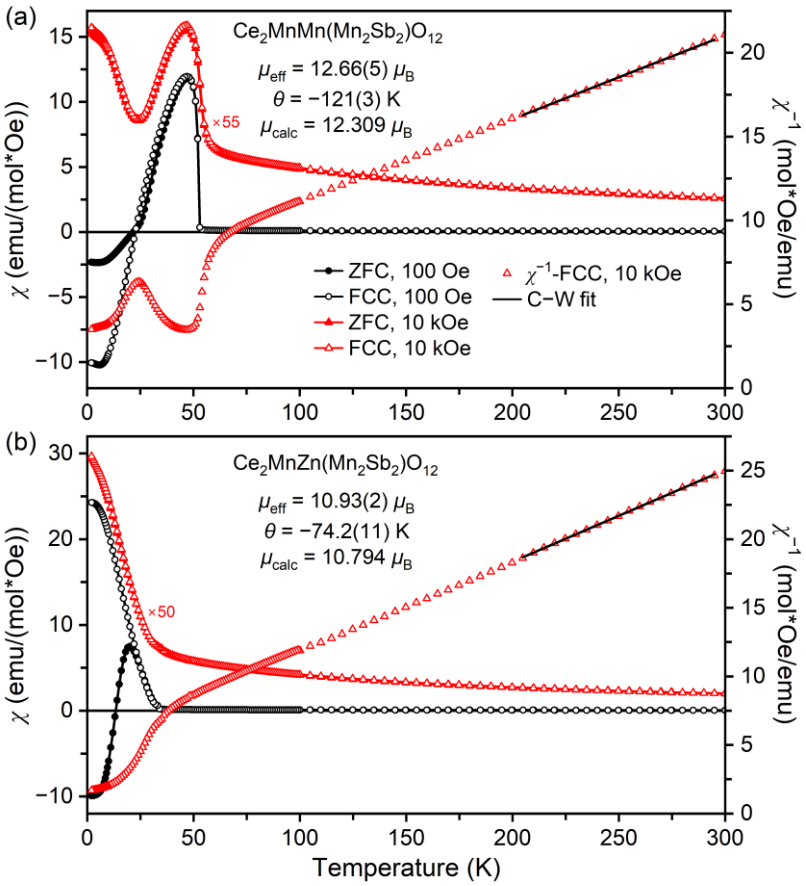

Figure 4.6 ZFC (filled symbols) and FCC (empty symbols) dc magnetic susceptibility ($\chi = M/H$) curves of $Ce_2MnM(Mn_2Sb_2)O_{12}$ with (a) M = Mn and (b) M = Zn measured at 100 Oe (black, circles) and 10 kOe (red, triangles). The black line gives the Curie–Weiss fit (C–W fit) using the FCC χ^{-1} versus T curves at 10 kOe.

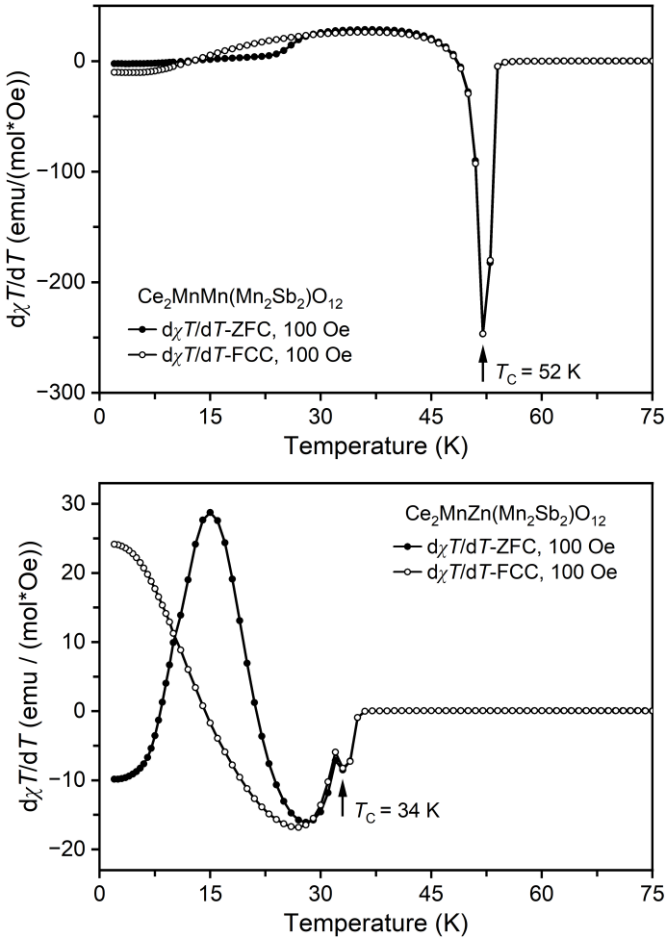

Figure 4.7 ZFC and FCC dχT/dT versus T curves of $Ce_2MnM(Mn_2Sb_2)O_{12}$ with M = Mn and Zn at H = 100 Oe.

The inverse magnetic susceptibility was fitted by the Curie–Weiss law at temperatures above 200 K. The Curie–Weiss parameters were obtained from the Curie–Weiss equation fit detailed in the Experimental section and concluded in **Table 4.4**. The experimentally determined effective magnetic moments (μ_{eff}) closely match the theoretically expected values (μ_{calc}) [51]. We note that the inclusion of Ce^{3+} moments ($2.4\mu_B$) [51] gave a better agreement between the calculated and experimental values, thus, giving an indirect support of the oxidation state of Ce. The negative values of the Curie–Weiss temperature (θ) indicated the dominance of AFM interactions.

We emphasize that negative magnetization was also observed on the ZFC curves of $Ce_2MnMn(Mn_2Sb_2)O_{12}$ and $Ce_2MnZn(Mn_2Sb_2)O_{12}$ measured at 100 Oe (**Figure 4.6**). In the majority of cases, negative magnetization on ZFC curves is due to artifacts caused

by two main reasons. The first reason is a negative trapped field inside a magnetometer where a negative trapped field produces a negative initial magnetization [52, 53], which sometimes cannot be switched to a positive value by a small, positive measurement/applied field because of large coercive fields of a material. The second reason is a sample insertion procedure for some models of magnetometers that are kept at low temperatures as the base temperature (for example, at 10 K or 100 K). In this case, negative magnetization on ZFC curves was observed even in positive trapped fields because samples were moved through a magnet below magnetic ordering temperatures, and no negative magnetization was observed when samples were moved through a magnet at 300 K [54]. In our current case, the base temperature of a magnetometer was 300 K; therefore, samples were moved through a magnet at 300 K, which is well above magnetic ordering temperatures.

Table 4.4 Angles (in deg) mediating the main magnetic interactions, ferrimagnetic Curie temperatures (T_C) and parameters of Curie–Weiss fits and M versus H Curves at T = 5 K for $Ce_2MnM(Mn_2Sb_2)O_{12}$ with M = Mn and Zn.

M	< Ce–O–Mn_B >			< $Mn_{A'}$–O1–Mn_B >	< $Mn_{A''}$–O2–Mn_B >
	O1	O2	O3		
Mn	83.0(3)	87.1(3)	102.6(3)	103.8(3)	104.7(4)
Zn	81.4(4)	85.5(3)	103.6(4)	103.9(4)	-

M	T_C (K)	μ_{eff} (μ_B/f.u.)	μ_{calc} (μ_B/f.u.)	θ (K)	M_R (μ_B/f.u.)	$M_{extr.}$ (μ_B/f.u.)	H_C (kOe)
Mn	52	12.71(5)	12.309	–121(3)	0.221	0.15	1.39
Zn	34	10.98(2)	10.794	–74.2(11)	0.622	0.67	0.48

Curie–Weiss fits were performed between 200 and 295 K using the FCC χ^{-1} versus T data at 10 kOe.

T_C is determined from sharp peaks on the 100 Oe FCC dχ/dT versus T curves.

M_R is the remnant magnetization at T = 5 K.

$M_{extr.}$ at T = 5 K is obtained by the extrapolation between 40 kOe and 70 kOe to zero field.

H_C is the coercive field at T = 5 K.

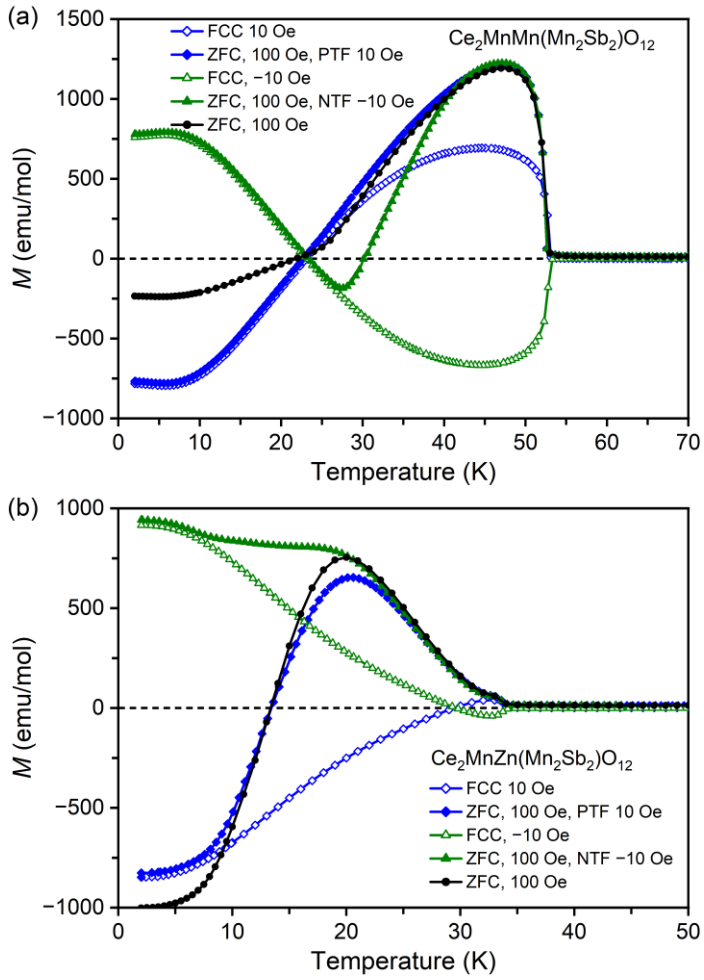

Figure 4.8 Magnetization (*M* versus *T*) curves of $Ce_2MnM(Mn_2Sb_2)O_{12}$ with (a) M = Mn and (b) M = Zn measured at different conditions and fields. PTF indicates a positive trapped field, and NTF represents a negative trapped field.

To check whether negative magnetization on ZFC curves of $Ce_2MnMn(Mn_2Sb_2)O_{12}$ and $Ce_2MnZn(Mn_2Sb_2)O_{12}$ was intrinsic or not we utilized the following procedure. We cooled samples in applied fields of 10 Oe and –10 Oe (applied after the magnet-reset procedure), which should simulate intentionally large positive and negative trapped fields (PTF and NTF), respectively. At the same time, we measured magnetization down to 2 K (this is equivalent to the FCC measurements at 10 Oe and –10 Oe). As shown in **Figure 4.8**, in the paramagnetic states, magnetization of both samples was positive at 10 Oe and negative at –10 Oe confirming the signs of the "trapped" fields; and such FCC curves at 10 Oe and –10 Oe were nearly symmetrical relative to the

temperature axis. Then, a measurement field of 100 Oe was applied at 2 K, and the ZFC curves were measured. The absolute values of magnetization did not change much on moving from 10 Oe to 100 Oe (and from –10 Oe to 100 Oe) at 2 K. As a result, magnetization remained negative when the trapped field was positive (10 Oe), and magnetization remained positive when the trapped field was negative (–10 Oe) due to the presence of negative magnetization phenomena in both compounds. Therefore, we can conclude that negative magnetization on ZFC curves in $Ce_2MnMn(Mn_2Sb_2)O_{12}$ and $Ce_2MnZn(Mn_2Sb_2)O_{12}$ is intrinsic (assuming that fields should approach zero values from the positive direction in all ZFC procedures) and originates from the existence of NME and finite positive trapped fields inside a magnetometer. It is interesting that magnetization changed sign two times (at 23 K and 30 K) in case of $Ce_2MnMn(Mn_2Sb_2)O_{12}$ when the "trapped" field was negative (–10 Oe) because the ZFC *M* versus *T* curve (at 100 Oe) followed the FCC *M* versus *T* curve (at –10 Oe) up to a certain temperature (about 25 K); the point where these curves are separated could be related to temperature dependence of coercive fields. For example, these curves start separating above about 7 K in $Ce_2MnZn(Mn_2Sb_2)O_{12}$. Therefore, ZFC curves of the M = Zn sample (obtained under negative trapped fields) do not show negative values, and the "compensation" temperature (about 13 K) on ZFC curves of the M = Zn sample (obtained under positive trapped fields) does not match with the compensation temperature of the FCC curves.

To further explore the NME in $Ce_2MnMn(Mn_2Sb_2)O_{12}$ and $Ce_2MnZn(Mn_2Sb_2)O_{12}$, FCC magnetic susceptibility measurements were performed under various applied magnetic fields. As shown in **Figure 4.9**(a), the magnetic susceptibility of $Ce_2MnMn(Mn_2Sb_2)O_{12}$ exhibits a consistent trend across different fields: a rapid increase below T_C, reaching a peak at $T\chi_{max}$ (47 K), followed by a decrease. NME is observed at low temperatures when $H \leq 600$ Oe, with T_{comp} shifting to lower values as the field increases (inset of **Figure 4.9**(a)) and a reduction in the NME component. For $H \geq 800$ Oe, only positive magnetization is observed, and the susceptibility shows a slight increase at ~23 K. Furthermore, the maximum values of the FCC curves above T_{comp} increase as the field decreases. As it will be further discussed below, the NME in $Ce_2MnMn(Mn_2Sb_2)O_{12}$ likely arises from FM ordering of Mn^{2+} at the A′ and A″ sites and an AFM arrangement of Mn^{2+} at the B site [34, 36]. These competing magnetic

interactions give rise to the complex temperature-dependent magnetization behavior. In contrast, $Ce_2MnZn(Mn_2Sb_2)O_{12}$ shows NME only at a significantly lower field range ($H \leq 20$ Oe), with T_{comp} decreasing from 29.6 K at $H = 10$ Oe to 28.5 K at $H = 20$ Oe) (**Figure 4.9**(b)). Below T_C, the magnetic susceptibility rapidly peaks at $T\chi_{max} = 32.6$ K, followed by either a continuous increase ($H \geq 40$ Oe) or a decrease ($H \leq 20$ Oe). The suppressed NME in $Ce_2MnZn(Mn_2Sb_2)O_{12}$ can be attributed to the presence of non-magnetic Zn^{2+} ions, which do not participate in magnetic exchange interactions.

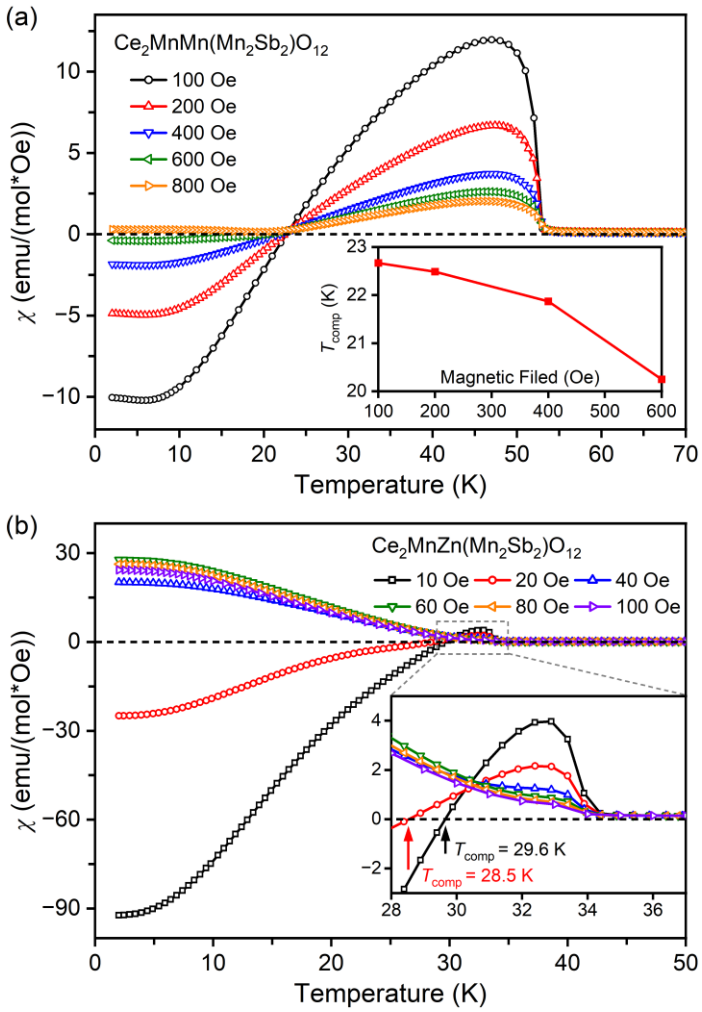

Figure 4.9 FCC dc magnetic susceptibility ($\chi = M/H$) curves of $Ce_2MnM(Mn_2Sb_2)O_{12}$ with (a) M = Mn and (b) M = Zn measured at different fields. The inset in (a) shows the plot of compensation temperature (T_{comp}) as a function of applied magnetic field. The inset in (b) shows a zoomed region near Curie temperature (T_C).

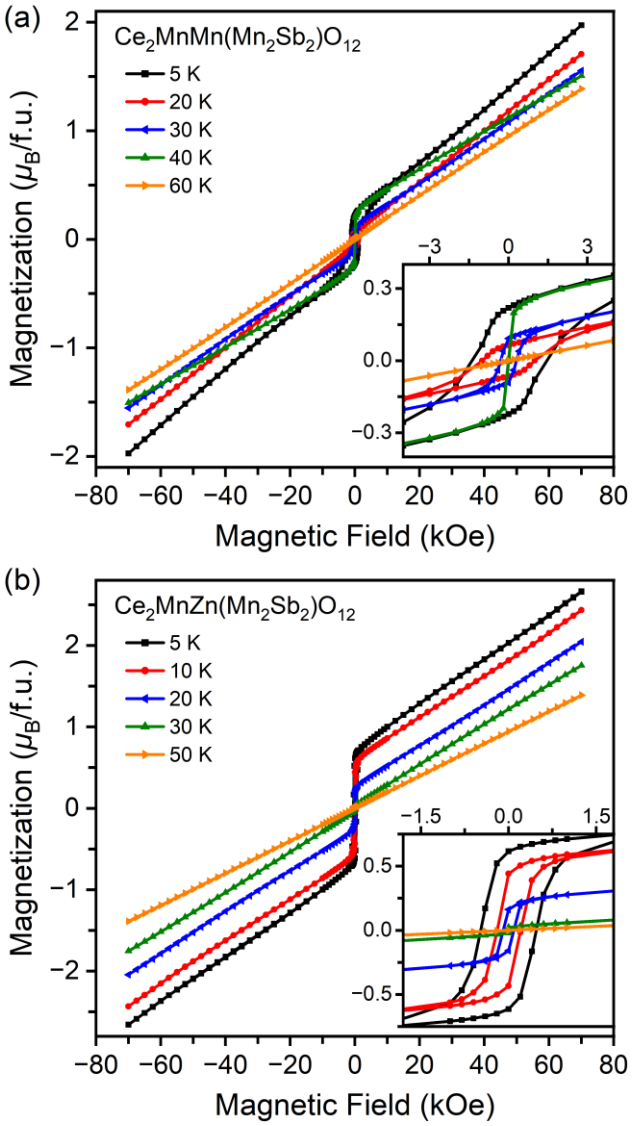

Figure 4.10 *M* versus *H* curves of $Ce_2MnM(Mn_2Sb_2)O_{12}$ with (a) M = Mn and (b) M = Zn at different temperatures. Each inset shows a zoomed region near zero field.

Isothermal magnetization curves (*M* versus *H*) at different temperatures are presented in **Figure 4.10**, with the corresponding parameters summarized in **Table 4.4**. The presence of hysteresis substantiates the presence of FM components in the magnetic ordering. At 5 K, both samples exhibit an incomplete wasp-waisted shape with low remnant magnetization (M_R) and coercive fields (H_C), attributed to the coexistence of competing FM and AFM interactions [55]. The unsaturated behavior of both samples under high magnetic fields indicates that AFM coupling is the dominant factor

influencing their magnetic properties. The extrapolated magnetization ($M_{extr.}$) determined via linear extrapolation, is quite small, reflecting the presence of strong magnetic competition and complex lattice coupling. As temperature increases, the hysteresis loop narrows and H_C decreases (see insets of **Figure 4.10** and **Figure 4.11**). Notably, a slight increase in M_R is observed around 40 K of $Ce_2MnMn(Mn_2Sb_2)O_{12}$, which corresponds to an anomaly in the 10 kOe ZFC and FCC curves (**Figure 4.6**(a)).

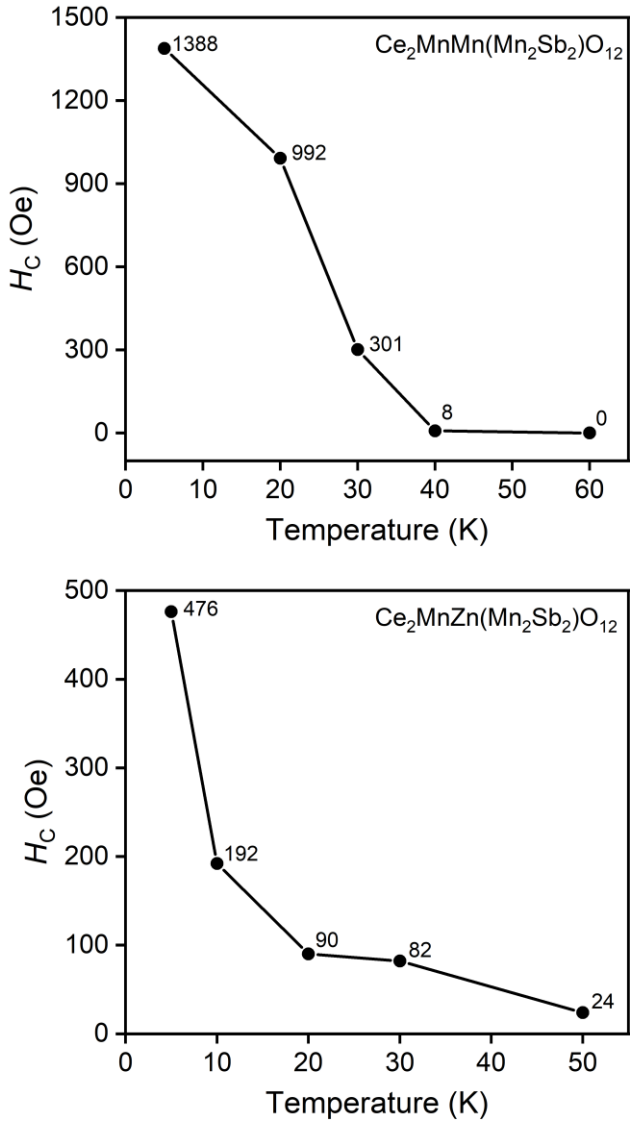

Figure 4.11 The coercive field (H_C) as a function of temperature for $Ce_2MnMn(Mn_2Sb_2)O_{12}$ and $Ce_2MnZn(Mn_2Sb_2)O_{12}$.

The specific heat (C_p) measurements at H = 0 and 90 kOe for $Ce_2MnMn(Mn_2Sb_2)O_{12}$ and $Ce_2MnZn(Mn_2Sb_2)O_{12}$ are presented in **Figure 4.12**(a). Pronounced anomalies are observed at their respective T_C, confirming the presence of long-range magnetic ordering. These anomalies reflect an increase in magnetic entropy as the system transitions from an ordered state to a disordered state. Interestingly, while the magnetic transition in $Ce_2MnMn(Mn_2Sb_2)O_{12}$ is suppressed under a field of 90 kOe, the transition in $Ce_2MnZn(Mn_2Sb_2)O_{12}$ remains relatively unchanged. This difference may be due to the substitution of Mn by Zn, which reduces the number of magnetic ions and potentially weakens the AFM coupling, leading to a reduced response of the magnetic order to external fields in $Ce_2MnZn(Mn_2Sb_2)O_{12}$. There is evidence for the appearance of the second magnetic transition near 40 K in $Ce_2MnMn(Mn_2Sb_2)O_{12}$ at 90 kOe (**Figure 4.12**(a)). In magnetic insulators, the C_p capacity is predominantly governed by lattice vibrations at higher temperatures and magnetic excitations at lower temperatures. To isolate the magnetic contribution from the total C_p, the lattice contribution ($C_{lattice}$) was estimated using the experimentally measured C_p of $Nd_2ZnZn(Zn_2Sb_2)O_{12}$, a compound with the same structure and paramagnetic behavior down to 2 K (**Figure 4.13**). This paramagnetic material features non-magnetic cations occupying the A′, A″, and B sites. The magnetic part of the heat capacity is calculated by subtracting the lattice part, $C_{mag} = C_p - C_{lattice}$ (the left axis of **Figure 4.12**(b)). The magnetic entropy (S_{mag}) was subsequently determined by integrating the C_{mag}/T (the right axis of **Figure 4.12**(b)). The expected magnetic entropy for Mn^{2+} moment is $S_{mag} = R\ln(2J + 1) = R\ln(6) \approx 14.89$ J K^{-1} mol^{-1}, where R = 8.314 J K^{-1} mol^{-1} is the universal gas constant. The S_{mag} for both samples gradually increases at low temperatures, nearing saturation around 100 K. At T = 100 K, S_{mag} for $Ce_2MnMn(Mn_2Sb_2)O_{12}$ is 51.2 J K^{-1} mol^{-1}, while for $Ce_2MnZn(Mn_2Sb_2)O_{12}$ is 40.5 J K^{-1} mol^{-1}. These values are slightly lower than the expected Boltzmann entropy estimated from the Mn content ($4R\ln6$ and $3R\ln6$, **Figure 4.12**(b)) due to difficulties in the precise estimation of the lattice contribution. The difference between the two is consistent with the reduction in S_{mag} due to the substitution of Mn by Zn at the A″ site, which reduces the number of magnetic moments contributing to the total entropy.

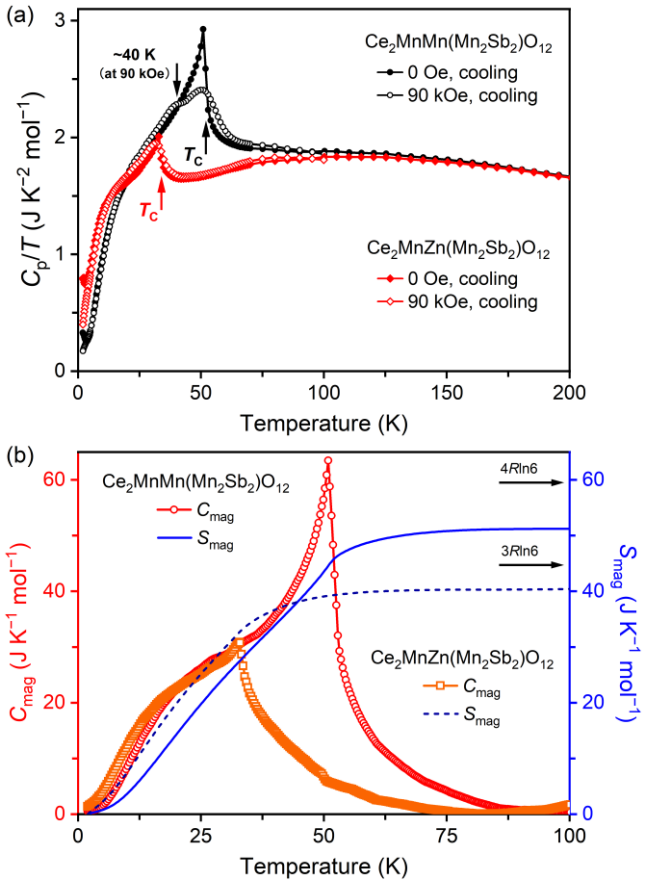

Figure 4.12 (a) Specific heat data of $Ce_2MnM(Mn_2Sb_2)O_{12}$ with M = Mn and Zn plotted as C_p/T versus T. Measurements were performed on cooling at H = 0 Oe and 90 kOe. (b) Temperature dependences of the magnetic contribution to the heat capacity (C_{mag}) and the magnetic entropy (S_{mag}) of $Ce_2MnM(Mn_2Sb_2)O_{12}$ with M = Mn and Zn at H = 0.

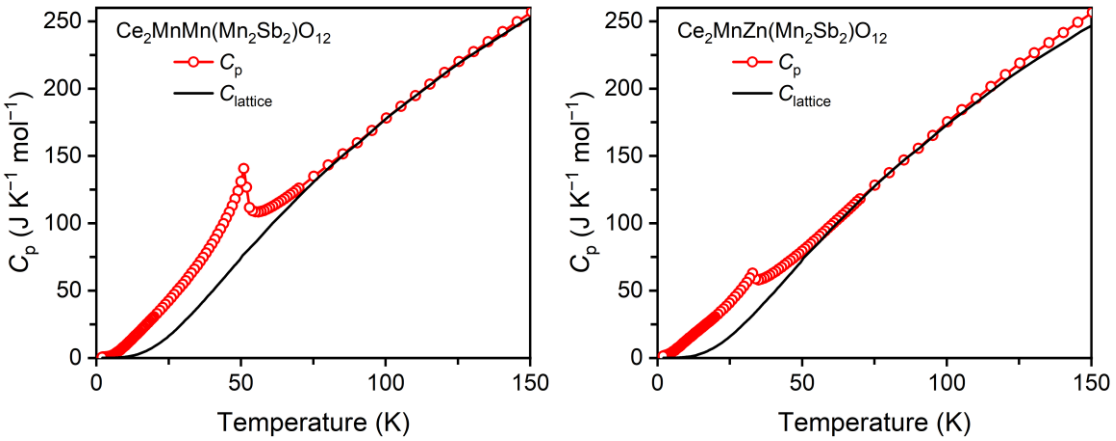

Figure 4.13 The heat capacity of $Ce_2MnM(Mn_2Sb_2)O_{12}$ with M = Mn and Zn as a function of temperature. The black line shows the estimated lattice contribution.

The relationship between magnetic entropy and temperature is used to study the magnetocaloric effect (MCE). Magnetic entropy change ($-\Delta S_{mag}$) is calculated based on the C_p data by using the following equation [56]:

$$\Delta S_{\text{mag}}(H_2, H_1) = \sum_{i=1}^{n} \frac{C_{H_2}(T_i) - C_{H_1}(T_i)}{T_i} \Delta T_i$$

where $C_{H_1}(T_i)$ and $C_{H_2}(T_i)$ are the values of C_p data measured in the fields of H_1 = 0 Oe and H_2 = 90 kOe at T_i, respectively. The result of temperature dependence of $-\Delta S_{mag}$ is presented in **Figure 4.14**, $-\Delta S_{mag}$ increases after cooling the sample from the high temperature and reaches a maximum near T_C.

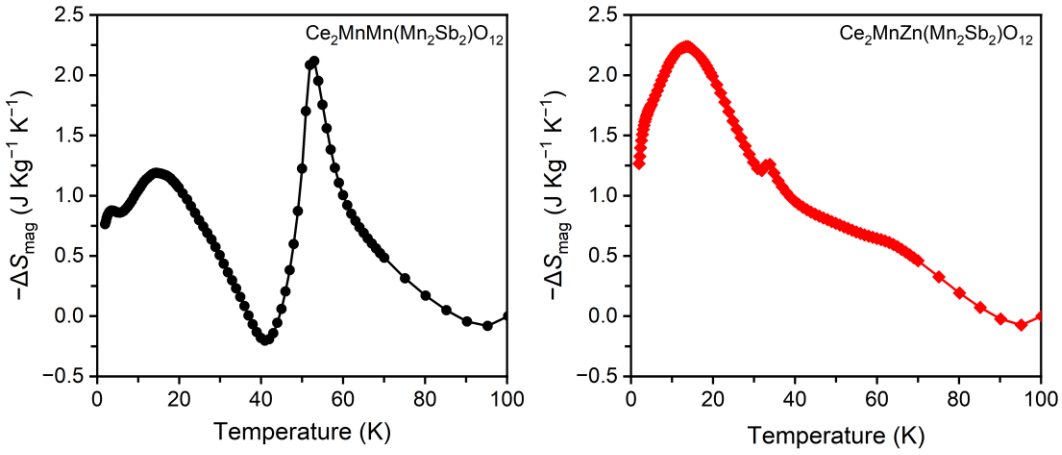

Figure 4.14 Temperature dependence of magnetic entropy change ($-\Delta S_{mag}$) under an applied magnetic field of H = 90 kOe for $Ce_2MnM(Mn_2Sb_2)O_{12}$ with M = Mn and Zn.

4.3.3 Discussion

The NME observed in $Ce_2MnM(Mn_2Sb_2)O_{12}$ (M = Mn and Zn) represents a remarkable phenomenon arising from the intricate interplay between magnetic sublattices and the crystal structure. Such a system belongs to one of the five known NME mechanisms [3], specifically those involving antiparallel ordering between two (or more) FM sublattices associated with distinct crystallographic sites. This discussion first addresses the mechanism of NME in $Ce_2MnMn(Mn_2Sb_2)O_{12}$ and then illustrates how substituting Mn^{2+} with nonmagnetic Zn^{2+} at the A″ site affects NME in

$Ce_2MnZn(Mn_2Sb_2)O_{12}$. The type and relative strength of magnetic interactions in both materials are critically determined by the geometry of M–O–M superexchange pathways, with the corresponding angles summarized in **Table 4**. In $Ce_2MnMn(Mn_2Sb_2)O_{12}$, the rock-salt ordering of B site Mn^{2+} and Sb^{5+} cations necessitates the involvement of super-superexchange Mn_B–O–Sb–O–Mn_B pathways, furthermore, the octahedral geometry of B site Mn^{2+} minimizes interactions with neighboring B sites. The square-planar coordination of A′ site Mn^{2+} and the tetrahedral coordination of A″ site Mn^{2+} prevent direct magnetic interactions between equivalent A′ and A″ sites. Consequently, the magnetic behavior of $Ce_2MnMn(Mn_2Sb_2)O_{12}$ is dominated by two key AFM superexchange pathways: $Mn_{A'}$–O–Mn_B and $Mn_{A''}$–O–Mn_B. The respective superexchange bond angles support moderate AFM coupling, consistent with the Goodenough-Kanamori-Anderson (GKA) rules [57]. A′ and A″ site Mn^{2+} moments align parallel to each other but antiparallel to B site Mn^{2+} moments, creating a FIM lattice [36, 55]. The AFM coupling mechanism has been experimentally confirmed in related compounds through neutron powder diffraction (NPD) studies, including $R_2MnMn(Mn_2Sb_2)O_{12}$ with R = La, Pr, and Nd [36, 55].

The schematic illustration of the spin configurations in $Ce_2MnMn(Mn_2Sb_2)O_{12}$ is presented in **Figure 4.15**, the temperature-dependent magnetic behavior exhibits four distinct regimes. (i) $T > T_C$: Above T_C, thermal agitation dominates, leading to paramagnetic behavior without long-range magnetic ordering. (ii) $T\chi_{max} < T < T_C$: As the system cools below T_C, magnetic ordering develops. The A′ and A″ site Mn^{2+} moments ($M_{MnA', A''}$) grow rapidly due to strong exchange interactions, while B site Mn^{2+} moments (M_{MnB}) increase more slowly due to dilution of the whole B sublattice. The sublattice moments align along the easy axis, dictated by magnetic anisotropy. Net magnetization (M_{net}) remains positive but small due to the imbalance between sublattices. At $T\chi_{max}$, magnetic susceptibility peaks, reflecting the system's heightened responsiveness to external fields. The near invariance of $T\chi_{max}$ across different fields (**Figure 4.9**(a)) suggests that local AFM coupling and thermal agitation, rather than external fields, govern this characteristic temperature. (iii) $T_{comp} < T < T\chi_{max}$: As the temperature decreases further, M_{MnB} grow significantly faster than $M_{MnA', A''}$. The fourfold coordination of both A′ and A″ sites impose strong local anisotropies that hinder rapid magnetic reorientation, enabling M_{MnB} to dominate. This imbalance causes M_{net} to decrease,

reaching zero at T_{comp} as opposing sublattice moments cancel out ($M_{MnA', A''} = M_{MnB}$). (iv) $T < T_{comp}$: Below T_{comp}, M_{MnB} dominate, leading to negative M_{net}. Strong AFM coupling between B and A′/A″ sites suppresses further alignment with external fields. This transition aligns with Néel theory [58], underscoring the roles of sublattice interactions and anisotropy in determining magnetic behavior.

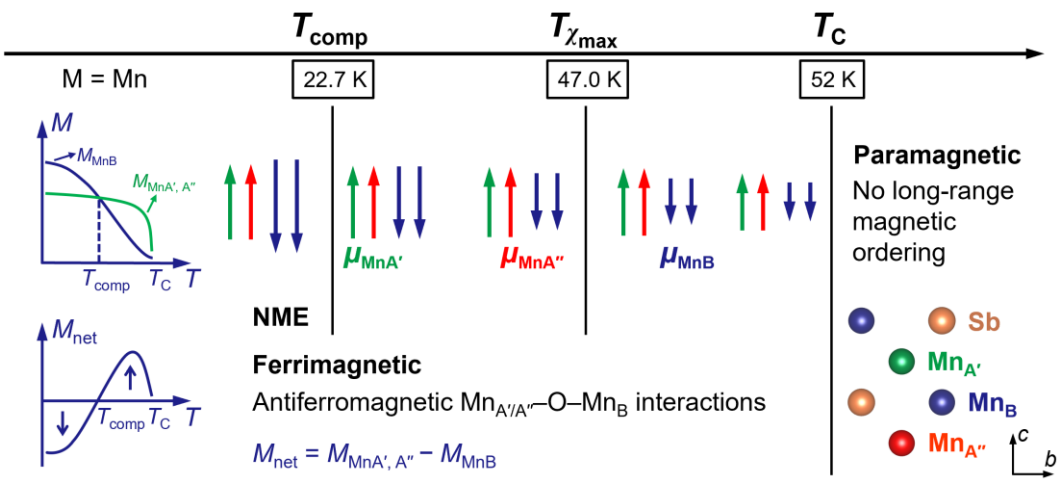

Figure 4.15 The schematic illustration of the spin configurations in $Ce_2MnMn(Mn_2Sb_2)O_{12}$. NME–negative magnetization effect.

The influence of external magnetic fields on NME is evident across these regimes. At low measurement magnetic fields (below coercive fields), one sublattice overcomes another sublattice in each domain, and the magnetic field cannot switch magnetization in domains resulting in a smooth M versus T (or χ versus T) curves across T_{comp}. On the other hand, an apparent broad maximum appears in larger magnetic fields (**Figure 4.6**). For example, the observed maximum on the 10 kOe ZFC and FCC curves of $Ce_2MnMn(Mn_2Sb_2)O_{12}$ is a typical feature of FIM materials with NME [13, 59]. Low-temperature minimum is also observed very close to T_{comp} (when the measurement field is not too high). The origin of this behavior lies again in NME, when the magnetic field is high enough (above coercive fields) to switch magnetization in domains to the opposite direction at T_{comp} because states with negative magnetization relative to the direction of a magnetic field are energetically unfavorable. One sublattice continues to overcome another sublattice, or the absolute values of magnetization continue to increase below

T_{comp} at any magnetic field.

Similar behavior of χ versus T curves was observed in $MnLaMnSbO_6$ [36, 55], when measured at 1 kOe, with a broad maximum below T_C = 48 K and a sharp unturn below 9 K. This is a typical feature of FIM materials with NME [13, 59]. Therefore, $MnLaMnSbO_6$ could also exhibit NME below 9 K at lower magnetic fields, and the ordered moments of Mn^{2+} at A′, A″, and B sites could be different in contrast to the assumptions of Refs. 36 and 55. Sm^{3+} cations usually show no or weak ordered magnetic moments in perovskite oxides [60], and $MnSmMnSbO_6$ also demonstrated a broad maximum on its χ versus T curves (at 1 kOe) [36]. On the other hand, $MnRMnSbO_6$ compounds from the same series with detectable R^{3+} ordered moments (R = Pr and Nd) [36, 55] showed no (direct or indirect) signs of NME. Therefore, we can assume that Ce^{3+} cations in $Ce_2MnMn(Mn_2Sb_2)O_{12}$ should have no or very weak ordered magnetic moments in order to show NME as this effect appears to be a competition of ordered moments of Mn at A′, A″, and B sites. For example, NME was observed in $Sm_2MnMn(Mn_2Ti_2)O_{12}$ [60]. However, another sample [34] with the same composition did not show NME suggesting that small variations in cation distributions could play a major role in the appearance of NME.

Substituting Mn^{2+} at the A″ site with nonmagnetic Zn^{2+} in $Ce_2MnZn(Mn_2Sb_2)O_{12}$ significantly affects its magnetic properties. Zn substitution eliminates the A″–O–B AFM pathway, reducing the overall AFM coupling. This weakens sublattice competition, result in higher remnant magnetization and diminished NME, as observed in $Ce_2MnZn(Mn_2Sb_2)O_{12}$. Moreover, the T_C and T_{comp} temperatures are closer in $Ce_2MnZn(Mn_2Sb_2)O_{12}$ than in $Ce_2MnMn(Mn_2Sb_2)O_{12}$. This proximity suggests that, just below T_C, a larger moment is induced on the A′ site than on the B sites. However, as there are no magnetic cations at the A″ site in $Ce_2MnZn(Mn_2Sb_2)O_{12}$, the M_{MnB} (from two Mn^{2+} cations) quickly overtakes the $M_{MnA'}$ (from one Mn^{2+} cation) resulting in T_{comp} being very close to T_C. On the other hand, in $Ce_2MnMn(Mn_2Sb_2)O_{12}$, the presence of magnetic Mn^{2+} cations at both the A′ and A″ sites leads to a more competitive interaction with the two Mn^{2+} cations at the B sites within the FIM structure. This competition allows M_{MnB} to surpass $M_{MnA', A''}$ at a much lower temperature, resulting in a more pronounced separation between T_C and T_{comp}. These findings highlight the critical role of cation composition and

site occupancy in dictating the magnetic behavior and NME of these complex perovskite-like oxides. We note that broad maxima were also observed in $Ce_2MnZn(Mn_2Sb_2)O_{12}$ between T_C and T_{comp} on χ versus T curves when measured at magnetic fields above 40 Oe (the inset of **Figure 4.9**(b)) in agreement with the general tendency discussed in the above paragraph. However, because T_C and T_{comp} are very close to each other, the maxima are very small.

4.4 Summary of chapter 4

In summary, this study presents the observation of the pronounced negative magnetization effect (NME) in A-site columnar-ordered quadruple perovskites, specifically $Ce_2MnM(Mn_2Sb_2)O_{12}$ (M = Mn and Zn). These compounds crystallize in the $P4_2/n$ (No. 86) space group, demonstrating complete rock-salt ordering of Mn and Sb at the B sites. The bond-valence sum analysis and charge balance confirm that cerium exists in the +3 oxidation state. The compounds exhibit distinct magnetic transitions at T_C = 52 K for M = Mn and T_C = 34 K for M = Zn. Field-cooled measurements under small magnetic fields reveal pronounced NME, which is further corroborated by zero-field-cooled curves under similar conditions. The observed NME is likely a consequence of the ferrimagnetic structures inherent to these materials. These findings underscore the critical influence of complex magnetic interactions and anisotropy coupling in governing their unique magnetic properties.

References in chapter 4

[1] Y. Ren; T. T. M. Palstra; D. I. Khomskii; E. Pellegrin; A. A. Nugroho; A. A. Menovsky; G. A. Sawatzky. Temperature-induced magnetization reversal in a YVO_3 single crystal. *Nature* **1998**, *396*, 441–444.

[2] O. Kahn. The magnetic turnabout. *Nature* **1999**, *399*, 21–22.

[3] A. Kumar; S. M. Yusuf. The phenomenon of negative magnetization and its implications. *Phys. Rep.* **2015**, *556*, 1–34.

[4] T. Okuno. Spin-Transfer Torques for Domain Wall Motion in Antiferromagnetically-Coupled Ferrimagnets. In *Magnetic Dynamics in Antiferromagnetically-Coupled Ferrimagnets: The Role of Angular Momentum*, Okuno, T. Ed.; Springer Singapore, 2020; pp 25–48.

[5] X. Xie; H. Che; H. Wang; G. Lin; H. Zhu. Negative zero-field-cooled magnetization in $YMn_{0.5}Cr_{0.5}O_3$ due to giant coercivity and trapped field. *Inorg. Chem.* **2018**, *57*, 175–180.

[6] B. Martínez; L. Balcells; J. Fontcuberta; X. Obradors; C. H. Cohenca; R. F. Jardim. Magnetic anisotropy and spin diffusion through spin disordered interfaces in magnetoresistive manganites. *J. Appl. Phys.* **1998**, *83*, 7058–7060.

[7] D. A. Garanin; H. Kachkachi. Surface contribution to the anisotropy of magnetic nanoparticles. *Phys. Rev. Lett.* **2003**, *90*, 065504.

[8] V. K. Lakhani; B. Zhao; L. Wang; U. N. Trivedi; K. B. Modi. Negative magnetization, magnetic anisotropy and magnetic ordering studies on Al^{3+}-substituted copper ferrite. *J. Alloy. Compd.* **2011**, *509*, 4861–4867.

[9] S. M. Yusuf; A. Kumar; J. V. Yakhmi. Temperature- and magnetic-field-controlled magnetic pole reversal in a molecular magnetic compound. *Appl. Phys. Lett.* **2009**, *95*, 182506.

[10] J. P. Zhao; J. Xu; S. D. Han; Q. L. Wang; X. H. Bu. A niccolite structural multiferroic metal-organic framework possessing four different types of bistability in response to dielectric and magnetic modulation. *Adv. Mater.* **2017**, *29*, 1606966.

[11] Y. Yang; R. B. Wilson; J. Gorchon; C.-H. Lambert; S. Salahuddin; J. Bokor. Ultrafast magnetization reversal by picosecond electrical pulses. *Sci. Adv.* **2017**, *3*, e1603117.

[12] A. M. Abakumov; A. A. Tsirlin; E. V. Antipov. Transition-Metal Perovskites. In *Comprehensive Inorganic Chemistry II: From Elements to Applications*, Reedijk, J., Poeppelmeier, K. Eds.; Vol. 2; Elsevier, 2013; pp 1–40.

[13] A. Dönni; V. Y. Pomjakushin; L. Zhang; K. Yamaura; A. A. Belik. Origin of negative magnetization phenomena in $(Tm_{1-x}Mn_x)MnO_3$: A neutron diffraction study. *Phys. Rev. B* **2020**, *101*, 054442.

[14] A. Kumar; S. M. Yusuf; C. Ritter. Nd-ordering-driven Mn spin reorientation and magnetization reversal in the magnetostructurally coupled compound $NdMnO_3$. *Phys. Rev. B* **2017**, *96*, 014427.

[15] S. Chatterjee; S. Halder; K. Das; K. Pradhan; I. Das. Magnetization reversal in nanocrystalline $Gd_{0.5}Sr_{0.5}MnO_3$. *Phys. Rev. B* **2024**, *110*, 155138.

[16] S. Vasala; M. Karppinen. $A_2B'B''O_6$ perovskites: A review. *Prog. Solid State Chem.* **2015**, *43*, 1–36.

[17] H. Y. Zhou; X. M. Chen. Structural distortions, orbital ordering and physical properties of double perovskite R_2CoMnO_6 calculated by first-principles. *J. Phys.: Condens. Matter* **2017**, *29*, 145701.

[18] A. Banerjee; J. Sannigrahi; S. Giri; S. Majumdar. Magnetization reversal and inverse exchange bias phenomenon in the ferrimagnetic polycrystalline compound Er_2CoMnO_6. *Phys. Rev. B* **2018**, *98*, 104414.

[19] Y. Long. A-site ordered quadruple perovskite oxides $AA'_3B_4O_{12}$. *Chin. Phys. B* **2016**, *25*, 078108.

[20] A. A. Belik; R. D. Johnson; D. D. Khalyavin. The rich physics of A-site-ordered quadruple perovskite manganites AMn_7O_{12}. *Dalton Trans.* **2021**, *50*, 15458–15472.

[21] A. A. Belik. Rise of A-site columnar-ordered $A_2A'A''B_4O_{12}$ quadruple perovskites with intrinsic triple order. *Dalton Trans.* **2018**, *47*, 3209–3217.

[22] A. A. Belik; D. D. Khalyavin; L. Zhang; Y. Matsushita; Y. Katsuya; M. Tanaka; R. D. Johnson; K. Yamaura. Intrinsic triple order in A-site columnar-ordered quadruple perovskites: Proof of concept. *ChemPhysChem* **2018**, *19*, 2449–2452.

[23] M. Azuma; I. Yamada; K. Yamaura; A. A. Belik; T. Yamamoto; M. Fukuda. High pressure studies of transition metal oxides. In *Comprehensive Inorganic Chemistry III*, Reedijk, J., Poeppelmeier, K. R. Eds.; Vol. 4; Elsevier, 2023; pp 681–718.

[24] N. Louis. Antiferromagnetism and Ferrimagnetism. *Proc. Phys. Soc. A* **1952**, *65*,

869–885.

[25] S. K. Kim; G. S. D. Beach; K. J. Lee; T. Ono; T. Rasing; H. Yang. Ferrimagnetic spintronics. *Nat. Mater.* **2022**, *21*, 24–34.

[26] T. A. Ostler; J. Barker; R. F. Evans; R. W. Chantrell; U. Atxitia; O. Chubykalo-Fesenko; S. El Moussaoui; L. Le Guyader; E. Mengotti; L. J. Heyderman; F. Nolting; A. Tsukamoto; A. Itoh; D. Afanasiev; B. A. Ivanov; A. M. Kalashnikova; K. Vahaplar; J. Mentink; A. Kirilyuk; T. Rasing; A. V. Kimel. Ultrafast heating as a sufficient stimulus for magnetization reversal in a ferrimagnet. *Nat. Commun.* **2012**, *3*, 666.

[27] I. Fita; V. Markovich; A. S. Moskvin; A. Wisniewski; R. Puzniak; P. Iwanowski; C. Martin; A. Maignan; R. E. Carbonio; M. U. Gutowska; A. Szewczyk; G. Gorodetsky. Reversed exchange-bias effect associated with magnetization reversal in the weak ferrimagnet $LuFe_{0.5}Cr_{0.5}O_3$. *Phys. Rev. B* **2018**, *97*, 104416.

[28] S. Ghosh; T. Komori; A. Hallal; J. Pena Garcia; T. Gushi; T. Hirose; H. Mitarai; H. Okuno; J. Vogel; M. Chshiev; J. P. Attane; L. Vila; T. Suemasu; S. Pizzini. Current-driven domain wall dynamics in ferrimagnetic nickel-doped Mn_4N Films: Very large domain wall velocities and reversal of motion direction across the magnetic compensation point. *Nano Lett.* **2021**, *21*, 2580–2587.

[29] S. Kawaguchi; M. Takemoto; K. Osaka; E. Nishibori; C. Moriyoshi; Y. Kubota; Y. Kuroiwa; K. Sugimoto. High-throughput powder diffraction measurement system consisting of multiple MYTHEN detectors at beamline BL02B2 of SPring-8. *Rev. Sci. Instrum.* **2017**, *88*, 085111.

[30] F. Izumi; T. Ikeda. A Rietveld-analysis programm RIETAN-98 and its applications to zeolites. *Mater. Sci. Forum* **2000**, *321–324*, 198–205.

[31] W. T. Fu; D. J. W. Ijdo. Crystal structure of $Mn_2Ln_3Sb_3O_{14}$ (*Ln*=La, Pr and Nd): A new ordered rhombohedral pyrochlore. *J. Solid State Chem.* **2014**, *213*, 165–168.

[32] Y. J. Shan; Y. Yoshioka; M. Wakeshima; K. Tezuka; H. Imoto. Synthesis, structure, and magnetic properties of the novel sodium cobalt tellurate $Na_5Co_{15.5}Te_6O_{36}$. *J. Solid State Chem.* **2014**, *211*, 63–68.

[33] L. Zhang; Y. Matsushita; K. Yamaura; A. A. Belik. Five-fold ordering in high-pressure perovskites RMn_3O_6 (R = Gd–Tm and Y). *Inorg. Chem.* **2017**, *56*, 5210–5218.

[34] A. A. Belik; L. Zhang; R. Liu; D. D. Khalyavin; Y. Katsuya; M. Tanaka; K. Yamaura. Valence variations by B-site doping in A-site columnar-ordered quadruple perovskites $Sm_2MnMn(Mn_{4-x}Ti_x)O_{12}$ with $1 \leq x \leq 3$. *Inorg. Chem.* **2019**, *58*, 3492–3501.

[35] R. Liu; R. Scatena; D. D. Khalyavin; R. D. Johnson; Y. Inaguma; M. Tanaka; Y. Matsushita; K. Yamaura; A. A. Belik. High-pressure synthesis, crystal structures, and properties of A-site columnar-ordered quadruple perovskites $NaRMn_2Ti_4O_{12}$ with R = Sm, Eu, Gd, Dy, Ho, Y. *Inorg. Chem.* **2020**, *59*, 9065–9076.

[36] E. Solana-Madruga; A. M. Arevalo-Lopez; A. J. Dos Santos-Garcia; E. Urones-Garrote; D. Avila-Brande; R. Saez-Puche; J. P. Attfield. Double double cation order in the high-pressure perovskites $MnRMnSbO_6$. *Angew. Chem. Int. Ed.* **2016**, *55*, 9340–9344.

[37] X. Liang; K. Yamaura; A. Belik. Three perovskite phases with different cation orders in $Sm_2MnMn(Mn_{4-x}Sb_x)O_{12}$. *Chem. - Eur. J.* **2024**, *30*, e202401960.

[38] X. Liang; K. Yamaura; A. A. Belik. B-site ordered and disordered phases in A-site columnar-ordered quadruple perovskites $Nd_2MnMn(Mn_{4-x}Sb_x)O_{12}$. *Ceram. Int.* **2024**, *50*, 53099–53106.

[39] A. A. Belik; L. Zhang; N. Terada; Y. Katsuya; M. Tanaka; Y. Matsushita; K. Yamaura. A-site-ordered quadruple perovskite manganite $CeMn_7O_{12}$ with trivalent cations. *J. Solid State Chem.* **2020**, *283*, 121161.

[40] T. Kolodiazhnyi; H. Sakurai; M. Avdeev; T. Charoonsuk; K. V. Lamonova; Y. G. Pashkevich; B. J. Kennedy. Giant magnetocapacitance in cerium sesquioxide. *Phys. Rev. B* **2018**, *98*, 054423.

[41] G. King; P. M. Woodward. Cation ordering in perovskites. *J. Mater. Chem.* **2010**, *20*, 5785–5796.

[42] A. M. Glazer. The classification of tilted octahedra in perovskites. *Acta Crystallogr. Sect. B* **1972**, *28*, 3384−3392.

[43] N. E. Brese; M. O'Keeffe. Bond-valence parameters for solids. *Acta Crystallogr. Sect. B* **1991**, *47*, 192–197.

[44] P. L. Roulhac; G. J. Palenik. Bond Valence Sums in Coordination Chemistry. The calculation of the oxidation state of cerium in complexes containing cerium bonded only to oxygen. *Inorg. Chem.* **2003**, *42*, 118–121.

[45] R. Shannon. Revised effective ionic radii and systematic studies of interatomic distances in halides and chalcogenides. *Acta Crystallogr. Sect. A* **1976**, *32*, 751–767.

[46] A. A. Belik; R. Liu; K. Yamaura. Realization of triple A-site cation ordering through the Dy/Mn/Zn combination in the ferrimagnetic $Dy_2MnZnMn_{4-x}Ti_xO_{12}$ perovskites. *Ceram. Int.* **2023**, *49*, 14327–14334.

[47] I. Yamada; H. Etani; M. Murakami; N. Hayashi; T. Kawakami; M. Mizumaki; S. Ueda; H. Abe; K. D. Liss; A. J. Studer; T. Ozaki; S. Mori; R. Takahashi; T. Irifune. Charge-order melting in charge-disproportionated perovskite $CeCu_3Fe_4O_{12}$. *Inorg. Chem.* **2014**, *53*, 11794–11801.

[48] J. Sánchez-Benítez; M. J. Martínez-Lope; J. A. Alonso. Preparation at moderate pressures, crystal and magnetic structure and magnetotransport of the ferrimagnetic $CeCu_3Mn_4O_{12}$ perovskite. *J. Appl. Phys.* **2010**, *107*, 103904.

[49] A. A. Belik; Y. Katsuya; M. Tanaka; K. Yamaura. Crystal structure and magnetic properties of A-site-ordered quadruple perovskite $CeCu_3Cr_4O_{12}$. *J. Alloy. Compd.* **2019**, *793*, 42–48.

[50] V. Chandragiri; K. K. Iyer; K. Maiti; E. Sampathkumaran. Magnetism of a rhombohedral-type pyrochlore-derived Kagome series, $Mn_2R_3Sb_3O_{14}$ (R= Rare-earths). *Mater. Res. Express* **2016**, *3*, 066102.

[51] C. Kittel. *Introduction to Solid State Physics*; John Wiley & Sons, 2005.

[52] N. Kumar; A. Sundaresan. On the observation of negative magnetization under zero-field-cooled process. *Solid State Commun.* **2010**, *150*, 1162–1164.

[53] Y. Yuan; K. Yang; C. Chen; X. Zheng; G. Yu; X. Luo; L. Wang; S. Ma; S. U. Rehman; Z. Zhong. Negative zero-field-cooled magnetization and magnetic switching in multiferroic $Lu_{0.5}Sc_{0.5}FeO_3$ ceramics. *J. Am. Ceram. Soc.* **2021**, *105*, 2058–2066.

[54] L. Zhang; N. Terada; R. D. Johnson; D. D. Khalyavin; P. Manuel; Y. Katsuya; M. Tanaka; Y. Matsushita; K. Yamaura; A. A. Belik. High-pressure synthesis, structures, and properties of trivalent A-site-ordered quadruple perovskites RMn_7O_{12} (R = Sm, Eu, Gd, and Tb). *Inorg. Chem.* **2018**, *57*, 5987–5998.

[55] E. Solana-Madruga; Á. M. Arévalo-López; A. J. Dos Santos-García; C. Ritter; C. Cascales; R. Sáez-Puche; J. P. Attfield. Anisotropic magnetic structures of the Mn*R*MnSbO_6 high-pressure doubly ordered perovskites (*R* = La, Pr, and Nd). *Phys.*

Rev. B **2018**, *97*, 134408.

[56] R. S. Joshi; P. S. A. Kumar. Magnetic Solid-State Materials. In *Comprehensive Inorganic Chemistry II: From Elements to Applications*, Reedijk, J., Poeppelmeier, K. Eds.; Vol. 4; Elsevier, 2013; pp 271–316.

[57] J. B. Goodenough. Theory of the role of covalence in the perovskite-type manganites [La, *M*(II)]MnO_3. *Phys. Rev.* **1955**, *100*, 564.

[58] M. L. Néel. Propriétés magnétiques des ferrites: ferrimagnétisme et antiferromagnétisme. *Ann. Phys.* **1948**, *12*, 137−198.

[59] A. Dönni; V. Y. Pomjakushin; L. Zhang; K. Yamaura; A. A. Belik. Magnetic properties and ferrimagnetic structures of Mn self-doped perovskite solid solutions $(Ho_{1-x}Mn_x)MnO_3$. *J. Alloy. Compd.* **2021**, *857*.

[60] A. M. Vibhakar; D. D. Khalyavin; P. Manuel; R. Liu; K. Yamaura; A. A. Belik; R. D. Johnson. Effects of magnetic dilution in the ferrimagnetic columnar ordered $Sm_2MnMnMn_{4-x}Ti_xO_{12}$ perovskites. *Phys. Rev. B* **2020**, *102*, 214428.

Chapter 5 Critical role of magnetic rare-earth cations in enhancing magnetic transition temperatures of A-site columnar-ordered quadruple perovskites $R_2MnZn(MnZnSb_2)O_{12}$ with R = La, Pr, Nd, and Sm

5.1 Introduction

Perovskite oxides have long been at the forefront of advanced ceramic research due to their tunable crystal structures and multifunctional properties, such as magnetoelectric coupling [1], multiferroicity [2], and magnetocaloric effect [3]. While conventional ambient-pressure synthesis has established the structure-property relationships in simple ABO_3-type perovskites [4], recent breakthroughs in high-pressure synthesis (> 5 GPa) have enabled the stabilization of more complex quadruple perovskites [5, 6], including $AA'_3B_4O_{12}$ and $A_2A'A''B_4O_{12}$ phase, which feature intricate sublattice arrangements. These developments open new avenues for exploring multi-ion-site synergies and the subtle interplay between crystal structure and magnetic properties.

In A-site ordered $AA'_3B_4O_{12}$-type quadruple perovskites (with the parent structure belonging to the *Im*-3 space group), the A site can generally accommodate various cations including both rare-earth and alkaline-earth ions [7, 8]. However, existing studies have predominantly focused on rare-earth ions (R^{3+}) in 12-fold coordination, while the A′ site is occupied by transition metals (e.g., Mn^{3+}) in square-planar coordination. For example, studies on the RMn_7O_{12} system (with the formula $[R^{3+}]_A[Mn^{3+}{}_3]_{A'}[Mn^{3+}{}_4]_BO_{12}$) have demonstrated that both the ionic radius and magnetic moment of R^{3+} critically influence the structural and magnetic properties [9]. Larger R^{3+} ions (e.g., La, Pr, Nd) tend to stabilize *I*2/*m* space group symmetry [10-12]. $LaMn_7O_{12}$ shows an orbital-ordered (OO) transition from a cubic to a monoclinic phase at T_{OO} = 650 K and exhibits dual magnetic transitions (e.g., Néel temperature T_{N1} = 78 K, T_{N2} = 21 K) [10, 13]. Intermediate-sized R^{3+} (Sm–Tb) maintain the monoclinic symmetry with slightly reduced T_{OO} (630–664 K) and show a single dominant magnetic transition (T_{N1} = 82–87 K) [14, 15], whereas smaller R^{3+} ions (e.g., Ho, Er, Y) induce lattice contraction and higher magnetic transition temperatures (e.g., T_N = 108 K for YMn_7O_{12}) [16]. Notably, when the A site is occupied

by non-rare-earth ions such as Ba^{2+}, the magnetic ordering temperature (T_{N1} = 59 K for $BaMn_7O_{12}$) is generally lower than those of rare-earth analogs [17], underscoring the complex role of the A-site cation in tuning magnetic interactions.

In contrast, A-site columnar-ordered $A_2A'A''B_4O_{12}$-type quadruple perovskites (space group of the parent structure is $P4_2/nmc$) exhibit an even more complex sublattice arrangement: the A site is theoretically compatible with diverse +1/+2/+3 cations (e.g., Na^+, Ca^{2+}, R^{3+}), although recent reports have mainly concentrated on rare-earth occupancy [18-20]. Specifically, the A site accommodates R^{3+} in 10-fold coordination, the A′ site adopts square-planar coordination, the A″ site in tetrahedral coordination, and the B site forms either an ordered or disordered sublattice [21, 22]. This unique structure enables multiple exchange pathways between magnetic cations. In principle, long-range magnetic ordering may be achieved via indirect exchange among A′-, A″-, and B-site (M–O–M), while the R^{3+} 4f electrons may participate in spin coupling via R–O–M superexchange pathways [20, 23]. However, research has largely centered on the magnetic interactions within the transition metal sublattice, leaving the role of R^{3+} local moments on global magnetic transition pathways systematically unexplored—particularly when R^{3+} coexists with unconventional Mn^{2+} valence states (as opposed to traditional Mn^{3+}/Mn^{4+}), where synergistic mechanisms remain elusive.

Overall, these observations underscore the significant impact of both R^{3+} 4f electrons and the multi-ion-site arrangement on the magnetic behavior of quadruple perovskites. In the present study, we focus on the A-site columnar-ordered quadruple perovskites, $R_2MnZn(MnZnSb_2)O_{12}$ (R = La, Pr, Nd, and Sm), which also exhibit additional rock-salt B-site ordering. These compounds were synthesized using a high-pressure, high-temperature method at approximately 6 GPa and 1600 K. Synchrotron X-ray powder diffraction data for the R = Nd sample (space group $P4_2/n$ (No. 86)) reveal that Zn^{2+} cations are located in one octahedral B site (together with Mn^{2+}) and in the tetrahedral A″ site even though small antisite disorder of Mn^{2+} and Zn^{2+} cations between the square-planar A′ site and octahedral B site exists. Sb^{5+} solely occupies the second B site. Magnetic measurements indicate that the R = La sample undergoes a long-range ferrimagnetic transition below T_C = 11 K despite the presence of antisite disorder and low concentration of magnetic Mn^{2+} cations. Other samples demonstrated enhanced ferrimagnetic transition temperatures of 21 K (R = Pr), 18 K (R = Nd), and 23 K (R =

Sm). These findings suggest that magnetic rare-earth cations promote exchange interactions between all magnetic cations and are involved in long-range ordering together with Mn^{2+} just below T_C. Our work aims to investigate the effects of different R^{3+} ions in $A_2A'A''B_4O_{12}$ quadruple perovskites, thereby deepening our understanding of magnetostructural coupling in complex oxides and guiding the design of novel functional materials with tailored magnetic properties.

5.2 Experimental details

$La_2MnZn(MnZnSb_2)O_{12}$ sample was prepared from stoichiometric mixtures of $LaSbO_4$, MnO, and ZnO. $LaSbO_4$ was prepared from a stoichiometric mixture of La_2O_3 and Sb_2O_3 by annealing in air at 1270 K for 96 h with several intermediate grindings. $Pr_2MnZn(MnZnSb_2)O_{12}$ sample was prepared from stoichiometric mixtures of Pr_6O_{11}, Mn_2O_3, ZnO, Sb_2O_3, and $KClO_4$. $R_2MnZn(MnZnSb_2)O_{12}$ samples with R = Nd and Sm were prepared from stoichiometric mixtures of R_2O_3, MnO_2, ZnO, and Sb_2O_3. The mixtures were placed in Pt capsules and treated at 6 GPa and about 1600 K for 2 h (heating time to the synthesis temperature was 10 min) by a high-pressure, high-temperature method in a belt-type high-pressure apparatus. After the heat treatments, the samples were cooled down to room temperature (RT) by turning off the heating current, and the pressure was slowly released. Before use, $LaSbO_4$ and R_2O_3 were dried in air at about 1300 K for 1 h and the other oxides (including Pr_6O_{11}) were dried in air at about 400 K for 4–8 h.

X-ray powder diffraction (XRPD) data were collected on a RIGAKU MiniFlex600 diffractometer using CuKα radiation at RT (2θ range of 10–70° with a step of 0.02°, and a scan speed of 3°/min). Synchrotron XRPD data were collected on the BL02B2 beamline of SPring-8 at RT between 1° and 83.02° at a 0.006° interval in 2θ with the wavelength of λ = 0.62007 Å [24]. The data from 5° were used in the refinements as no experimental reflections were observed below 5°. The samples were placed into Lindemann glass capillary tubes (inner diameter: 0.2 mm), which were rotated during measurements. The Rietveld analysis of all XRPD data was performed using the *RIETAN-2000* program [25].

Magnetic measurements were performed on a SQUID magnetometer (Quantum Design, MPMS3) between 2 K and 150 K (or 400 K) in an applied magnetic field of 100 Oe and 10 kOe under both zero-field-cooled (ZFC) and field-cooled on cooling (FCC)

conditions. Isothermal magnetization measurements were performed between –70 and 70 kOe at different temperatures. Specific heat was measured on a Quantum Design PPMS-9T instrument on cooling at magnetic fields of 0 Oe and 90 kOe.

5.3 Results and discussion

5.3.1 Crystal Structure

The crystal structure $Nd_2MnZn(MnZnSb_2)O_{12}$ was refined using structure parameters of $Nd_2MnMn(Mn_{4-x}Sb_x)O_{12}$ as the initial model [21]. The synchrotron XRPD patterns of $Nd_2MnZn(MnZnSb_2)O_{12}$ confirmed the $P4_2/n$ space group (**Figure 5.1**), consistent with columnar A-site ordering and rock-salt-type B-site ordering structure. It contained 0.75 wt% $La_3Mn_2Sb_3O_{14}$-type pyrochlore [26] (space group R-3m, a = 7.4673(3) Å and c = 17.5310(8) Å) and 0.18 wt% Pt impurities (due to contamination from Pt capsule). The structure parameters are presented in **Table 5.1**, the bond lengths, bond angles, bond-valence sum (BVS) [27] and distortion parameters are summarized in **Table 5.2**. The refined cation distribution reveals Nd^{3+} exclusively occupying the 10-fold-coordinated A site at the 4*e* Wyckoff position (0.25, 0.75, *z*), with a BVS of +2.94, confirming its +3 oxidation state. The square-planar A′ site (M1-SQ, 2*b* (0.25, 0.25, 0.75)) exhibits minor antisite disorder between Mn^{2+} and Zn^{2+} (occupation factors refined under the constraint g(Mn) + g(Zn) = 1), while the tetrahedral A″ site (Zn-T, 2*a* (0.75, 0.75, 0.75)) is fully occupied by Zn^{2+}. At the octahedral B sites, one B site (M2-Oc, 4*c* (0, 0.5, 0.5)) is shared by Mn^{2+} and Zn^{2+}, whereas Sb^{5+} exclusively occupies the other B site (Sb-Oc, 4*d* (0, 0, 0.5)) site. Despite the 20% electron count difference between Mn^{2+} (23 electrons) and Zn^{2+} (28 electrons), the antisite disorder at the A′ and B sites was resolvable due to the high sensitivity of synchrotron XRPD. The Nd–O bond lengths include two elongated bonds (2.933(11) Å), a feature shared with isostructural $R_2MnMn(Mn_2Sb_2)O_{12}$ (R = Nd and Sm) perovskites [21, 22]. The Zn–O bond lengths (1.963–2.015 Å) align with values reported for Zn^{2+} in tetrahedral coordination within $R_2MnZn(Mn_{4-x}Ti_x)O_{12}$ (R= Sm and Dy) systems [28, 29], supporting the structural stability of the A″ site. The Sb–O bonds are short (1.963(7)–1.989(6) Å), resulting in elevated BVS value (+5.48) that exceed the ideal +5 oxidation state, a trend consistently observed in other A-site columnar-ordered quadruple perovskites where Sb occupies the B-site [21, 22].

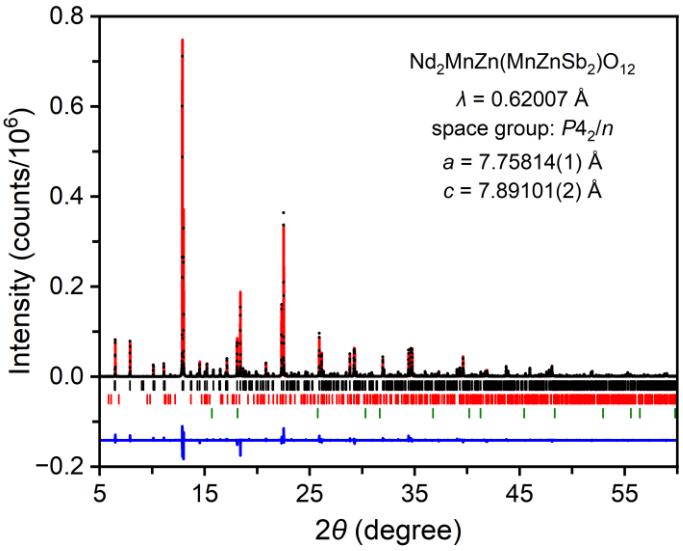

Figure 5.1 Fragments of experimental (black circles), calculated (red line), and difference (blue line) synchrotron X-ray powder diffraction patterns of $Nd_2MnZn(MnZnSb_2)O_{12}$ at T = 295 K. The first black row of tick marks shows possible Bragg reflection positions of the main perovskite phase. Second red and third green rows are minor amounts of $La_3Mn_2Sb_3O_{14}$-type pyrochlore impurity (0.75%) and Pt impurity (0.18%).

Table 5.1 Structure parameters of $Nd_2MnZn(MnZnSb_2)O_{12}$ at 295 K from synchrotron X-ray powder diffraction data (λ = 0.62007 Å).

site	WP	x	y	z	B_{iso} (Å^2)	
Nd	4*e*	0.25	0.75	0.77584(6)	0.486(7)	
M1-SQ	2*b*	0.25	0.25	0.75	0.64(7)	
Zn-T	2*a*	0.75	0.75	0.75	1.00(6)	R_{wp} = 10.87%
M2-Oc	4*c*	0	0.5	0.5	0.50(2)	R_p = 8.31%
Sb-Oc	4*d*	0	0	0.5	0.307(8)	R_I = 4.16%
O1	8*g*	–0.0567(11)	0.5748(11)	0.2346(8)	0.68(11)	R_F = 2.82%
O2	8*g*	–0.2341(11)	–0.0462(6)	0.5876(6)	0.53(10)	
O3	8*g*	–0.2584(10)	0.0672(6)	–0.0331(6)	0.22(7)	

Crystal system: tetragonal; space group: $P4_2/n$ (No. 86, cell choice 2), Z = 2. Molecular weight: 985.5168 g/mol. a = 7.75814(1) Å, c = 7.89101(1) Å, and V = 474.9503(10) Å^3; WP: Wyckoff position. g(Nd) = g(Zn-T) = g(Sb-Oc) = g(O1) = g(O2) = g(O3) = 1, where g is the occupation factor, g(M1-SQ) = 0.816Mn + 0.184Zn, and g(M2-Oc) = 0.592(8)Mn + 0.408Zn. SQ: square-planar (site), T: tetrahedral (site), Oc: octahedral (site).

Table 5.2 Selected bond lengths (Å), bond angles (deg), octahedral distortion parameters (Δ), and bond valence sums (BVS) for $Nd_2MnZn(MnZnSb_2)O_{12}$ at T = 295 K.

Nd–O1(×2)	2.760(11)	M2–O1(×2)	2.217(6)	Sb–O1(×2)	1.989(6)
Nd–O1(×2)	2.933(11)	M2–O2(×2)	2.205(8)	Sb–O2(×2)	1.976(8)
Nd–O2(×2)	2.541(5)	M2–O3(×2)	2.088(7)	Sb–O3(×2)	1.963(7)
Nd–O3(×2)	2.384(4)	BVS (M2)	1.98	BVS (Sb)	5.48
Nd–O3(×2)	2.477(5)	Δ ($M2O_6$)	7.2×10^{-4}	Δ (SbO_6)	2.9×10^{-5}
BVS (Nd)	2.94				
M1–O1(×4)	2.028(5)	Zn–O2(×4)	2.039(5)	M2–O1–Sb	142.4(6)
M1–O2(×4)	3.100(5)	Zn–O3(×4)	2.999(5)	M2–O2–Sb	133.9(4)
BVS (M1)	2.13	BVS (Zn)	1.74	M2–O3–Sb	144.7(4)

BVS $= \sum_{i=1}^{N} v_i$, where $v_i = \exp[(R_0 - l_i)/B]$, N is the coordination number, l_i is a bond length, B = 0.37, $R_0(Nd^{3+})$ = 2.117, R_0(M1 = 0.816Mn^{2+} + 0.184Zn^{2+}) = 0.816 × $R_0(Mn^{2+})$ + 0.184 × $R_0(Zn^{2+})$ = 1.774, $R_0(Zn^{2+})$ = 1.704, R_0(M2 = 0.592Mn^{2+} + 0.408Zn^{2+}) = 0.592 × $R_0(Mn^{2+})$ + 0.408 × $R_0(Zn^{2+})$ = 1.755, $R_0(Sb^{5+})$ = 1.942. $\Delta = (1/N)\sum_{i=1}^{N}[(l_i - l_{av})/l_{av}]^2$, where $l_{av} = (1/N)\sum_{i=1}^{N} l_i$ is the average distance.

The rare-earth stability range of A-site columnar-ordered quadruple perovskites under specific synthesis conditions is strongly governed by the occupation of A′, A″, and B-site cations, subject to stringent steric and charge-matching constraints [6, 20]. For instance, $R_2MnMnMn_4O_{12}$ is stabilized only for R = Gd–Er and Y [30], while $R_2MnMn(MnTi_3)O_{12}$ exhibits a stability range limited to R = Nd–Gd [31]. To probe the structural adaptability of the $R_2MnZn(Mn_2Sb_2)O_{12}$ system, we conducted exploratory syntheses with R = Ce, Nd, Sm, Eu, Dy, and Yb. Preliminary results indicate that the target A-site columnar-ordered and B-site rock-salt-ordered structure ($P4_2/n$) is stabilized for R = Ce, Nd, and Eu, whereas R = Dy and Yb yield a double-perovskite phase ($P2_1/n$) with statistical cation disorder at the A-site (unpublished data). This suggests that smaller R^{3+} ions (e.g., Dy^{3+}: 1.027 Å, Yb^{3+}: 0.985 Å, in an 8-fold coordination) [32] disrupt the geometric tolerance required for columnar ordering due to A-site size mismatch, triggering structural dimensionality reduction. Guided by this finding, we systematically investigated the stability of the current $R_2MnZn(MnZnSb_2)O_{12}$ system with larger R^{3+} ions spanning La–Nd and Sm–Gd. Despite attempts across this broader ionic radius range

(La^{3+}: 1.160 Å to Gd^{3+}: 1.053 Å, in an 8-fold coordination), only R = La, Pr, Nd, and Sm successfully retained the A-site columnar-ordered B site rock-salt-ordered framework ($P4_2/n$). This result highlights the critical role of the modified cationic combination at A′ (Mn^{2+}/Zn^{2+}), A″ (Zn^{2+}), and B-sites (Mn^{2+}/Zn^{2+}, Sb^{5+}) in modulating structural tolerance. Consequently, this study focuses on R = La, Pr, Nd, and Sm to ensure a consistent columnar-ordered and rock-salt-ordered platform for probing magnetic interactions.

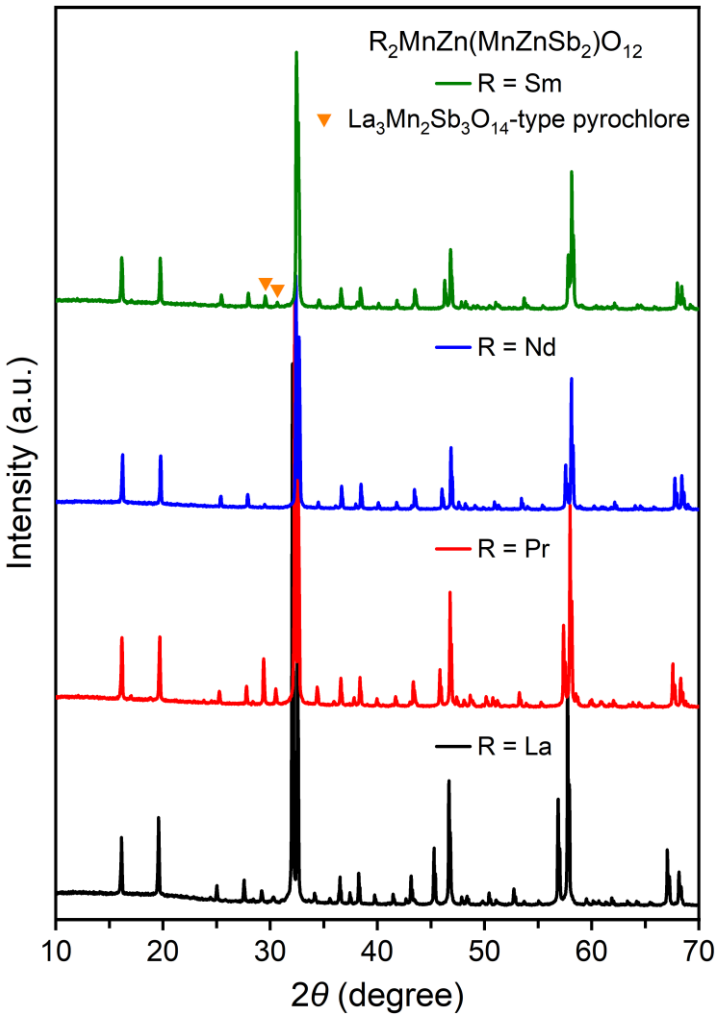

Figure 5.2 Laboratory XRPD patterns of $R_2MnZn(MnZnSb_2)O_{12}$ with R = La, Pr, Nd, and Sm. The orange triangles show characteristic peaks of $La_3Mn_2Sb_3O_{14}$-type pyrochlore impurity.

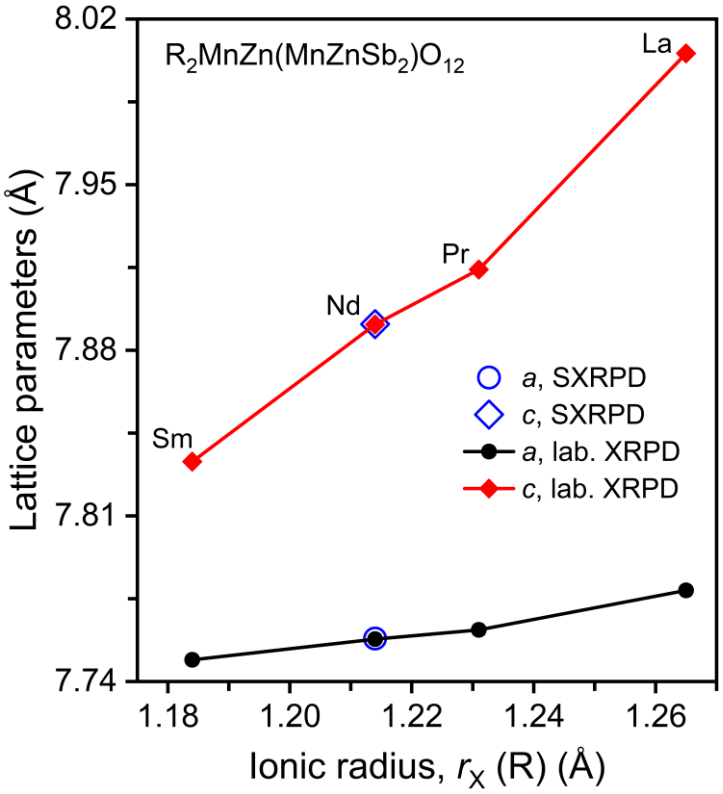

Figure 5.3 Compositional dependence of the room-temperature lattice parameters (*a* and *c*; space group $P4_2/n$) in $R_2MnZn(MnZnSb_2)O_{12}$ (R = La, Pr, Nd, Sm) as a function of the ionic radius of R^{3+} cations in the 10-fold coordination (see the text for details).

Figure 5.2 presents the laboratory XRPD patterns of $R_2MnZn(MnZnSb_2)O_{12}$ (R = La, Pr, Nd, Sm), confirming the $P4_2/n$ space group for all samples, albeit with minor $La_3Mn_2Sb_3O_{14}$-type pyrochlore impurities. As shown in **Figure 5.3**, both lattice parameters *a* and *c* decrease monotonically with reducing R^{3+} ionic radii, consistent with the expected Vegard's law behavior [33]. Since the ionic radii for most R^{3+} cations in a 10-fold coordination environment are not available, we estimated them by adding 0.105 Å to their ionic radii in an 8-fold coordination. This adjustment is based on the observed average differences in ionic radii between adjacent coordination numbers: approximately 0.055 Å between 8-fold and 9-fold coordination, and 0.05 Å between 9-fold and 10-fold (extrapolated from the trend up to 12-fold coordination) [32]. The synchrotron XRPD results of the $Nd_2MnZn(MnZnSb_2)O_{12}$ align perfectly with laboratory data, validating the structural reliability. **Figure 5.4** illustrates the crystal structure of $R_2MnZn(MnZnSb_2)O_{12}$

(R = La, Pr, Nd, Sm), representative of the A-site columnar-ordered and B-site rock-salt-ordered quadruple perovskite (space group $P4_2/n$, No. 86). In this structure, Mn/Zn (M2) and Sb atoms occupy octahedral centers, with M2/SbO_6 octahedra alternately corner-connected in a rock-salt arrangement [34]. The structure features two in-phase and one out-of-phase octahedral tilts (Glazer notation: $a^+a^+c^-$) [35], generating 10- and 4-coordinated environments around the A and A′/A″ sites, respectively [20]. Significantly, the 10-coordinated A-site RO_{10} polyhedra (right panel of **Figure 5.4**) form edge-sharing columns along the *c*-axis. The square-planar A′-site $M1O_4$ units (M1 = Mn/Zn) and tetrahedral A″-site ZnO_4 units are spatially separated but connected to the A-site RO_{10} polyhedra via edge-sharing and corner-sharing modes, respectively.

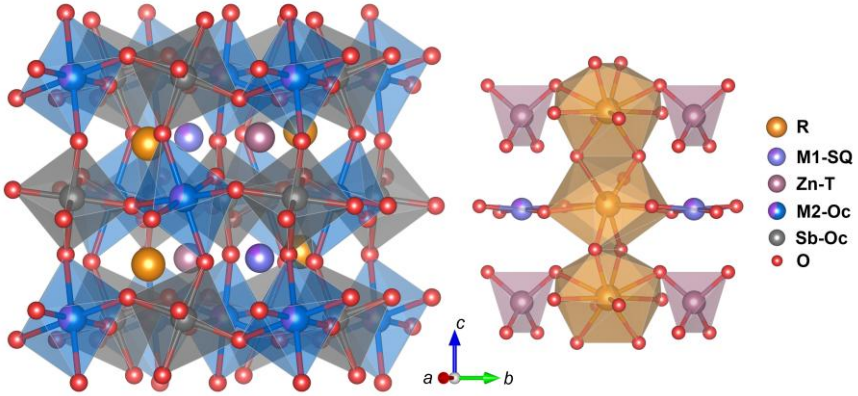

Figure 5.4 Crystal structure of $R_2MnZn(MnZnSb_2)O_{12}$ with R = La, Pr, Nd, and Sm in a polyhedral presentation. The rock-salt-type arrangement of $(Mn/Zn)O_6 = M2O_6$ and SbO_6 octahedra is shown on the left. The columnar-type arrangement of RO_{10} polyhedra, $(Mn/Zn)O_4 = M1O_4$ square planar units, and ZnO_4 tetrahedra is shown on the right.

5.3.2 Magnetic properties

The ZFC and FCC dc magnetic susceptibility susceptibility ($\chi = M/H$) curves of $R_2MnZn(MnZnSb_2)O_{12}$ (R = La, Pr, Nd, Sm) measured at 100 Oe and 10 kOe are shown in **Figures 5.5–5.6**. For the R = La sample, the ZFC and FCC curves nearly overlap at both field (no divergence), yet the $d\chi/dT$ versus T curves at 100 Oe (**Figure 5.7**) reveal a sharp peak at ordering temperature (T_C = 11 K), confirming the weak ferrimagnetic (FIM) order. In contrast, the samples containing magnetic R^{3+} (Pr, Nd, Sm) display a marked divergence between the ZFC and FCC curves at 100 Oe. The peaks in $d\chi/dT$ appear at higher temperatures—approximately 21 K for R = Pr, 18 K for R = Nd, and 23 K for R = Sm—suggesting an enhancement of the long-range T_C due to the participation of the R^{3+} (**Figure 5.7**). As shown in **Figure 5.8**, the magnetic susceptibility rapidly increases with cooling below T_C, characteristic of FIM ordering. On the other hand, the divergence persists at 10 kOe for Pr and Sm samples but with suppressed T_C. The inverse magnetic susceptibility (χ^{-1} versus T) curves followed the Curie–Weiss law at temperatures above 200 K, and were fitted by the Curie−Weiss equation (see **section 1.2.4**). The negative values of the Curie–Weiss temperature (θ = −84.4(8) to −36.8(3) K, **Table 5.3**) indicated the dominance of antiferromagnetic (AFM) interactions. The μ_{eff} align well with theoretical values (μ_{calc}) [36]. Intriguingly, the $|\theta|$ order (Sm > Nd > La > Pr) does not correlate with T_C trends (Sm > Pr > Nd > La). This discrepancy can be understood by recognizing that while $|\theta|$ reflects the average strength of AFM coupling, T_C is determined by the cooperativity of long-range order—a factor enhanced by additional exchange pathways provided by magnetic R^{3+} (Pr^{3+}, Nd^{3+}, Sm^{3+}) that are absent in nonmagnetic La^{3+}. In other words, although La exhibits a moderate $|\theta|$, its lack of extra R–O–Mn exchange channels results in a significantly lower T_C compared to the magnetic R^{3+} containing samples (discussed later).

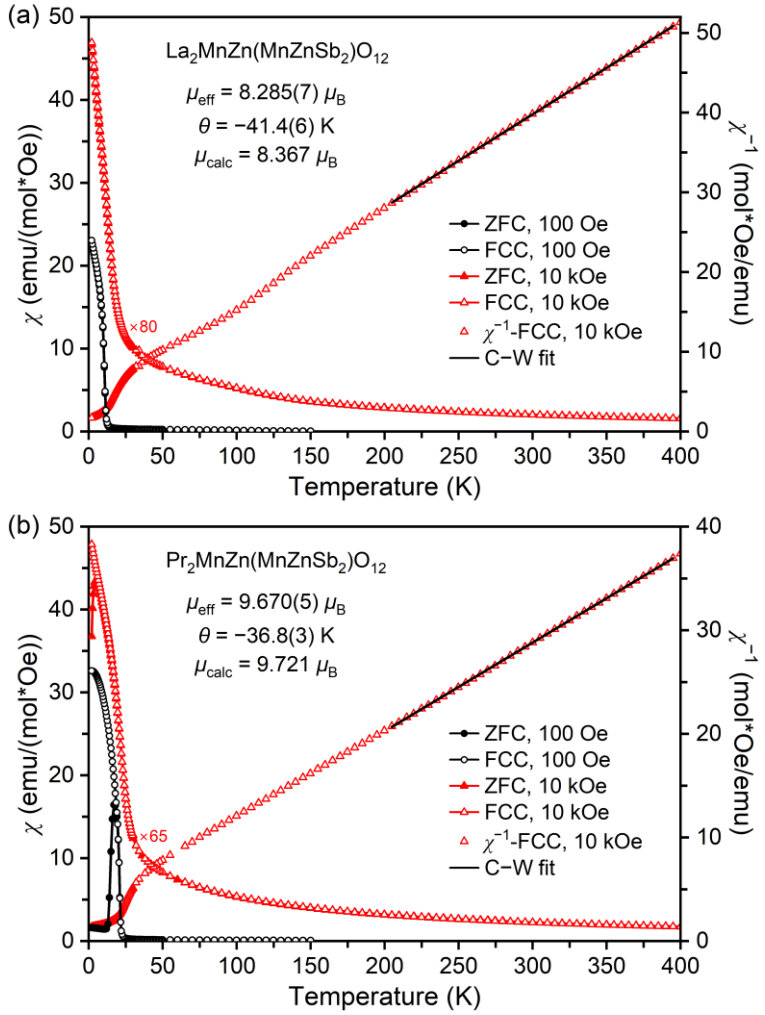

Figure 5.5 ZFC (filled symbols) and FCC (empty symbols) dc magnetic susceptibility ($\chi = M/H$) curves of (a) $La_2MnZn(MnZnSb_2)O_{12}$ and (b) $Pr_2MnZn(MnZnSb_2)O_{12}$ measured at 100 Oe (black, circles) and 10 kOe (red, triangles). The black line gives the Curie–Weiss fit (C–W fit) using the FCC χ^{-1} versus T curves at 10 kOe.

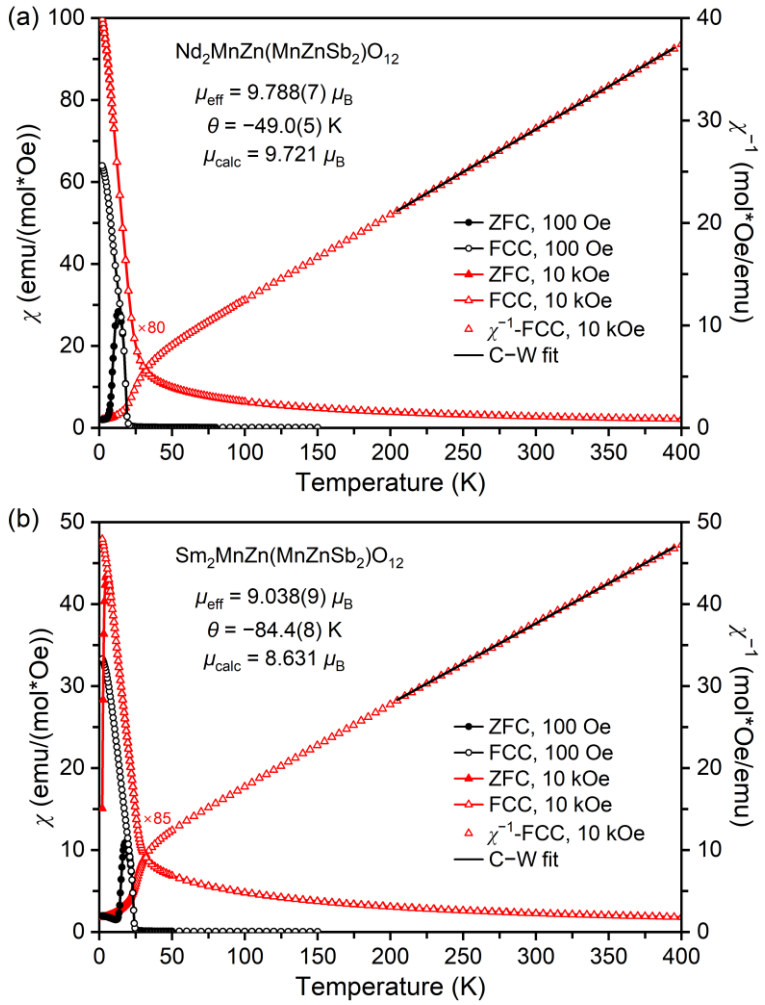

Figure 5.6 ZFC (filled symbols) and FCC (empty symbols) dc magnetic susceptibility ($\chi = M/H$) curves of (a) $Nd_2MnZn(MnZnSb_2)O_{12}$ and (b) $Sm_2MnZn(MnZnSb_2)O_{12}$ measured at 100 Oe (black, circles) and 10 kOe (red, triangles). The black line gives the Curie–Weiss fit (C–W fit) using the FCC χ^{-1} versus T curves at 10 kOe.

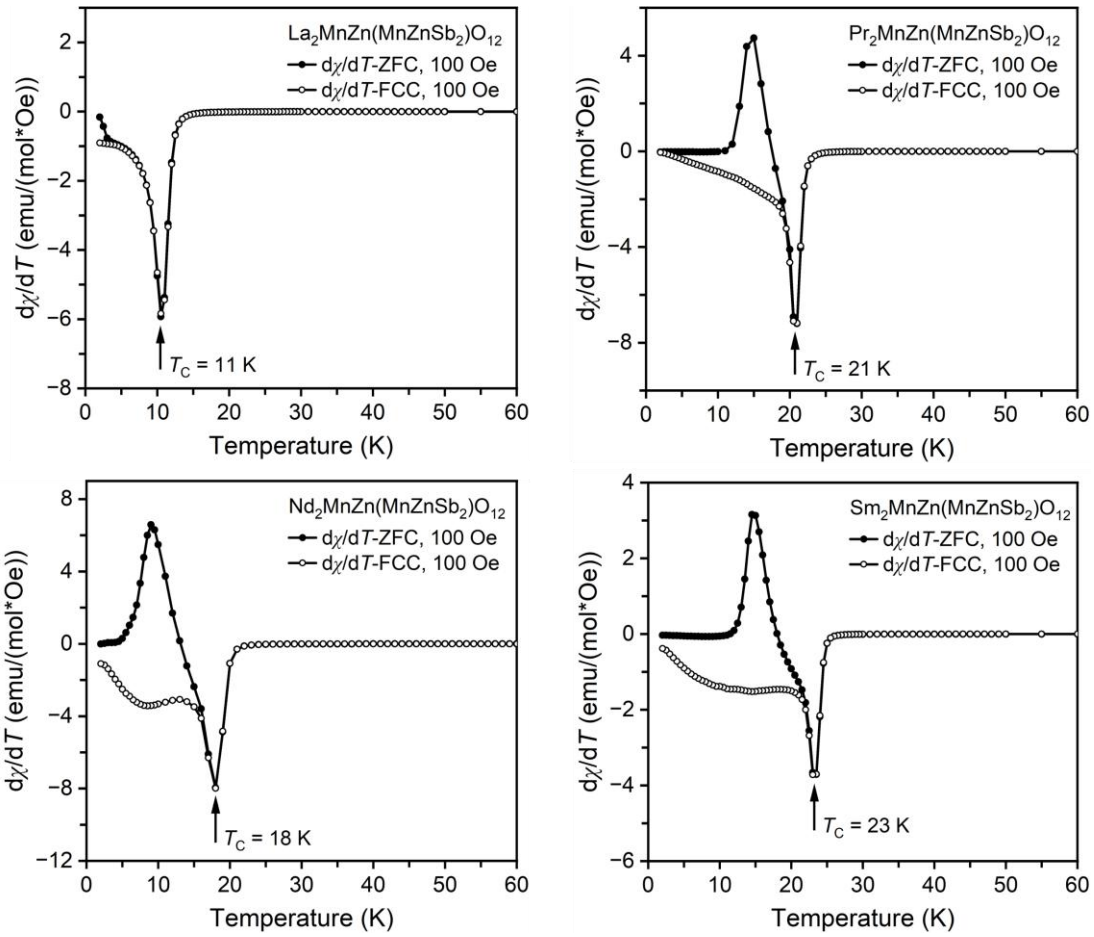

Figure 5.7 ZFC and FCC dχ/dT versus T curves of $R_2MnZn(MnZnSb_2)O_{12}$ with R = La, Pr, Nd, and Sm at 100 Oe.

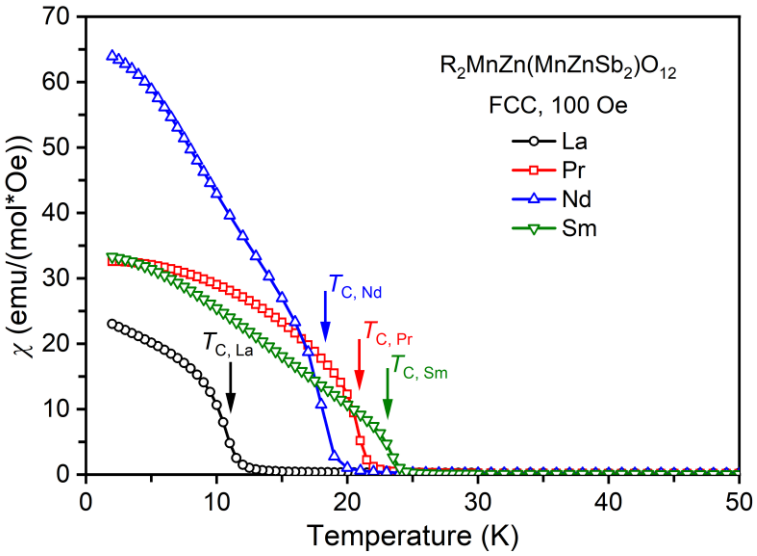

Figure 5.8 Comparison of FCC dc magnetic susceptibility (χ = M/H) curves of $R_2MnZn(MnZnSb_2)O_{12}$ with R = La, Pr, Nd, and Sm measured at 100 Oe.

Table 5.3 Temperatures of magnetic anomalies (T_C), parameters of Curie–Weiss fits, and parameters of M versus H curves at T = 5 K for $R_2MnZn(MnZnSb_2)O_{12}$.

R	T_C (K)	μ_{eff} (μ_B/f.u.)	μ_{calc} (μ_B/f.u.)	θ (K)	M_S (μ_B/f.u.)	M_R (μ_B/f.u.)	H_C (kOe)
La	11	8.285(7)	8.367	–41.4(6)	2.11	0.195	0.063
Pr	21	9.670(5)	9.721	–36.8(3)	3.23	0.800	3.102
Nd	18	9.788(7)	9.721	–49.0(5)	3.73	1.222	0.286
Sm	23	9.038(9)	8.631	–84.4(8)	1.96	0.737	3.765

Curie–Weiss fits were performed between 200 and 395 K (or 200 and 295 K) using the FCC χ^{-1} versus T data at 10 kOe.

M_S is the magnetization value at T = 5 K and H = 70 kOe.

M_R is the remnant magnetization at T = 5 K.

H_C is the coercive field at T = 5 K.

T_C is determined from sharp peaks on the 100 Oe FCC dχ/dT versus T curves.

Isothermal magnetization curves (*M* versus *H*) for the four samples at different temperatures is illustrated in **Figure 5.9** as an example, it exhibits pronounced hysteresis below T_C, with loop size diminishing upon warming and vanishing above T_C, consistent with temperature-dependent magnetic anisotropy. The *M* versus *H* curves of all samples at 5 K are shown in **Figure 5.10** and parameters are summarized in **Table 5.3**; they demonstrated step-like hysteresis with small coercive fields H_C (0.063 kOe to 3.765 kOe) which is typical for FIM materials. All samples display non-saturating M_S up to 70 kOe, indicative of predominant AFM coupling. This aligns with the negative θ values and mirrors behavior in related columnar-ordered perovskites [21, 22].

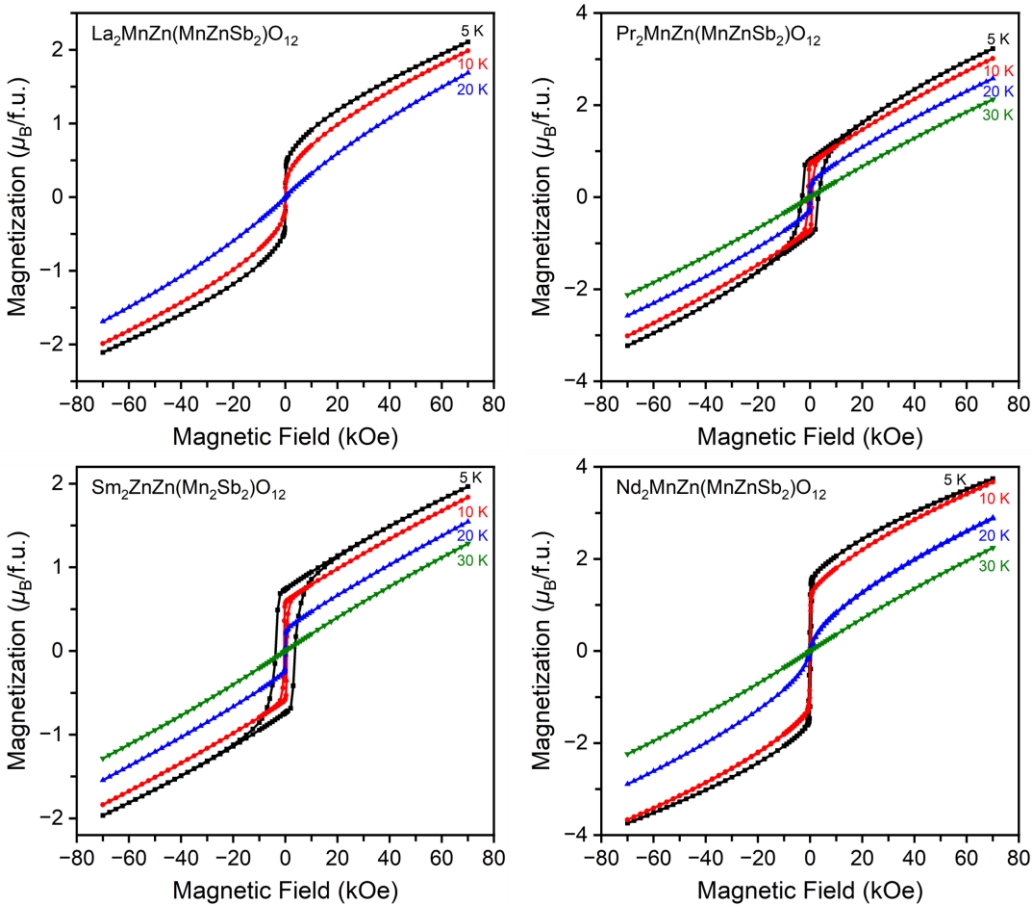

Figure 5.9 *M* versus *H* curves of $R_2MnZn(MnZnSb_2)O_{12}$ with R = La, Pr, Nd, and Sm at different temperatures.

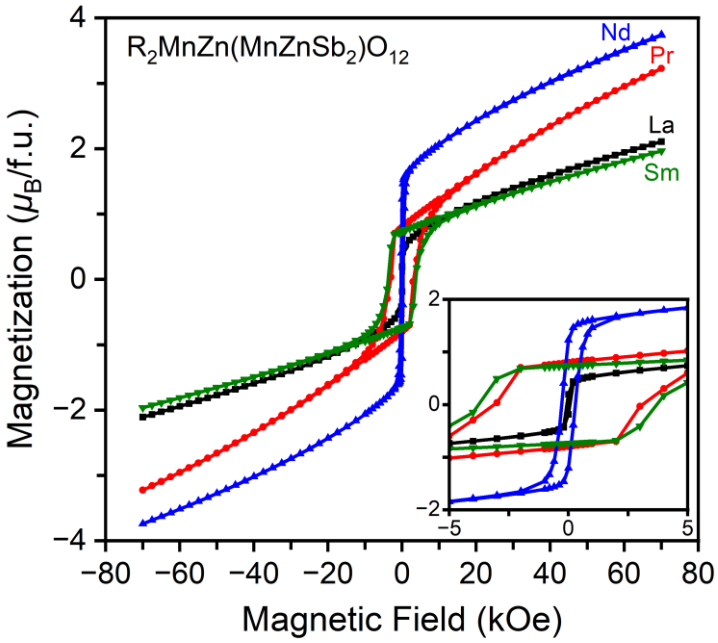

Figure 5.10 Comparison of *M* versus *H* curves of $R_2MnZn(MnZnSb_2)O_{12}$ with R = La, Pr, Nd, and Sm measured at *T* = 5 K.

5.3.3 Heat capacity

The specific heat (C_p) data of $R_2MnZn(MnZnSb_2)O_{12}$ (R = La, Pr, Nd, Sm) measured at *H* = 0 and 90 kOe for are shown in **Figures 5.11**–**5.12**. Pronounced anomalies at respective T_C confirm the presence of long-range magnetic ordering, reflecting entropy accumulation during the disorder-to-order transition. At higher temperatures, C_p capacity is predominantly due to lattice vibrations, whereas at lower temperatures magnetic excitations dominate. To isolate the magnetic contribution (C_{mag}), the lattice contribution ($C_{lattice}$) was estimated using the C_p data of $Nd_2ZnZn(Zn_2Sb_2)O_{12}$—a compound with the same structure but nonmagnetic A′, A″, and B sites and paramagnetic behavior down to 2 K (unpublished data; **Figures 5.13**–**5.14**). C_{mag} was calculated as $C_p - C_{lattice}$, and the magnetic entropy (S_{mag}) was obtained by integrating C_{mag}/T. For La sample (nonmagnetic R^{3+}), the theoretical S_{mag} arises solely from two Mn^{2+} ions ($J = 5/2$, $R\ln(2J + 1) = R\ln 6 \approx$ 14.9 J K^{-1} mol^{-1} per Mn, where R = 8.314 J K^{-1} mol^{-1} is the universal gas constant), yielding a total of 29.8 J K^{-1} mol^{-1}. As shown in **Figure 5.15**, the experimental S_{mag} for all samples gradually increases at low temperatures, nearing saturation around 80 K. At

T = 80 K, S_{mag} for $La_2MnZn(MnZnSb_2)O_{12}$ is 23.2 J K^{-1} mol^{-1}, this value reaches ~78% of the expected Boltzmann entropy, suggesting incomplete entropy release due to short-range correlations or crystal field effects, as observed in canted AFM systems.

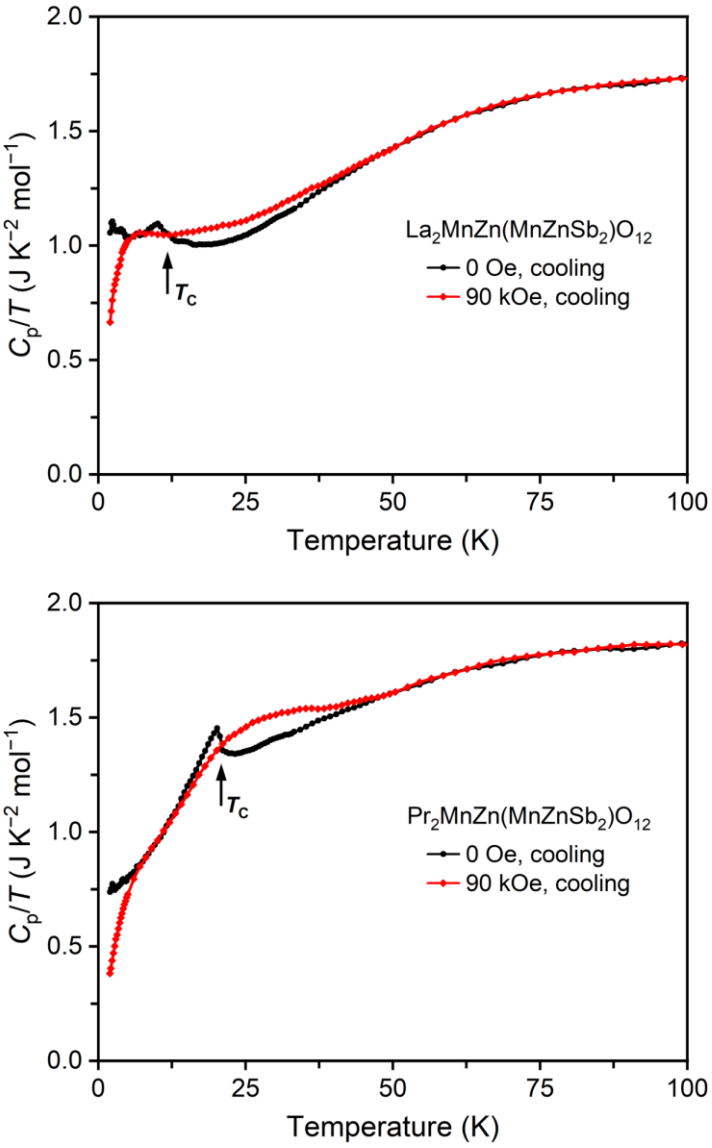

Figure 5.11 Specific heat data of $R_2MnZn(MnZnSb_2)O_{12}$ with R = La and Pr plotted as Cp/T versus T at H = 0 and 90 kOe during cooling.

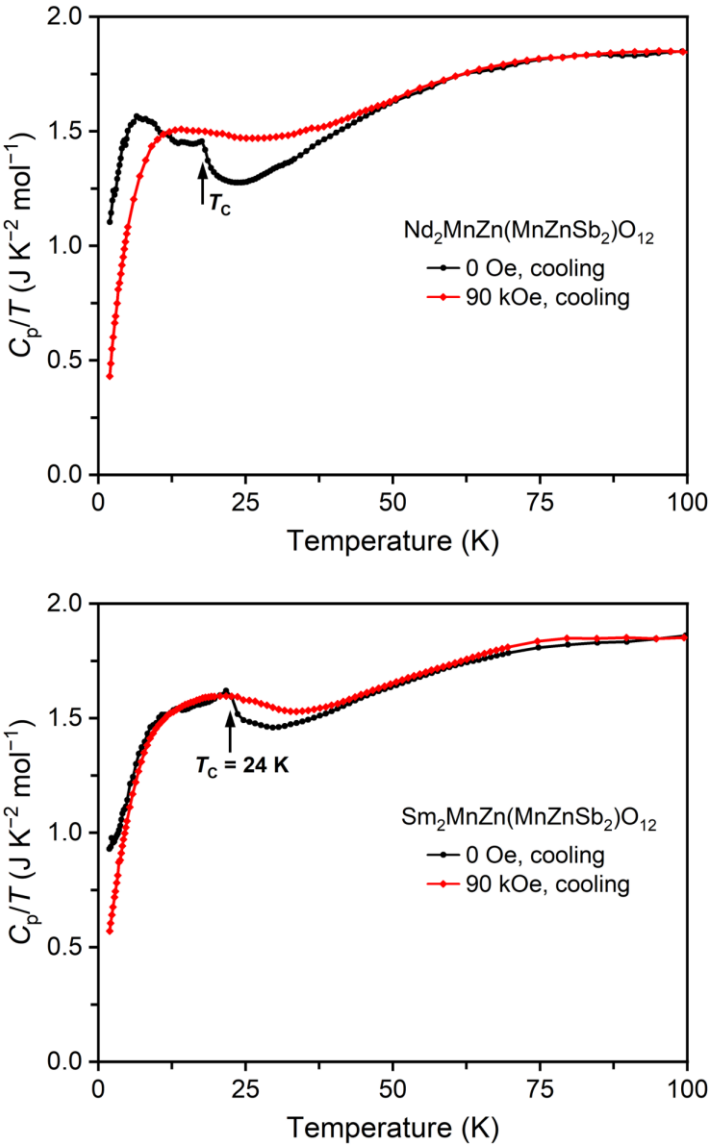

Figure 5.12 Specific heat data of $R_2MnZn(MnZnSb_2)O_{12}$ with R = Nd and Sm plotted as *C*p/*T* versus *T* at *H* = 0 and 90 kOe during cooling.

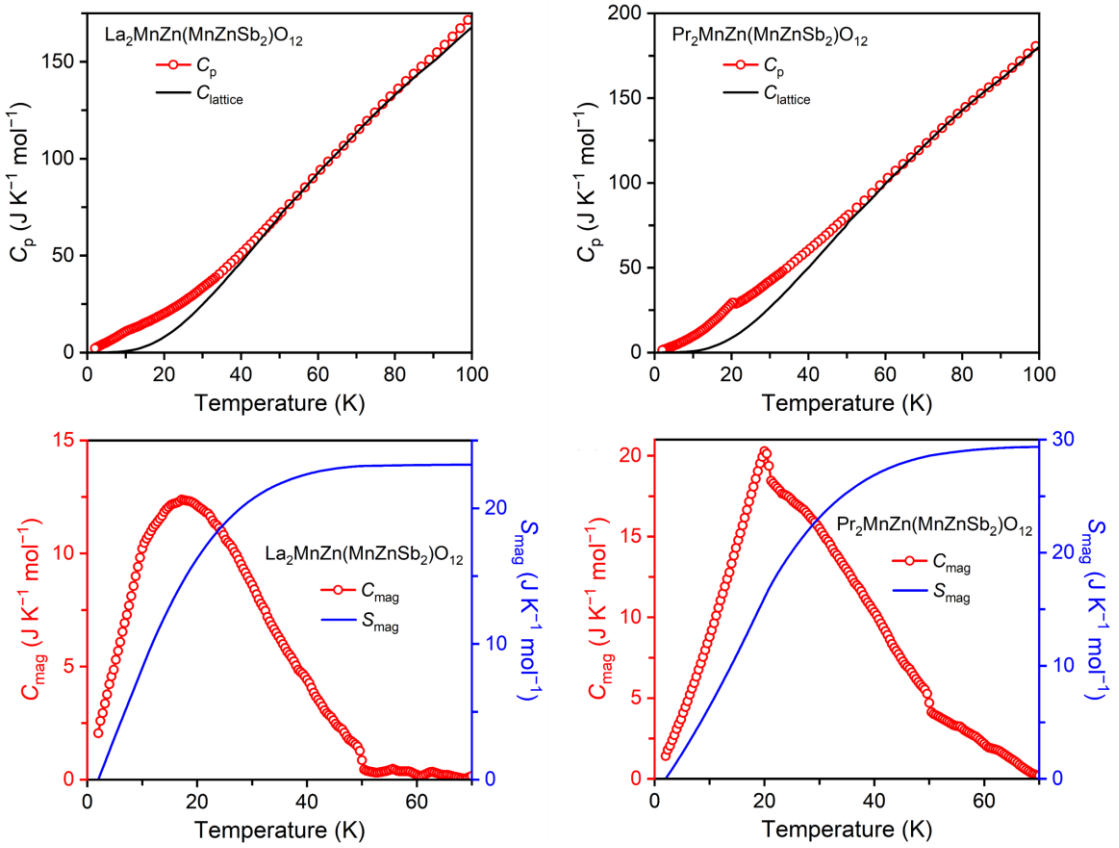

Figure 5.13 The heat capacity of $R_2MnZn(MnZnSb_2)O_{12}$ with R = La and Pr as a function of temperature (upper panels). The black line shows the estimated lattice contribution. Temperature dependences of the magnetic contribution to the heat capacity (C_{mag}) and the magnetic entropy (S_{mag}) of $R_2MnZn(MnZnSb_2)O_{12}$ with R = La and Pr (lower panels).

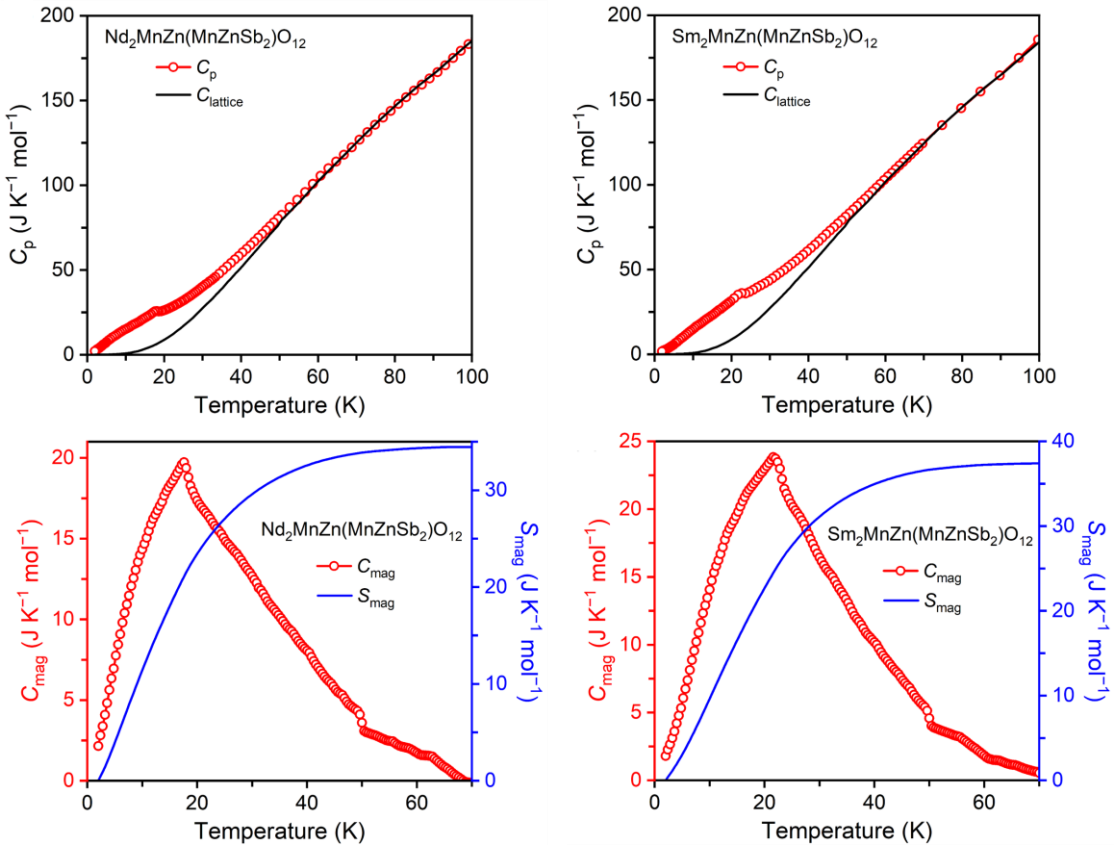

Figure 5.14 The heat capacity of $R_2MnZn(MnZnSb_2)O_{12}$ with R = Nd and Sm as a function of temperature (upper panels). The black line shows the estimated lattice contribution. Temperature dependences of the magnetic contribution to the heat capacity (C_{mag}) and the magnetic entropy (S_{mag}) of $R_2MnZn(MnZnSb_2)O_{12}$ with R = Nd and Sm (lower panels).

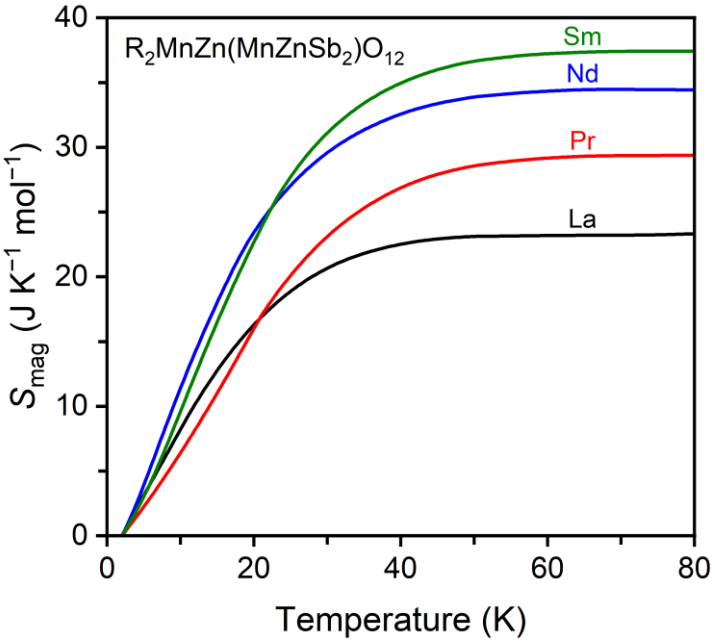

Figure 5.15 Comparison of temperature dependence of the magnetic entropy (S_{mag}) of $R_2MnZn(MnZnSb_2)O_{12}$ (R = La, Pr, Nd, Sm).

Table 5.4 Theoretical and experimental magnetic entropy (S_{mag}) values (J K^{-1} mol^{-1}) with contributions from R^{3+} ions for $R_2MnZn(MnZnSb_2)O_{12}$ and their enhancements (ΔS_{mag}) over the La sample.

R	R^{3+} contribution	theoretical S_{mag}	experimental S_{mag}	ΔS_{mag}
La	-	29.8	23.2	-
Pr	36.4	66.2	29.3	6.1
Nd	38.2	68.0	34.5	11.3
Sm	29.8	59.6	37.4	14.2

For Pr, Nd, and Sm samples (**Table 5.4**), the theoretical S_{mag} includes contributions from both Mn^{2+} and R^{3+} ions (Pr^{3+}: $J = 4$, $R\ln 9 \approx 18.2$; Nd^{3+}: $J = 9/2$, $R\ln 10 \approx 19.1$; Sm^{3+}: $J = 5/2$, $R\ln 6 \approx 14.9$ J K^{-1} mol^{-1}). The experimental values (Pr: 29.3; Nd: 34.5; Sm: 37.4 J K^{-1} mol^{-1}) fall below theoretical sums (Pr: 66.2; Nd: 68.0; Sm: 59.6 J K^{-1} mol^{-1}) but show significant enhancements over La sample. Notably, Sm sample exhibits the largest S_{mag} increment compared with La sample (ΔS_{mag} = 14.2 J K^{-1} mol^{-1}), while Pr and Nd samples show smaller yet distinct gains (ΔS_{mag} = 6.1–11.3 J K^{-1} mol^{-1}). Thus, the data

indicate that the magnetic R^{3+} ions (Pr^{3+}, Nd^{3+}, Sm^{3+}) play a significant role in enhancing the long-range magnetic order, as evidenced by both the higher T_C values and increased S_{mag}. The systematic increase in S_{mag} from La to Sm underscores the impact of the additional R–O–Mn exchange interactions, which, despite some entropy loss, contribute to the stabilization of the ordered state.

5.3.4 Discussion

In isostructural $P4_2/n$ $Nd_2MnMn(Mn_2Sb_2)O_{12}$ [37], the Mn^{2+} ions at the A′ and A″ sites are connected only indirectly via NdO_{10} polyhedra, whereas the B-site Mn^{2+} ions interact solely through Mn_B–O–Sb–O–Mn_B supersuperexchange pathways. Therefore, neither the Mn^{2+} ions within the A′/A″ sublattice nor those within the B-site sublattice can establish effective direct magnetic interactions among themselves. Neutron powder diffraction studies reveal that, despite the lack of direct bridging oxygen, the Mn^{2+} ions at the A′ and A″ sites exhibit a parallel alignment. In contrast, the B-site Mn^{2+} ions are directly connected to those at the A′/A″ sites via oxygen, leading to their AFM coupling and thereby establishing an overall FIM framework. In current $R_2MnZn(MnZnSb_2)O_{12}$ system, nonmagnetic Zn^{2+} is substituted at the A″ and B sites, resulting in complete replacement of Mn^{2+} at the A″ site and reducing the B-site Mn^{2+} occupancy. This modification eliminates the original A′–A″ ferromagnetic (FM) correlation and renders the A′–B AFM exchange ($Mn_{A'}$–O–Mn_B) dominant. Consequently, the overall magnetic coupling is weakened (with T_C decreasing from 76 K in the parent system to 18 K (Nd sample) and a significant reduction in the C_p anomaly) [21, 37], producing a more "pure" FIM network. This simplified exchange scheme amplifies the influence of the rare-earth ions on the magnetic properties.

In $R_2MnZn(MnZnSb_2)O_{12}$ system, the 10-coordinate R^{3+} ions at the A site, together with the Mn^{2+} ions at the A′ and B sites, are interconnected through oxygen (see **Figure 5.4**). When magnetic R^{3+} ions (Pr^{3+}, Nd^{3+}, Sm^{3+}) are introduced, two additional superexchange channels become operative. First, an R–O–$Mn_{A'}$ pathway establishes an AFM exchange between the R^{3+} ion and the Mn^{2+} ions at the A′ site. Second, an R–O–Mn_B pathway can mediate a FM exchange with the B-site Mn^{2+} ions—likely facilitated by local structural distortions such as tilted octahedra. The strength of these interactions depends on the effective hybridization between the R 4*f* orbitals and the Mn 3*d* orbitals

via oxygen [15, 38, 39]. Together, these "dual" exchange pathways compensate for the intrinsic competition within the $Mn_{A'}$–O–Mn_B network and remarkably enhance the stability of the long-range magnetic order at higher temperatures. It is noteworthy that although Pr^{3+} (3.5 μ_B) and Nd^{3+} (3.5 μ_B) possess larger magnetic moments than Sm^{3+} (1.5 μ_B) [36], the highest T_C is observed for the Sm sample. This disparity indicates that the enhancement in T_C is not determined solely by the magnitude of the R^{3+} ion's magnetic moment but is critically influenced by its anisotropy and by the effectiveness of the additional R–O–Mn exchange channels.

Specifically, in the La sample, the nonmagnetic La^{3+} (with an empty 4*f* shell) contributes no extra exchange, so its magnetic properties rely solely on the $Mn_{A'}$–O–Mn_B interactions—resulting in lower T_C and S_{mag}. In contrast, Sm^{3+} exhibits strong spin–orbit coupling and a partially unquenched orbital moment, leading to significant magnetic anisotropy. Moreover, in $SmMnO_3$ and $SmFeO_3$, Sm has been shown to exhibit pronounced magnetic anisotropy and high coercivity [40-42], and the dependence of the Sm 4*f* charge distribution on its strong magnetic anisotropy has also been discussed in Sm-containing alloys [43, 44]. This anisotropy not only stabilizes the magnetic structure but also enhances both the R–O–$Mn_{A'}$ and R–O–Mn_B exchanges, yielding the highest T_C and S_{mag}. Although Pr^{3+} and Nd^{3+} have larger moments, their magnetic anisotropy is moderate due to less pronounced crystal field effects compared to Sm^{3+} [45-47]; nevertheless, they effectively strengthen the magnetic exchange relative to La, albeit not to the extent observed for Sm^{3+}. Collectively, these findings demonstrate that in these quadruple perovskites the enhancement of long-range magnetic order and the associated increases in T_C and S_{mag} upon substituting magnetic R^{3+} ions arise primarily from the establishment of additional R–O–Mn exchange pathways rather than from the R^{3+} ion's moment size alone.

5.4 Summary of chapter 5

The high-pressure synthesis of A-site columnar and B-site rock-salt ordered quadruple perovskites $R_2MnZn(MnZnSb_2)O_{12}$ (R = La, Pr, Nd, Sm) reveals a unique magnetic framework. Synchrotron XRPD confirms the $P4_2/n$ structure for the Nd sample, with Zn^{2+} selectively occupying the tetrahedral A″ site and one octahedral B site (alongside Mn^{2+}), while Sb^{5+} fully occupies the second B site. Zn^{2+} substitution eliminates

the intrinsic A′-A″ Mn^{2+} ferromagnetic correlation in parent systems, simplifying the magnetic network to A′-B antiferromagnetic exchange. Despite antisite disorder and low Mn^{2+}, all samples exhibit long-range ferrimagnetic order, with magnetic rare-earth ions (Pr^{3+}, Nd^{3+}, Sm^{3+}) significantly enhancing T_C (La: 11 K → Sm: 23 K). This enhancement originates from R^{3+}-mediated superexchange via 4*f*–3*d* orbital hybridization, where Sm^{3+} achieves the highest T_C and coercivity (H_C = 3.765 kOe) due to strong magnetic anisotropy. These findings advance the design of magnetostructurally coupled oxides for spintronic and magnetocaloric applications, emphasizing the untapped potential of rare-earth-mediated exchange in functional ceramics.

References in chapter 5

[1] N. A. Spaldin; R. Ramesh. Advances in magnetoelectric multiferroics. *Nat. Mater.* **2019**, *18*, 203–212.

[2] A. A. Belik. Hybrid multiferroic behavior in the double perovskite $(Ca_{0.5}Mn_{1.5})MnWO_6$. *Chem. Mater.* **2024**, *36*, 7604–7609.

[3] Q. Wang; Q. Wu; H. Cheng; X. Li; N. Yu; M. Pan; Y. Yu; J. Fang; X. Hu; H. Ge; H. Yang. Review of the research on oxides in low-temperature magnetic refrigeration. *J. Eur. Ceram. Soc.* **2023**, *43*, 6665–6680.

[4] C. Artini. Crystal chemistry, stability and properties of interlanthanide perovskites: A review. *J. Eur. Ceram. Soc.* **2017**, *37*, 427–440.

[5] K. Lin; Q. Li; R. Yu; J. Chen; J. P. Attfield; X. Xing. Chemical pressure in functional materials. *Chem. Soc. Rev.* **2022**, *51*, 5351–5364.

[6] M. Azuma; I. Yamada; K. Yamaura; A. A. Belik; T. Yamamoto; M. Fukuda. High pressure studies of transition metal oxides. In *Comprehensive Inorganic Chemistry III*, Reedijk, J., Poeppelmeier, K. R. Eds.; Vol. 4; Elsevier, 2023; pp 681–718.

[7] A. N. Vasil'ev; O. S. Volkova. New functional materials $AC_3B_4O_{12}$ (Review). *Low Temp. Phys.* **2007**, *33*, 895–914.

[8] J. Ding; X. Zhu. Research progress on quadruple perovskite oxides. *J. Mater. Chem. C* **2024**, *12*, 9510–9561.

[9] A. A. Belik; R. D. Johnson; D. D. Khalyavin. The rich physics of A-site-ordered quadruple perovskite manganites AMn_7O_{12}. *Dalton Trans.* **2021**, *50*, 15458–15472.

[10] H. Okamoto; M. Karppinen; H. Yamauchi; H. Fjellvåg. High-temperature synchrotron X-ray diffraction study of $LaMn_7O_{12}$. *Solid State Sciences* **2009**, *11*, 1211–1215.

[11] F. Mezzadri; M. Calicchio; E. Gilioli; R. Cabassi; F. Bolzoni; G. Calestani; F. Bissoli. High-pressure synthesis and characterization of $PrMn_7O_{12}$ polymorphs. *Phys. Rev. B* **2009**, *79*, 014420.

[12] A. A. Belik; R. Liu; L. Zhang; N. Terada; M. Tanaka; K. Yamaura. Multiple magnetic transitions and complex magnetic behaviour of the perovskite manganite $NdMn_7O_{12}$. *J. Solid State Chem.* **2022**, *309*, 122969.

[13] A. Prodi; E. Gilioli; R. Cabassi; F. Bolzoni; F. Licci; Q. Huang; J. W. Lynn; M.

Affronte; A. Gauzzi; M. Marezio. Magnetic structure of the high-density single-valent e_g Jahn-Teller system $LaMn_7O_{12}$. *Phys. Rev. B* **2009**, *79*, 085105.

[14] L. Zhang; N. Terada; R. D. Johnson; D. D. Khalyavin; P. Manuel; Y. Katsuya; M. Tanaka; Y. Matsushita; K. Yamaura; A. A. Belik. High-Pressure synthesis, structures, and properties of trivalent A-site-ordered quadruple perovskites RMn_7O_{12} (R = Sm, Eu, Gd, and Tb). *Inorg. Chem.* **2018**, *57*, 5987–5998.

[15] R. D. Johnson; D. D. Khalyavin; P. Manuel; L. Zhang; K. Yamaura; A. A. Belik. Magnetic structures of the rare-earth quadruple perovskite manganites RMn_7O_{12}. *Phys. Rev. B* **2018**, *98*, 104423.

[16] M. Verseils; F. Mezzadri; D. Delmonte; B. Baptiste; Y. Klein; S. Shcheka; L. C. Chapon; T. Hansen; E. Gilioli; A. Gauzzi. Effect of chemical pressure induced by La^{3+} /Y^{3+} substitution on the magnetic ordering of $(AMn_3)Mn_4O_{12}$ quadruple perovskites. *Phys. Rev. Mater.* **2017**, *1*, 064407.

[17] N. Imamura; M. Karppinen; T. Motohashi; D. Fu; M. Itoh; H. Yamauchi. Positive and negative magnetodielectric effects in A-site ordered $(BiMn_3)Mn_4O_{12}$ perovskite. *J. Am. Chem. Soc.* **2008**, *130*, 14948–14949.

[18] R. Scatena; R. Liu; V. V. Shvartsman; D. D. Khalyavin; Y. Inaguma; K. Yamaura; A. A. Belik; R. D. Johnson. Hybrid improper ferroelectricity in columnar $(NaY)MnMnTi_4O_{12}$. *Angew. Chem. Int. Ed.* **2023**, *62*, e202305994.

[19] K. Leinenweber; J. Parise. High-pressure synthesis and crystal structure of $CaFeTi_2O_6$, a new perovskite structure type. *J. Solid State Chem.* **1995**, *114*, 277–281.

[20] A. A. Belik. Rise of A-site columnar-ordered $A_2A'A''B_4O_{12}$ quadruple perovskites with intrinsic triple order. *Dalton Trans.* **2018**, *47*, 3209–3217.

[21] X. Liang; K. Yamaura; A. A. Belik. B-site ordered and disordered phases in A-site columnar-ordered quadruple perovskites $Nd_2MnMn(Mn_{4-x}Sb_x)O_{12}$. *Ceram. Int.* **2024**, *50*, 53099–53106.

[22] X. Liang; K. Yamaura; A. Belik. Three perovskite phases with different cation orders in $Sm_2MnMn(Mn_{4-x}Sb_x)O_{12}$. *Chem. - Eur. J.* **2024**, *30*, e202401960.

[23] A. M. Vibhakar; D. D. Khalyavin; P. Manuel; R. Liu; K. Yamaura; A. A. Belik; R. D. Johnson. Effects of magnetic dilution in the ferrimagnetic columnar ordered $Sm_2MnMnMn_{4-x}Ti_xO_{12}$ perovskites. *Phys. Rev. B* **2020**, *102*, 214428.

[24] S. Kawaguchi; M. Takemoto; K. Osaka; E. Nishibori; C. Moriyoshi; Y. Kubota; Y. Kuroiwa; K. Sugimoto. High-throughput powder diffraction measurement system consisting of multiple MYTHEN detectors at beamline BL02B2 of SPring-8. *Rev. Sci. Instrum.* **2017**, *88*, 085111.

[25] F. Izumi; T. Ikeda. A Rietveld-Analysis Programm RIETAN-98 and its Applications to Zeolites. *Mater. Sci. Forum* **2000**, *321–324*, 198–205.

[26] W. T. Fu; D. J. W. Ijdo. Crystal structure of $Mn_2Ln_3Sb_3O_{14}$ (*Ln*=La, Pr and Nd): A new ordered rhombohedral pyrochlore. *J. Solid State Chem.* **2014**, *213*, 165–168.

[27] N. E. Brese; M. O'Keeffe. Bond-valence parameters for solids. *Acta Crystallogr. Sect. B* **1991**, *47*, 192–197.

[28] A. A. Belik; R. Liu; K. Yamaura. Spin-glass to long-range order to spin-glass evolution of magnetic properties with the composition in $Sm_2MnZnMn_{4-x}Ti_xO_{12}$ (x = 1, 2, and 3) perovskites. *J. Alloy. Compd.* **2023**, *932*, 167727.

[29] A. A. Belik; R. Liu; K. Yamaura. Realization of triple A-site cation ordering through the Dy/Mn/Zn combination in the ferrimagnetic $Dy_2MnZnMn_{4-x}Ti_xO_{12}$ perovskites. *Ceram. Int.* **2023**, *49*, 14327–14334.

[30] L. Zhang; Y. Matsushita; K. Yamaura; A. A. Belik. Five-fold ordering in high-pressure perovskites RMn_3O_6 (R = Gd–Tm and Y). *Inorg. Chem.* **2017**, *56*, 5210–5218.

[31] A. A. Belik; L. Zhang; R. Liu; D. D. Khalyavin; Y. Katsuya; M. Tanaka; K. Yamaura. Valence variations by B-site doping in A-site columnar-ordered quadruple perovskites $Sm_2MnMn(Mn_{4-x}Ti_x)O_{12}$ with $1 \leq x \leq 3$. *Inorg. Chem.* **2019**, *58*, 3492–3501.

[32] R. Shannon. Revised effective ionic radii and systematic studies of interatomic distances in halides and chalcogenides. *Acta Crystallogr. Sect. A* **1976**, *32*, 751–767.

[33] L. Vegard. Die Konstitution der Mischkristalle und die Raumfüllung der Atome. *Z. Physik* **1921**, *5*, 17–26.

[34] G. King; P. M. Woodward. Cation ordering in perovskites. *J. Mater. Chem.* **2010**, *20*, 5785–5796.

[35] A. M. Glazer. The classification of tilted octahedra in perovskites. *Acta Crystallogr. Sect. B* **1972**, *28*, 3384−3392.

[36] C. Kittel. *Introduction to Solid State Physics*; John Wiley & Sons, 2005.

[37] E. Solana-Madruga; A. M. Arevalo-Lopez; A. J. Dos Santos-Garcia; E. Urones-Garrote; D. Avila-Brande; R. Saez-Puche; J. P. Attfield. Double double cation order in the high-pressure perovskites $MnRMnSbO_6$. *Angew. Chem. Int. Ed.* **2016**, *55*, 9340–9344.

[38] B. H. Kim; B. I. Min. Nearest and next-nearest superexchange interactions in orthorhombic perovskite manganites $R$$MnO_3$ (R=rare earth). *Phys. Rev. B* **2009**, *80*, 064416.

[39] M. Mochizuki; N. Furukawa. Microscopic model and phase diagrams of the multiferroic perovskite manganites. *Phys. Rev. B* **2009**, *80*, 134416.

[40] J.-S. Jung; A. Iyama; H. Nakamura; M. Mizumaki; N. Kawamura; Y. Wakabayashi; T. Kimura. Magnetocapacitive effects in the Néel N-type ferrimagnet $SmMnO_3$. *Phys. Rev. B* **2010**, *82*, 212403.

[41] A. Ali Khan; A. Ahlawat; P. Deshmukh; R. K. Sharma; VelagaSrihari; R. Singh; R. Vaish; A. K. Karnal; S. Satapathy. Effect of AFM and FM exchange interaction on magnetic anisotropy properties of single domain $SmFeO_3$ at nanoscale. *J. Magn. Magn. Mater.* **2020**, *502*, 166505.

[42] D. Amoroso; B. Dupé; M. J. Verstraete. Unraveling the role of Sm 4*f* electrons in the magnetism of $SmFeO_3$. *Phys. Rev. B* **2023**, *107*, 104427.

[43] B. Das; R. Choudhary; R. Skomski; B. Balasubramanian; A. K. Pathak; D. Paudyal; D. J. Sellmyer. Anisotropy and orbital moment in Sm-Co permanent magnets. *Phys. Rev. B* **2019**, *100*, 024419.

[44] R. Skomski; D. J. Sellmyer. Anisotropy of rare-earth magnets. *J. Rare Earth* **2009**, *27*, 675–679.

[45] A. A. Mukhin; V. Y. Ivanov; V. D. Travkin; A. M. Balbashov. Magnetic anisotropy and ground state of the rare-earth ions in $PrMnO_3$ and $NdMnO_3$. *J. Magn. Magn. Mater.* **2001**, *226–230*, 1139–1141.

[46] P. Novak; K. Knizek; M. Marysko; Z. Jirak; J. Kunes. Crystal field and magnetism of Pr^{3+} and Nd^{3+} ions in orthorhombic perovskites. *J. Phys.: Condens. Matter* **2013**, *25*, 446001.

[47] J. Hemberger; M. Brando; R. Wehn; V. Y. Ivanov; A. A. Mukhin; A. M. Balbashov; A. Loidl. Magnetic properties and specific heat of $R$$MnO_3$ (R=Pr, Nd). *Phys. Rev. B* **2004**, *69*, 064418.

Chapter 6 General conclusions and future prospects

6.1 General conclusions

This study presents a systematic study of the A-site columnar ordered quadruple perovskites $R_2MnM(MnMSb_2)O_{12}$ (R is a rare earth element, M = Mn or Zn), focusing on their structural evolution, cation ordering, and complex magnetic properties behaviors driven by aliovalent doping and rare-earth substitution. All compounds were successfully synthesized using high-pressure high-temperature (HPHT) techniques, which are essential to stabilize these highly ordered and dense perovskite phases that are inaccessible under ambient conditions.

Chapter 3 studies the solid solution $Nd_2MnMn(Mn_{4-x}Sb_x)O_{12}$, where it was shown that the controllable regulation of the Mn oxidation state can be achieved by introducing aliovalent doping of Sb^{5+}, and two different B-site ordered structure regions could be obtained: a B-site disordered structure (space group $P4_2/nmc$) is formed in the range of $0.8 \leq x \leq 1.0$, and it is transformed into a rock-salt type ordered structure (space group $P4_2/n$) when $1.6 \leq x \leq 2.0$. Magnetic transition temperature (T_C) shows different trends with the change of x value, revealing the complex coupling relationship between cation order and magnetic interaction.

Chapter 4 shifts its focus to the Ce-based compounds $Ce_2MnM(Mn_2Sb_2)O_{12}$ (M = Mn, Zn), which contain the maximum amount of Sb and exhibit a remarkable negative magnetization effect (NME) under low-field field-cooled conditions. full rock-salt B-site ordering, and bond-valence sum calculations supported the presence of Ce^{3+}. The single magnetic transition observed in both compounds showed composition-dependent compensation points, suggesting that NME is closely related to their ferrimagnetic structures.

Chapter 5 extends the study to a new series $R_2MnZn(MnZnSb_2)O_{12}$ (R = La, Pr, Nd, and Sm), highlighting the influence of different rare-earth cations and non-magnetic Zn^{2+} on structure and magnetism. Synchrotron X-ray powder diffraction data of the Nd compound revealed a high degree of cation ordering with minor antisite disorder between A′ and B sites. Magnetic studies show that rare-earth elements can significantly improve T_C, indicating that they play an important role in enhancing the exchange interaction

between magnetic cations.

In summary, this study emphasizes the critical roles of isovalent and aliovalent doping in governing the structural order and magnetic responses of A-site columnar-ordered quadruple perovskites synthesized under high pressure. By systematically introducing aliovalent Sb^{5+} and varying rare-earth cations (R = Ce, La, Pr, Nd, Sm), we demonstrate that cation charge, size, and distribution significantly affect cation ordering and magnetic interactions, leading to tunable structural motifs and magnetic behaviors such as ferrimagnetism and negative magnetization effects. The findings highlight aliovalent doping as a tool to modulate oxidation states and B-site ordering, while isovalent rare-earth substitution alters exchange interactions and enhances magnetic transition temperatures. Crucially, this work underscores high-pressure synthesis as an essential technique to stabilize these highly ordered and functionally rich perovskite phases that are otherwise inaccessible under ambient conditions.

6.2 Future prospects

This study has demonstrated that aliovalent doping and rare-earth substitution are effective strategies for modulating cation distributions and magnetic behaviors in A-site columnar ordered quadruple perovskites. On this basis, several future directions can be envisioned to further expand this material family.

First, the design of new aliovalent doping systems remains a promising approach for tailoring both B-site oxidation states and ordering patterns. Preliminary data suggest that replacing Sb^{5+} with W^{6+} or Ta^{5+} can lead to the formation of new compounds. Systematic investigations into such substitutions may reveal new ordering regimes and offer a deeper understanding of the interplay between charge balance and structural stability.

Second, the coordination diversity of Zn^{2+} provides a unique opportunity for structural tuning. While Zn typically favors tetrahedral or octahedral coordination environments, our recent findings indicate that it can also be stabilized in square-planar coordination when occupying the A′ site of $A_2A'A''B_4O_{12}$ quadruple perovskites. This suggests that selective substitution of magnetic Mn^{2+} by non-magnetic Zn^{2+} at specific crystallographic positions (such as the A′, A″, and B sites of $A_2A'A''B_4O_{12}$ quadruple perovskites) may yield new magnetic behaviors or magneto-structural coupling

phenomena.

Third, neutron diffraction will be essential for directly resolving the magnetic structures and their evolution, particularly in systems exhibiting compensation behaviors or negative magnetization. Such experiments will provide microscopic insights into the spin arrangements and their coupling with lattice degrees of freedom.

From an application perspective, the observed negative magnetization and tunable ferrimagnetism open up possibilities for device-oriented research. These materials may find use in low-field magnetic sensors, memory elements, or spintronic platforms where compensation phenomena or controlled magnetic switching are required.

Finally, the high-pressure high-temperature (HPHT) synthesis method employed in this work has proven to be an enabling tool for accessing metastable compounds with complex cation arrangements and unconventional coordination geometries. Further development of HPHT synthesis, including finer control of thermodynamic parameters and in situ monitoring techniques, will be crucial for constructing new functional perovskites beyond the thermodynamic limits of ambient conditions.

Overall, the approaches and results presented in this thesis not only provide a blueprint for the rational design of ordered perovskite systems, but also pave the way for future discoveries in magnetic and multifunctional oxide materials.

Appendix A Structural and magnetic data for $Nd_2MnMn(Mn_{4-x}Sb_x)O_{12}$

Table A.1 Results of refinements of occupation factors of the cation sites in $Nd_2MnMn(Mn_{4-x}Sb_x)O_{12}$ (x = 0.8, 0.9, and 1.0); space group $P4_2/nmc$; SQ: square-planar, T: tetrahedral, Oc: octahedral.

x	0.8	0.9	1.0
g(Nd) [a]	0.9356(18)	0.9388(20)	0.9304(18)
B(Nd) (Å^2)	1.320(11)	1.270(13)	1.275(12)
g(Mn1-SQ)	0.603(4)	0.607(5)	0.604(4)
B(Mn1) (Å^2)	1.41(8)	1.78(10)	1.78(9)
g(Mn2-T)	1.164(7)	1.140(7)	1.141(7)
B(Mn2) (Å^2)	0.87(5)	0.71(6)	0.81(6)
g(Mn/Sb-Oc)[a]	0.8Mn+0.2Sb	0.775Mn+0.225Sb	0.75Mn+0.25Sb
B(Mn/Sb) (Å^2)	0.939(15)	0.917(17)	0.943(16)
g(Mn/Sb-Oc)[b]	0.803(2)Mn+0.197Sb	0.778(3)Mn+0.222Sb	0.753(3)Mn+0.247Sb
B(Mn/Sb) (Å^2)	0.922(16)	0.956(16)	0.929(16)
Impurities: $NdMn_7O_{12}$	2.3 %, a = 7.6254 Å, b = 7.2819 Å, c = 7.5637 Å, β = 91.210°	–	–
pyrochlore	0.1 %, a = 10.2864 Å	0.4 %, a = 10.2965 Å	0.2 %, a = 10.2976 Å

[a]All structural and non-structural parameters were refined simultaneously except the occupation factors, g(Mn/Sb-Oc), of the Mn/Sb-Oc site, which were fixed at the nominal values. In this model, only Nd was assumed at the Nd site, and only Mn – at the Mn1-SQ and Mn2-T sites. Deviations from 1 (or from 0.5 for the Mn1-SQ site) indicate the presence of small anti-site disorders.

[b]All structural and non-structural parameters were refined simultaneously except the g(Nd) for the Nd site and g(Mn1-SQ) for the Mn1 site, and the refinements in this model started from the results reported in **Table 3.4**. The following constraint was used, g(Sb)

= 1 – *g*(Mn), for the Mn/Sb-Oc site. These results demonstrate that the refined occupations of the Mn/Sb-Oc site were close to the nominal values.

Table A.2 Results of refinements of occupation factors of the cation sites in $Nd_2MnMn(Mn_{4-x}Sb_x)O_{12}$ (x = 1.5, 1.6, and 1.7); space group $P4_2/n$; SQ: square-planar, T: tetrahedral, Oc: octahedral.

x	1.5	1.6	1.7
g(Nd) [a]	0.965(3)	0.969(4)	0.967(4)
B(Nd) (Å^2)	1.019(11)	0.929(14)	0.848(11)
g(Mn1-SQ)	0.562(5)	0.585(5)	0.558(5)
B(Mn1) (Å^2)	1.53(9)	1.44(10)	1.21(9)
g(Mn2-T)	1.066(8)	1.072(9)	1.052(9)
B(Mn2) (Å^2)	0.55(5)	0.37(6)	0.43(6)
g(Mn3-Oc)[a]	1 fixed	1 fixed	1 fixed
B(Mn3) (Å^2)	0.70(3)	0.74(4)	0.70(3)
g(Sb-Oc)	0.904(3)	0.914(4)	0.941(3)
B(Sb) (Å^2)	0.673(16)	0.489(17)	0.446(13)
g(Mn3-Oc)[b]	0.978(3)	0.991(4)	0.982(4)
B(Mn3) (Å^2)	0.71(3)	0.74(4)	0.69(3)
g(Sb-Oc)	0.760(4)Sb+0.240Mn	0.805(5)Sb+0.195Mn	0.851(4)Sb+0.149Mn
B(Sb) (Å^2)	0.628(16)	0.456(17)	0.424(14)
Impurities:			
Pnma-$GdFeO_3$-type	–	1.5 %, a = 5.7002 Å, b = 7.5970 Å, c = 5.4087 Å	3.6 %, a = 5.7308 Å, b = 7.5836 Å, c = 5.4096 Å
pyrochlore	2.0 %, a = 10.3148 Å	1.1 %, a = 10.3191 Å	1.9 %, a = 10.3241 Å
$P4_2/nmc$	9.1 %, a = 7.6791 Å, c = 7.8334 Å	–	–

[a]All structural and non-structural parameters were refined simultaneously except for the occupation factors, g(Mn3-Oc), of the Mn3-Oc site, which were fixed at unity. In this model, only Nd was assumed at the Nd site, only Mn – at the Mn1-SQ, Mn2-T, and Mn3-Oc sites, and only Sb – at the Sb-Oc site. Deviations from 1 (or from 0.5 for the Mn1-SQ site) indicate the presence of small anti-site disorders.

[b]All structural and non-structural parameters were refined simultaneously except for the g(Nd) for the Nd site and g(Mn1-SQ) for the Mn1 site, and the refinements in this model started from the results reported in **Table 3.5**. The following constraint was used, g(Mn) = 1 – g(Sb), for the Sb-Oc site. These results demonstrate that the refined occupations of the Sb-Oc site were close to the nominal values.

Table A.3 Results of refinements of occupation factors of the cation sites in $Nd_2MnMn(Mn_{4-x}Sb_x)O_{12}$ (x = 1.8, 1.9, and 2.0); space group $P4_2/n$; SQ: square-planar, T: tetrahedral, Oc: octahedral.

x	1.8	1.9	2.0
g(Nd)[a]	0.990(4)	0.981(6)	0.976(7)
B(Nd) (Å^2)	0.806(10)	0.704(13)	0.620(14)
g(Mn1-SQ)	0.559(5)	0.531(8)	0.531(9)
B(Mn1) (Å^2)	0.96(8)	0.96(12)	0.79(12)
g(Mn2-T)	1.059(8)	1.031(13)	1.012(15)
B(Mn2) (Å^2)	0.52(5)	0.42(7)	0.35(8)
g(Mn3-Oc)[a]	1 fixed	1 fixed	1 fixed
B(Mn3) (Å^2)	0.72(3)	0.65(4)	0.63(4)
g(Sb-Oc)	0.952(3)	0.969(5)	0.988(6)
B(Sb) (Å^2)	0.398(11)	0.401(16)	0.365(17)
g(Mn3-Oc)[b]	0.976(3)	0.995(6)	0.993(6)
B(Mn3) (Å^2)	0.63(3)	0.61(4)	0.58(4)
g(Sb-Oc)	0.891(4)Sb+0.109Mn	0.944(7)Sb+0.056Mn	0.984(8)Sb+0.016Mn
B(Sb) (Å^2)	0.383(11)	0.393(17)	0.360(17)
Impurities:	1.0 %, a = 5.7503 Å,	0.5 %, a = 5.7764 Å,	0.5 %, a = 5.8020 Å,
Pnma-$GdFeO_3$-type pyrochlore	b = 7.5842 Å, c = 5.4106 Å	b = 7.5775 Å, c = 5.4152 Å	b = 7.5721 Å, c = 5.4184 Å
	1.5 %, a = 10.3349 Å	0.3 %, a = 10.3381 Å	–
unknown phase[c]	–	$a = b$ = 7.4552 Å, c = 8.8154 Å, $\alpha = \beta$ = 90°, γ = 120°	$a = b$ = 7.4667 Å, c = 8.8133 Å, $\alpha = \beta$ = 90°, γ = 120°

[a]All structural and non-structural parameters were refined simultaneously except for the occupation factors, g(Mn3-Oc), of the Mn3-Oc site, which were fixed at unity. In this model, only Nd was assumed at the Nd site, only Mn – at the Mn1-SQ, Mn2-T, and Mn3-Oc sites, and only Sb – at the Sb-Oc site. Deviations from 1 (or from 0.5 for the Mn1-SQ site) indicate the presence of small anti-site disorders.

[b]All structural and non-structural parameters were refined simultaneously except for the g(Nd) for the Nd site and g(Mn1-SQ) for the Mn1 site, and the refinements in this model started from the results reported in **Table 3.6**. The following constraint was used, g(Mn) = 1 – g(Sb), for the Sb-Oc site. These results demonstrate that the refined occupations of the Sb-Oc site were close to the nominal values.

[c]All reflections of an unknown phase could be indexed in space group R-3.

Table A.4 Structure parameters of $Nd_2MnMn(Mn_{4-x}Sb_x)O_{12}$ (x = 1.8, 1.9, and 2.0) at T = 295 K from synchrotron X-ray powder diffraction data.

x	1.8	1.9	2
a (Å)	7.80190(2)	7.81513(3)	7.82890(3)
c (Å)	7.90843(2)	7.91024(3)	7.91111(4)
V (Å^3)	481.394(2)	483.128(3)	484.886(4)
g(Nd)	0.982(4)Nd+0.018Mn	0.978(6)Nd+0.022Mn	0.974(7)Nd+0.026Mn
z(Nd)	0.77672(2)	0.77681(9)	0.77667(10)
B(Nd) (Å^2)	0.800(10)	0.700(14)	0.614(14)
g(Mn1-SQ)	0.457(3)Mn+0.043Nd	0.474(5)Mn+0.026Nd	0.469(5)Mn+0.031Nd
z(Mn1)	0.7806(5)	0.7783(8)	0.7772(8)
B(Mn1) (Å^2)	1.11(8)	1.05(13)	0.92(13)
g(Mn2-T)	0.960(5)Mn+0.040Nd	0.974(8)Mn+0.026Nd	1Mn
B(Mn2) (Å^2)	0.55(5)	0.45(8)	0.29(7)
g(Mn3-Oc)	1Mn	1Mn	1Mn
B(Mn3) (Å^2)	0.73(2)	0.63(3)	0.58(3)
g(Sb/Mn-Oc)	0.9Sb+0.1Mn	0.95Sb+0.05Mn	1Sb
B(Sb/Mn) (Å^2)	0.381(10)	0.398(16)	0.379(16)
x(O1)	–0.0489(11)	–0.0485(14)	–0.0473(15)
y(O1)	0.5641(11)	0.5768(13)	0.5726(15)
z(O1)	0.2341(6)	0.2355(10)	0.2335(11)
B(O1) (Å^2)	0.79(11)	0.80(17)	0.67(18)
x(O2)	–0.2345(11)	–0.2358(17)	–0.2349(20)
y(O2)	–0.0389(6)	–0.0419(9)	–0.0404(10)
z(O2)	0.5808(6)	0.5839(9)	0.5827(10)
B(O2) (Å^2)	0.59(10)	0.89(16)	0.71(17)
x(O3)	–0.2591(10)	–0.2585(16)	–0.2551(17)
y(O3)	0.0628(5)	0.0659(8)	0.0663(9)
z(O3)	–0.0326(5)	–0.0312(9)	–0.0313(9)
B(O3) (Å^2)	0.57(8)	0.59(12)	0.52(13)
R_{wp} (%)	7.38	12.01	13.12
R_p (%)	5.22	6.64	6.91
R_I (%)	3.26	4.42	4.71
R_F (%)	3.06	3.24	3.08
Impurities	pyrochlore: 1.5% *Pnma*-per.: 1.0%	pyrochlore: 0.3% *Pnma*-per.: 0.5%	*Pnma*-per.: 0.5%

Crystal data: space group $P4_2/n$ (No. 86, cell choice 2), Z = 2.

Nd – 4*e* site (0.25, 0.75, *z*); Mn1-SQ – 4*f* site (0.25, 0.25, *z*); Mn2-T – 2*a* site (0.75, 0.75, 0.75); Mn3-Oc – 4*c* site (0, 0.5, 0.5); Sb/Mn-Oc – 4*d* site (0, 0, 0.5); O1, O2 and

O3 – 8*g* site (*x*, *y*, *z*).

g(O1) = *g*(O2) = *g*(O3) = 1, *g* is the occupation factor.

SQ: square-planar (site), T: tetrahedral (site), Oc: octahedral (site).

Pnma-per.: a $GdFeO_3$-type perovskite phase with *Pnma* symmetry.

Because of the presence of an unidentified impurity in the *x* = 1.9 and 2.0 samples, only a ratio of the weight fractions of the phases is relevant (not absolute values).

Table A.5 Bond lengths (Å), bond angles (deg), bond-valence sum (BVS), and distortion parameters of $(Mn/Sb)O_6$ (Δ) in $Nd_2MnMn(Mn_{4-x}Sb_x)O_{12}$ (x = 0.8, 0.9, and 1.0) at T = 295 K from synchrotron X-ray powder diffraction data.

x	0.8	0.9	1.0
Nd–O1 ×2	2.393(4)	2.401(5)	2.413(4)
Nd–O1 ×2	2.533(4)	2.533(5)	2.476(4)
Nd–O2 ×2	2.475(4)	2.467(5)	2.522(4)
Nd–O3 ×4	2.771(1)	2.778(1)	2.785(11)
BVS(Nd^{3+})	+3.04	+3.03	+2.99
Mn1–O3 ×4	2.037(4)	2.034(5)	2.056(5)
Mn1–O2 ×2	2.808(4)	2.827(5)	2.808(5)
Mn1–O1 ×2	3.065(5)	3.067(5)	3.050(5)
Mn1–Mn1	0.581(6)	0.561(7)	0.586(7)
BVS($Mn1^{2+}$)	+2.24	+2.25	+2.14
Mn2–O2 ×4	2.104(5)	2.109(5)	2.119(4)
Mn2–O1 ×4	2.872(4)	2.874(4)	2.884(4)
BVS($Mn2^{2+}$)	+1.93	+1.90	+1.85
Mn/Sb–O1 ×2	1.968(1)	1.970(1)	1.974(1)
Mn/Sb–O2 ×2	2.015(2)	2.019(2)	2.022(1)
Mn/Sb–O3 ×2	2.090(1)	2.091(2)	2.083(1)
Δ(Mn/Sb)	6.2×10^{-4}	6.0×10^{-4}	4.8×10^{-4}
BVS(Mn^{3+})	+2.96	+2.94	+2.94
BVS(Sb^{5+})	+4.85	+4.81	+4.81
Mn/Sb–O1–Mn/Sb×2	148.9(3)	149.3(3)	149.9(3)
Mn/Sb–O2–Mn/Sb×2	140.4(3)	140.4(3)	141.1(3)
Mn/Sb–O3–Mn/Sb×2	142.89(12)	142.50(13)	142.96(12)

BVS = $\sum_{i=1}^{N} v_i$, $v_i = \exp[(R_0 - l_i)/B]$, N is the coordination number, B = 0.37, $R_0(Nd^{3+})$ = 2.117, $R_0(Mn^{2+})$ = 1.79, $R_0(Mn^{3+})$ = 1.76, $R_0(Sb^{5+})$ = 1.942.

Table A.6 Bond lengths (Å), bond angles (deg), bond-valence sum (BVS), and distortion parameters of $Mn3O_6$ and $(Sb/Mn)O_6$ (Δ) in $Nd_2MnMn(Mn_{4-x}Sb_x)O_{12}$ (x = 1.5, 1.6, and 1.7) at T = 295 K from synchrotron X-ray powder diffraction data.

x	1.5	1.6	1.7
Nd–O1 ×2	2.659(8)	2.737(14)	2.951(11)
Nd–O1 ×2	2.998(8)	2.932(14)	2.736(11)
Nd–O2 ×2	2.495(4)	2.502(5)	2.516(5)
Nd–O3 ×2	2.395(4)	2.373(5)	2.389(4)
Nd–O3 ×2	2.499(4)	2.486(5)	2.484(4)
BVS(Nd^{3+})	+3.02	+3.04	+2.97
Mn1–O3 ×2	3.147(5)	3.159(6)	3.176(6)
Mn1–O2 ×2	2.891(5)	2.869(6)	2.892(6)
Mn1–O1 ×2	2.095(4)	2.103(5)	2.099(5)
Mn1–O1 ×2	2.122(4)	2.138(5)	2.130(5)
Mn1–Mn1	0.526(7)	0.585(8)	0.512(8)
BVS($Mn1^{2+}$)	+1.85	+1.80	+1.81
Mn2–O3 ×4	2.969(4)	2.996(5)	3.005(4)
Mn2–O2 ×4	2.096(5)	2.093(6)	2.099(5)
BVS($Mn2^{2+}$)	+1.91	+1.92	+1.89
Mn3–O1 ×2	2.194(5)	2.205(6)	2.210(5)
Mn3–O2 ×2	2.164(10)	2.170(12)	2.174(10)
Mn3–O3 ×2	2.078(9)	2.085(11)	2.111(10)
Δ(Mn3)	5.2×10^{-4}	5.5×10^{-4}	3.5×10^{-4}
BVS($Mn3^{2+}$)	+2.32	+2.27	+2.19
Sb/Mn–O1 ×2	1.991(5)	1.963(6)	1.967(5)
Sb/Mn–O2 ×2	1.979(10)	1.986(12)	1.988(10)
Sb/Mn–O3 ×2	1.961(9)	1.980(11)	1.959(9)
Δ(Sb/Mn)	4.0×10^{-5}	2.4×10^{-5}	3.9×10^{-5}
BVS(Sb^{5+})	+5.46	+5.47	+5.54
BVS(Mn^{3+})	+3.34	+3.34	+3.39
Mn3–O1–Sb/Mn ×2	141.8(4)	142.8(6)	142.3(5)
Mn3–O2–Sb/Mn ×2	138.4(3)	138.2(3)	138.6(3)
Mn3–O3–Sb/Mn ×2	147.2(3)	145.6(3)	146.2(3)

BVS = $\sum_{i=1}^{N} v_i$, v_i = exp[($R_0 - l_i$)/B], N is the coordination number, B = 0.37, $R_0(Nd^{3+})$ = 2.117, $R_0(Mn^{2+})$ = 1.79, $R_0(Mn^{3+})$ = 1.76, $R_0(Sb^{5+})$ = 1.942.

Table A.7 Bond lengths (Å), bond angles (deg), bond-valence sum (BVS), and distortion parameters of $Mn3O_6$ and $(Sb/Mn)O_6$ (Δ) in $Nd_2MnMn(Mn_{4-x}Sb_x)O_{12}$ (x = 1.8, 1.9, and 2.0) at T = 295 K from synchrotron X-ray powder diffraction data.

x	1.8	1.9	2.0
Nd–O1 ×2	2.767(11)	2.718(13)	2.732(15)
Nd–O1 ×2	2.911(11)	3.002(13)	2.984(15)
Nd–O2 ×2	2.523(4)	2.536(7)	2.534(8)
Nd–O3 ×2	2.422(4)	2.419(7)	2.416(7)
Nd–O3 ×2	2.497(4)	2.475(7)	2.476(7)
BVS(Nd^{3+})	+2.84	+2.87	+2.87
Mn1–O3 ×2	3.151(5)	3.178(8)	3.190(1)
Mn1–O2 ×2	2.892(5)	2.196(9)	2.924(8)
Mn1–O1 ×2	2.139(4)	2.080(7)	2.111(8)
Mn1–O1 ×2	2.168(4)	2.106(7)	2.137(8)
Mn1–Mn1	0.485(7)	0.448(13)	0.430(13)
BVS($Mn1^{2+}$)	+1.65	+1.91	+1.76
Mn2–O3 ×4	2.986(5)	3.016(7)	3.021(7)
Mn2–O2 ×4	2.126(4)	2.093(7)	2.111(8)
BVS($Mn2^{2+}$)	+1.77	+1.91	+1.82
Mn3–O1 ×2	2.195(5)	2.217(8)	2.215(8)
Mn3–O2 ×2	2.189(8)	2.194(13)	2.199(14)
Mn3–O3 ×2	2.096(8)	2.099(12)	2.078(13)
Δ(Mn3)	4.4×10^{-4}	5.5×10^{-4}	8.0×10^{-4}
BVS($Mn3^{2+}$)	+2.22	+2.17	+2.22
Sb/Mn–O1 ×2	1.955(5)	1.986(8)	1.968(9)
Sb/Mn–O2 ×2	1.961(8)	1.986(13)	1.978(14)
Sb/Mn–O3 ×2	1.959(8)	1.972(12)	2.002(13)
Δ(Sb/Mn)	1.7×10^{-6}	1.1×10^{-5}	5.2×10^{-5}
BVS(Sb^{5+})	+5.74	+5.40	+5.38
BVS(Mn^{3+})	+3.51	+3.30	–
Mn3–O1–Sb/Mn ×2	144.6(5)	140.4(6)	142.0(7)
Mn3–O2–Sb/Mn ×2	140.0(3)	138.4(4)	147.6(3)
Mn3–O3–Sb/Mn ×2	148.3(3)	147.4(4)	147.3(4)

BVS = $\sum_{i=1}^{N} v_i$, v_i = exp[($R_0 - l_i$)/B], N is the coordination number, B = 0.37, $R_0(Nd^{3+})$ = 2.117, $R_0(Mn^{2+})$ = 1.79, $R_0(Mn^{3+})$ = 1.76, $R_0(Sb^{5+})$ = 1.942.

Table A.8 Lattice parameters and symmetry of $Nd_2MnMn(Mn_{4-x}Sb_x)O_{12}$ at T = 295 K from X-ray powder diffraction (CuKα radiation) data and synchrotron X-ray powder diffraction data.

x	Symmetry	a (Å)	c (Å)	data source
0.2	$P4_2/nmc$	7.62054	7.83736	X-ray powder diffraction (lab. CuKα radiation) data
0.4	$P4_2/nmc$	7.59926	7.88087	
0.6	$P4_2/nmc$	7.58994	7.90285	
0.8	$P4_2/nmc$	7.58303	7.92141	
0.9	$P4_2/nmc$	7.6012	7.9144	
1.0	$P4_2/nmc$	7.6252	7.8925	
1.2	$P4_2/nmc$	7.6329	7.8828	
	$P4_2/n$	7.7349	7.9024	
1.4	$P4_2/nmc$	7.6582	7.8437	
	$P4_2/n$	7.7577	7.9034	
0.6	$P4_2/nmc$	7.59071	7.90578	synchrotron X-ray powder diffraction data
0.8	$P4_2/nmc$	7.58349	7.92523	
0.9	$P4_2/nmc$	7.59899	7.91997	
1.0	$P4_2/nmc$	7.62652	7.89916	
1.2	$P4_2/nmc$	7.63438	7.88749	
	$P4_2/n$	7.73002	7.90639	
1.4	$P4_2/nmc$	7.65951	7.84658	
	$P4_2/n$	7.75955	7.90452	
1.5	$P4_2/n$	7.74834	7.90920	
	$P4_2/nmc$	7.67908	7.83334	
1.6	$P4_2/n$	7.76781	7.90366	
1.7	$P4_2/n$	7.78827	7.90647	
1.8	$P4_2/n$	7.80190	7.90843	
1.9	$P4_2/n$	7.81513	7.91024	
2.0	$P4_2/n$	7.82890	7.91111	

For tetragonal symmetries ($P4_2/nmc$ and $P4_2/n$), $a = b$ and $\alpha = \beta = \gamma = 90°$.

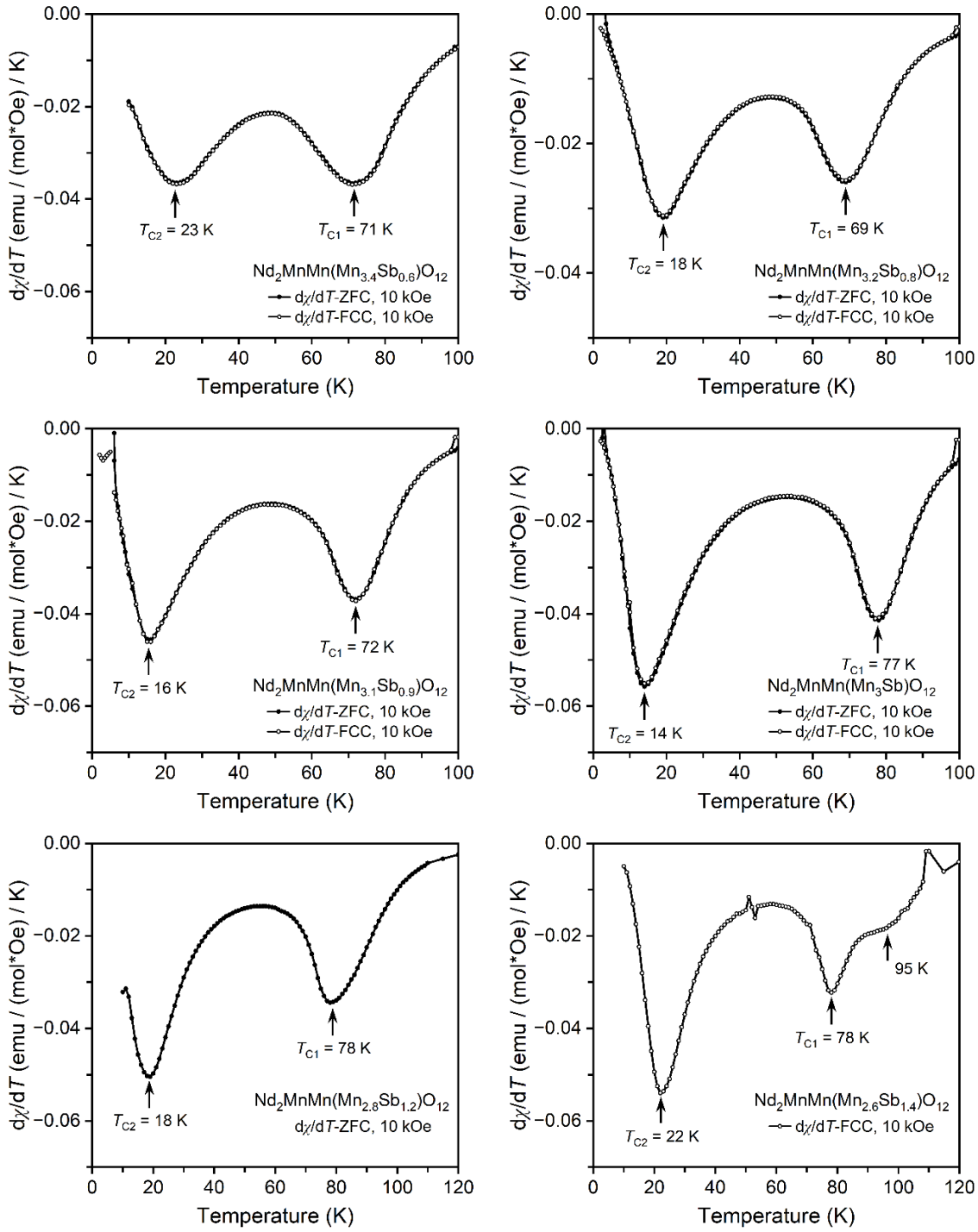

Figure A.1 10 kOe ZFC (filled symbols) and FCC (empty symbols) dχ/dT versus T curves of $Nd_2MnMn(Mn_{4-x}Sb_x)O_{12}$ with x = 0.6, 0.8, 0.9, 1.0, 1.2, and 1.4.

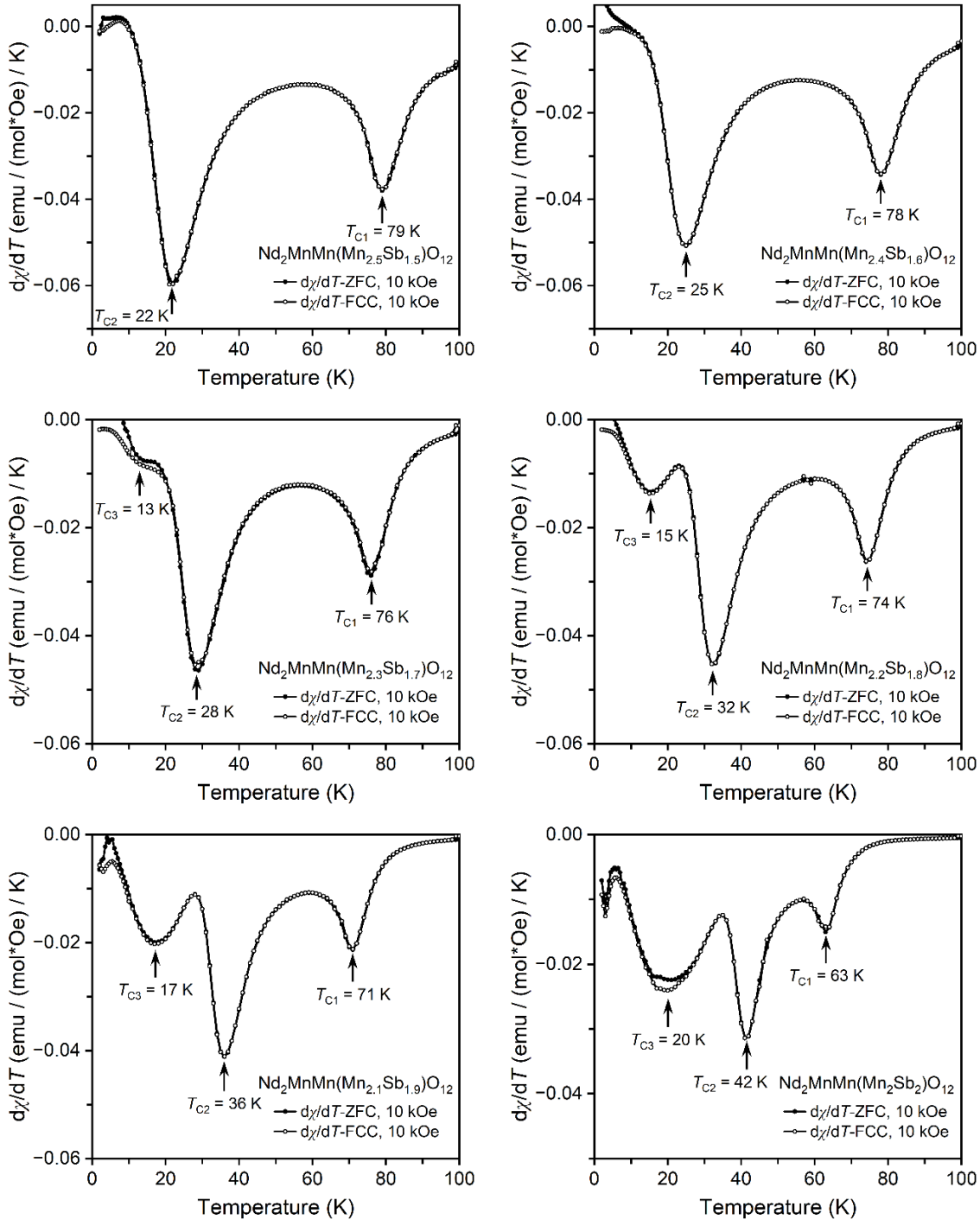

Figure A.2 10 kOe ZFC (filled symbols) and FCC (empty symbols) dχ/dT versus T curves of $Nd_2MnMn(Mn_{4-x}Sb_x)O_{12}$ with $1.5 \leq x \leq 2.0$.

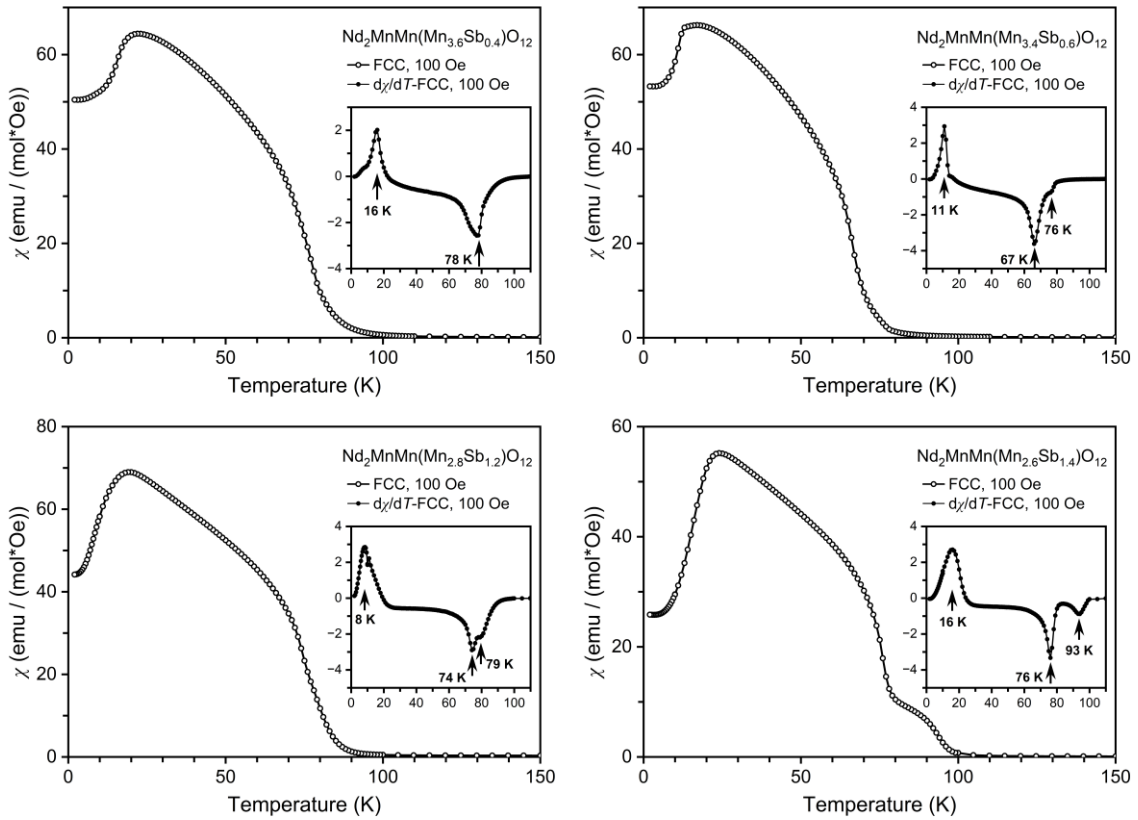

Figure A.3 FCC dc magnetic susceptibility ($\chi = M/H$) curves of $Nd_2MnMn(Mn_{4-x}Sb_x)O_{12}$ with x = 0.4, 0.6, 1.2, and 1.4 measured at 100 Oe. The inset shows 100 Oe FCC $d\chi/dT$ versus T curves.

Appendix B Three perovskite phases with different cation orders in $Sm_2MnMn(Mn_{4-x}Sb_x)O_{12}$

Cation order, which can be controlled by synthesis conditions and stoichiometry, plays an important role in properties of perovskite materials. Here we show that aliovalent doping by Sb^{5+} in $Sm_2MnMn(Mn_{4-x}Sb_x)O_{12}$ quadruple perovskite solid solutions can control cation orders in both A and B sites. Samples with $0.4 \le x \le 2$ were synthesized by a high-pressure, high-temperature method at 6 GPa and 1770 K. Three regions with different cation orders were found at $0.5 \le x \le 1.0$, $x = 1.5$–1.6, and $x = 1.8$. The $0.5 \le x \le 1.0$ compositions have a B-site-disordered and A-site columnar-ordered structure with space group $P4_2/nmc$; the $x = 1.5$ and 1.6 samples have a B-site rock-salt-ordered and A-site columnar-ordered structure with space group $P4_2/n$; the $x = 1.8$ sample has a B-site rock-salt-ordered and A-site-disordered structure with space group $P2_1/n$. All the samples show one ferrimagnetic transition: T_C increases from 35 K to 73 K for $0.5 \le x \le 1.0$, T_C = 81 K for $x = 1.5$ and 1.6, and $T_C = 53$ K for $x = 1.8$. Only representative results are included here to highlight the key findings.

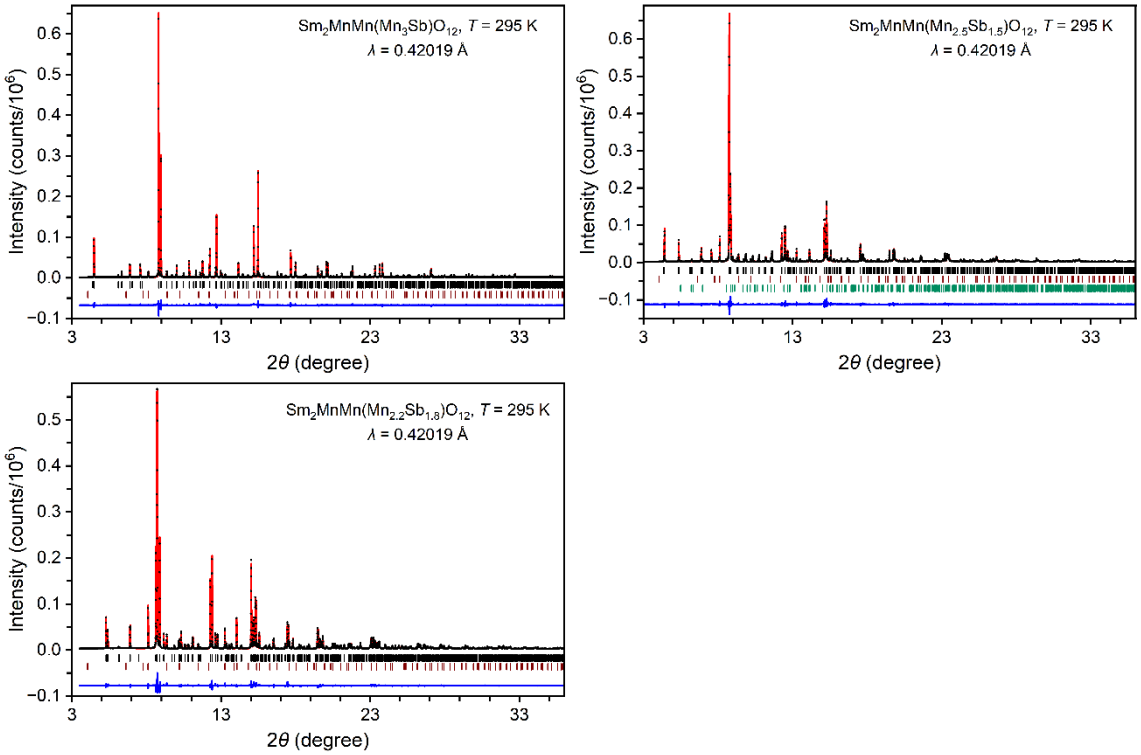

Figure B.1 Fragments of experimental (black crosses), calculated (red line), and difference (blue line) synchrotron X-ray powder diffraction (XRPD) patterns of $Sm_2MnMn(Mn_{4-x}Sb_x)O_{12}$ with x = 1, 1.5, and 2 at T = 295 K. Synchrotron XRPD pattern of $Sm_2MnMn(Mn_3Sb)O_{12}$ as a representative example of the $P4_2/nmc$ space group, the tick marks show possible Bragg reflection positions of the main perovskite phase (the first black row) and pyrochlore impurity (the second red row). Synchrotron XRPD pattern of $Sm_2MnMn(Mn_{2.5}Sb_{1.5})O_{12}$ as a representative example of the $P4_2/n$ space group, the tick marks show possible Bragg reflection positions of the main perovskite phase (the first black row), pyrochlore impurity (the second red row), and impurity with *Pnma* symmetry (the third green row). For $Sm_2MnMn(Mn_{2.2}Sb_{1.8})O_{12}$ with $P2_1/n$ space group, the tick marks show possible Bragg reflection positions of the main perovskite phase (the first black row) and pyrochlore impurity (the second red row).

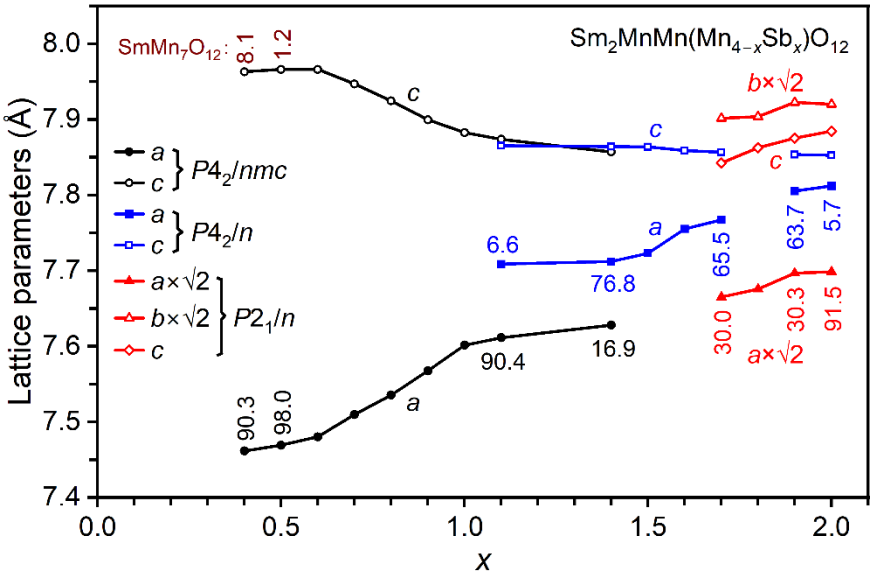

Figure B.2 Compositional dependence of the lattice parameters in $Sm_2MnMn(Mn_{4-x}Sb_x)O_{12}$ solid solutions for $0.4 \le x \le 2.0$ from synchrotron XRPD data at room temperature. Numbers show weight fractions (in %) of corresponding phases for multi-phased samples. Sample with x = 0.4 crystallized in space group $P4_2/nmc$ and contained about 8.1 wt. % of $SmMn_7O_{12}$ perovskite $AA'_3B_4O_{12}$-type impurity; Samples with $0.5 \le x \le 1.0$ have a B-site-disordered and A-site columnar-ordered structure with space group $P4_2/nmc$; the x = 1.5 and 1.6 samples have a B-site rock-salt-ordered and A-site columnar-ordered structure with space group $P4_2/n$; the x = 1.8 sample has a B-site rock-salt-ordered and A-site-disordered structure with space group $P2_1/n$. Samples with x = 1.7, 1.9, 2.0 were a mixture of $P4_2/n$ and $P2_1/n$ phases, and the x = 2.0 sample additionally contained an unidentified impurity (all impurity peaks could be indexed in space group $R\bar{3}$ with a = 7.4299 Å and c = 8.7800 Å). See **Table B.1** for details.

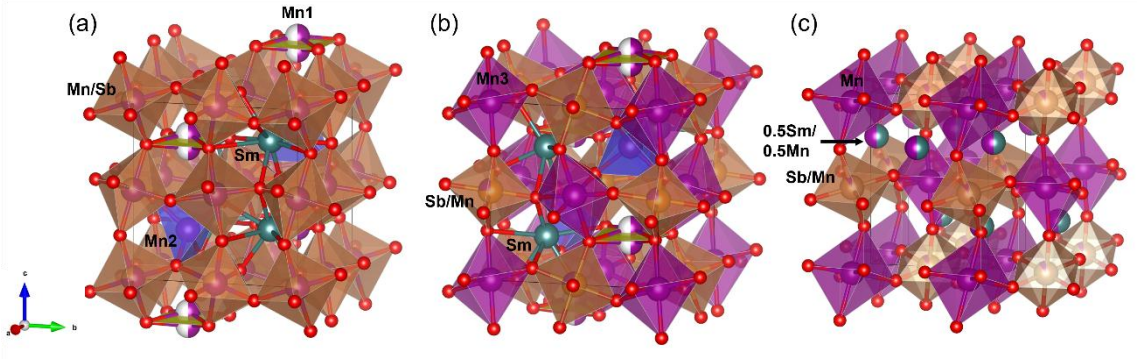

Figure B.3 Fragments of crystal structures of $Sm_2MnMn(Mn_{4-x}Sb_x)O_{12}$ with different space groups in a polyhedral presentation. a) $P4_2/nmc$, b) $P4_2/n$, and c) $P2_1/n$. $Mn1O_4$ square-planar (yellow), $Mn2O_4$ tetrahedra (blue), $(Mn/Sb)O_6$ or $(Sb/Mn)O_6$ octahedra (orange), and $Mn3O_6$ or MnO_6 octahedra (purple) are shown.

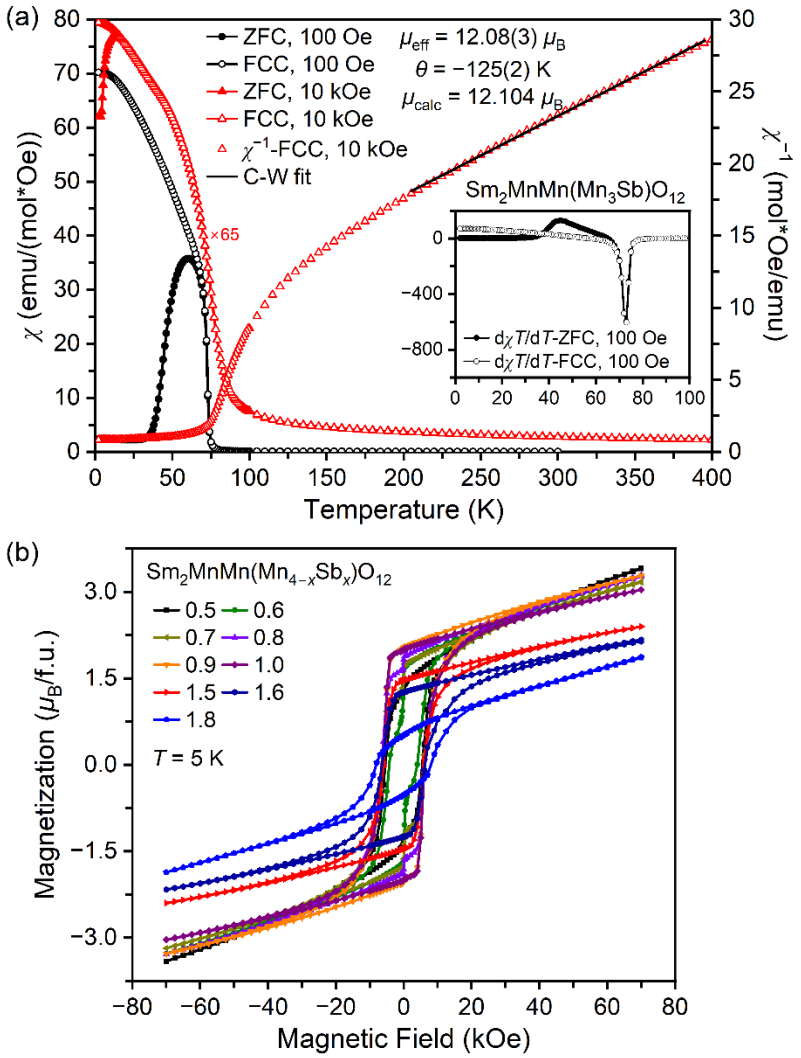

Figure B.4 (a) ZFC (filled symbols) and FCC (empty symbols) dc magnetic susceptibility ($\chi = M/H$) curves of $Sm_2MnMn(Mn_{4-x}Sb_x)O_{12}$ with x = 1.0 measured at 100 Oe (black, circles) and 10 kOe (red, triangles). The black line gives the FCC χ^{-1} versus T curves at 10 kOe with the Curie–Weiss fit (C–W fit). The inset shows 100 Oe ZFC and FCC $d\chi T/dT$ versus T curves. (b) M versus H curves of $Sm_2MnMn(Mn_{4-x}Sb_x)O_{12}$ with $x = 0.5 \leq x \leq 1.0$, 1.5, 1.6, and 1.8 at 5 K. See **Table B.2** for details.

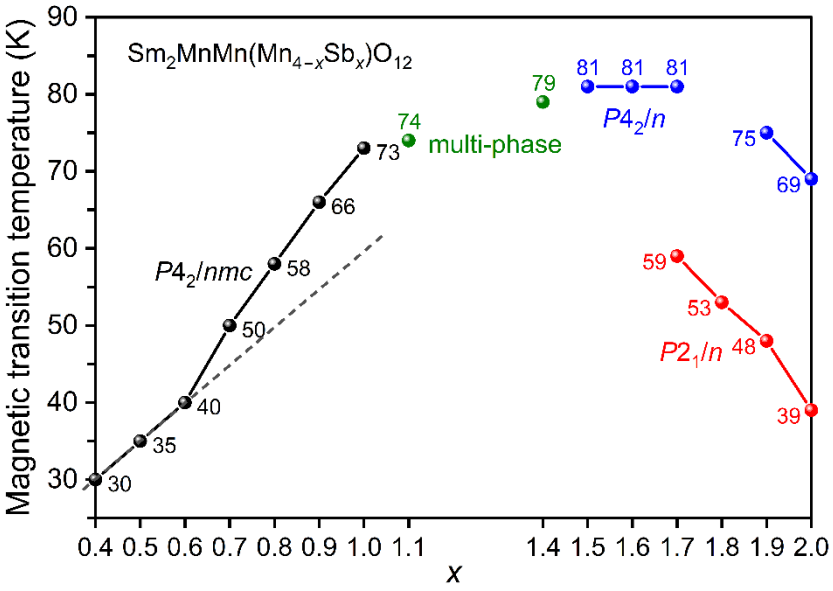

Figure B.5 The ferrimagnetic Curie temperature (T_C) of $Sm_2MnMn(Mn_{4-x}Sb_x)O_{12}$ with $0.4 \leq x \leq 1.1$ and $1.4 \leq x \leq 2.0$. Numbers show the T_C values in K. See **Table B.2** for details.

Table B.1 Lattice parameters and symmetry of $Sm_2MnMn(Mn_{4-x}Sb_x)O_{12}$ at T = 295 K from synchrotron X-ray powder diffraction data.

x	Symmetry	a (Å)	b (Å)	c (Å)	β (°)
0.4	$P4_2/nmc$	7.46151		7.96307	
0.5	$P4_2/nmc$	7.46910		7.96619	
0.6	$P4_2/nmc$	7.48014		7.96614	
0.7	$P4_2/nmc$	7.50953		7.94695	
0.8	$P4_2/nmc$	7.53536		7.92448	
0.9	$P4_2/nmc$	7.56748		7.89950	
1.0	$P4_2/nmc$	7.60131		7.88261	
1.1	$P4_2/nmc$	7.61131		7.87379	
	$P4_2/n$	7.70880		7.86524	
1.4	$P4_2/nmc$	7.62790		7.85699	
	$P4_2/n$	7.71198		7.86390	
1.5	$P4_2/n$	7.72306		7.86363	
1.6	$P4_2/n$	7.75512		7.85881	
1.7	$P4_2/n$	7.76709		7.85648	
	$P2_1/n$	5.41991	5.58726	7.84227	90.2908
1.8	$P2_1/n$	5.42746	5.58884	7.86242	90.2732
1.9	$P4_2/n$	7.80522		7.85344	
	$P2_1/n$	5.44235	5.60207	7.87506	90.2301
2.0	$P4_2/n$	7.81194		7.85250	
	$P2_1/n$	5.44356	5.60033	7.88457	90.2325

Table B.2 Temperatures of magnetic anomalies and parameters of Curie–Weiss fits and M versus H curves at T = 5 K for $Sm_2MnMn(Mn_{4-x}Sb_x)O_{12}$ with $x = 0.5 \leq x \leq 1.0$, 1.5, 1.6, and 1.8.

x	T_C (K)	μ_{eff} (μ_B/f.u.)	μ_{calc} (μ_B/f.u.)	θ (K)	M_S (μ_B/f.u.)	M_R (μ_B/f.u.)	H_C (kOe)
0.5	35	11.91(3)	12.145	–114(2)	3.411	1.355	4.00
0.6	40	11.84(2)	12.137	–113.9(11)	3.276	1.616	5.46
0.7	50	12.08(3)	12.128	–127(2)	3.180	1.678	5.82
0.8	58	12.00(2)	12.120	–114(2)	3.265	1.830	6.19
0.9	66	12.29(2)	12.112	–119.0(12)	3.280	2.029	6.23
1.0	73	12.08(3)	12.104	–125(2)	3.036	2.000	6.15
1.5	81	12.06(2)	12.062	–110.2(12)	2.399	1.467	5.86
1.6	81	12.23(1)	12.054	–115.1(7)	2.164	1.263	6.20
1.8	53	12.14(2)	12.037	-102.5(13)	1.859	0.518	7.98

Appendix C Ca_2CuWO_6: A triclinically-distorted double perovskite with low-dimensional magnetic behavior

$A_2CuB'O_6$ double perovskites with A = Sr and Ba and B′ = W, Te, and Mo have received a lot of attention in the literature as material candidates for the spin-liquid ground state and frustrated spin lattices. However, Ca analogues have not been reported yet. In this work, the Ca_2CuWO_6 double perovskite was synthesized by a high-pressure, high-temperature method at 6 GPa and between 1370 and 2020 K. The crystal structure was studied by synchrotron X-ray powder diffraction between 100 K and 1000 K. Ca_2CuWO_6 crystallizes in the triclinic space group $P\bar{1}$ between 100 K and 1000 K with the onset of partial decomposition above 750 K. Room-temperature lattice parameters are a = 5.68435 Å, b = 7.51261 Å, c = 5.49548 Å, α = 90.0703°, β = 94.7634°, and γ = 90.2311°. Ca_2CuWO_6 demonstrates low-dimensional magnetic properties with the broad maximum of the magnetic susceptibility around 60 K caused by the dominant second-neighbor interactions within the deformed square planes of the Cu^{2+} ions. A long-range antiferromagnetic order takes place at T_N = 32 K. A magnetic field-induced transition was observed at 28 kOe (at 2 K and 5 K), 29 kOe (at 10 K), 30 kOe (at 15 K), 32 kOe (at 20 K), and 36 kOe (at 25 K). Solid solutions $Ca_{2-x}Sr_xCuWO_6$ with x = 0.5, 1, and 1.5 were also prepared. The x = 0.5 and 1 samples crystallize in the space group $P\bar{1}$ at room temperature, while the x = 1.5 sample has monoclinic symmetry (space group $P2_1/n$). They also show low-dimensional magnetic behavior, T_N = 32–34 K, and magnetic field-induced transitions. Only representative results are included here to highlight the key findings.

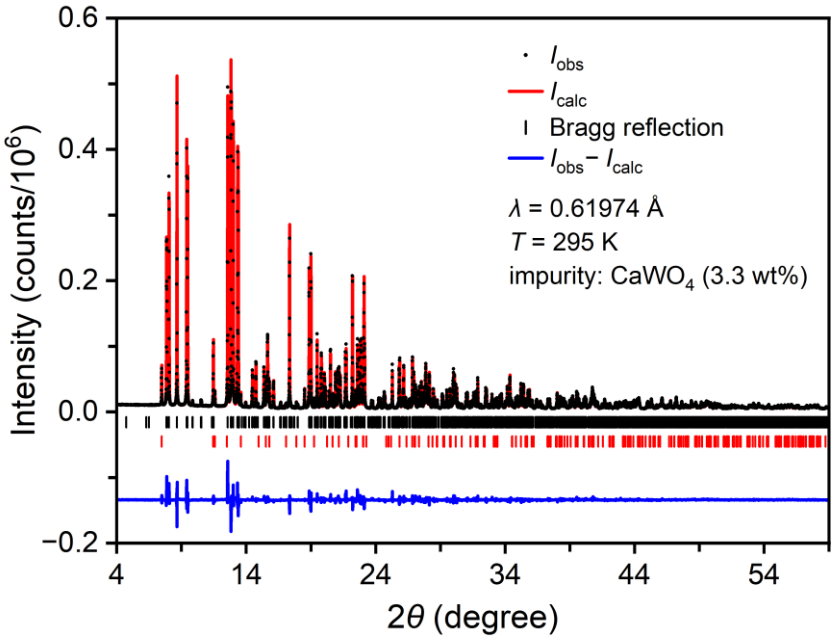

Figure C.1 Fragments of the experimental (black circles), calculated (red line), and difference (blue line at the bottom) synchrotron X-ray powder diffraction (XRPD) patterns of Ca_2CuWO_6 at T = 295 K. The tick marks show possible Bragg reflection positions of the main perovskite phase (the first black row) and $CaWO_4$ impurity (the second red row). The Rietveld refinement confirmed that Ca_2CuWO_6 crystallizes in the triclinic space group P–1 which has never been observed in the other members of the A_2MWO_6 family. See **Table C.1** for details.

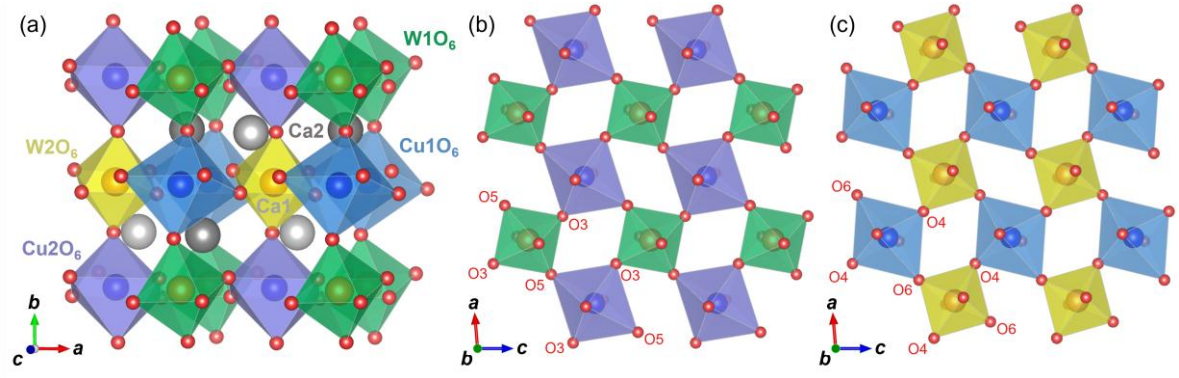

Figure C. 2 (a) Fragments of the Ca_2CuWO_6 crystal structure with the *P*–1 space group in a polyhedral presentation. The $Cu1O_6$, $Cu2O_6$, $W1O_6$, and $W2O_6$ octahedra are shown. The Ca atoms are presented by large grey spheres. Two types of octahedral arrangements along the *b* axis with (b) $Cu2O_6$-$W1O_6$ and (c) $Cu1O_6$-$W2O_6$ types. The highly distorted CuO_6 octahedra with the sizable octahedral distortion parameter (Δ(Cu)) can be ascribed to the Jahn–Teller (JT) effect of the Cu^{2+} ions. See **Table C.2** for details.

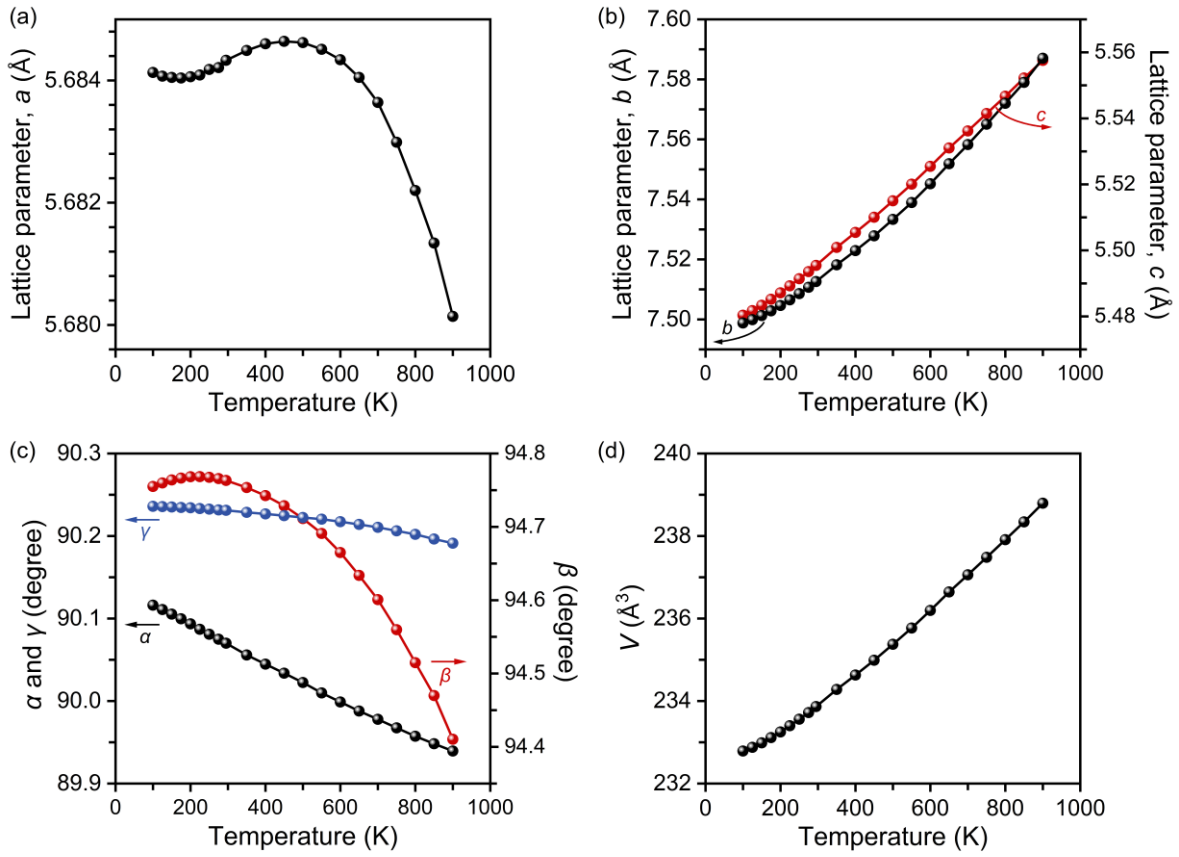

Figure C.3 Unit-cell parameters (*a*, *b*, *c*, *α*, *β*, and *γ*) and volume (*V*) as a function of temperature for Ca_2CuWO_6 from synchrotron XRPD data measured on heating. It demonstrates anisotropic thermal expansion above 450 K and partially decomposes above about 750 K.

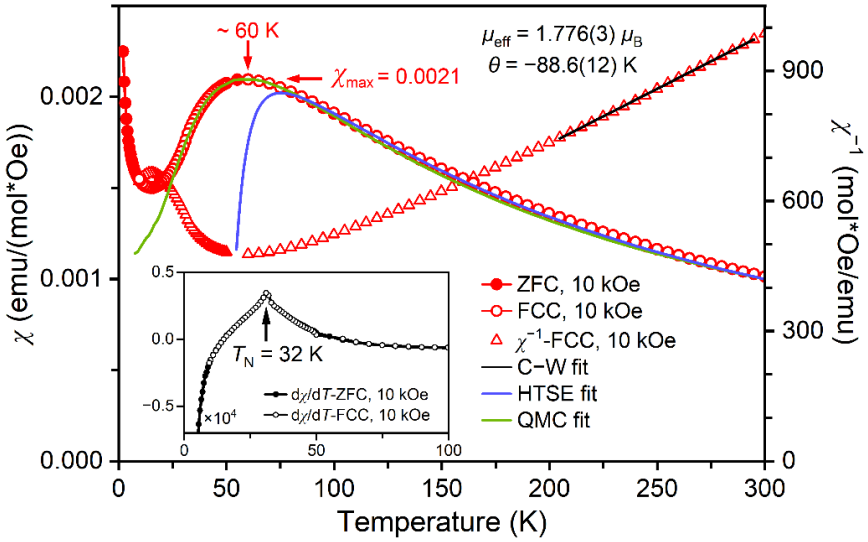

Figure C.4 ZFC (filled red circles) and FCC (empty red circles) dc magnetic susceptibility ($\chi = M/H$) curves for Ca_2CuWO_6 measured at 10 kOe. The black line shows the Curie–Weiss fit (C–W fit) of the FCC χ^{-1} versus T curve. The high-temperature series expansion (HTSE) and quantum Monte-Carlo (QMC) fits, as described in the text, are also shown. The inset presents the dχ/dT versus T curves. A broad maximum of the magnetic susceptibility is observed at around 60 K originating from low-dimensional magnetism – a characteristic feature commonly observed in the A_2CuWO_6 double perovskites. The temperature at which these maxima occur serves as an indicator of the magnitude of the predominant antiferromagnetic (AFM) exchange interactions. With decreasing temperature, a long-range AFM order takes place below T_N (Néel temperature) = 32 K, as evidenced by peaks in the ZFC and FCC dχ/dT versus T curves.

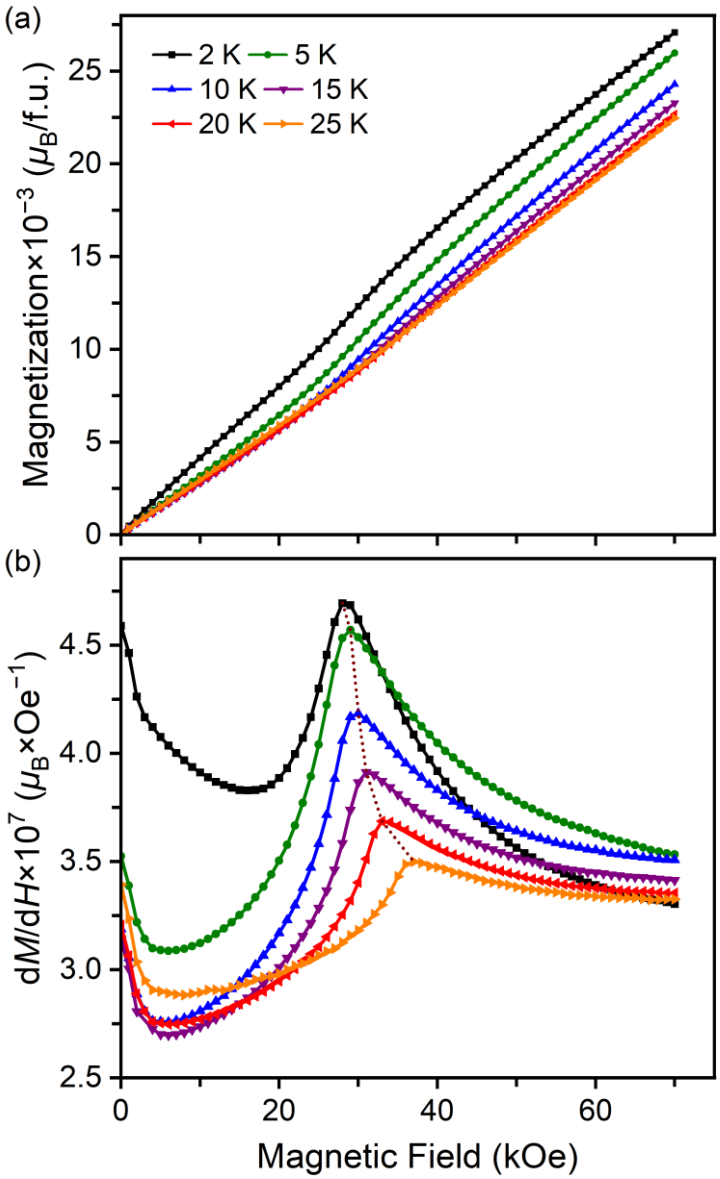

Figure C.5 (a) *M* versus *H* curves and (b) derivative of magnetization curves (d*M*/d*H* versus *H*) for Ca_2CuWO_6 at different temperatures. The dotted line is drawn for eye. There was almost no hysteresis near the origin (zero magnetic field) suggesting a purely AFM state. Furthermore, the *M* versus *H* curves at different temperatures indicate a magnetic field-induced transition at 28 kOe (at 2 K and 5 K), 29 kOe (at 10 K), 30 kOe (at 15 K), 32 kOe (at 20 K), and 36 kOe (at 25 K).

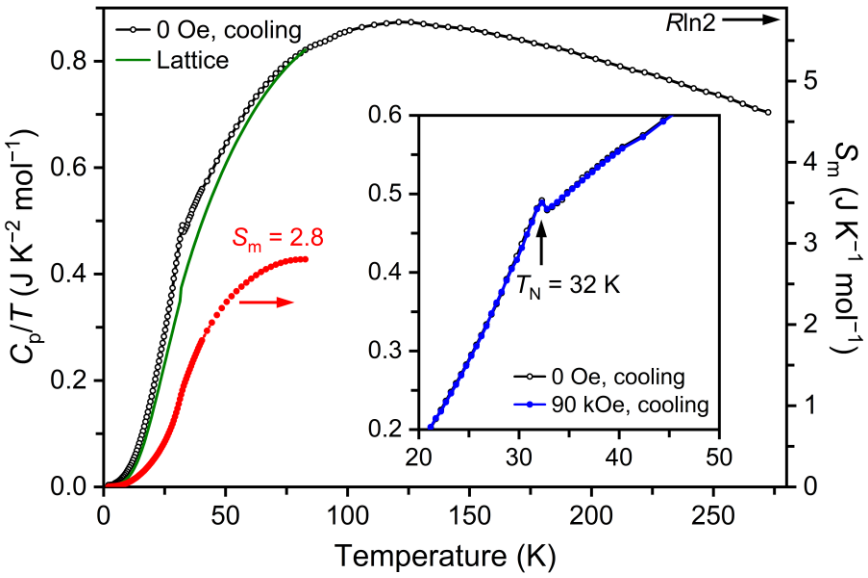

Figure C.6 Specific heat data, C_p/T (empty circles; measured on cooling at H = 0 Oe) and magnetic entropy, S_m (filled red circles), of Ca_2CuWO_6 as a function of T are shown in the left and right y axes, respectively. The green line shows the estimated lattice contribution (see the text). The inset presents the C_p/T versus T measured on cooling at H = 0 Oe (empty circles) and 90 kOe (filled blue circles) in the vicinity of T_N.

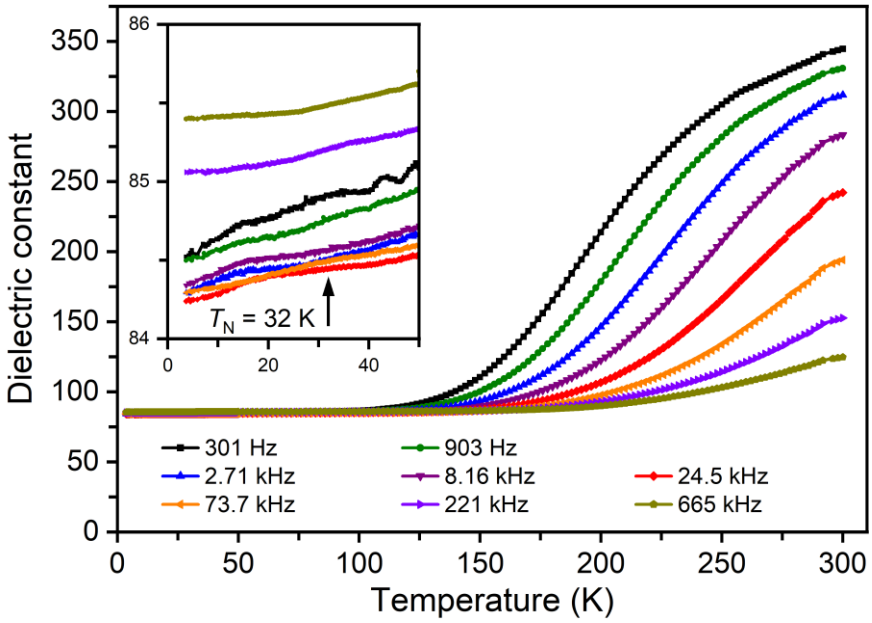

Figure C.7 Frequency-dependent (from 301 Hz to 665 kHz) dielectric constant of Ca_2CuWO_6 as a function of temperature measured at H = 0 Oe on heating. The inset shows a zoomed part in the vicinity of T_N.

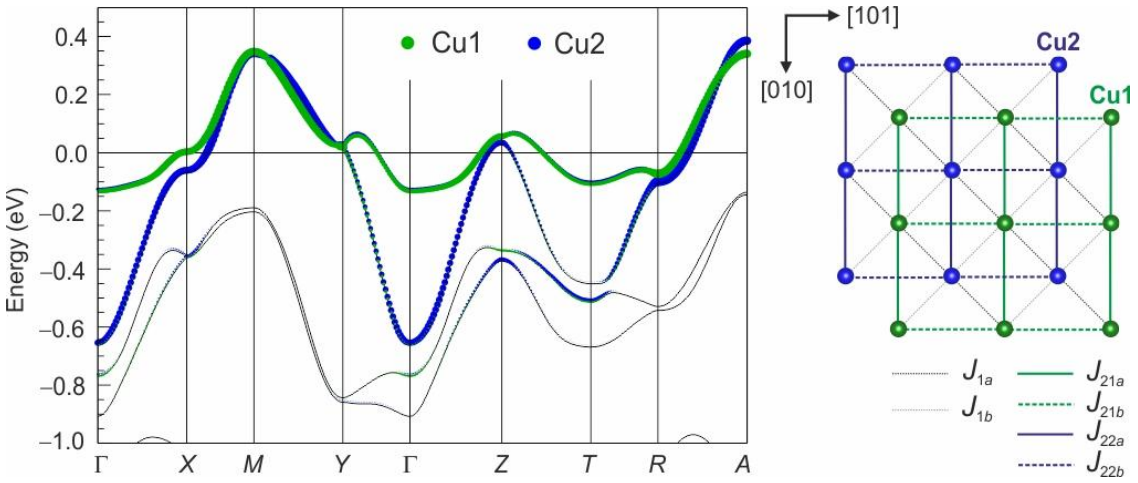

Figure C.8 Left: PBE band structure of Ca_2CuWO_6 with the band weights due to the Cu1 and Cu2 $d_{x^2-y^2}$ orbitals. The Fermi level is at zero energy. Right: spin lattice of Ca_2CuWO_6 (see Table IV for the list of the exchange couplings). The Fermi level is crossed by two bands with the predominant Cu $d_{x^2-y^2}$ character that corresponds to the highest-energy crystal-field level of Cu^{2+} in the distorted octahedral coordination. Each of the two bands is formed by Cu1 and Cu2, respectively, with only a weak hybridization. This separation of the orbital characters indicates that the magnetic sublattices of Cu1 and Cu2 are largely decoupled. Indeed, the hopping parameters extracted from the Wannier fit of the two $d_{x^2-y^2}$ bands reveal stronger couplings within each sublattice and much weaker couplings between the sublattices (**Table C.4**). Each sublattice represents a deformed square lattice (rectangular lattice) lying in the (10-1) plane of the crystal structure. Whereas the Cu1 sublattice is almost regular, the Cu2 sublattice shows a sizable difference between the couplings along the [010] and [101] directions within the plane. The leading interplane hopping is about 5 meV, at least one order of magnitude smaller than the in-plane hoppings. Therefore, Ca_2CuWO_6 should be understood as a quasi-2D antiferromagnet, in agreement with the experiment.

Table C.1 Structure parameters of Ca_2CuWO_6 at 295 K from synchrotron X-ray powder diffraction data.

site	WP	*g*	*x*	*y*	*z*	B_{iso} (Å^2)
Ca1	2*i*	1	0.0547(5)	0.2522(3)	1.0021(5)	0.71(5)
Ca2	2*i*	1	0.5519(5)	0.2497(3)	0.5150(5)	0.77(5)
Cu1	1*e*	1	0.5	0.5	0	1.12 (8)
Cu2	1*b*	1	0	0	0.5	0.11(6)
W1	1*d*	1	0.5	0	0	0.44(2)
W2	1*g*	1	0	0.5	0.5	0.23(2)
O1	2*i*	1	0.4720(12)	0.2454(11)	0.0867(13)	0.25(14)
O2	2*i*	1	0.9736(13)	0.2590(11)	0.4270(14)	0.59(15)
O3	2*i*	1	0.3119(11)	0.0467(9)	0.7016(13)	0.59(14)
O4	2*i*	1	0.7059(12)	0.5521(10)	0.3037(13)	0.92(15)
O5	2*i*	1	0.2283(12)	0.9438(9)	0.1658(13)	0.96(15)
O6	2*i*	1	0.8353(12)	0.4563(10)	0.7766(12)	0.73(13)

Synchrotron X-ray powder diffraction (λ = 0.61974 Å); *d* range used in the refinement: from 0.532 Å to 8.879 Å. Crystal system: triclinic; space group: *P*–1 (No. 2, origin choice 1), *Z* = 2. Molecular weight: 423.5384 g/mol. *a* = 5.68435(1) Å, *b* = 7.51261(2) Å, *c* = 5.49548(1) Å, α = 90.0703(2)°, β = 94.7634(2)°, γ = 90.2310(2)°, and *V* = 233.8677(8) Å^3; R_{wp} = 5.94%, R_p = 4.50%, R_I = 2.26%, and R_F = 1.19%. WP = Wyckoff position. *g* is the occupation factor.

Table C.2 Selected bond lengths, angles, octahedral distortion parameters (Δ), and bond valence sums (BVS) for Ca_2CuWO_6 at T = 295 K.

Ca1–O1	2.379(8)	Ca2–O1	2.360(8)
Ca1–O2	2.418(9)	Ca2–O2	2.485(8)
Ca1–O3	2.768(8)	Ca2–O3	2.670(8)
Ca1–O4	2.696(8)	Ca2–O3	2.336(8)
Ca1–O5	2.651(8)	Ca2–O4	2.719(8)
Ca1–O5	2.311(8)	Ca2–O4	2.362(8)
Ca1–O6	2.554(8)	Ca2–O5	2.531(8)
Ca1–O6	2.282(8)	Ca2–O6	2.581(8)
BVS (Ca1)	2.06	BVS (Ca2)	1.99
Cu1–O1 ×2	1.980(8)	Cu2–O2 ×2	1.991(8)
Cu1–O4 ×2	2.008(7)	Cu2–O3 ×2	2.040(7)
Cu1–O6 ×2	2.375(7)	Cu2–O5 ×2	2.374(7)
BVS (Cu1)	2.01	BVS (Cu2)	1.92
Δ (Cu1)	7.2×10^{-3}	Δ (Cu2)	6.4×10^{-3}
W1–O5 ×2	1.903(7)	W2–O2 ×2	1.857(8)
W1–O1 ×2	1.914(8)	W2–O6 ×2	1.879(7)
W1–O3 ×2	1.915(7)	W2–O4 ×2	1.946(7)
BVS (W1)	6.17	BVS (W2)	6.49
Δ (W1)	8.1×10^{-6}	Δ (W2)	4.0×10^{-4}
Cu1–O1–W1	149.3(5)	Cu2–O2–W2	155.0(5)
Cu1–O4–W2	146.5(5)	Cu2–O3–W1	146.3(4)
Cu1–O6–W2	150.3(4)	Cu2–O5–W1	148.1(4)

$\text{BVS} = \sum_{i=1}^{N} v_i$, $v_i = \exp[(R_0 - l_i)/B]$, N is the coordination number, l_i is a bond length, B = 0.37, $R_0(Ca^{2+})$ = 1.967, $R_0(Cu^{2+})$ = 1.679, $R_0(W^{6+})$ = 1.921.

Table C.3 Lattice parameters of $Ca_{2-x}Sr_xCuWO_6$ (x = 0, 0.5, 1, 1.5, and 2) at T = 295 K from the synchrotron[a] and laboratory[b] X-ray powder diffraction data, the Néel temperatures (T_N), and main parameters extracted from the magnetic susceptibility curves: position (T_{max}) and height (χ_{max}) of the susceptibility maximum, the effective moment and Curie-Weiss temperature (from the Curie–Weiss fits), as well as J_1 and J_2 (from the HTSE fits above 80 K for x = 0, above 90 K for x = 0.5, 1, 1.5, and above 100 K for x = 2).

x	0[a]	0.5[a]	1[a]	1.5[a]	2[b]
space group	P–1	P–1	P–1	$P2_1/n$	$I4/m$
a (Å)	5.68435(1)	5.68310(3)	5.67677(3)	5.67514(2)	5.4284(1)
b (Å)	7.51261(2)	7.56989(3)	7.62931(4)	7.68165(3)	= a
c (Å)	5.49548(1)	5.56063(3)	5.62368(3)	5.65900(3)	8.4155(2)
α (°)	90.0703(2)	89.9575(6)	89.8954(5)	90	90
β (°)	94.7634(2)	94.8187(4)	94.7683(3)	94.8384(3)	90
γ (°)	90.2310(2)	90.2037(4)	90.1552(5)	90	90
V (Å^3)	233.8677(8)	238.374(2)	242.717(2)	245.822(2)	247.986(9)
μ_{eff} (μ_B/f.u.)	1.776(3)	1.693(4)	1.689(3)	1.907(9)	1.649(9)
θ (K)	–88.6(12)	–83.6(9)	–101.2(11)	–163(4)	–155(4)
T_N (K)	32	32	33	34	24 [34]
χ_{max} (emu/(mol*Oe))	0.0021	0.0020	0.0017	0.0017	0.0013
T_{max} (K)	60	55	65	72	72
$T_{max}/\|\theta\|$	0.677	0.658	0.642	0.442	0.465
J_1 (K)	18	15	9	6	6
J_2 (K)	65	68	78	85	97

Table C.4 Magnetic couplings in Ca_2CuWO_6: interatomic distances d_i, hopping parameters t_i (from the Wannier fits), and exchange couplings J_i (from the mapping analysis).

		d_i (Å)	t_i (meV)	J_i (K)
J_{1a}	Cu1–Cu2	5.323	43	9
J_{1b}	Cu1–Cu2	5.343	43	9
J_{21a}	Cu1–Cu1	7.513	78	54
J_{21b}	Cu1–Cu1	7.571	80	51
J_{22a}	Cu2–Cu2	7.513	95	80
J_{22b}	Cu2–Cu2	7.571	79	50

List of appended publications

1. Scientific papers

1. **Xuan Liang**; Kazunari Yamaura; Alexei A. Belik. Negative Magnetization Phenomena in A-site Columnar-Ordered Quadruple Perovskites $Ce_2MnM(Mn_2Sb_2)O_{12}$ with M = Mn and Zn. *Inorg. Chem.* **2025** (Accepted).

2. **Xuan Liang**; Kazunari Yamaura; Alexander A. Tsirlin; Alexei A. Belik. Ca_2CuWO_6: A triclinically distorted double perovskite with low-dimensional magnetic behavior. *Phys. Rev. B* **2025**, *111*, 094432.

3. **Xuan Liang**; Kazunari Yamaura; Alexei A. Belik. B-site ordered and disordered phases in A-site columnar-ordered quadruple perovskites $Nd_2MnMn(Mn_{4-x}Sb_x)O_{12}$. *Ceram. Int.* **2024**, *50*, 53099–53106.

4. **Xuan Liang**; Kazunari Yamaura; Alexei A. Belik. Three perovskite phases with different cation orders in $Sm_2MnMn(Mn_{4-x}Sb_x)O_{12}$. *Chem. - Eur. J.* **2024**, *30*, e202401960.

2. Oral presentation

1. **Xuan Liang**; Kazunari Yamaura; Alexei A. Belik. “Three perovskite phases with different cation orders in $Sm_2MnMn(Mn_{4-x}Sb_x)O_{12}$”; The 34ed Annual Meeting of MRS-J, Dec., 16–18, 2024, Yokohama, Japan.

Acknowledgement

I would like to express my deepest gratitude to Prof. Kazunari Yamaura for giving me the opportunity to pursue my studies at the Graduate School of Chemical Sciences and Engineering (CSE), Hokkaido University, as well as at the Research Center for Materials Nanoarchitectonics (MANA), National Institute for Materials Science (NIMS). His warm encouragement and profound expertise have been a constant source of strength throughout my academic journey and personal life.

I am especially indebted to my co-supervisor, Dr. Alexei. A. Belik, for his unwavering support and insightful mentorship. His patient guidance and thoughtful instruction not only sharpened my scientific thinking but also inspired me to approach research with curiosity and rigor. His meticulous feedback on my writing and analysis greatly improved the quality of my work.

I also wish to thank the Assoc. Prof. Yoshihiro Tsujimoto in our group for his invaluable technical guidance, particularly in the use of high-pressure apparatus and other experimental techniques, which were central to my research.

My sincere appreciation goes to Ms. Etsuko Sakai , our group secretary. Her tireless assistance in both administrative and everyday matters has been essential to my smooth adaptation to life and research in Japan.

I am grateful to Dr. Yuichi Shirako, Dr. Rachida Lamouri, Dr. Xun Kang, Dr. Hiroaki Hayashi, Dr. Yu Meng, Mr. Shaoxuan Li, and the PhD students—Zhijun Li and Hongbo Yuan—for their support, friendship, and help both in research and daily life.

I also extend my heartfelt thanks to the administrative staff of CSE Office at Hokkaido University for their dedication and assistance over the past three years.

I am especially grateful to my dear friends Lei Xu, Yawen Du, and Wenyan Xiong, whose companionship and support outside the lab helped me stay grounded and cheerful throughout my PhD journey.

Last but not least, I would like to express my deepest gratitude to my girlfriend Yarui Luo, my parents Aishan Liang and Shaoqin Dai, and my sisters Ying Liang and Rui Min. Your unconditional love, unwavering support, and constant encouragement have been the foundation upon which this thesis stands.